



**HAL**  
open science

# Low-level visual cortex and motion perception: an MRI study

Nicolas Wotawa

► **To cite this version:**

Nicolas Wotawa. Low-level visual cortex and motion perception: an MRI study. Neurons and Cognition [q-bio.NC]. Université Nice Sophia Antipolis, 2006. English. NNT: . tel-00071516

**HAL Id: tel-00071516**

**<https://theses.hal.science/tel-00071516>**

Submitted on 23 May 2006

**HAL** is a multi-disciplinary open access archive for the deposit and dissemination of scientific research documents, whether they are published or not. The documents may come from teaching and research institutions in France or abroad, or from public or private research centers.

L'archive ouverte pluridisciplinaire **HAL**, est destinée au dépôt et à la diffusion de documents scientifiques de niveau recherche, publiés ou non, émanant des établissements d'enseignement et de recherche français ou étrangers, des laboratoires publics ou privés.

# PHD THESIS

prepared at the INRIA of Sophia Antipolis, Odyssee Lab.,  
presented at the

**University of Nice-Sophia Antipolis**

Doctoral School in Sciences and Technologies of Information  
and of Communication

for obtaining the title of

**DOCTOR OF SCIENCE**

Specialized in Automatic, Signal and Image Processing

**Nicolas Wotawa**

April, 3rd 2006

Low-level visual cortex and  
motion perception: an MRI study

Advisor	Pr. Olivier Faugeras	INRIA, Sophia-Antipolis, France
Reviewers	Pr. Christoph Segebarth	INSERM, Grenoble, France
	Pr. Andrew Smith	Royal Holloway University London (RHUL), UK
Examinators	Dr. Éric Castet	CNRS, Marseille, France
	Pr. Guy Orban	Katholieke Universiteit Leuven (KUL), Belgium
	Dr. Bertrand Thirion	CEA-SHFJ, Orsay, France



UNIVERSITÉ NICE-SOPHIA ANTIPOLIS - UFR Sciences

École Doctorale STIC

(Sciences et Technologies de l'Information et de la Communication)

# THÈSE

pour obtenir le titre de

DOCTEUR EN SCIENCES

de l'UNIVERSITÉ de Nice-Sophia Antipolis

Discipline: Automatique, Traitement du Signal et des Images

présentée et soutenue par

Nicolas WOTAWA

## Systeme visuel cortical de bas niveau et perception du mouvement: une étude par IRM

*Thèse dirigée par Prof. Olivier FAUGERAS*

Soutenue le 3 avril 2006

### Composition du jury:

<i>Président</i>	Dr. Éric CASTET	CNRS, Marseille, France
<i>Rapporteurs</i>	Pr. Christoph SEGEBARTH	INSERM, Grenoble, France
	Pr. Andrew SMITH	Royal Holloway University London (RHUL), UK
<i>Examineurs</i>	Pr. Guy ORBAN	Katholieke Universiteit Leuven (KUL), Belgium
	Dr. Bertrand THIRION	CEA-SHFJ, France



# Remerciements

Le présent rapport décrit 3 années et demi de recherche dans un cadre pluridisciplinaire, ce qui m'a conduit à collaborer et échanger avec de nombreuses personnes qui apparaissent plus ou moins explicitement dans les chapitres qui suivent. Je souhaite donc mentionner plus particulièrement chacune d'entre elles dans ces quelques lignes.

Je tiens tout d'abord à remercier Olivier Faugeras pour sa confiance à mon égard tout au long de cette thèse. Son excellence scientifique, ses qualités humaines rares et son inaltérable enthousiasme resteront pour moi un modèle pour la suite.

Je remercie vivement Éric Castet pour son encadrement officieux d'une bonne part de ce travail. Je me demande bien où en serait cette thèse sans son aide précieuse, depuis la conception méticuleuse d'une expérience psychovisuelle jusqu'aux subtilités de la rédaction d'un article scientifique en passant par les innombrables séances de soutien psychologique face à mes éternels doutes et interrogations.

Je remercie également vivement Bertrand Thirion pour m'avoir largement mis le pied à l'étrier ainsi que pour sa grande disponibilité tout au long de ce travail et ce jusqu'à la soutenance.

Je suis très reconnaissant envers les professeurs Andy Smith et Christoph Segebarth pour avoir accepté sans hésitation la lourde tâche de juger ce travail en tant que rapporteurs de cette thèse. Je remercie aussi Guy Urban pour avoir accepté d'être membre du jury, ainsi que pour son accueil dans son laboratoire à Louvain.

Durant ces années, j'ai été amené à me rendre régulièrement à Marseille. D'une part auprès de l'équipe du centre IRMf de Marseille où ont été conduites les expériences: Muriel aux commandes du scanner, Bruno, indispensable travailleur de l'ombre, et Jean-Luc et ses conseils avisés. Je vous remercie chaleureusement tous les trois pour votre accueil amical et votre aide précieuse. Dans l'équipe DyVA d'autre part, où j'ai pu découvrir la recherche en neurosciences et en psychophysique. Un grand merci à Guillaume (le grand Manitou), Louis, Fred, Laurent, Ivo et Bruno.

Merci également à tous les "cobayes" qui ont bien voulu me prêter leur cerveau et subir

mes stimuli psychédéliques durant les manips .

Bien sûr, je n'oublierai pas les joyeux compagnons de l'équipe Odyssée: Jean-Phi et sa notoire "incompétence" scientifique dont j'ai, entre autres choses, bien souvent abusée; Christophe, maître incontesté de l'imagerie de diffusion, ceinture noire du dépannage informatique et trésor de gentillesse et d'enthousiasme; Manu, triomphal combattant des viscosités des ombres et catalyseur des algorithmes récalcitrants; Max, enthousiaste relecteur de cette thèse (pourrais-je un jour te renvoyer la balle?); l'épicurien Françouë, pilier de la bonne ambiance du projet et maître yogi en devenir; Sylvaing-le nurd, impeccable surfeur de la vie et de l'avis ("mais mec, j't'explique..."); Camilo, l'éclectique chamane colombien; Adrien, source infinie des rythmes (et jurons) qui font vibrer les couloirs du labo; Jérôme, aussi timide qu'adorable; Lucéro et ses inoubliables éternuements anisotropes; Maria-José, concentrée de bonnes énergies chiliennes; Marie-Cécile pour son indispensable soutien administratif et moral; Kristel qui a admirablement assuré l'interim durant la période de ma soutenance; Maureen, toujours prête pour un topo sur les subtilités de l'analyse de Fourier ou la dernière BD parue; Théo, avatar du dieu Informatique qui m'aura appris le rituel essentiel en la matière (RTFM...); Pierre et Thierry, qui m'ont permis de faire mes premiers pas de l'autre côté du miroir universitaire; Nour, pour nos discussions amicales toujours ponctuées de son rire chaleureux (quand refait-on le monde à nouveau sur la route de Marseille?); à Paris, je pense aussi à Geoffrey, compagnon de philosophie sur la thèse et la vie, Thomas dont je garderai de très bons souvenirs en conférences, Olivier trop vite parti de Sophia mais retrouvé avec plaisir (et par hasard!) au Canada. Je n'oublie pas non plus Mikaël, David, Christophe, Gerardo, Fred, Jacques, Lionel, Jan, Ivan, Ketty, Demian, Karim, Sandrine, Xavier, Lila, Florent, Robert.

Je souhaite également remercier les membres du personnel de l'INRIA pour leur disponibilité et leurs compétences infaillibles qui nous facilitent tant la vie administrative pourtant si...pratique. Plus particulièrement, merci à Valérie, Paule et Maryse.

J'adresse une pensée émue à mes amis de toujours qui comptent beaucoup pour moi, en particulier Jean, Guillaume, Chab, Julien et Caro. J'espère que nous continuerons longtemps à partager ces petits et grands moments de la vie et à refaire le monde, inlassablement.

J'exprime toute ma gratitude à mes parents, Annie et Michel, mon frère Guiguib, ma soeur Guisoeur et mon "bof" Pedro, mes grands parents Cécile et Pierre: vos preuves d'amour sont un soutien essentiel à mon cheminement.

Enfin, je terminerai par ma reine, Appoline, que je remercie du fond du coeur pour sa patience (victime du fameux forfait "soir et week-end" du thésard) et son amour. Et maintenant, en route vers de nouvelles aventures...





À ma Leech.



# Abstract

The evolution of cerebral imaging technologies combined with specific image processing algorithms contribute to improving our knowledge of the brain functioning, in particular regarding visual perception. This thesis contributes to current understanding implied in visual motion perception in humans, based on complementary information brought by different Magnetic Resonance Imaging (MRI) modalities.

The first part of this work focuses on functional MRI (fMRI) identification of low-level visual areas. We detail the fMRI retinotopic mapping procedure we developed, from the stimulus design to the final anatomo-functional analysis. A specific functional localization of the hMT/V5+ complex is also obtained with a block design. These methods, optimized according to some stimulation parameters, allow the extraction of individually defined and homogeneous Regions Of Interest (ROI).

In the second part, we characterize functionally these previously identified low-level visual areas. Based on the recent fMR-Adaptation paradigm, which allows to investigate the sensitivity of a cortical region to quantitative variations of a given feature, we demonstrate a functional differentiation across areas regarding their relative sensitivity to visual direction of motion.

Lastly, we combine fMRI and Diffusion Tensor MRI (DTI) to study the anatomical connectivity within the low-level visual cortex. Based on state of the art white matter fibers mapping algorithms, this characterization gives insights on the network of areas implied, among others, in visual motion processing.

Key words: visual cortex, fMRI, retinotopy, motion perception, direction selectivity, adaptation, DTI, anatomical connectivity.



# Résumé

L'évolution des technologies d'imagerie cérébrale alliée aux développements d'algorithmes spécifiques de traitement d'images permettent d'améliorer nos connaissances sur le fonctionnement du cerveau, en particulier s'agissant de la perception visuelle. L'objectif de ce travail de thèse est de contribuer à la compréhension des aires corticales impliquées dans la perception visuelle du mouvement chez l'homme, en analysant l'information des signaux de différentes modalités complémentaires d'Imagerie par Résonance Magnétique (IRM).

Une première partie concerne l'identification individuelle des aires visuelles de bas-niveau. Nous détaillons la méthode de cartographie rétinotopique par IRM fonctionnelle (IRMf) que nous avons développée, depuis la conception des stimuli visuels à l'analyse anatomo-fonctionnelle finale. Par ailleurs, une localisation fonctionnelle du complexe hMT/V5+ est obtenue par un paradigme en bloc. Ces méthodes, optimisées suivant certains paramètres de la stimulation, permettent d'extraire pour tout individu des Régions d'Intérêt homogènes.

Dans un deuxième temps, nous proposons une caractérisation fonctionnelle des différentes aires visuelles primaires. En se fondant sur le paradigme récent d'IRM d'adaptation qui permet d'étudier la sensibilité d'une région cérébrale à des variations quantitatives d'un paramètre de la stimulation, nous démontrons une différenciation de la sensibilité à la direction du mouvement dans les aires étudiées.

Enfin, nous décrivons une expérience combinant les modalités d'IRMf et d'IRM de diffusion (IRMd) dans le but d'étudier la connectivité anatomique au sein du cortex visuel primaire. Cette caractérisation, établie en s'appuyant sur des algorithmes récents de cartographie des fibres de matière blanche, donne des indices sur le réseau d'aires notamment impliquées dans le traitement du mouvement visuel.

Mots clés: cortex visuel, IRMf, rétinotopie, perception du mouvement, selectivité à la direction, adaptation, IRMd, connectivité anatomique.



# Contents

<b>Introduction et contributions (in french)</b>	<b>19</b>
<b>1 Introduction and contributions</b>	<b>27</b>
1.1 Context . . . . .	27
1.2 Thesis outline . . . . .	28
1.3 Contributions . . . . .	30
1.4 Other contributions . . . . .	32
<b>2 Magnetic Resonance Imaging and the human visual brain</b>	<b>35</b>
2.1 A quick tour in the anatomy of the human brain . . . . .	36
2.1.1 The central nervous system . . . . .	36
2.1.2 The neuron . . . . .	38
2.1.3 Structure and organization of the grey matter . . . . .	39
2.1.4 White matter connections . . . . .	42
2.2 The visual system . . . . .	44
2.2.1 From the eyes to the cortex . . . . .	44
2.2.2 The visual cortex . . . . .	45
2.3 Magnetic Resonance Imaging . . . . .	53
2.3.1 MRI principles . . . . .	53
2.3.2 Functional MRI: the B.O.L.D. signal . . . . .	59
2.3.3 Diffusion MRI . . . . .	64
2.4 Experimental setup . . . . .	68
2.4.1 The subject . . . . .	68
2.4.2 The scanner and the stimulation device . . . . .	68
2.4.3 Visual stimuli . . . . .	69
2.4.4 MR data acquisition . . . . .	70
<b>3 Anatomical image analysis</b>	<b>73</b>
3.1 Motivation . . . . .	74
3.2 Method overview . . . . .	75
3.3 Hemisphere identification . . . . .	75
3.3.1 Bias correction . . . . .	76
3.3.2 Grey level histogram analysis . . . . .	77

3.3.3	Skull stripping . . . . .	78
3.3.4	Brain mask segmentation . . . . .	79
3.4	Cortical surfaces extraction . . . . .	79
3.4.1	Algorithm 1: BrainVISA . . . . .	79
3.4.2	Algorithm 2: ABSOLUt . . . . .	82
3.4.3	Cortical surfaces extraction . . . . .	83
3.4.4	Algorithms comparison . . . . .	83
3.5	Cortical surface inflating . . . . .	84
3.6	Volumetric data projection . . . . .	87
<b>4</b>	<b>Functional data analysis</b>	<b>89</b>
4.1	Preprocessing . . . . .	90
4.1.1	Motion correction . . . . .	91
4.1.2	Anatomical/Functional image alignment . . . . .	92
4.1.3	Correction of the inter-slice gap or <i>slice-timing</i> . . . . .	93
4.1.4	Isotropic spatial smoothing . . . . .	94
4.1.5	Cortical surface constrained smoothing . . . . .	94
4.1.6	Temporal filtering . . . . .	99
4.2	Statistical analysis of fMRI data . . . . .	102
4.2.1	Problem statement . . . . .	102
4.2.2	Classification of methods . . . . .	102
4.2.3	The General Linear Model . . . . .	104
4.2.4	Non-parametric HRF estimation . . . . .	109
4.2.5	Frequency domain analysis . . . . .	112
4.2.6	Multivariate analysis methods . . . . .	112
<b>5</b>	<b>Visual areas mapping</b>	<b>117</b>
5.1	Retinotopic areas mapping . . . . .	118
5.1.1	The cortical retinotopic organization . . . . .	118
5.1.2	Experimental protocol . . . . .	124
5.1.3	Functional images preprocessing . . . . .	125
5.1.4	Statistical analysis . . . . .	126
5.1.5	Angular values computation . . . . .	133
5.1.6	Angle maps analysis . . . . .	135
5.1.7	Mapping reproducibility . . . . .	143
5.1.8	Mapping efficiency . . . . .	145
5.1.9	Area delineation . . . . .	149
5.1.10	Conclusion . . . . .	154
5.2	Functional mapping of hMT+ . . . . .	155
5.2.1	The hMT+ complex . . . . .	155
5.2.2	hMT+ localizer: previous work . . . . .	156
5.2.3	hMT+ optimal mapping . . . . .	156

5.2.4	Results . . . . .	159
5.2.5	Conclusion . . . . .	168
<b>6</b>	<b>fMR-adaptation of direction selectivity</b>	<b>169</b>
6.1	Introduction . . . . .	170
6.1.1	Problem statement . . . . .	170
6.1.2	fMR-adaptation: principle and previous work . . . . .	170
6.1.3	Direction selectivity and fMR-adaptation . . . . .	173
6.2	Experimental procedure . . . . .	173
6.2.1	Subjects . . . . .	173
6.2.2	MRI data acquisition. . . . .	173
6.2.3	Visual stimuli. . . . .	174
6.2.4	Defining the visual areas. . . . .	174
6.2.5	The adaptation stimulus. . . . .	174
6.2.6	Attentional measurements. . . . .	176
6.3	fMRI data analysis. . . . .	177
6.3.1	Visual areas identification experiment . . . . .	177
6.3.2	Adaptation experiment . . . . .	177
6.4	Results . . . . .	178
6.4.1	BOLD signal adaptation . . . . .	179
6.4.2	Direction selectivity . . . . .	179
6.4.3	Quantitative comparisons between areas . . . . .	181
6.4.4	Responses to stimulus transient . . . . .	184
6.5	Discussion . . . . .	185
6.5.1	Motion direction selectivity . . . . .	185
6.5.2	Macaque/human homologies in V1 and MT . . . . .	187
6.5.3	Attention, adaptation and direction tuning . . . . .	187
6.5.4	fMR-adaptation methodology . . . . .	188
6.6	Conclusion . . . . .	189
<b>7</b>	<b>Anatomical connectivity in the low-level visual cortex</b>	<b>191</b>
7.1	DTI connectivity mapping and the human visual brain: state of the art . . . . .	192
7.1.1	DTI connectivity mapping techniques . . . . .	192
7.1.2	Human visual cortex connectivity: previous work . . . . .	193
7.2	Methods . . . . .	195
7.2.1	MR data acquisition . . . . .	195
7.2.2	Processing pipeline . . . . .	196
7.2.3	Connectivity maps and fiber tracts computation . . . . .	200
7.2.4	Seed voxels placement . . . . .	203
7.3	Results . . . . .	205
7.3.1	Optic radiations . . . . .	205
7.3.2	Callosal connections . . . . .	208

7.3.3	hMT+ intra-hemispheric connectivity . . . . .	209
7.4	Discussion . . . . .	210
7.4.1	Visual cortex connectivity . . . . .	211
7.4.2	Methodological issues . . . . .	214
7.5	Conclusion . . . . .	216
<b>8</b>	<b>Conclusion and perspectives</b>	<b>217</b>
8.1	Summary of our contributions . . . . .	217
8.2	Perspectives . . . . .	218
	<b>Conclusion et perspectives (in french)</b>	<b>221</b>
	<b>Bibliography</b>	<b>225</b>

# Introduction et contributions



## Contexte

Comprendre les processus complexes réalisés par notre cerveau afin d'interagir avec le monde est assurément l'un des plus grands défis scientifiques de la recherche contemporaine. Au-delà d'apporter des débuts de réponses à des questions philosophiques telles que la relation entre notre perception individuelle et le monde "réel", cette quête peut avoir de nombreuses retombées dans le domaine de la santé, suggérer de nouvelles architectures d'ordinateurs, des interfaces homme-machine ou des algorithmes biologiquement inspirés, etc... Cela concerne tout particulièrement le système visuel, la vision étant indéniablement notre sens le plus sollicité dans la vie courante.

Jusqu'au milieu du vingtième siècle, la théorie dominante sur le système visuelle ne faisait état que d'une aire visuelle unique. De nombreuses aires visuelles ont été découvertes depuis chez différents mammifères, en particulier l'homme. Quatre critères principaux sont couramment utilisés pour identifier ces subdivisions du cortex visuel: (i) l'architecture cellulaire locale du cortex (ii) les motifs de connections entre les différentes zones corticales, (iii) les propriétés fonctionnelles des neurones et (iv) l'organisation rétinotopique. Les deux dernières méthodes ont pu être rapidement appliquées à l'homme grâce aux techniques de neuroimagerie. En revanche, la résolution spatiale limitée de ces techniques non-invasives restreint l'utilisation des critères d'architecture anatomique *in vivo*. Par ailleurs, seule une minorité d'études de neuroimagerie du système visuel combinent plusieurs de ces critères à ce jour.

La technique d'imagerie par résonance magnétique (IRM) figure comme un outil privilégié pour aborder ces questions. L'IRM permet en particulier d'obtenir des images anatomiques de haute résolution, une mesure indirecte de l'activité neuronale via l'IRM fonctionnelle (IRMf) et l'organisation macroscopique des fibres de matière blanche via l'IRM de diffusion (IRMd). Dans cette thèse, nous avons utilisé ces trois modalités de l'IRM pour affiner la caractérisation du cortex visuel de bas niveau, avec un accent particulier sur la perception du mouvement.

## Organisation de la thèse

Cette thèse est organisée en 6 chapitres après cette introduction générale. Le premier chapitre rappelle les principales connaissances actuelles concernant le système visuel cortical et présente les différentes modalités d'IRM utilisées dans ce travail. Cette partie reste relativement générale, un état de l'art plus précis ouvrant les chapitres suivants. Dans le deuxième chapitre, nous détaillons deux approches de traitement des images anatomiques que nous avons employées. Nous présentons ensuite les principales méthodes de traitement et d'analyse des images fonctionnelles, en introduisant notamment une nouvelle approche de lissage des données fonctionnelles contraint à la surface corticale. Le chapitre 5 traite de la cartographie de différentes aires visuelles de bas niveau, suivant le critère de rétinotopie d'une part et la spécificité fonctionnelle du complexe human MT (noté hMT+) d'autre part. Grâce à un paradigme d'IRM d'adaptation, nous démontrons dans le chapitre 6 la spécificité fonctionnelle de chacune des aires ainsi identifiées dans le traitement de la direction du mouvement. Le dernier chapitre présente quant à lui une étude de la connectivité de matière blanche entre les différentes aires visuelles en se fondant sur une méthode récente d'analyse des images d'IRMd. Nous terminons cette thèse par une conclusion générale sur nos contributions puis suggérons quelques directions futures de ce travail (cette partie est également disponible en français).

### Chapitre 2

Ce chapitre propose un survol des connaissances actuelles sur le cerveau humain (1ère section) avant de détailler plus précisément l'état de l'art sur le système visuel (2ème section). Nous rappelons ensuite les principes fondamentaux de l'IRM, en insistant sur les modalités d'IRMf et d'IRMd. La section 4 présente enfin le dispositif expérimental disponible au centre IRMf où nous avons conduit nos expériences et les paramètres spécifiques aux différentes séquences permettant respectivement d'acquérir les images anatomiques, fonctionnelles et de diffusion.

### Chapitre 3

La segmentation individuelle des différents tissus du cerveau et l'extraction d'un modèle géométrique de la surface corticale sont grandement profitables à l'analyse et à la visualisation des images fonctionnelles et de diffusion. Nous détaillons dans ce chapitre deux algorithmes que nous avons utilisés: la plate-forme logicielle BrainVISA, développée au sein de l'Institut Fédératif de Recherche n°49 et une approche complémentaire, avec le logiciel ABSOLUt récemment développé dans le laboratoire Odyssee. Ces deux méthodes fournissent une segmentation précise des différents tissus du cerveau et une reconstruction des surfaces internes et externes du cortex. Il est important de souligner qu'au delà du réglage de quelques paramètres, aucune correction manuelle n'est requise. Nous justifions enfin notre choix en

faveur de l'approche implémentée dans le logiciel ABSOLUt en nous fondant sur une comparaison qualitative de ses résultats avec ceux de BrainVISA.

## Chapitre 4

Une expérience classique en IRMf conduit à l'obtention d'un jeu de données 4D, *i.e.* une ou plusieurs séries temporelles d'images 3D. Des traitements spécifiques sont alors requis pour compenser certains artefacts liés à l'acquisition des images et en extraire l'information d'intérêt. Cette information peut correspondre à la détection de zones d'activation ou encore à l'estimation de la forme locale de la réponse BOLD dans certaines régions du cerveau. La première section se penche sur les prétraitements couramment appliqués aux données d'IRMf. Nous y introduisons en particulier une nouvelle approche au problème du lissage des données IRMf contraint à la surface corticale. Cette technique, reposant sur la méthode des ensembles de niveaux (level sets), offre des avantages à la fois pratiques et théoriques par rapport à la technique classique de filtrage 3D isotrope mais aussi par rapport aux approches de régularisation fondées sur un maillage explicite de la surface corticale. La seconde section donne une synthèse des principales approches d'analyse statistique des données d'IRMf, en insistant plus particulièrement sur deux méthodes: la méthode standard implémentée dans le logiciel SPM du Functional Imaging Laboratory à Londres, et une méthode d'estimation non-paramétrique de la réponse BOLD développée au sein de l'Institut Fédératif de Recherche n°49.

## Chapitre 5

Ce chapitre est dédié à l'identification de différentes aires du cortex visuel. Il est divisé en deux sections distinctes, suivant le critère employé pour révéler ces aires. La première section est ainsi une description de la méthode de cartographie des aires rétinotopiques par IRMf. Après un état de l'art des différentes approches décrites dans la littérature, nous détaillons notre procédure depuis la génération des stimuli visuels jusqu'à l'analyse anatomo-fonctionnelle finale. Nous présentons différentes configurations de stimuli envisagées pour optimiser la durée d'acquisition et la qualité des cartes du champs visuel correspondantes, puis nous comparons nos résultats avec ceux rapportés dans la littérature. Nous détaillons enfin la procédure retenue pour segmenter différentes aires visuelles retinotopiques et extraire des régions d'intérêt tri-dimensionnelles pour chacune d'entre elles. La seconde section de ce chapitre est dédiée à la méthode de cartographie fonctionnelle du complexe hMT+. À l'instar de la méthode de rétinotopie, différentes configurations de stimuli sont testées afin d'optimiser la procédure. Les résultats obtenus sont finalement confrontés à ceux décrits dans la littérature.

## Chapitre 6

Partant de l'identification précise de différentes aires visuelles de bas niveau décrite précédemment, ce chapitre présente une caractérisation de leur spécificité fonctionnelle respective par rapport à la direction du mouvement. Cette expérience repose sur le paradigme d'IRMf d'adaptation. Ce chapitre s'ouvre par une revue de ce récent paradigme, en insistant sur ses applications à l'étude du système visuel. Nous détaillons ensuite notre expérience d'IRMf d'adaptation événementielle. Une estimation robuste de la réponse hémodynamique permet d'évaluer pour chaque aire la sélectivité à la direction du mouvement et d'en déduire les proportions respectives de deux sous-populations neuronales sensibles à cet attribut visuel. Le complexe hMT+, directement suivi par l'aire V3A, apparaissent comme les plus sélectifs à la direction. Une forte sélectivité à la direction est également trouvée dans les aires V1 et V4v, confirmant ainsi les observations d'une récente étude d'IRMf menée chez le macaque. En outre, ces résultats valident la capacité du paradigme d'adaptation à préciser la ségrégation fonctionnelle des aires visuelles primaires, tout en soulignant l'aspect dynamique de la sélectivité fonctionnelle des neurones.

## Chapitre 7

Nous proposons de raffiner notre connaissance du cortex visuel humain en étudiant un autre aspect fondamental de l'organisation du cerveau: la connectivité anatomique. Nous commençons par un état de l'art des méthodes de cartographie de la connectivité anatomique à partir des images du tenseur de diffusion (DTI), en mettant l'accent sur leurs applications au cortex visuel. Notre approche, combinant cartographie des aires visuelles et une méthode géométrique d'analyse des données de DTI récemment développée au laboratoire est ensuite présentée. Une chaîne de traitement complète permet l'analyse conjointe des informations complémentaires apportées par chacune des modalités d'IRM dans un espace de référence. Après une première validation de notre approche sur les radiations optiques, une topologie des connections interhémisphériques entre aires visuelles au sein du splenium est mise en évidence. Une évaluation de la connectivité entre le complexe hMT+ et les différentes aires rétinotopiques est également exposée. Ces résultats, ainsi que leurs implications théoriques et méthodologiques, sont discutés dans une dernière section.

Nous concluons cette thèse en rappelant nos contributions principales avant de suggérer quelques directions futures de ce travail.

## Contributions

Les contributions de cette thèse sont à la fois méthodologiques et expérimentales. D'un point de vue méthodologique, ce travail propose de nouvelles approches à l'analyse des données d'IRM et constitue une validation de différents algorithmes récemment développés dans ce domaine:

- Nous introduisons au chapitre 3 une nouvelle approche pour le lissage des données IRMf contraint à la surface du cortex. Cette démarche s'appuie sur la méthode des ensembles de niveaux pour lisser directement l'image fonctionnelle le long de la direction parallèle à la surface corticale. Cette nouvelle technique est comparée à la méthode classique de filtrage 3D isotrope ainsi qu'à une approche de régularisation des données fonctionnelles projetées sur un modèle explicite (maillage) de la surface corticale. Comparativement au classique filtrage isotrope, les méthodes incorporant l'information de la géométrie propre au cortex de l'individu sont naturellement moins sujettes à un indésirable mélange d'informations provenant de tissus hétérogènes. En outre, la méthode de lissage des données fonctionnelles fondée sur les ensembles de niveaux présente les avantages suivants par rapport aux méthodes reposant sur une représentation explicite de la surface corticale: (i) tout d'abord, aucune projection des données fonctionnelles sur la surface corticale n'est requise, ce qui évite le choix souvent arbitraire de la méthode de projection; (ii) en conséquence, le choix de la technique de projection utilisée pour visualiser les résultats finaux d'une analyse peut alors être effectué a posteriori, ce qui confère davantage de souplesse à la chaîne globale des traitements; (iii) enfin, l'implantation de la méthode de lissage fondée sur les ensembles de niveaux conduit à un traitement plus efficace des données du point de vue computationnel. Le seul inconvénient de la méthode par ensemble de niveaux provient de la nécessité de disposer d'une représentation implicite (i.e. sous forme d'un ensemble de niveaux) de la surface corticale. Toutefois, cette étape est exécutée efficacement par un algorithme de la librairie ABSOLUt. Nous illustrons les résultats obtenus avec les différentes approches sur deux jeux de données réelles d'expériences IRMf portant sur des macaques et sur des humains. Cette contribution méthodologique a été présentée à la conférence Human Brain Mapping en 2004 [251].
- L'optimisation de paramètres fondamentaux des stimuli utilisés pour les expériences de rétino-topie d'une part et d'identification fonctionnelle du complexe hMT+ d'autre part est décrite dans le chapitre 5. Grâce à ces procédures, l'identification fiable de nombreuses aires visuelles de bas niveau est obtenue en environ 30 minutes avec un scanner IRM à 3 Tesla, en incluant l'acquisition d'une image anatomique de haute résolution. De plus, nous avons implanté une

méthode d'extraction de régions d'intérêt tri-dimensionnelles correspondant à chaque aire visuelle rétinotopique.

La procédure de cartographie des aires rétinotopiques a été présentée à la conférence Human Brain Mapping en 2003 [252].

- La validation de nouveaux algorithmes sur des jeux de données expérimentales constitue une étape nécessaire en vue de leur intégration à la complexe chaîne de traitement des images IRM. Le présent travail apporte quelques éclairages en ce sens. Nous comparons tout d'abord dans le chapitre 3 deux outils de segmentation récents et discutons leurs avantages et inconvénients respectifs. Par ailleurs, les résultats de l'expérience présentée au chapitre 6 constituent une validation supplémentaire du paradigme d'IRMf d'adaptation. De plus, ce même chapitre illustre la sensibilité accrue qu'il est possible d'obtenir avec des approches alternatives au modèle linéaire généralisé classiquement utilisé pour l'analyse des données IRMf. C'est en particulier le cas de la méthode d'estimation non-paramétrique de la réponse hémodynamique que nous avons adoptée dans cette étude. Enfin, les implications méthodologiques de l'étude de la connectivité anatomique à partir d'images DTI, détaillée dans le chapitre 7, sont de deux ordres. D'une part, cette étude prouve qu'il est possible de combiner les informations provenant de différentes modalités d'IRM, dans notre cas l'information des images anatomique, fonctionnelle et de diffusion. D'autre part, cette expérience est une première validation de la technique de résolution par Fast Marching du problème de cartographie de la connectivité anatomique fondée sur une modélisation Riemannienne des images DTI. Ce cadre méthodologique est en cours de soumission à la conférence Computer Vision and Pattern Recognition (CVPR), tandis que les résultats préliminaires sur le cortex visuel ont été présentés à la conférence Human Brain Mapping en 2005 [250].

D'un point de vue plus expérimental, cette thèse apporte de nouveaux éclairages sur l'organisation fonctionnelle et anatomique du cortex visuel de bas niveau:

- l'expérience décrite au chapitre 6 conduit à une estimation de la sélectivité à la direction du mouvement dans différentes aires visuelles de bas niveau. Les résultats confirment que cette sélectivité dépend de l'aire considérée. Ainsi, le complexe hMT+ et l'aire V3A sont les plus sélectifs, suivis de V1, V3, V4v puis V2. Cet ordre étaye l'idée de traitement hiérarchique de l'information au sein du cortex visuel. De plus, les mesures obtenues sont plus précises que les résultats précédents, bien que le paradigme d'adaptation utilisé soit relativement peu contraignant. Les indices de sélectivité observés dans l'aire V1 et hMT+ sont singulièrement comparables à ceux rapportés dans une expérience sim-

ilaire effectuée sur le macaque. Cette observation peut constituer une preuve supplémentaire de l’homologie de ces zones corticales dans les deux espèces. Enfin, les sélectivités à la direction particulièrement importantes observées dans les aires V1 et V4v ravivent la notion d’une sélectivité fonctionnelle dépendante du contexte. Ce travail est en cours de soumission à la revue *Journal of Vision*.

- L’expérience combinant les données d’IRMf et d’IRMd exposée dans le dernier chapitre permet de reconstruire les radiations optiques reliant le Corps Genouillé Latéral à l’aire V1. De plus, nos résultats confirment la topologie des connections occipito-callosales dans le splenium. Nous présentons enfin la première caractérisation de la connectivité anatomique entre le complexe hMT+ et les aires rétinotopiques occipitales. V1 révèle systématiquement les plus forts indices de connectivité, ce qui est cohérent avec les données recueillies chez l’animal. D’autre part, les plus faibles indices de connectivité avec hMT+ se trouvent invariablement dans l’aire V4, ce qui est cohérent avec l’idée de ségrégation de voies parallèles ventrales et dorsales de traitement de l’information visuelle. Cette partie est en cours de soumission à *NeuroImage*.

## Autres contributions

Dans un souci de cohérence, certaines contributions réalisées durant ce travail de thèse ne sont pas incluses dans le présent manuscrit. Nous les mentionnons rapidement ci-dessous.

- La procédure de cartographie rétinotopique est actuellement appliquée par l’équipe DyVA<sup>1</sup>, INCM, CNRS, Marseille pour étudier l’organisation corticale auprès de patients souffrant de dysfonctionnements de la rétine. Ceux-ci incluent des pathologies telles que les scotomes visuels ou la dégénérescence maculaire liée à l’âge (DMLA). Deux séries d’expériences ont déjà été menées sur 8 sujets sains. Les cartes rétinotopiques de ces sujets ont été dans un premier temps acquises et reconstruites suivant la méthode décrite au chapitre 5. Dans un second temps, un paradigme en blocs alternant entre un fond gris et un damier couvrant le champs visuel complet et papillotant a été présenté aux mêmes sujets. Dans les deux types d’expérience, des conditions avec 4 scotomes circulaires peri-fovéaux de différentes tailles et placés à différentes excentricités ont été ajoutées. Les projections corticales des différents scotomes ont pu être identifiées et leurs relations confirmées quantitativement, en comparant les positions corticales et les surfaces des zones corticales inactivées avec les valeurs connues de rayon, excentricité et surface des scotomes dans le champ visuel. Au delà du transfert de la technique complète de cartographie rétinotopique,

---

<sup>1</sup>[www.incm.cnrs-mrs.fr/en.equipedyyva.php](http://www.incm.cnrs-mrs.fr/en.equipedyyva.php)

j'ai conçu les stimuli ainsi que les programmes d'analyse des données issues du paradigme en bloc. Ce travail a donné lieu à deux présentations à des conférences d'ophtalmologie en mai 2005, l'une à la conférence ARVO (Association for Research in Vision and Ophthalmology) [103] et l'autre au Congrès Annuel de la Société Française d'Ophtalmologie [102]. Suite à cette première phase de validation, une étude de la représentation corticale auprès de patients atteints de pathologie rétinienne est actuellement menée par Dr. Louis Hoffart, ophtalmologue à l'hôpital de la Timone à Marseille et étudiant en thèse dans l'équipe DyVA.

- J'ai contribué à une expérience d'IRMf menée chez le macaque et conduite par le Professeur Guy A. Orban et Mr. Koen Nelissen au laboratoire de neuro-psycho-physiologie de l'université catholique de Louvain<sup>2</sup>. L'étude porte sur le traitement de la vitesse du mouvement visuel dans le cortex du macaque. Cette expérience fut une initiation à l'expérimentation animale ainsi qu'aux contraintes spécifiques liées à l'environnement hospitalier. Certaines données de cette expérience sont utilisées dans le chapitre 4 pour valider notre méthode de lissage des données IRMf contraint à la surface corticale.
- J'ai conçu un programme paramétrique permettant de générer les stimuli visuels d'une expérience IRMf portant sur la perception du mouvement transparent. Cette expérience a été réalisée dans le cadre du réseau de recherche "Perception for Recognition and Action"<sup>3</sup>. L'analyse des données fonctionnelles est en cours de réalisation.
- Enfin, mon travail de thèse inclue une part importante de développement logiciel. J'ai écrit de nombreux scripts Matlab et shells pour automatiser la plupart des étapes de traitements d'images utilisées dans cette thèse. La plupart comprend une interface fondée sur le logiciel SPM pour permettre une interaction aisée avec l'utilisateur. Certaines de ces méthodes ont été transférées auprès de l'équipe DyVA, au Centre IRMf de Marseille et au laboratoire de neuro-psycho-physiologie de Louvain.

---

<sup>2</sup><http://134.58.34.1/index.php>

<sup>3</sup><http://pra.psy.gla.ac.uk/>

# Chapter 1

## Introduction and contributions

### 1.1 Context

Understanding the complex processes taking place in our brain to interact in the world is undoubtedly one of the greatest scientific challenges of current research. Beyond bringing possible answers to some old age philosophical questions, for instance regarding the relation between individual perception and the "actual" world, this quest may provide several outcomes in healthcare, be an inspiration source for enhanced computer hardware architecture, computer-human interfaces and biologically inspired algorithms, etc. It is in particular the case with the visual system since vision is probably the most called-upon sense in our daily life.

Until the middle of the twentieth century, the main theory of the visual perception and the brain considered a single visual cortical area. Since then however, various visual areas have been discovered in mammals, including humans. Four main criteria are now commonly used to identify these subdivisions of the visual cortex: (i) local anatomical architecture of cortical cells, (ii) white matter connectivity patterns across cortical zones, (iii) global functional properties of neurons and (iv) retinotopic organization. The last two methods were rapidly applied to humans thanks to neuroimaging techniques. On the other hand, the low spatial resolution relative to cells dimensions actually reached by these non-invasive techniques limited the use of the anatomical architecture criteria *in vivo*. Besides, to date only a small proportion of visual neuroimaging experiments use more than one of these criteria. The exciting -and relaxing, since it is not rare that subjects fall asleep while lying inside the tunnel- technique of Magnetic Resonance Imaging (MRI) is a particularly promising tool to tackle these issues. It indeed offers the possibility, among others, to obtain high resolution anatomical images and, at reasonable spatial resolution, indirect measurements of neural activity through functional MRI (fMRI) and of white matter connections through diffusion weighted MRI (DWI).

In this thesis, we use these three different modalities of MRI to characterize the human low-level visual cortex, with a particular emphasis on motion direction perception.

## 1.2 Thesis outline

This thesis is organized in 6 chapters (following this introduction). The first one is an introduction to current knowledge about the cortical visual system and the MRI modalities we used. In the second chapter, we detail the approaches we applied to the anatomical image processing. We then describe different processing methods to analyze BOLD signal images, including a new surface-based approach to perform the spatial smoothing of fMRI data. Chapter 5 deals with visual areas mapping, for which we developed a complete retinotopic mapping experiment as well as a specific functional identification of the hMT+ complex. Based on the identification of these areas, we demonstrate, with an fMRI adaptation paradigm, a functional characterization of motion direction selectivity for each area (chapter 6). The last chapter presents a study of white matter connectivity across the same visual areas, using a recently developed framework to analyze Diffusion Tensor Images (DTI), a particular model of DWI. We finally close this thesis with a general conclusion about our contributions and future work.

### Chapter 2

We give in this chapter an overview of the human brain (section 1) before detailing more specifically current knowledge on the visual system (section2). We then recall the basic principles underlying the Magnetic Resonance Imaging technique, emphasizing on the modalities of fMRI and DWI we used in this thesis. We finally present the experimental setup available at the Centre IRMf de Marseille where we recorded our data and give the parameters of the different scanner sequences we used for our anatomical, functional and diffusion-weighted images.

### Chapter 3

The segmentation of the individual brain tissues and the extraction of a geometrical model of the cortical surface are of great interest for the analysis and display of functional and diffusion weighted images. We detail in this chapter two algorithms we used: the BrainVISA software, developed within the Institute Fédératif de Recherche n°49, and a complementary approach, ABSOLUt, recently developed at the Odysée Laboratory. The two methods allow an accurate segmentation of the different brain tissues and a reconstruction of the inner and outer grey matter surfaces. Importantly, beyond a few parameters tuning, no manual editing is required. We then justify our choice in favor of the ABSOLUt software approach based on a comparison of their respective outcomes.

### Chapter 4

A typical fMRI experiment results in a 4D dataset. Specific processing is then

required to correct for some acquisition artifacts and extract the information of interest. This information can be the detection of activation loci or the estimation of the local BOLD response shape in specific zones. The first section deals with the preprocessing usually applied to fMRI datasets. In particular, we introduce a new approach to address the problem of fMRI data smoothing along the cortical surface. This method, based on the level set framework, offers theoretical and practical advantages over the typical 3D-isotropic smoothing technique as well as mesh-based approaches proposed so far. In the second section, we review the main approaches proposed for the statistical analysis of fMRI data, with a particular emphasis on two methods we used: the standard SPM framework and a non-parametric estimation method of the BOLD response.

## **Chapter 5**

This chapter is divided into two parts, each corresponding to a specific criterium we used to delineate distinct low-level visual areas. In the first part, we describe the fMRI retinotopic mapping procedure we employed to segment the early occipital retinotopic areas. After a review of the different approaches described in the literature, we detail our procedure, from the stimuli generation to the final anatomo-functional analysis. We describe different stimulus configurations we tried to optimize the acquisition process as well as the resulting maps quality and then compare our results with the literature. We finally detail the procedure to segment the visual areas and extract 3D Regions Of Interest for each retinotopic area identified. In the second part, we present the functional mapping we used to localize the hMT+ complex. Similarly to the retinotopic mapping experiment, we varied some stimulus parameters to optimize the procedure. We finally confront our results with the literature.

## **Chapter 6**

Based on the precise identification of the low-level visual areas, we give in this chapter a characterization of their respective functional selectivity to motion direction we obtain with an fMR-adaptation paradigm. We start by a review of fMR-adaptation literature, with an emphasis on its applications to the visual system. We then detail our event-related fMR-adaptation experiment. A robust estimation of the hemodynamic response function allows to estimate the direction tuning and corresponding proportions of two functional sub-populations with respect to this feature. The human MT complex (hMT+), directly followed by V3A, appears to be the more direction selective. We also find high direction selectivity in areas V1 and V4v, thus confirming similar observations reported in a macaque fMRI study. In addition, these results validate the fMR-adaptation paradigm ability to assess the functional segregation of early visual areas, while

stressing the necessity to take into account dynamic aspects of the functional selectivity to low-level features.

## Chapter 7

Finally, we propose to refine our knowledge of the human visual cortex by studying another fundamental aspect of the brain: the anatomical connectivity. We first review the state of the art in DTI connectivity mapping approaches and their applications to the visual cortex. We then present our approach which combines the functional and retinotopic identification of the visual areas with a recently developed geometrical framework to analyze DTI data. A complete processing pipeline is developed to allow the analysis of the complementary information brought by each MRI modality in a common reference frame. After a first validation of our approach on the well-known optic radiations, we characterize the possible topology of interhemispheric connections of the low-level visual cortex areas within the splenium. An evaluation of the connectivity between the hMT+ complex and the different retinotopic areas is also given. We finally discuss our results and their theoretical and methodological implications.

We conclude this thesis by recalling our main contributions before suggesting various future directions emerging from this work.

## 1.3 Contributions

The contributions of the current thesis are both methodological and experimental. From a methodological point of view, our work offers new approaches to MRI data analysis and provides a validation of various state of the art algorithms developed in the field:

- We introduce in chapter 3 a new cortical surface based approach for fMRI data smoothing. This method takes advantage of the level set framework to directly smooth the functional images along a direction parallel to the cortical surface. We compare this method with the classical 3D-isotropic technique and with a mesh-based smoothing approach similar to that already proposed in the literature. Naturally, cortical surface based methods are less prone to undesired mixing of voxel information than the classical 3D-isotropic filtering. Moreover, the level set method appears more adapted to fMRI data smoothing than the mesh-based approaches in many respects: (i) first and foremost, a projection to assign the functional data onto the cortical surface is not required, avoiding a somewhat arbitrary choice; (ii) consequently, the choice of a projection method to visualize the results of the data analysis can be done a posteriori, which is more flexible; (iii) the implementation is computationally

more efficient than the mesh-based approaches. The only drawback of our level set approach over mesh-based approaches is the necessity to compute a level set function representing the cortical surface. However, this step is efficiently performed by a dedicated algorithm implemented in the ABSOLU<sub>t</sub> library. We illustrate the different approaches on a macaque monkey and a human dataset. This methodological contribution was presented at the Human Brain Mapping (HBM) conference in 2004 [251].

- The optimization of fundamental stimuli parameters for the retinotopic mapping procedure and the functional identification of hMT+ are described and discussed in chapter 5. The retinotopic mapping procedure was presented at the HBM conference in 2003 [252]. Using these procedures, the reliable identification of various low-level visual areas can be achieved in approximately 30 minutes of scans at 3T, including the obtention of a high resolution anatomical image. Additionally, we implemented a method to extract 3D Regions Of Interest corresponding to each retinotopic visual area.
- The validation of newly introduced algorithms on real experimental data is a necessary step to optimize the MRI processing pipelines. We first compare in chapter 3 two state of the art anatomical image segmentation tools and discussed their respective advantages and drawbacks. Second, the results we obtain in the fMR-adaptation study presented in chapter 6 constitute a further validation of this experimental paradigm. Besides, this chapter illustrates the improved sensitivity of alternative statistical approaches to the classical GLM analysis of fMRI data, such as the non-parametric HRF estimation framework we applied. Finally, the methodological implications of the DTI-based anatomical connectivity experiment detailed in chapter 7 is twofold. First it proves the feasibility to combine the different information provided by anatomical, functional and diffusion-weighted MR images. Second, it gives a first validation of the Fast Marching implementation of the Riemannian approach to DTI connectivity mapping. The methodological framework is currently submitted to the Computer Vision and Pattern Recognition (CVPR) conference, and preliminary results of the experimental validation on the visual cortex were presented at the HBM conference in 2005 [250].

From a more experimental point of view, our thesis brings new insights regarding the functional and anatomical organization of the low level visual cortex:

- The experiment reported in chapter 6 gives an estimation of direction selectivity in various low-level visual areas. It confirms that motion direction selectivity is area specific in low-level visual cortex. Furthermore, we obtain finer measurements of this particular feature with a minimally constraining adaptation

paradigm. Our results suggest a global hierarchy among the different visual areas. hMT+ and V3A are the most direction selective, followed by V1, V3, V4v and V2. This ordering supports the notion of hierarchical processing in the visual cortex. The direction indices we observed in V1 and hMT+ are interestingly similar to those reported in a recent macaque experiment, which might be another evidence of the homologies between the two species. Additionally, the unexpectedly high direction selectivity we observed in V1 and V4v revives the notion of context-dependent neuronal tuning. This work is currently submitted to *Journal of Vision*.

- The combined DTI-fMRI experiment we expose in the last chapter allows to reconstruct the optic radiations linking the LGN and V1. It confirms the topology of occipito-callosal connections in the splenium. We also report the first preliminary characterization of the anatomical connectivity between hMT+ and the occipital retinotopic areas. As expected from animal studies, V1 exhibits the highest connectivity index values. On the other hand, V4 systematically shows the lowest connectivity index values with hMT+. This result is consistent with the view of segregated ventral and dorsal processing streams. This part is currently submitted to *NeuroImage*.

## 1.4 Other contributions

For sake of coherence and conciseness, some contributions made during this PhD could not be included in this manuscript. They are shortly mentioned below.

- The retinotopic mapping procedure is currently applied by the DyVA team<sup>1</sup>, INCM, CNRS, Marseille to study the cortical organization in patients suffering from retinal diseases. This includes pathologies such as visual scotomas or age-related macular degeneration. Two sets of experiments were already ran on 8 healthy subjects. Retinotopic maps were first reconstructed using the mapping technique described in chapter 5. Second, a block paradigm consisting of a grey background alternating with a fullfield, flickering checkerboard was used to stimulate the complete central visual field. In both experiments, conditions with 4 peri-foveal scotomas of different sizes and centered at different eccentricities were interleaved. The cortical projections of each artificial scotoma were identified and confirmed their relations by quantitative analysis: the measured cortical positions and surfaces of the inactivated cortical zones were compared with the known values of radius, eccentricity and surface of scotomas in the visual field.

Beyond the transfer of the whole retinotopic mapping technique, I designed

---

<sup>1</sup>[www.incm.cnrs-mrs.fr/en.equipeddyva.php](http://www.incm.cnrs-mrs.fr/en.equipeddyva.php)

the stimuli and the analysis programs for the block design experiment. This work led to 2 presentations at ophthalmology conferences in may 2005, one at the ARVO conference (Association for Research in Vision and Ophthalmology) [103] and the other at the Congrès Annuel de la Société Française d’Ophtalmologie (French Ophthalmology Society Annual Conference) [102]. Following this first validation step, the mapping of the cortical representation in patients presenting retinal pathology is currently under study by Louis Hoffart, ophthalmologist at la Timone hospital in Marseille and PhD student at the DyVA team.

- I contributed to perform a macaque monkey fMRI experiment conducted by Professor Guy A. Orban and Mr Koen Nelissen at the Laboratorium voor Neuro- en Psychofysiologie<sup>2</sup>, K.U.Leuven. The goal of this experiment was to study visual motion velocity processing in the macaque monkey brain. This was an interesting opportunity to be introduced to animal experiments and specific constraints related to the work in an hospital environment. Note that some datasets related to this experiment are used in chapter 4 to validate our cortical surface based fMRI smoothing method.
- I designed the parametric program to generate the visual stimuli used in an fMRI experiment related to motion transparency perception. This experiment was performed within the Perception for Recognition and Action<sup>3</sup> Research Training Network. The functional data analysis is currently under study.
- Last but not least, my PhD work includes software development. I wrote Matlab and shell scripts to automate several image processing tools used in this thesis. Most of them include an SPM based interface to allow a user-friendly interaction with the user. I transferred parts of these methods to the DyVA team, the Centre IRMf de Marseille and the Laboratorium voor Neuro- en Psychofysiologie.

---

<sup>2</sup><http://134.58.34.1/index.php>

<sup>3</sup><http://pra.psy.gla.ac.uk/>



## Chapter 2

# Magnetic Resonance Imaging and the human visual brain

### Contents

---

<b>2.1</b>	<b>A quick tour in the anatomy of the human brain . . . . .</b>	<b>36</b>
2.1.1	The central nervous system . . . . .	36
2.1.2	The neuron . . . . .	38
2.1.3	Structure and organization of the grey matter . . . . .	39
2.1.4	White matter connections . . . . .	42
<b>2.2</b>	<b>The visual system . . . . .</b>	<b>44</b>
2.2.1	From the eyes to the cortex . . . . .	44
2.2.2	The visual cortex . . . . .	45
<b>2.3</b>	<b>Magnetic Resonance Imaging . . . . .</b>	<b>53</b>
2.3.1	MRI principles . . . . .	53
2.3.2	Functional MRI: the B.O.L.D. signal . . . . .	59
2.3.3	Diffusion MRI . . . . .	64
<b>2.4</b>	<b>Experimental setup . . . . .</b>	<b>68</b>
2.4.1	The subject . . . . .	68
2.4.2	The scanner and the stimulation device . . . . .	68
2.4.3	Visual stimuli . . . . .	69
2.4.4	MR data acquisition . . . . .	70

---

The human brain is reputable of being the most complex physical object in the world. Its complexity arises as soon as one considers its anatomical organization and is further emphasized by its rich functional organization. However, brain imaging techniques, in particular Magnetic Resonance Imaging (MRI), allow to get various complementary information about this organ.

We start this chapter by a quick tour from the nervous system to the subdivisions of the human brain. We more specifically insist on two brain tissues we particularly targeted in this work: grey matter and white matter. The main part of the grey matter is found in the cerebral cortex, where most neural processing take place, and the white matter relays information across different brain locations. We then account the main facts about the human visual system organization, with a particular emphasis on imaging contributions. Section 3 introduces the MRI technique and how it can be used to infer neuronal activity (fMRI) and anatomical connectivity (Diffusion MRI). We finally detail the experimental setup and imaging sequences used in this thesis.

## 2.1 A quick tour in the anatomy of the human brain

The nervous system is the master piece of the organism to retrieve, convey and process information brought from the inside and the outside of the body. It also manages the vast majority of functions to react to our environment. The paragraphs below aim at giving a rough description of the brain anatomy. For a far more complete and detailed view of the brain structures, various atlases and books are now available. For instance, we refer the interested reader to the excellent Duvernoy atlas [58] or, for those keen on web pages, the on-line atlas of Prof. Dominic Hasboun<sup>1</sup>.

### 2.1.1 The central nervous system

We begin our journey in the nervous system by dividing it into two major parts which in turn can be divided into two sub-parts:

- the Peripheral Nervous System. It comprises (i) the Somatic Nervous System, whose nerves carry the information from and to the sensory organs and the muscles and (ii) the Automatic Nervous system, involved in the regulation of vital functions such as breathing, blood circulation, digestion or hormones secretion;
- the Central Nervous System. The CNS is composed of the spinal chord located within the vertebral column and the brain housed by the skull. The CNS nerves lie inside the cerebrospinal fluid (CSF).

---

<sup>1</sup><http://www.chups.jussieu.fr/ext/neuranat/index.html>

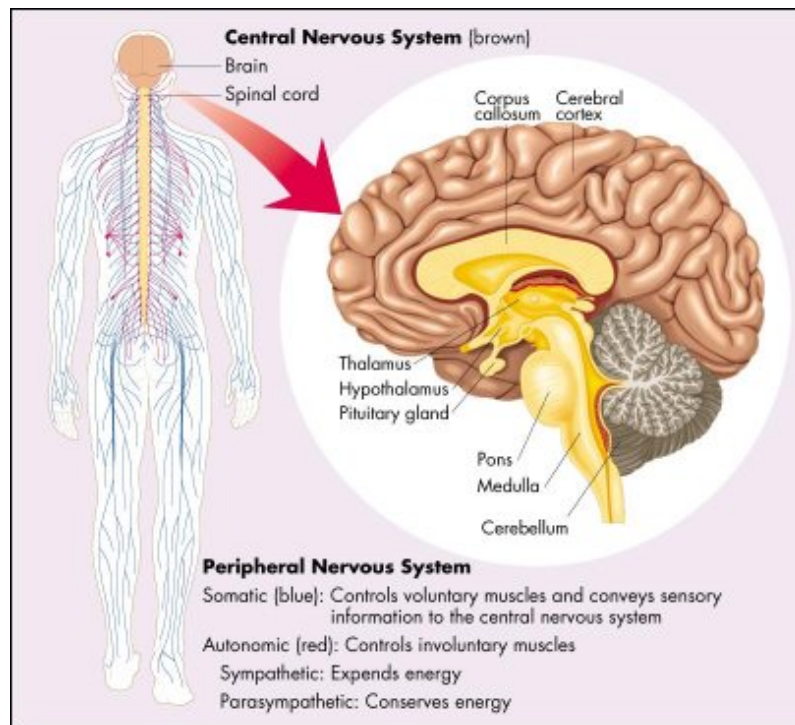


Figure 2.1: Subdivisions of the nervous system and close up on the brain. From [http://mywebpages.comcast.net/epollak/PSY255\\_pix/PSY255\\_pix.htm](http://mywebpages.comcast.net/epollak/PSY255_pix/PSY255_pix.htm)

Figure 2.1 illustrates the subdivisions of the nervous system with an emphasis on the brain represented in a mid-sagittal section. This virtual plane, corresponding to the body's median plane, splits the brain into two roughly symmetrical parts, called the two hemispheres. Each hemisphere communicates with the other through a large bundle of nerve fibers, the corpus callosum, and a smaller fiber bundle called the anterior commissure.

Pursuing our dissection one step further within the brain yields to distinguish three parts:

1. the rhombencephalon or hindbrain comprises the cerebellum, the pons and the medulla oblongata;
2. the mesencephalon or mid-brain made of the tectum, the tegmentum and the cerebral aqueduct;
3. the prosencephalon, or forebrain, composed of two main units, one known as the diencephalon containing the thalamus and hypothalamus and the other called the telencephalon holding the basal ganglia and the cerebral cortex.

We now focus our description on parts of the prosencephalon which was particularly studied in this thesis. Before describing the main facts about grey and white matter

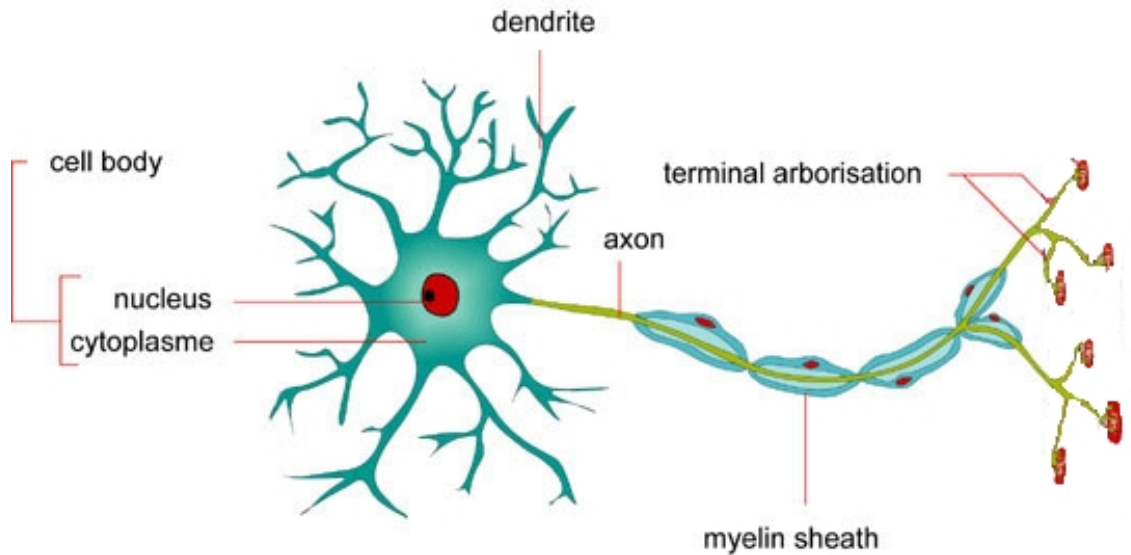


Figure 2.2: Schematic structure of a neuron. Adapted from *www.infovisual.info*

tissues, we temporarily have to interrupt our dissection-like description to introduce the main structural element of the brain: the neuron.

### 2.1.2 The neuron

The nervous system comprises 100 billion ( $10^{11}$ ) neurons. One important characteristic of neurons is that they have excitable membranes which allow them to generate and propagate electrical signals. The primary role of neurons is to process and transmit this neural information. If neurons exhibit a high diversity both in shape and size (there are over 200 different kinds of neurons), they nonetheless share a common structure, as illustrated in figure 2.2. Like all the cells in the human body, every neuron has a cell body, i.e. a membrane that surrounds its cytoplasm and a nucleus that contains its genes. This part is also called the soma. What distinguishes the neurons from other cells is their extensions, which they use to send and receive information. The dendrites are the extensions that conduct the electrical stimulation received from other cells to the soma. On the other hand, the axon carries nerve signals away from the neuron. Each neuron has many dendrites but only one axon, although it usually undergoes extensive branching called terminal arborisation. Such a structure enables communication with many target cells, mostly neurons but also other cells like muscles. Neurons communicate with one another through synapses, term derived from the Greek "syn" (together) and "haptin" (join). Hence a synapse is found where an axon terminal of one cell impinges upon a dendrite or the soma of another, or less commonly to another

axon. Each neuron has on average 1,000 synaptic connections to other neurons, which yields to a number of 100 trillion ( $10^{14}$ ) connections (synapses) between neurons in the brain. The vast majority of the synapses found in the human brain are chemical synapses, i.e. the information transfer from the axon terminal to the next neuron is supplied by specific molecules known as neurotransmitters.

From a macroscopical point of view, aggregates of neuron's soma and dendrites form the grey matter where the main information processing is thought to be performed while the neuron's axons behave as the wiring network within the brain, which constitutes the white matter.

### **2.1.3 Structure and organization of the grey matter**

Grey matter forms the superficial part of the brain, some nuclei within the brain and the deep parts of the spinal cord. It is so-called because, in post-mortem sections, it has a grey color due to all the grey nuclei in the cells that make it up. In fact, in the living body, grey matter is pink. Grey matter is thus mainly composed of the bodies of the neurons. But it also comprises the nonmyelinated sections of processes (axons and dendrites), including processes just emerging from the neurons, and cells which are thought to mainly support and protect the neurons in various ways.

#### **The cerebral cortex**

With 75% of the  $10^{11}$  neurons found in the brain, the cerebral cortex is the most important grey matter part. From a macroscopical point of view, the cortex is roughly a sheet of tissue that makes up the outer layer of the brain. This is actually the origin of the Latin word *cortex*, which means outer layer or bark. Along the evolution, the surface of the cerebral cortex becomes more and more folded to allow an increase of its surface in the limited volume of the skull. This folding process creates grooves on the surface of the brain called sulci and bumps or ridges called gyri. The two hemispheres of the brain are separated by a prominent central fissure. Each hemisphere is then made up of six lobes. The frontal lobe, located anterior to the central sulcus, the parietal lobe found dorsally to the same central sulcus, the temporal lobe on the most lateral part of the cortex and the occipital lobe which occupies the most occipital part of the cortex (figure 2.3). In addition, neurologists consider an internal lobe, called the limbic system, which lies along the medial part of the cortex and the insular cortex buried within the lateral sulcus (also known as Sylvian fissure).

The thickness of the cerebral cortex varies from 2.5 to 6 mm. Neuroanatomists have observed that the cortical neurons appear to be organized in various layers

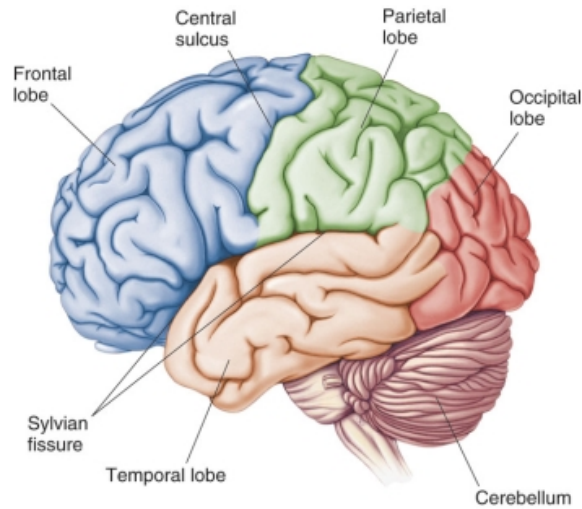


Figure 2.3: Cortical lobes. From [www.bioon.com/book/biology/whole/image/1/1-8.tif.jpg](http://www.bioon.com/book/biology/whole/image/1/1-8.tif.jpg)

(usually six) tangentially to the cortical surface. These layers can be distinguished histologically, functionally and through the connectivity pattern they exhibit with each other.

Neuroanatomists also noticed that the neurons distribution and size are not homogeneous across the cortex. This led some of them to propose a parcellation of the cortex into distinct zones, i.e. cortical "areas" with coherent cells structure. The most famous ones are the cytoarchitectonic maps of Brodmann [17] based on microscopical studies of local cellular and laminar structure (figure 2.4).

Despite this general laminar architecture parallel to the cortical surface, a neuron may be part of different layers through its dendrites. This communication in a direction orthogonal to the cortical surface suggested the concept of cortical columns. Physiological studies confirmed this columnar organization, showing that neurons in a vertical section of the cortex often share similar functional properties. We will illustrate this notion below in the visual system.

### **Other grey matter nuclei**

The cortex is not the only grey matter part of the brain. The basal ganglia, such as the putamen and the caudate nucleus, are as well composed of grey matter. It is also the case for the thalamus. The latter comprises many different pairs of nuclei, most of which project to the cortex. Some are sensory relay nuclei, i.e. nuclei that receive signals from sensory receptors, process them, and then transmit them to the appropriate areas of sensory cortex. For example, the Lateral Geniculate Nuclei (LGN), the Medial Geniculate Nuclei (MGN), and the Ventral Posterior Nuclei (VPN) are important relay stations in the visual, auditory, and somatosensory systems, respectively.

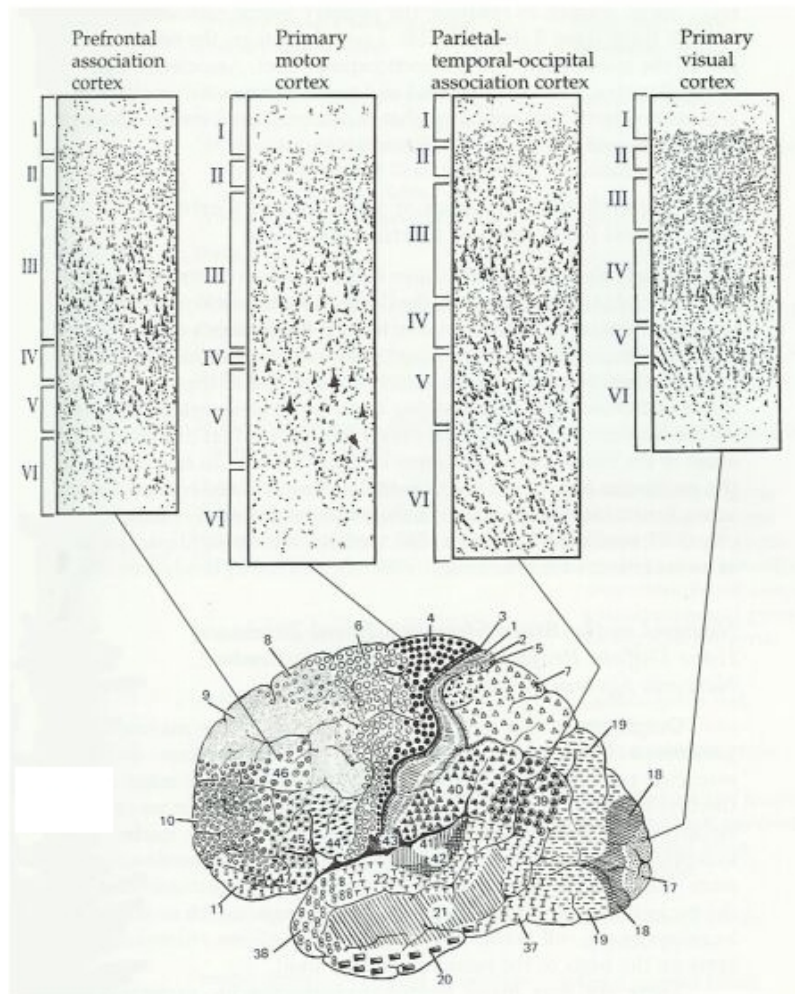


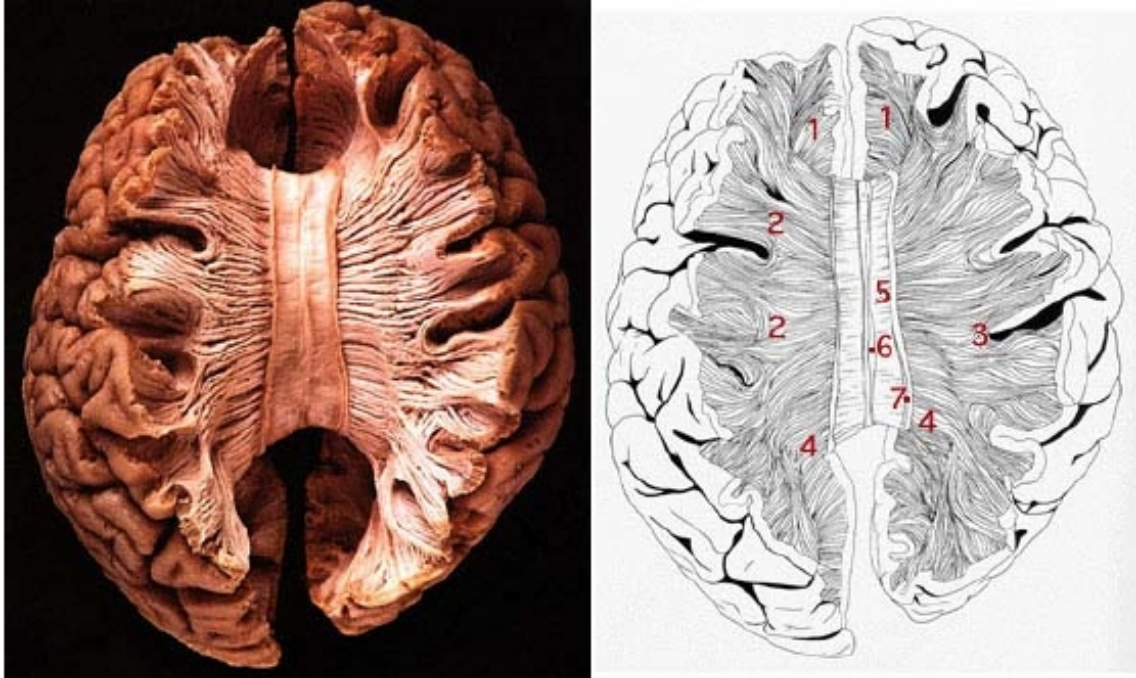
Figure 2.4: Brodmann areas and cortical layers cytoarchitecture. Notice the great differentiation in cortical layers thickness, for instance the predominance of the input layers II and IV in the primary visual cortex or of the output layers III and V in the primary motor cortex. From [www.unige.ch/cyberdocuments/theses2003/RivaraC-B](http://www.unige.ch/cyberdocuments/theses2003/RivaraC-B)

### 2.1.4 White matter connections

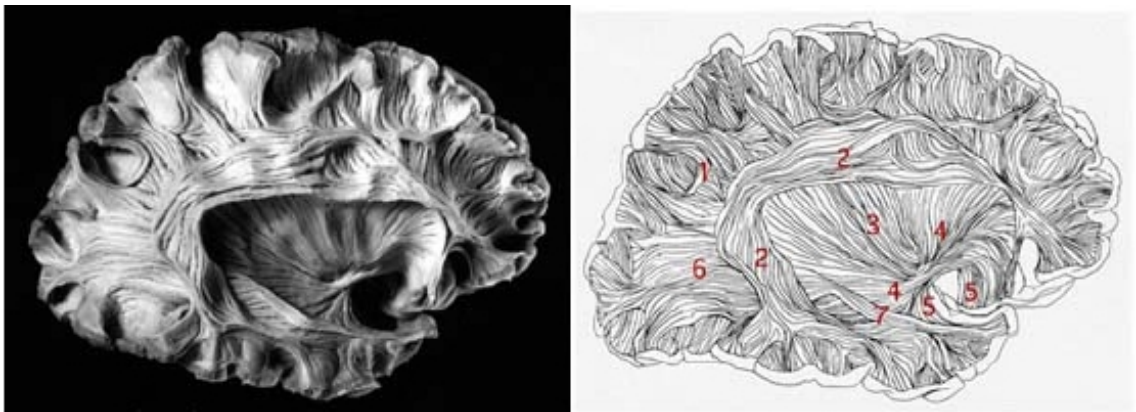
White matter is composed of axonal nerve fibers, covered by a myelin sheath giving its distinctive color. It is found in the inner layer of the cortex, the optic nerves, the central and lower areas of the brain (notably the brainstem) and surrounding the central shaft of grey matter in the spinal cord. The white matter axons can be distributed diffusely or concentrated in bundles, also referred to as tracts or fiber pathways.

Three main types of neural tracts are found in the white matter:

- The **Projection tracts** establish connections between the cerebral cortex and subcortical structures. Two types of projection tracts can be distinguished: ascending tracts and descending tracts. Ascending tracts carry sensory information from different parts of the body to the cerebral cortex. All sensory information, except olfactory, end up in the primary sensory cortex by the means of the thalamo-cortical fibers. The thalamus receives the somesthetic, gustatory, visual and auditory stimuli through these ascending pathways. Descending tracts carry motor commands from the motor cortex down to the muscles and glands through the lower brain structures and the spinal cord. They reach structures like the thalamus, the red nucleus, the medulla and serve muscles of the torso, extremities, facial and neck region.
- The **Association tracts** are the communication paths between different cortical areas within a given hemisphere. They can be divided into two categories: short and long association tracts. Short association tracts build up connections between regions of a given lobe. The smallest link adjacent cortical zones separated by a sulcus, hence their name of U-shaped fibers (see for instance the short arcuate bundles, identified with the label 1 on bottom part of figure 2.5). Long association fibers establish connections between different cerebral lobes and often form a bundle macroscopically visible.
- The **Commissural tracts** are bundles of axons connecting a region in one hemisphere to another region of the opposite hemisphere. The corpus callosum (figure 2.5 top) is the most important of the commissural tracts and can be broken down into four parts: The rostrum (anterior most part) and the genu (anterior curvature) are made up of fibers connecting the anterior and ventral parts of the frontal lobes. The corpus (large middle portion) links posterior portions of the frontal lobes as well as the parietal lobes. Finally, the splenium (caudal curvature) enables communications between the temporal and occipital lobes.



1. Frontal forceps 2. Corpus callosum commissural fibers 3. Short arcuate fibers 4. Occipital forceps 5. Indusium griseum 6. Medial longitudinal stria 7. Lateral longitudinal stria



1. Short arcuate bundles, 2. Superior longitudinal fasciculus, 3. External capsule, 4. Inferior occipitofrontal fasciculus, 5. Uncinate fasciculus, 6. Sagittal stratum, 7. Inferior longitudinal fasciculus.

Figure 2.5: Various white matter bundles seen from above after partial removal of the cerebral hemispheres (top) and in a sagittal slice (bottom). From <http://www.vh.org/adult/provider/anatomy/BrainAnatomy/BrainAnatomy.html>

## 2.2 The visual system

In this section, we start by a brief description of the path conveying the visual information from the eyes to the visual primary visual cortex. We then present the organization of the visual cortex. For more precise descriptions, see for instance [166, 24, 119].

### 2.2.1 From the eyes to the cortex

In primates (in particular in humans), the visual system includes many anatomical elements, from the eyes to the cortex. A human eye is approximately 2.5 cm long and weighs 7 grams. Six bands of muscles allow the control of its displacements to probe the environment. Light goes successively through the cornea, the aqueous humor, and the pupil, whose size is controlled by a muscle, the iris (giving the eye its external color). Next it passes through the lens, whose shape is controlled by the ciliary muscles, before entering the vitreous humor. It finally strikes the retina, which is covered with over 125 million photosensitive receptors of two families:

- **the cones** make a population of around 8 millions cells. Mainly concentrated in the center of the retina, also known as the fovea, the cones are responsible for chromatic and normal lighting condition vision (or photopic);
- **the rods**, which are estimated at around 120 millions. Rods are found everywhere except in the fovea. They deal with black and white perception and low-lighting conditions (or scotopic).

These photosensitive receptors translate lighting information into electrical information, transmitted to the optical nerves via the ganglion cells. The two optical nerves cross, forming the optic chiasm, after which information is transmitted separately for each visual hemifield (separated vertically with respect to the head position): the information from photons striking the left (respectively right) parts of both retina and corresponding to the right (left) visual field is brought together to form the left (right) optical tractus. Nonetheless, visual signals from the two eyes remain segregated in the LGN (and even latter in area V1).

The vast majority of the optical tracts fibers get projected to a part of the thalamic sensory relay system, the Lateral Geniculate Nucleus (LGN). The LGN approximately count 1 million cells, corresponding to the number of optical fibers. Finally, the LGN axons form the optic radiations which vanish in the primary visual cortex, centered around the calcarine fissure (figure 2.6).

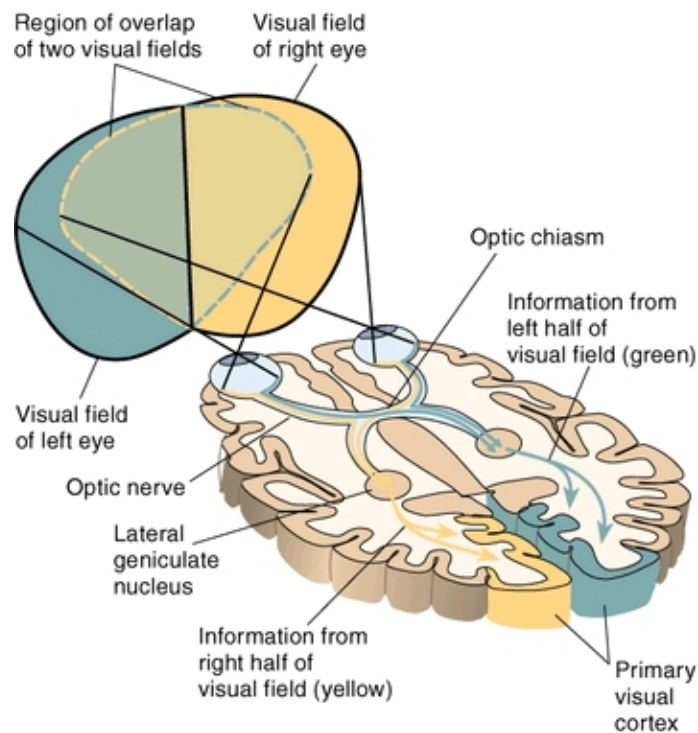


Figure 2.6: The path of the visual information from the eyes to the primary visual cortex.

This figure is borrowed from:

<http://homepage.psy.utexas.edu/homepage/Class/Psy308/Salinas/Vision/Vision.html>

## 2.2.2 The visual cortex

### From a single to multiple visual areas

Until the middle of the twentieth century, the major theory about the visual cortex considered a single area located at the occipital pole [105, 256]. As we mentioned above, this part of the cortex receives its major inputs from the LGN. Besides, patients who underwent damage to this zone suffered from severe blindness. Finally, the cytoarchitecture found there was easily distinguishable from surrounding cortical tissue (from which came the name "striate cortex"). Around this single visual area, a large expanse of the cortical surface extending to the parietal and temporal lobes was called the association cortex. Its function could be to associate distinct visual signals together or with complementary information from other sensory systems. However, an electrophysiology study performed by Hubel and Wiesel in 1965 [110] demonstrated some areas in the cat association cortex where neurons responded only to visual stimulations. Several studies further confirmed this finding, revealing various purely visual areas in the macaque and the owl monkey. To date, over 30 areas could be differentiated in the macaque monkey based on four main criteria [68]: (i) local cortical cells architecture, (ii) connectivity patterns across areas, (iii) global functional selectivity and (iv) retinotopy. In humans, the last two criteria

were successfully used to unveil several areas. We make below a list of current areas reported in the literature, grouping them with their anatomical location. Note that there is no systematic consensus across areas definition and labeling, emphasizing the technical as well as theoretical difficulties of such a task [254, 238].

### Early posterior occipital areas

The purely human visual areas are found mostly in the occipital lobe. All these areas exhibit a distinctive retinotopic map, although their low eccentricity representations are difficult to separate at the spatial resolution currently obtained with fMRI.

- V1, also known as striate cortex, primary visual area or Brodmann area 17, is viewed as the entry of the visual cortex. As already mentioned above, it receives most outputs of the LGN. V1 contains a complete (mirror) representation of the contralateral hemifield. Beyond this retinotopy, neurons in V1 are organized into sub-regions, each specialized in the analysis of a given visual feature. Hence, cortical columns predominantly responding to the information coming from a single eye and called ocular dominance columns have been shown in human V1 using fMRI [150, 28] (figure 2.7-A). Within these populations, it has been shown in animals study that neurons are further functional selective to local contrast orientation (such as an object border) or direction of motion. V1 regions also contain neurons that are selective for color. These regions are called blobs due to their blotchy appearance when the brain is stained with Cytochrome Oxidase (CO staining). The inter-blob regions contain orientation columns. Such an organization, which is repeated throughout V1 in an orderly manner, is referred to as hypercolumn. Figure 2.7-B) shows a model of V1 hypercolumn. Human V1 BOLD response to contrast variations has been shown to be limited for a low contrast (below 6%) and to increase monotonically with contrast increase [217]. It was shown to contain cells functionally selective to orientation [217], direction [113], color [61].
- V2, also called prestriate area, is subdivided into two parts: V2v (for *ventral*) and V2d (for *dorsal*). They respectively represent the upper and lower contralateral quarterfield. In non-human primates, area V2 mainly receives its inputs from V1. The neurons organization of V2 is described by the striped pattern that it exhibits after CO-staining. V2 is made up of pale stripes, thin stripes, and thick stripes. Neurons within the pale stripes of V2 receive input from the V1 inter-blob regions, and exhibit orientation selectivity but not motion selectivity. Neurons within the thin stripes of V2 receive input from the color blobs in V1, and exhibit color selectivity but not form or motion selectivity. Neurons within the thick stripes of V2 receive input from layer 4B

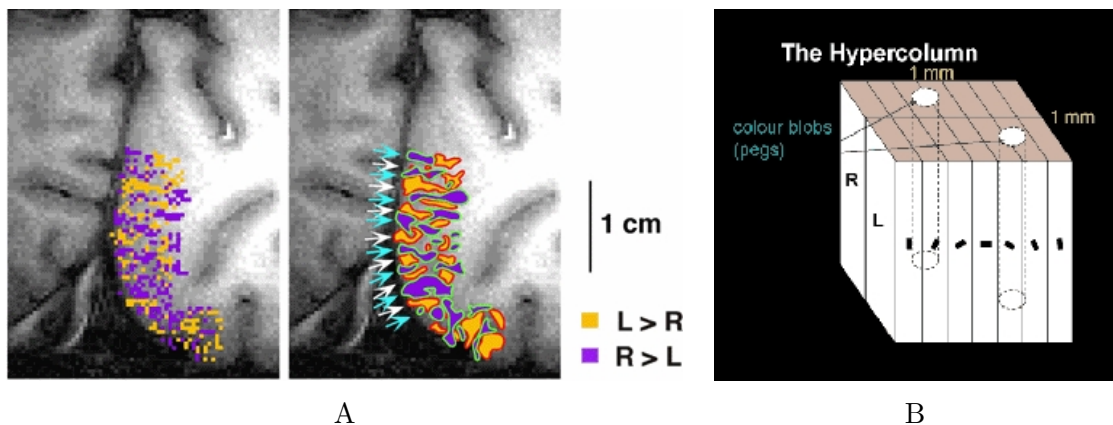


Figure 2.7: Examples of the functional neuronal organization in V1. A) Human V1 ocular dominance columns demonstrated with fMRI (Reproduced from [28]). B) Hypercolumn model with ocular dominance, orientation and color selective columns (from <http://web.psych.ualberta.ca/iwinship/vision>).

of V1 (which contains many motion selective neurons), and exhibit orientation and some motion selectivity.

- V3, like V2, is subdivided into two parts: V3v ventrally (sometimes also called VP, in reference to the Ventral Posterior area in monkeys), representing the upper quadrant and V3d dorsally, representing the lower quadrant. V3 neurons exhibit a high selectivity to low contrast and reach a saturation level at about 6% [218]. The functional selectivity of human V3 nonetheless appears different from monkeys: in macaque, V3 is moderately motion and direction selective, which has not been observed in humans [161, 224].

### Dorsal areas

A set of areas has been found dorsally to area V3d. Various reports suggest the involvement of this region in motion and depth perception.

- V3A, for V3 *Accessory*, is found at the posterior section of the intraparietal sulcus, posteriorly to V3d. V3A presents a complete representation of the contralateral hemifield and a foveal representation distinct to the confluent V1-V2-V3 central representations. V3A neurons seem to exhibit a similar contrast response than area V3 [224], i.e. a high sensitivity to low contrast. Human V3A also presents a strong responsivity to visual motion, contrarily to macaque V3 [224, 234].
- V3B is located dorsally to V3d and laterally to V3A. At current imaging resolution, V3B foveal representation appears confluent with that of V3A. Recent field map measurements suggest a complete representation of the contralat-

eral hemifield [177] and not only a quarterfield mentioned in the first reports [202, 57].

- KO, for Kinetic Occipital, was discovered by the group of Orban [233] through its marked responsiveness to moving boundaries (kinetic contours). It is located anterior and lateral to V3 and V3A and posterior to hMT/V5+. It has been suggested that KO could partially or totally overlap with V3B [202, 254].
- V7 is located anteriorly and dorsally to V3A and represents the complete contralateral hemifield [177]. However, the eccentricity and polar angle maps seem to run in parallel [227]. V7 neurons receptive fields differ from those of V3A and V3B, either in size or in their spatial distribution [177].

### **Ventral areas**

Several evidences demonstrate the strong responsiveness to color stimuli in the ventral occipital cortical surface [148, 95, 15]. There is however no consensus about the retinotopic organization of the visual cortex located ventrally to V3v. Different views are currently disputed. The group of Tootell describe an upper quadrant representation adjacent to V3v they label V4v. Moving further ventrally, they consider a complete hemifield representation, named V8, running perpendicular to that of V4v [95]. The group of Wandell describe a complete hemifield representation adjacent to V3v, labeled hV4 followed laterally by two hemifield maps of the central 5 degrees labeled V0-1 and VO-2 [15]. McKeefry and Zeki refer to a V4 complex with a complete hemifield named V4 and at least an upper quadrant named V4 $\alpha$ . Tyler and colleagues have yet another view, with a region similar to hV4 and an upper quarterfield found medially to it named VMO (VentralMedial Occipital), and a subsequent upper quadrant representation labeled Ventral Occipital Foveal (VOF) referring to its mostly foveal representation. Subsequent measurements are needed to clarify this issue and clearly attribute the respective functional role of the delineation obtained.

### **Lateral areas**

- The human MT/V5 complex, or hMT/V5+, is easily defined by its strong functional selectivity to motion stimuli [257, 218, 233, 202]. It is typically found at the junction of the ascending limb of the inferior temporal sulcus (ALITS) and the lateral occipital sulcus (LO) [241, 56]. This zone is referred to as a complex since it is thought to comprise human equivalent to macaque's MT, MST, FST and perhaps adjacent areas. Some efforts have been made to segment hMT/V5+ into distinct components [55, 112]. In monkeys, MT/V5 and surrounding areas have been extensively studied (for a review, see for

instance [11]). The main hallmarks regarding MT/V5 is its organization into direction columns [2], comparable to orientation columns in V1 and the strong myelinated inputs it receives from V1. Regarding hMT/V5+ cells, it was shown among others to have a high selectivity to low contrast but a limited responsivity to equiluminant motion stimuli [218], suggesting a magnocellular dominated area (see below). Furthermore, it was demonstrated that hMT/V5+ contains pattern motion cells [114]. hMT+ responds both to first and second order motion [202] and is more generally involved in many aspects of visual perception implying motion [208, 161, 255].

- The Lateral Occipital zone is, as indicated by its name, a region on the lateral occipital lobe, more specifically close to the Lateral Occipital Sulcus (LOS), adjacent to the early retinotopic areas and extending up to hMT+ laterally. The more dorsal portion was shown to be involved in motion and attention task [208, 224, 42], while the ventral part is highly responsive to objects recognition [91]. To date, the retinotopic organization in the Lateral Occipital zone appears elusive, although some measurements of eccentricity representations were reported [222, 227]. Various subdivisions and labeling have been proposed in the Lateral Occipital region. For instance, the group of Malach proposed at least two subregions: LO (Lateral Occipital) located dorsally and pFus (posterior fusiform) more ventrally along the fusiform gyrus [91]. The group of Orban refers to LOS and distinguishes a motion-sensitive part, a shape-sensitive part and a mixed part including area KO [163].

Various subsequent visual areas were functionally identified in the human cortex further away from areas and zones we have just presented above. These areas were mostly defined by their functional selectivity to features including motion [209], biological motion [92, 229], faces [120], places [64], letters [101], etc...The retinotopic organization in these areas is still unclear and may not follow the same principles as in the early posterior areas [227].

### **Parallel processing pathways**

From the above list of areas, it is presumed that the visual information is not processed as a block in a single stream of information. In fact, different visual features, such as motion or color, are separated and processed in parallel systems. This separation is found as early as in the LGN, where two<sup>2</sup> main types of cells are found in segregated layers: magno and parvo. Magno and parvo cells differ in many respects:

---

<sup>2</sup>Note that a minority third LGN neurons type, known as konio cells, has been reported; konio cells function is less understood but supposed to play a minor role in visual information processing.

- magno cells have a higher temporal but lower spatial resolution (with larger receptive fields) than parvo cells,
- magno cells exhibit a lack of color sensitivity contrarily to parvo cells,
- a high sensitivity at low contrast accompanied with a rapid saturation is found in magno cells while parvo cells response increases gradually with luminance contrast.

A comparable segregation is found within the visual cortex, which is classically subdivided into:

- a ventral or occipito-temporal pathway involved in color, patterns and shape processing; it answers the "What?" question,
- a dorsal or occipito-parietal pathway involved in spatial relation and objects motion processing; it answers the "Where?" question.

This sketchy subdivision of the visual cortex, primarily demonstrated with monkeys lesion studies [228], seems to hold in humans as suggested by several patients studies [69]. However, this view was further refined by the british psychologists Milner and Goodale [152] who distinguish both pathways regarding the cognitive task they serve:

- the dorsal stream is implied in visual guidance of actions toward objects,
- the ventral stream is responsible for the analysis of visual inputs to allow object recognition and conscious visual perception.

Note also that such a segregation is not perfectly respected and various communications are established between both pathways, allowing interactions between the respective visual features they process (see figure 2.8).

### **Hierarchical organization**

Another general and important principle in the visual brain is its hierarchical organization. According to this principle, the different areas of a given pathway can be hierarchically ordered, from low-level areas processing simple visual attributes such as the orientation of an edge or local motion direction to high-level areas dealing with more complex information such as object identification or complex motion. This hierarchy principle has emerged from different observations along the visual pathways: (i) the increasing receptive field size (i.e. the portion of the visual field "perceived" by a cell), (ii) an increased complexity in neurons receptive field properties, (iii) a progressive lost of retinotopy.

In this model, information is processed in a "bottom-up" fashion from low-order to higher order areas. The result of the computation performed at level  $n$  is transmitted to level  $n + 1$  through feedforward connections.

Once again, the hierarchy principle does not account perfectly for the actual visual

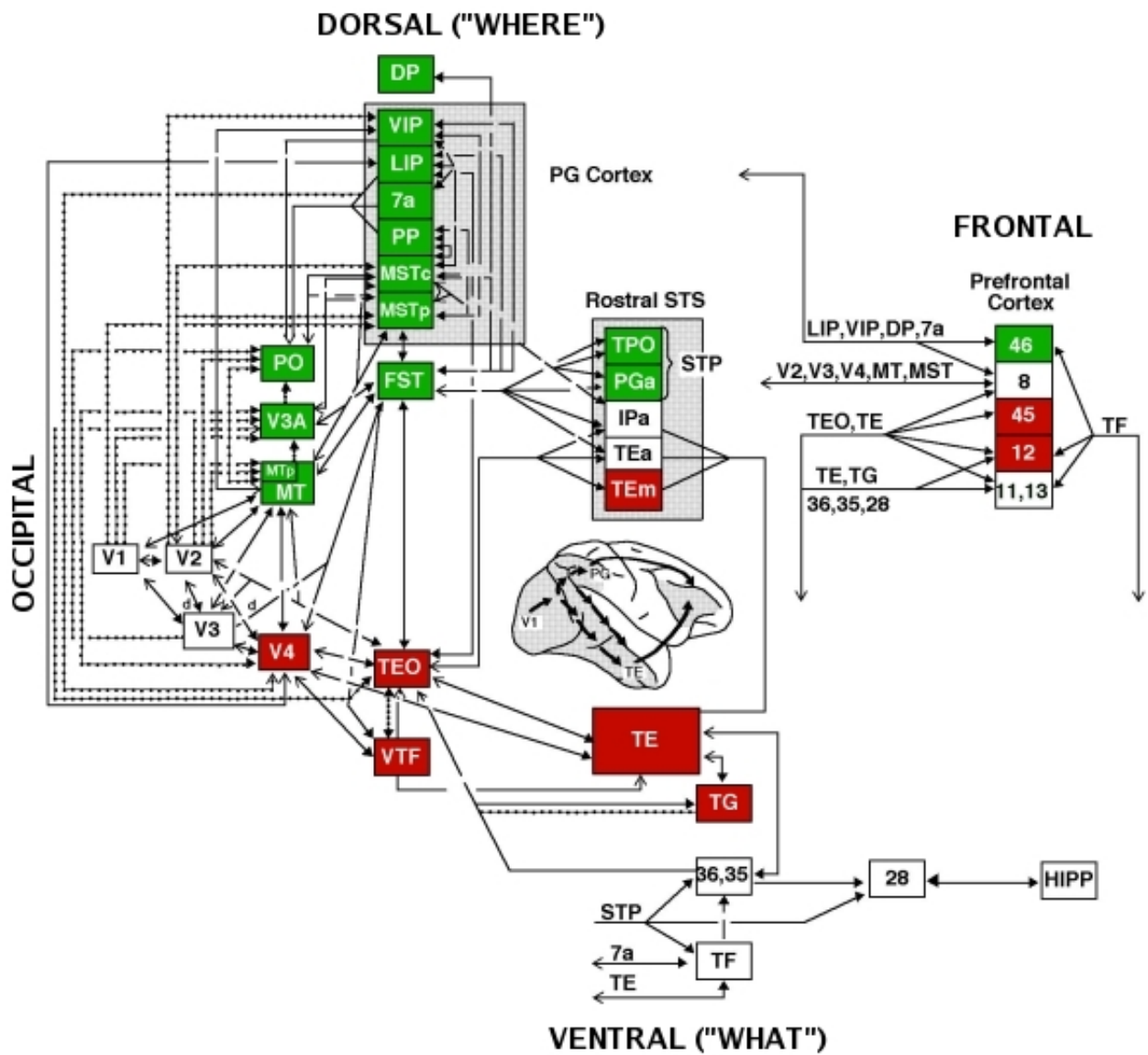


Figure 2.8: Parallel pathways and hierarchical processing in the monkey visual cortex. Modified from <http://lbc.nimh.nih.gov/people/ungerleider/science.jpg>

information processing in the brain. For instance, feedback connections from higher to lower order visual areas allow "top-down" information flow involved, among others, in attentional modulations.

The recent non invasive exploration of the human visual cortex has already provided extensive information and insight about its anatomical and functional organization. This research was possible thanks to the discovery and improvements of neuroimaging techniques, among which MRI has played an important role.

## 2.3 Magnetic Resonance Imaging

First demonstrated on small test tube samples in the beginning of the 70's by Paul Lauterbur [129], MRI allows to acquire non-invasively 3D images at high spatial resolution. Various modalities can be obtained with the same device: detailed anatomy (structural MRI), functional activity (fMRI), water-molecules diffusion (DWI), blood flow measurements (perfusion imaging), distribution of various metabolites (MR Spectroscopy Imaging), blood vessels (MR Angiography).

The first part of this section briefly exposes the basic principles of MR imaging, before giving the outlines of functional and diffusion-weighted MRI.

### 2.3.1 MRI principles

Magnetic Resonance Imaging has its foundations on rich and complex theories including electromagnetism and quantum physics, however it can be understood with relatively simple physical models. The underlying mathematical model implies Bloch equation which describes the relation between nuclear magnetization and magnetic field.

#### Physical model

An atom is made of electrons, holding a negative charge and rotating around a nucleus. The latter is subdivided in nucleons, specifically protons charged positively and neutrons with no charge. We distinguish three types of motion in an atom: the electrons both rotating around their own axis and in orbits around the nucleus, and the nucleus rotating around itself. MRI is based on the latter motion. Some nuclei have the property to align in a magnetic field if their mass number is odd, i.e. if the sum of protons and neutrons is odd. This is named angular moment or *spin*. Among others,  $^1H$  atoms, which represent 99.89% of naturally found hydrogens atoms and are widely represented in biological system, have a spin. On the other hand, carbon atoms mainly found under the  $^{12}C$  configuration are not prone to Nuclear Magnetic Resonance (NMR). Hence, MRI techniques are mainly considering  $^1H$  atoms.

Spin nuclei being positively charged, their motion induces a magnetic field. Conversely, the resulting magnetic moment can be oriented by the application of a magnetic field. This reciprocity is largely used in MRI. From a macroscopical point of view, no resulting field can be observed directly since each spin has its own, independent, random orientation (figure 2.9-a). However, when placed in an exterior magnetic field  $\vec{B}_0$ , the spin directions align parallel to this field (figure 2.9-b). More precisely, a spin rotates within a cone around  $\vec{B}_0$ : this is the spin *precession*. The spin rotation frequency, or Larmor frequency, is related to  $\vec{B}_0$  through its gyromag-

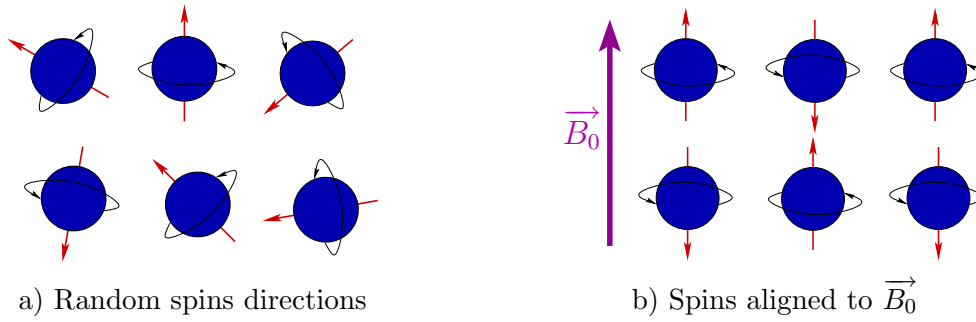


Figure 2.9: Random directions of spins in the absence of an external magnetic field (a) and aligned spins in the presence of an external magnetic field  $\vec{B}_0$  (b). Note that the actual spin rotation around  $\vec{B}_0$  occurs within a cone around  $\vec{B}_0$ .

netic ratio  $\gamma$ :

$$\omega_0 = \gamma \|\vec{B}_0\| \quad (2.1)$$

$\gamma$  depends on the atomical nucleus type. We have  $\gamma = 4257.43 \text{ Hz/G}^3$  for  $^1\text{H}$  atoms, implying a rotation frequency of  $f_{1\text{H}} = 63.86 \text{ MHz}$  in a 1.5 T magnetic field.

Given this type of rotation velocity, we can consider the spin induced field direction to be aligned with the cone symmetry axis, i.e. parallel to  $\vec{B}_0$ . Some are aligned in the same direction (parallel or *spin up*), while the other are in the opposite direction (antiparallel or *spin down*).

From a quantum physics point of view, the difference between both spin states is viewed as a difference in the energy level. Little energy is required to switch from the lower to the higher energy state. In the presence of an external magnetic field, the difference between the two populations is increased by an increase of the magnetic field strength. Applying Boltzmann relation, one can estimate that at the ambient temperature within a 1.5 T field, there is a difference of 10 in favor of low energy protons among a total of 1 million protons. Although very small at first sight, this difference becomes significant considering the huge amount of protons in a relatively tiny volume. For instance, a single gram of water contains  $6,7 \cdot 10^{22}$  protons! This imbalance between low and high energy protons results in a global magnetic field oriented in  $\vec{B}_0$  direction, called the net magnetization vector  $\vec{M}$ . As shown on figure 2.10,  $\vec{M}$  can be splitted into two parts:

- a longitudinal component  $\vec{M}_z$ , i.e. parallel to  $\vec{B}_0$ ;
- a transverse component  $\vec{M}_{xy}$ , orthogonal to  $\vec{B}_0$ . At equilibrium after a sufficient exposition time to  $\vec{B}_0$ , this component is null. All the individual spins are indeed precessing, but they are all out of phase with each other.

---

<sup>3</sup>G, for Gauss, is the magnetic field strength measure unit. For instance, the earth magnetic field equals 0.5G. More currently used in MRI is the Tesla (T), with the relation: 1 T = 10.000 G.

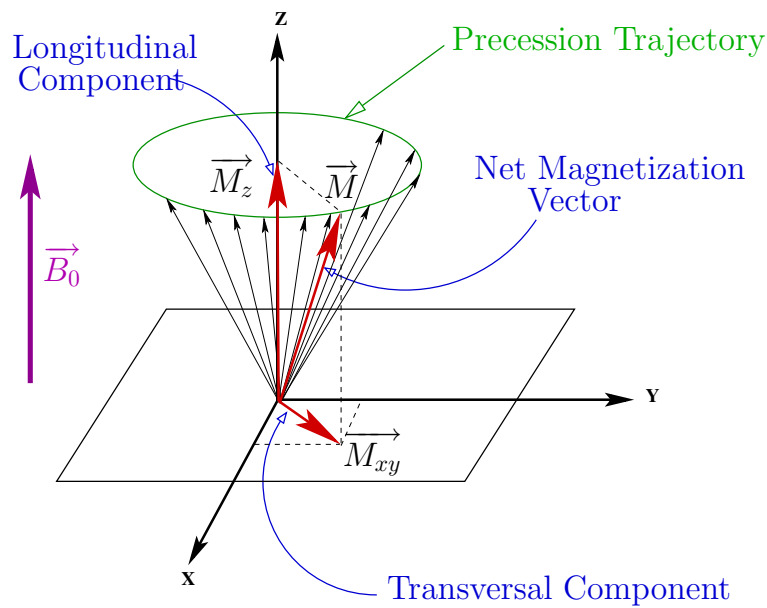


Figure 2.10: The net magnetization vector  $\vec{M}$ , decomposed into a longitudinal component  $\vec{M}_z$  and a transverse component  $\vec{M}_{xy}$ .

### Excitation phase

By applying a transient oscillating electromagnetic field, or electromagnetic radio-frequency (RF), with a frequency equal to the Larmor frequency of target nuclei, the difference between both energy spins can be temporally altered. This is a typical *resonance* mechanism (giving the "R" of MRI). The RF pulse duration is related with a flip angle of  $\vec{M}$ . A 90 degrees pulse suppresses the longitudinal component (figure 2.11) while a 180 degrees pulse, or "inversion pulse", completely inverts the longitudinal component through an excess of antiparallel spins.

Resonance may further induce a second effect so the spins magnetic moments may get synchronized, or in phase, i.e. they may be found at the same location on the precession trajectory, hence increasing the transversal component of  $\vec{M}$ . A receiver coil, which may be the same as that used to apply the RF pulse, allows to record the small voltage induced by the magnetization rotation in the transverse plane.

### Relaxation phase

When the RF is switched off, the spins begin to give off their energy, hence getting back to the equilibrium state. It results in two processes: an increase of the longitudinal component to its value before the RF pulse and a progressive decay of the transverse magnetization to zero.

### Spin lattice relaxation (T1)

The spin lattice relaxation is based on the energy exchange between protons and

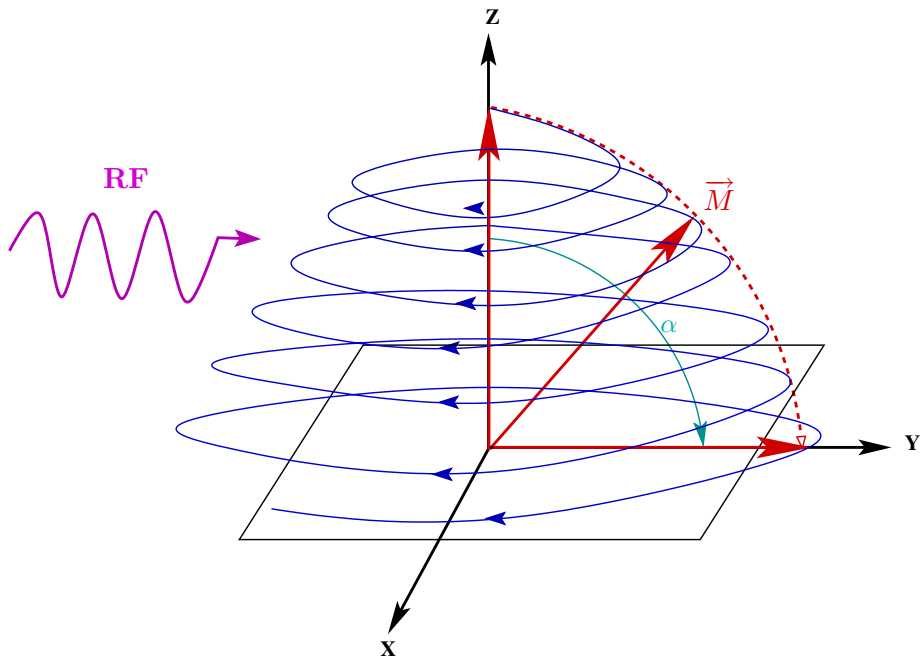


Figure 2.11: Excitation phase: the energy given by the RF pulse flips the net magnetization vector  $\vec{M}$  of an angle  $\alpha$  (here  $\alpha = 90^\circ$ ).

surrounding molecules. This energy dissipation is characterized by the restoration of the longitudinal component to its equilibrium value. This recovery process is modeled by an exponential function characterized by a time constant  $T_1$ , the period for the longitudinal magnetization to recover 63% of its equilibrium value (figure 2.12). For a 90-degree excitation pulse, we have:

$$M_z = M(1 - e^{-\frac{t}{T_1}})$$

The recovery process is considered as finished after 5  $T_1$  periods.

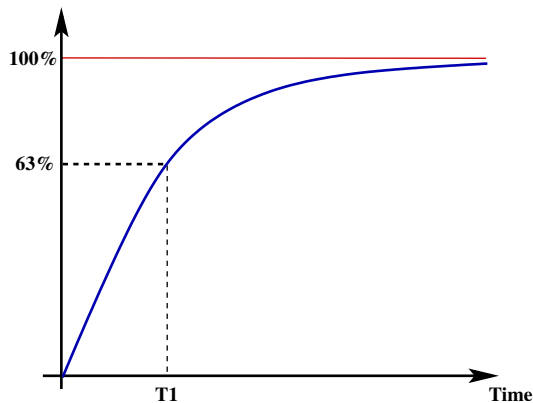


Figure 2.12: Spin lattice relaxation describes the longitudinal component recovery as a function of time and is characterized by the  $T_1$  constant.

### Spin-spin relaxation (T2)

Spin-spin relaxation refers to the loss of net magnetization in the transverse plane related to protons dephasing. Spins do not only give up their energy to surrounding lattice molecules but also to other neighboring nonexcited spins. This process is also modeled by an exponential function characterized by another time constant T2, which corresponds to the period for the transversal component to lose 63% of its value just after the RF pulse:

$$M_{xy} = M_0 e^{-\frac{t}{T_2}}$$

This dephasing is actually further increased by local magnetic field inhomogeneities, since the Larmor frequency will also be nonuniform throughout the region. A time constant slightly different to T2, T2\*, is therefore used. The transverse component induces a current in a coil, known as Free Induction Decay (FID). The T2\* constant can be evaluated through the convex envelop of the FID curve (figure 2.13).

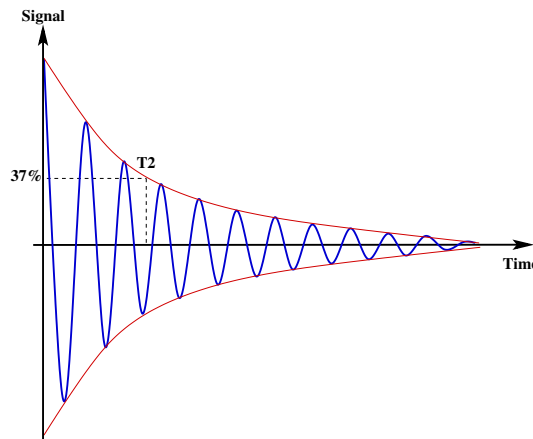


Figure 2.13: Spin-spin relaxation describes the exponential decrease of the transversal component as a function of time and is characterized by the T2 constant.

The different biological tissues are characterized by respective T1 and T2 values, as shown in table 2.1. The intensities of MR images comes from these values.

Tissue	T1 (ms)	T2 (ms)
CSF	800-20000	110-2000
Grey matter	1090-2150	61-109
White matter	760-1080	61-100
Fat	200-750	53-94

Table 2.1: T1 and T2 in various brain tissues.

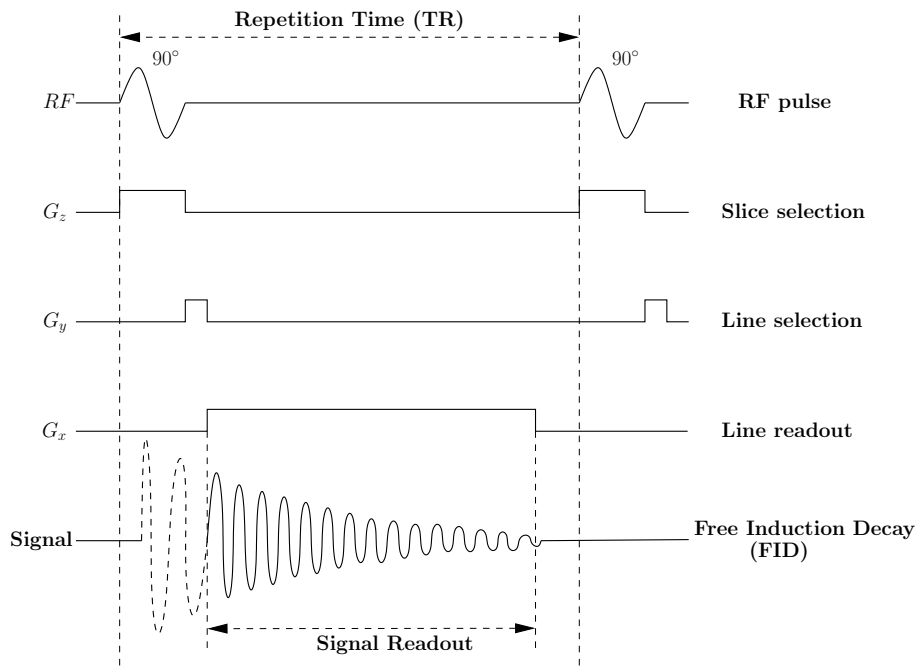


Figure 2.14: A highly simplified MRI pulse sequence timing diagram.

### Image construction through pulse sequence

A pulse sequence is a series of RF pulses and/or magnetic field gradients applied to a sample to produce a specific form of MR signal. It is indeed possible to encode and thus recover the MR signal from specific regions in the volume of interest by means of RF and linear gradients applied along the 3 spatial directions.

Figure 2.14 illustrates a basic pulse sequence. A first gradient  $G_z$  in the  $\vec{B}_0$  magnetic field direction results in a linear intensity variation of the magnetic field that can be used to select a slice. In this case, a slice is a plane orthogonal to  $\vec{B}_0$  with a typical thickness of 1-10mm. Based on relationship (2.1), the spins of a given slice are hence characterized by a specific Larmor frequency. After the RF pulse at the frequency related to the target slice, two transient gradients are applied to encode the  $x$  and  $y$  dimensions in the slice plane. A first gradient  $G_y$  in the  $y$  direction induces a phase shift related to the position along the  $y$  axis: this is the *phase encoding*. A second gradient  $G_x$  in the remaining  $x$  direction is applied, leading to a precession frequency variation along the  $x$  axis: this is the *frequency encoding*. This process actually performs an acquisition of the plane data in the frequency space (or *k-space*). An inverse Fourier transform finally maps these data in the 3D space.

A pulse sequence is first characterized by the delay between two similar RF pulses, called the Repetition Time (TR). The other parameters of interest depend on the actual sequence. Indeed, different pulse sequences were developed to measure the relaxation times. For instance, Gradient Echo simply repeats the Free Induction

Decay described above and allows to sample  $T2^*$ . Most sequences often comprise additional RF pulses following the slice selection one, to partially refocus the transverse magnetization and produce an echo, leading to a more reliable measure. Spin-Echo is thus the application of a 90 degree pulse followed by a 180 degree pulse after a time  $TE/2$ . This second pulse, which refocuses the transverse magnetization and results in an echo at time  $TE$  (Echo Time), removes local field inhomogeneities dephasing, hence allowing to directly measure the  $T2$  decay. On the other hand, Inversion Recovery, which relies on a 180 degree pulse followed after a time  $TI$  (Inversion Time) by a 90 degree pulse, enhances the  $T1$  weighting. The choice of the specific pulse sequence parameters ( $TR$ ,  $TE$ ,  $TI$ ,...) finally determines the image contrast. Two distinct tissues may for instance have similar  $T1$  values but distinct  $T2$  values, so the choice of the sequence depends on the information of interest.

The straightforward application of a given pulse sequence allows to get a static image contrasting different tissues. However, based on the same principles, it is possible to indirectly image dynamic processes such as oxygen flow or the motion of water molecules.

### **2.3.2 Functional MRI: the B.O.L.D. signal**

Although the brain represents 2% of the total body mass, it receives 12-15% of the blood outgoing from the heart and consumes 20% of the oxygen breathed. Functional imaging techniques, and in particular BOLD fMRI, build on this high metabolic demand to derive an indirect measure of neuronal activity.

#### **Hemodynamic coupling**

Neuronal activity requires energy, supplied by an increase of the energetic metabolism. Oxygen and glucose consumption is indeed locally increased during a neuronal activation. However, the brain is not able to store oxygen, which is actually brought by the blood (figure 2.15). The first evidence of a coupling between cerebral blood flow (CBF) and neuronal activity was obtained by Roy and Sherrington who, in the end of the 19th century, reported a local change of the cortical tissue color correlated with stimulation [183]. The brain color changes observed was related to blood oxygenation. A century later, such effects could be confirmed in vivo by Positron Emission Topography [181] using radioactive oxygen  $H_2O^{15}$ .

#### **Magnetic properties of hemoglobin and BOLD signal**

The intensity changes we might be able to observe in the MR images is based on magnetic properties of hemoglobin which change with its oxygenation, as first shown by [170]. Hemoglobin can indeed be found under two configurations: oxyhemoglobin

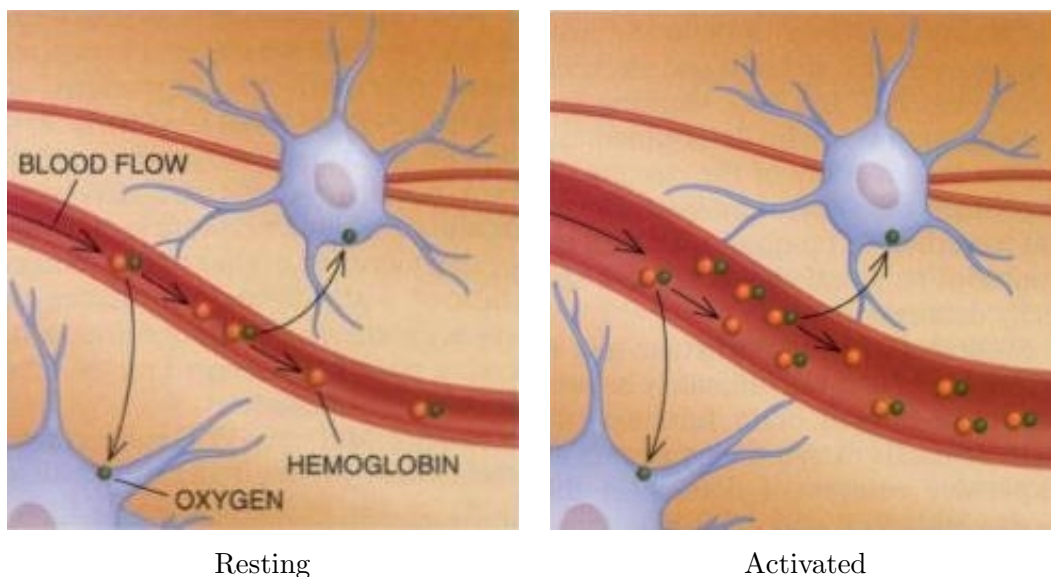


Figure 2.15: Oxygen extraction is increased during neuronal activation, thereby increasing the level of deoxyhaemoglobin (Hb) in the blood. The latter is nonetheless over-compensated by a local increase in the blood flow, leading to a net reduction of the ratio  $Hb/HbO_2$  that can be measured with MRI. (From [180])

( $HbO_2$ ), which carries 4 oxygen molecules and is diamagnetic, and deoxyhemoglobin (Hb), depleted of oxygen and paramagnetic. Therefore, oxyhemoglobin has no effect on the local magnetic field while deoxyhemoglobin locally adds magnetic field gradients, increasing the  $T2^*$  value<sup>4</sup>. Hence, voxels with high Hb concentration yield to a lower signal than tissue with high  $HbO_2$  concentration. In 1990, Ogawa et al. [158, 159] first mapped  $T2^*$  variations related to cortical blood oxygenation changes at the level of capillaries and venules surrounding activated brain areas. This signal is referred to as BOLD, for Blood Oxygen Level Dependent.

But why do we actually measure the contrary, i.e. a signal increase during local neural activation? In fact, an activation induces a significant increase in CBF that occurs without an increase of similar magnitude in oxygen extraction. For instance, assume that during "rest" neuronal activity, if arterials supply 100% of oxygenated blood, 40% are locally consumed. Blood returning to veins is therefore made of 40% of deoxygenated blood and 60% of oxygenated blood. During a neural activity, blood supply increases more than needed, leading to modified proportions in the arterials close to 37-63%. This results in a corresponding local reduction in the ratio  $Hb/HbO_2$ , leading to a signal increase.

Various models based on different hypotheses have been proposed to explain this oversupply of oxygenated blood as compared to oxygen extraction, see e.g. [19].

<sup>4</sup>A similar effect can be obtained with paramagnetic contrast agent such as Gadolinium or MION used in animal experiments. Note however that the signal is then negatively correlated with neural activity.

There is thus no simple relation between neural activity and the BOLD signal since the signal magnitude not only depends on these magnetic properties, but also on the current blood volume and the local vascular geometry. Various models of the hemodynamic coupling have been proposed so far (e.g. [6]), but the precise underlying mechanism is still unknown. Nonetheless, the work of Logothetis *et al.* [138] combining electrophysiological recordings and fMRI suggests a high correlation between local field potentials (thought to reflect more cortical inputs and local intracortical processing than spiking activity) and the BOLD signal.

### **Hemodynamic Response Function**

From a temporal point of view, electrical and synaptical activity to a transient cognitive process generally lasts a few milliseconds, while the vascular changes duration are a few seconds. The time course of human BOLD response to a similar brief neuronal process, seen as a temporal impulse response function, is called the hemodynamic response function (HRF). The amplitude and precise shape of the HRF varies significantly not only across subjects but also across brain locations, experimental tasks or scanning sessions in a given subject. Some examples of this HRF variability is shown in figure 2.16. Nonetheless, the rough shape systematically comprises a first delay of the response ( $\approx 2$  s), followed by a ramp of 3-8 s before slowly returning to baseline. In some cases, an initial dip of 1-2 s and/or a signal undershoot up to 20 s before the return to the baseline can be observed. Note that negative BOLD signals, significantly anticorrelated to the positive BOLD have also be reported (in particular in the visual cortex) and the underlying physiological and neural substrates are currently under study [204, 199]. Apart from this high variability of the HRF shape, the response to longer stimuli ( $>8$  s) can hardly be predicted from a linear prediction based on the HRF.

### **Echo Planar Imaging**

As a complete image acquisition with the sequences mentioned above is relatively long (a few minutes) with respect to the physiological events of interest in fMRI (a few seconds), faster acquisition techniques have been developed. Echo Planar Imaging (EPI) is the most famous one. EPI relies on rapidly oscillating gradients to allow a complete slice acquisition from the signal generated by a single RF pulse. This results in a dramatic reduced acquisition time (30-100 ms per slice), nonetheless at the expense of a lower spatial resolution. Alternative sequences, among others SMASH or SENSE, have been more recently proposed to allow parallel acquisitions with multiple coils. Such imaging improvements will certainly bring important improvements in the near future.

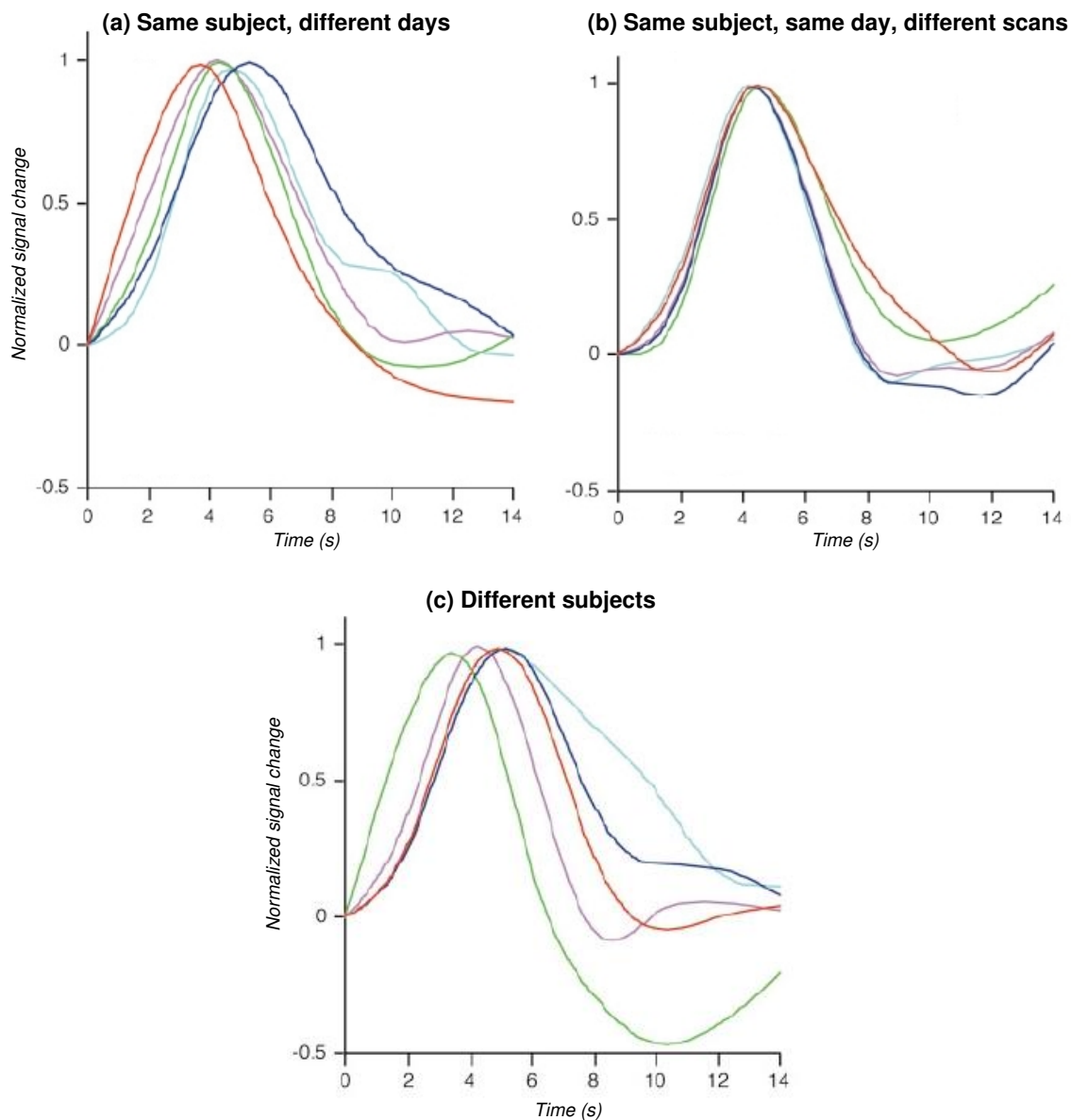


Figure 2.16: Variability of the Hemodynamic Response Function across days (a) and scans (b) within subject and across subjects (c). The BOLD signal from central sulcus is sinc interpolated and normalized to maximum. Modified from [1].

### Measuring the BOLD signal: activation detection paradigms

It is not possible to localize an activation with a single BOLD image. In fact, the signal of interest is the variation of the BOLD intensity. Besides there is no prior absolute signal level that can be used as baseline. A typical fMRI experiment hence consists of several runs (or sessions) consisting of alternating periods of (various) stimulus and control tasks. A run usually lasts 5 mins. Throughout each run, BOLD sensitive images are acquired at a specific temporal frequency, leading to a time series of images. Using EPI sequences, the typical functional images sampling

period is around 3 seconds for a complete volume. However, the acquisition can be restricted to a particular brain region of interest, such as the occipital pole, thus increasing the sampling period. Regarding spatial localization, the typical voxel size spans a few  $\text{mm}^3$ .

Different paradigms, called experimental designs, have been introduced to organize the sequence of tasks the subject undergoes during the scanning session. A given experiment can generally be labeled within one of the following experimental designs families:

- **Block design:** each experimental condition is submitted to the subject in relatively long presentation periods, or epochs, of typically 20 s. A run is a succession of alternated conditions presented in a random fashion. This kind of design is considered as optimal for activation detection purpose [136], since it is not much dependent on the BOLD response model choice. On the other hand, it is relatively time consuming since it precludes the use of more than a few different conditions in a single run.

- **Event-related design:** a run is in this case a series of brief events of the different experimental conditions. With an optimal events distribution, this kind of design is optimal for HRF shape characterization [136]. Besides, they are less prone to subjects fatigue. On the other hand, their detection power is relatively weak. Note that most fMR-adaptation experiments (see chapter 6) can be included in this category.

- **Periodic or Fourier design:** this design is particularly useful for periodic parametric stimulations such as used in retinotopic mapping experiments (see chapter 5). A given stimulus parameter is varied periodically, so that neurons selective to a given parameter value (or range of values) are activated periodically. The time series analysis consists of a Fourier transform at the stimulation frequency. The signals of interest are then the amplitude, indicating the local selectivity of the underlying neuronal population and the phase, related to a given parameter value of the stimulation.

We have stressed that the BOLD signal used in human fMRI is a complex phenomenon still not completely understood and requiring specific paradigms. However, the major advantage of this imaging method is its ability to noninvasively allow high spatial resolution cortical activity measures. Hence, fMRI is more and more used the neuroscience, with an exponential increase of study since its discovery in the 1990's.

### 2.3.3 Diffusion MRI

Diffusion MRI is the unique non-invasive technique that allows to probe and quantify the diffusion of water molecules in the body. By modeling the local anisotropy of this diffusion process, it becomes possible to indirectly infer local tissue architecture such as white matter fibers.

#### Physical principles

Above the absolute zero temperature, molecules freely moving in an isotropic medium are prone to many shocks one against another, implying many random changes of their motion direction. This phenomenon can be modeled as a Brownian motion, which from a macroscopical scale can be seen as a diffusion process. In an isotropic medium, the probability of a molecule to move a distance  $r$  during a time  $\tau$  follows a Gaussian law  $\mathcal{N}(0, \Sigma)$  with  $\Sigma = 6D\tau$ . The constant  $D$ , known as diffusion coefficient, measures the molecules mobility in the isotropic case and depends on the molecule-type and the medium properties. For example, at normal brain temperature, 68% of the water molecules diffuse in 50ms in a sphere of 17  $\mu\text{m}$  diameter.

In anisotropic biological tissues, water molecules mobility is constrained by obstacles formed by surrounding structures, such as the axonal membranes in the brain. In this case, the scalar diffusion coefficient  $D$  can be replaced by a multilinear operator. The most popular of them is the rank-2 diffusion tensor proposed by Basser *et al.* [8]:

$$D = \begin{pmatrix} D_{xx} & D_{xy} & D_{xz} \\ D_{yx} & D_{yy} & D_{yz} \\ D_{zx} & D_{zy} & D_{zz} \end{pmatrix}$$

where  $D$  is a real symmetric and definite-positive matrix, therefore related to a quadratic form modeling intrinsic diffusion properties of the tissue. The diffusion coefficient  $d$  related to any direction  $\vec{g} \in \mathbb{R}^3$  is given by:

$$d = \vec{g}^\top D \vec{g}$$

It then follows that the probability to find a molecule initially at position  $x_0$  at  $x$  after a delay  $\tau$  is given by:

$$P(x|x_0, \tau) = \frac{1}{\sqrt{(4\pi\tau)^3 |D|}} \exp\left(-\frac{(x-x_0)^\top D^{-1}(x-x_0)}{4\tau}\right)$$

The problem of Diffusion Tensor Imaging (DTI) is to estimate the 6 independent parameters of  $D$ . This can be achieved with a minimum of 6 diffusion-weighted images, each measuring a  $T2$  signal attenuation related to the diffusion coefficient in a specific direction  $\vec{g}_i$ , plus one unweighted  $T2$  image. The diffusion-weighted

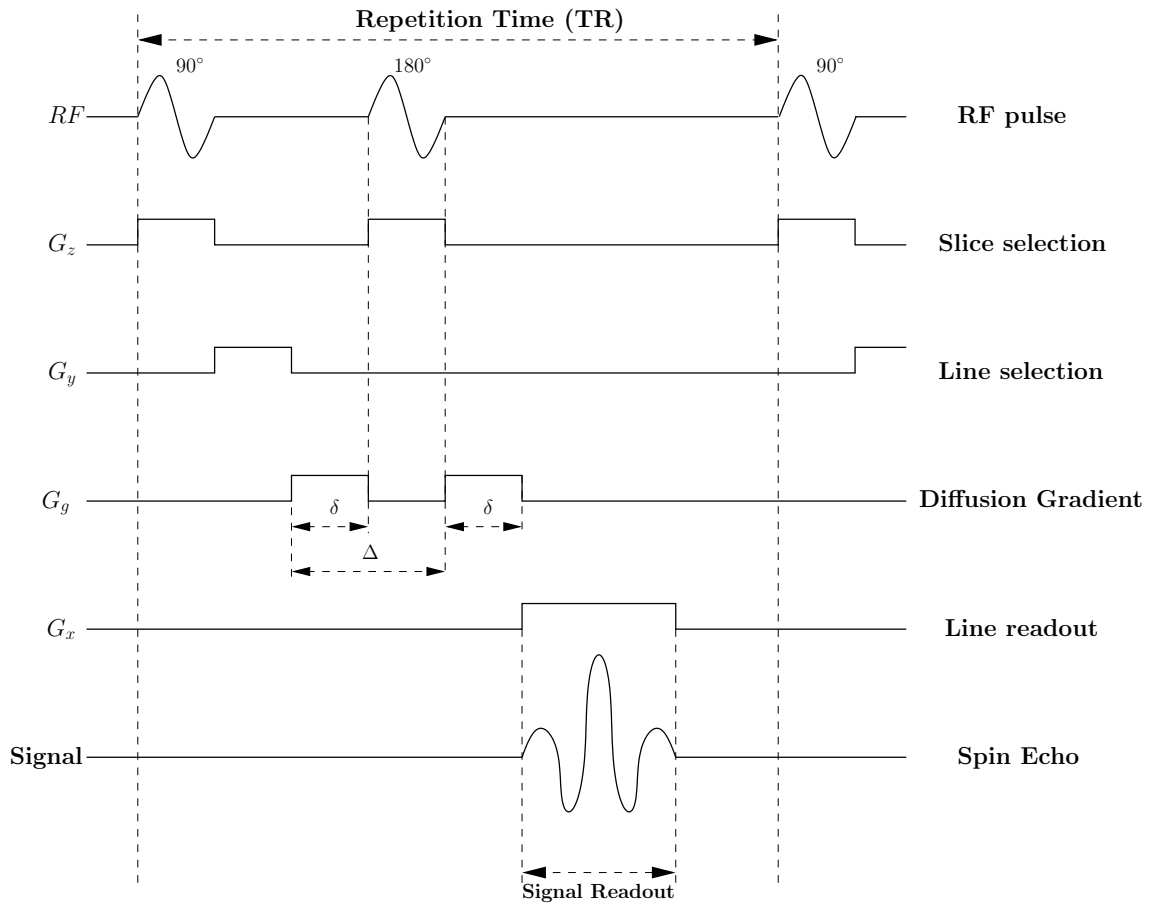


Figure 2.17: Stejskal-Tanner imaging sequence.

images can be obtained with appropriate imaging sequence using diffusion gradients in the direction  $\vec{g}_i$  of different amplitude and strengths.

### Imaging sequence

To measure water molecules diffusion in a given direction  $g$  (for sake of clarity, we note  $g = \vec{g}$  in the remainder), the Stejskal-Tanner imaging sequence [206] is used (figure 2.17). This sequence uses two gradient pulses  $G_g$  in the direction  $g$ , before and after a 180 degrees refocusing pulse controlling the diffusion weighting. More specifically, a first 90 degrees RF is applied to flip the magnetization in the transverse plane. The first gradient pulse then causes a phase shift for all these spins. Finally, the 180 degrees pulse combined with the second gradient pulse cancels this phase shift only for static spins. On the other hand, spins under Brownian motion during the time period  $\Delta$  separating the two pulses undergo different phase shifts by the two gradient pulses, resulting in an increased  $T_2$  signal attenuation. Figure 2.18 shows examples of diffusion-weighted images acquired with two different directions, illustrating the direction specific attenuation related to white matter fibers orientation.

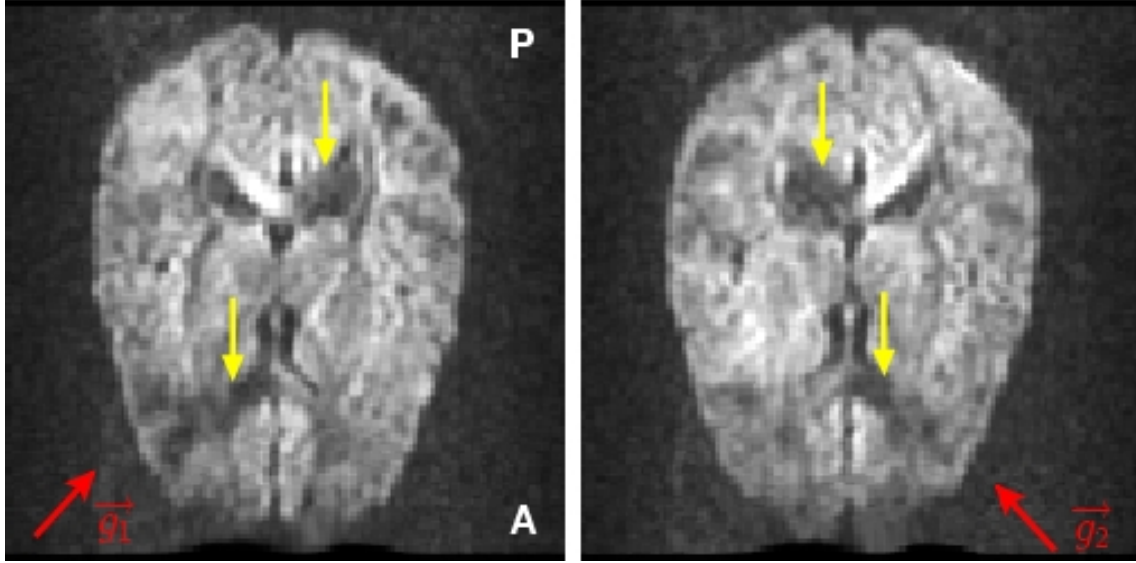


Figure 2.18: Axial slice of diffusion-weighted images (DWI) with two different diffusion gradient directions (red arrows). MR signal attenuation is found in regions having fibers mostly aligned with diffusion gradient direction (yellow arrows).

Signal attenuation observed can be modeled by the following equation [206]:

$$S(g) = S_0 e^{(-bg^\top Dg)} \quad (2.2)$$

where  $b$  is the diffusion weighting factor depending on scanner parameters and proposed by Le Bihan *et al.* [131]:

$$b = \gamma^2 \delta^2 \left( \Delta - \frac{\delta}{3} \right) |\mathbf{G}_g|^2$$

with  $|\mathbf{G}_g|^2$  the magnitude of the pulse,  $\delta$  its duration and  $\Delta$  the time separating two pulses (see figure 2.17).

Hence, signal attenuation, i.e. signal sensitivity to water molecules diffusion, is stronger if the diffusion coefficient  $d = g^\top Dg$  is important. Note also the importance of the  $b$  factor that has to be appropriately tuned compared to  $d$  to avoid either a very low signal attenuation if  $b$  is too small or a poor SNR if  $b$  is too high. A typical value filling this trade-off is  $b = 1000 s.mm^{-2}$ .

For each slice, images are collected with one or more  $b$  and at least 6 independent gradient directions  $S(g_i)$  and 1 unweighted  $T_2$  image ( $S_0$ ). The diffusion tensor  $D$  can then be estimated at each voxel using the  $S(g_i)$  and  $S_0$ . The classical method to derive the tensors uses least square technique, but various alternative methods have been proposed. We will come back to this particular point in chapter 7. We finally end-up with a diffusion tensor image, i.e. a 3D image with 6

parameters describing the local tensor  $D$ . From the eigenvalue decomposition of  $D$ , one can visualize the diffusion in each voxel by a diffusion ellipsoid: the directions of the main axes are given by the eigenvectors of  $D$  and their lengths are proportional to the respective eigenvalues. If all the eigenvalues are of the same magnitude, the ellipsoid will be spherical, while if one of the eigenvalues is much greater than the others, it will have the form of a cigar. Figure 2.19 illustrates the corresponding ellipsoids field in an axial slice. The blue (respectively red) color refers to elongated anisotropic (resp. spherical isotropic) ellipsoids.

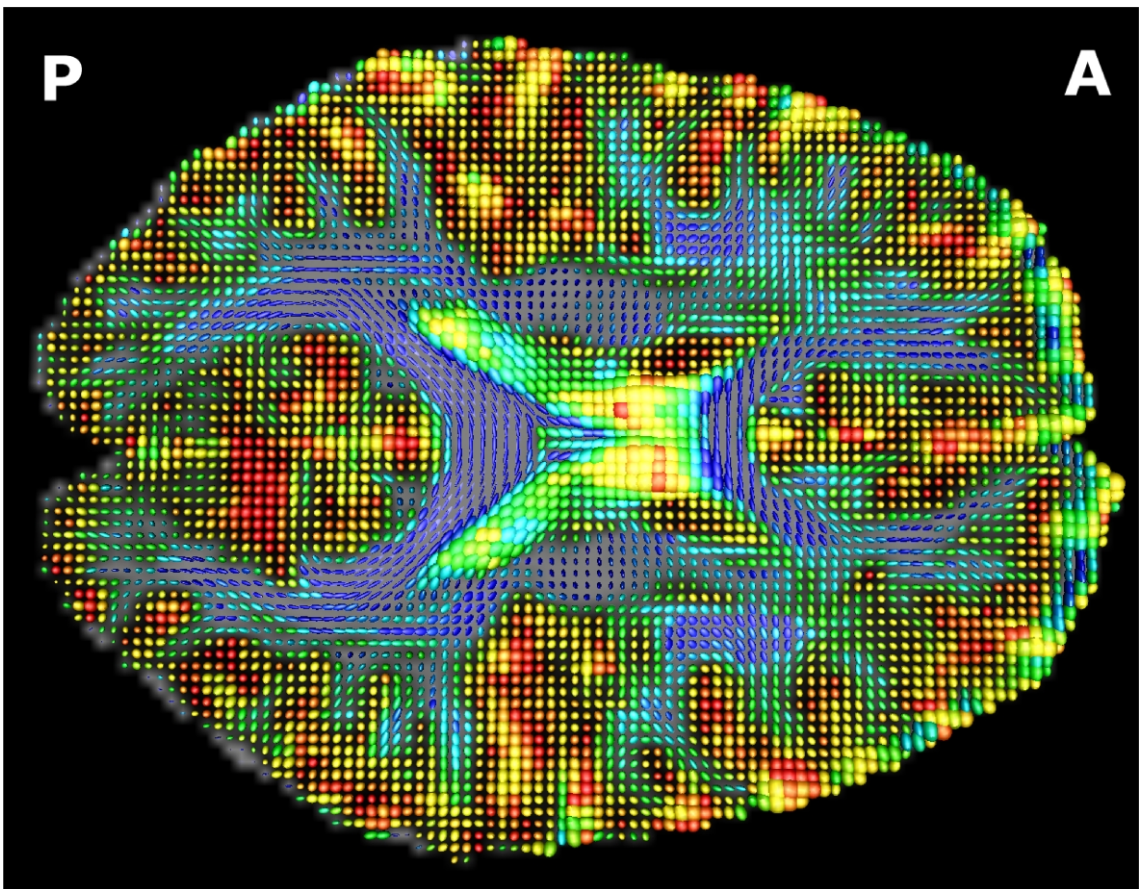


Figure 2.19: Axial slice of a Diffusion Tensor image. At each voxel, an ellipsoid represents the estimated diffusion tensor.

Note that to better describe the complexity of water motion, higher order models have been proposed [74, 226, 165, 21, 48]. The idea is to consider a discrete spherical function modeling the diffusion coefficient in  $N$  directions ( $N$  typically between 50 and 300) and measure the MR signal attenuation along each direction at each voxel. This obviously requires longer acquisition times, as  $N$  gradient directions have to be sampled.

## 2.4 Experimental setup

This section describes the experimental environment and scanning sequences used in this work.

### 2.4.1 The subject

No constraints are applied to the subjects we recruited for our different experiments, except those induced by the MR scanner: a complete absence of metal parts in the body, including vascular clips, neuronal implants, pace-makers, etc...This also excludes glasses, but lenses could replace them if any correction is needed.

As a rule of thumb, the idea for any global non-pathologic study is to use healthy right and left-handed men and women. This is the guideline we followed in order to obtain the results we present in this document.

All subjects gave written informed consent and were retributed for their participation. The different experiments were approved by the local ethic committee (CCPPRB Marseille 02/56).

### 2.4.2 The scanner and the stimulation device

The MRI scanner we used is located at la Timone fMRI center<sup>5</sup> in Marseille, France. It is a BRUCKER MEDSPEC 30/80 AVANCE, with a 3T magnet and a body coil. A picture of the scanner is shown in figure 2.20.

The subject lies inside the coil, with an antenna around his head. The visual



Figure 2.20: The 3T MR scanner of la Timone, Marseille and the bird-cage antenna. From <http://irmfmrs.free.fr/>

stimuli used in the fMRI experiments are displayed at 72Hz by a SONY video-projector, placed in a custom-designed Faraday cage inside the scanner room, onto a large adjustable mirror then onto a translucent screen inside the bore at the back of subject's head and finally reflected by a custom designed mirror placed at 5cm

---

<sup>5</sup><http://irmfmrs.free.fr>

above subject's eyes (see figure 2.21). The video projection was synchronized with the acquisition through a trigger sent by the scanner at the beginning of each scan. A custom designed keyboard was used when subjects were instructed to report some special events, such as the fixation control and attentional tasks used in our fMRI experiments. Both the stimulus presentation and subject's behavioral responses were controlled by a PC positioned outside the scanner room thanks to specific LabView<sup>6</sup> programs developed by Dr Bruno Nazarian, research engineer at the centre IRMf.

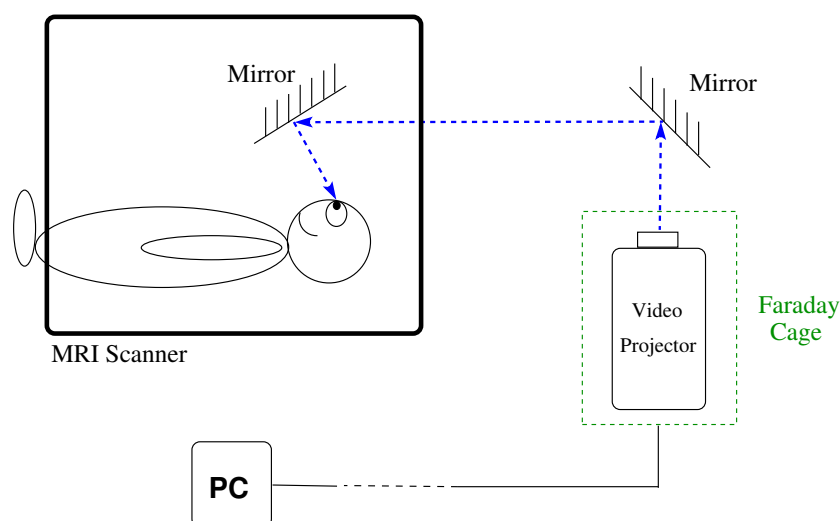


Figure 2.21: The visual stimuli projection system of our experimental setup

### 2.4.3 Visual stimuli

Stimuli were generated under Matlab 6.1 using the Image Processing Toolbox (Matlab, The Mathworks), providing an avi file with eighteen 300x300 pixels frames per second and lasting 5mn04sec. The video presentation setup leads to a display subtending a visual angle of  $20.9^\circ \times 20.9^\circ$ . This size is for the moment limited by the size of the coil and the visual stimulation setup. During the first 5 and last 2 scans, a mid-grey level image with the  $0.5^\circ$  red fixation cross was shown to the subjects. The first volumes are classically discarded from the analysis (typically corresponding to 10 seconds) to allow the magnetization to stabilize to a steady state. The stimulation of interest therefore starts after a few volumes have been acquired. The last 2 scans were acquired to allow slice-timing corrections (see section 4.1).

<sup>6</sup>Labview web site: [www.ni.com/labview](http://www.ni.com/labview)

#### 2.4.4 MR data acquisition

##### High resolution anatomical images

The acquisition of the cerebral anatomy of a given subject was done through a 3D-gradient echo sequence with inversion-recovery. The technical characteristics of the latter are the following:

- Echo-Time (TE): 5ms
- Repetition-Time (RT): 25msec
- Inversion-Time (IT): 800ms
- Field of view:  $256 \times 192 \times 192 \text{ mm}^3$
- Acquisition matrix:  $256 \times 192 \times 104$  (for a resolution of  $1 \times 1 \times 1.5 \text{ mm}^3$ )
- Reconstruction matrix:  $256 \times 256 \times 128$  (for a resolution of  $1 \times 0.75 \times 1.22 \text{ mm}^3$ )

This leads to a 15 minutes sequence to get a high resolution anatomical image.

##### Functional images

The functional images were acquired with a fast-imaging Echo-Planar sequence with the custom bird-cage head coil. In order to reduce the repetition time (RT) -and thus the time needed to acquire each functional image- while still preserving a high spatial resolution, we have restricted our functional scans to the occipital region of the brain rather than the complete head, since we are interested in the low-level visual cortex areas located in this region. We first started with 18 3mm thick slices with an inplane resolution of  $3\text{mm} \times 3\text{mm}$ , oriented approximately perpendicular to the calcarine sulcus. The corresponding TR was 1.5s ( $18 \times 83.33\text{ms}$ ). Thanks to acquisition sequence refinements performed by our colleagues at the Centre IRMf de Marseille, we then switched to either a  $2 \times 2 \times 2\text{mm}^3$  or a  $2 \times 2 \times 3\text{mm}^3$  voxel resolution sequence, using 20 slices to cover a sufficient portion of the brain. The 2mm slice thickness was sufficient for the retinotopic mapping experiment whereas we used the 3mm slice thickness sequence when we considered the hMT+ area, i.e. in the functional localization of the latter (see chapter 5) and for the adaptation experiment (see chapter 6). Both sequences require 103ms to acquire a single slice, leading to a RT of 2060ms for 20 slices. This RT was slightly increased to 2111ms artificially for each image in order to get a good synchronization between the presentation device (refreshing at 72Hz and showing 18 different images per second) and the volumes acquisition. Indeed, within a TR of 2111ms, we can present  $18 \times 2.111 \approx 38$  different images (whereas  $18 \times 2.060$  does not lead to an integer number of images). Acquisition of the multiple slices is interleaved, meaning that even slices are acquired sequentially before odd slices.

### **Diffusion-weighted images**

In a first pilot experiment performed on 3 subjects, we tried different acquisition parameters to obtain the best diffusion weighted images. We fixed TR=10000ms, TE=86ms and the voxel size 2x2x2 mm<sup>3</sup>. 30 gradient directions were used, each with 3 different b-values: 400, 1000 and 1500 s.mm<sup>-2</sup>. The SNR was low for b=1500 s.mm<sup>-2</sup>. Besides, the estimated tensors fields were merely different using both b=400 s.mm<sup>-2</sup> and b=1000 s.mm<sup>-2</sup> or only the latter b value images. Finally, we used 12 diffusion directions, which is consistent with other studies [99] and allowed us to increase the number of repetitions to achieve a better SNR. In the subsequent experiments, we used b=1000 s.mm<sup>-2</sup> and 12 gradient directions repeated 6 (first session) or 12 times (second session).



# Chapter 3

## Anatomical image analysis

### Contents

---

<b>3.1</b>	<b>Motivation</b>	<b>74</b>
<b>3.2</b>	<b>Method overview</b>	<b>75</b>
<b>3.3</b>	<b>Hemisphere identification</b>	<b>75</b>
3.3.1	Bias correction	76
3.3.2	Grey level histogram analysis	77
3.3.3	Skull stripping	78
3.3.4	Brain mask segmentation	79
<b>3.4</b>	<b>Cortical surfaces extraction</b>	<b>79</b>
3.4.1	Algorithm 1: BrainVISA	79
3.4.2	Algorithm 2: ABSOLUt	82
3.4.3	Cortical surfaces extraction	83
3.4.4	Algorithms comparison	83
<b>3.5</b>	<b>Cortical surface inflating</b>	<b>84</b>
<b>3.6</b>	<b>Volumetric data projection</b>	<b>87</b>

---

The aim of this chapter is to describe the algorithms used to extract a geometric model of the cortex from an individual high resolution anatomical image. The general process is twofold: first, segment the tissues of interest in the original image and second, extract a bidimensional model of the cortical surface. After recalling some goals of anatomical analysis, we give an overview of the algorithms used at each step and compare the resulting bidimensional models obtained from two alternative methods. We finally describe the inflating algorithm used to unfold the latter model.

### 3.1 Motivation

As mentioned in chapter 2, the brain is composed of various anatomical structures and tissue types, the functions and relations of which are more and more investigated in research and clinical studies. Identifying distinct tissues can be a preliminary step for various image processing such as voxel-based morphometry or image coregistration, to constrain appropriate computations within a given anatomically homogeneous part of the brain. For instance, the anatomical connectivity study we present in chapter 7 relies on such a segmentation, in order to restrict the computation of the estimated fibers within the white matter tissue. A tissue classification is also a prerequisite to extract geometric models of the cerebral cortex. These models of the cortical sheet are not only of great interest for the visualization and interpretation of the brain activity obtained from functional imaging (shown in chapter 5), but they can also provide a frame to cortically constrained processing. Two examples of surface based computations are detailed in our work: fMRI data smoothing following the cortical geometry (see paragraph 4.1.5) and surface based retinotopic area delineation (paragraph 5.1.9).

Firstly, brain structures, such as the white matter tissue or the cortex, differ greatly in shape and size across subjects, making impossible the use of a single fixed model. A T1 anatomical image is therefore acquired for each subject to provide the individual structural information. Furthermore, a manual structure identification for each subject is particularly inappropriate as awkward and potentially expert dependent, urging the use of automatic and efficient algorithms. Basically, we could see the cortex as a strongly folded sheet of tissue. It is thus a 2D surface embedded in 3D space. Ideally, finding this surface in the MR anatomical image comes down to determining the grey level value of the voxels corresponding to the cortex in the brain. A similar approach could be devised for the white matter tissue viewed as the high grey level value volume included inside the cortical surface. Actually, many image distortions prevent us from applying these straightforward procedures: (i) because of its relatively large size, the anatomical voxel often holds different tissues that are averaged together, phenomenon called partial volume effect; (ii) depending

on the acquisition sequence used, some tissues do not differentiate clearly in the image; (iii) heterogeneities in the coil also lead to a non-uniformity of the grey level in the image (bias), changing the grey level of a given tissue across the volume.

Numerous techniques based on different assumptions and frameworks have been proposed to perform anatomical image processing. Establishing a comprehensive list of every available packages is beyond the purpose of this work. Furthermore, an exhaustive comparison of the different packages is still missing to date.

We detail below two methods we have particularly explored. They provide reliable results and successful highly automated computation. The first one, called BrainVISA, is a free and open source software suit, developed at the CEA-SHFJ, Orsay, France<sup>1</sup> and presented e.g. in [38] (see also more specific references given below). A recent comparison performed on three commonly used cortical surface reconstruction softwares, namely INCsurf [207], Freesurfer<sup>2</sup> [45] and BrainVISA, concluded in favor of the latter [122]. The second method, called ABSOLUt for Automatic Brain Segmentation Odyssee Lab. Utilities, was very recently developed at the Odyssee laboratory by Jean-Philippe Pons and Florent Ségonne [67, 175] and generally leads to finer results than BrainVISA with respect to cerebral anatomy representation accuracy and topological properties of the reconstructed surfaces.

## 3.2 Method overview

Our anatomical processing can be split into two main sub-procedures. Firstly, starting from the initial whole brain anatomical image, two binary images (or masks) are computed, corresponding to subsets of voxels from each hemisphere. Secondly, each hemisphere is labeled with respect to the Cerebro-Spinal Fluid (CSF), the grey matter and the white matter (noted GM and WM respectively), and the interfaces between the latter are then tessellated.

The approach used to segment of interest and extract cortical surfaces models for each hemisphere relies mainly on the BrainVISA software but various steps are alternatively processed using the ABSOLUt software.

## 3.3 Hemisphere identification

The first step of the hemisphere identification procedure is meant to correct for the intensity bias mentioned above. It is then followed by a histogram analysis to detect the range of values for the different tissues of interest, after what morphomathematical operations are applied to the image to remove skin, bone, fat and other

---

<sup>1</sup>The BrainVISA package can be found at <http://brainvisa.info/index.html>

<sup>2</sup>The Freesurfer package can be found at <http://surfer.nmr.mgh.harvard.edu>

non-brain tissues and also to compute a labeled image of both hemispheres and the cerebellum. To perform these steps, we use the BrainVISA software.

### 3.3.1 Bias correction

If one observes a standard quality grey-level MR-anatomical brain image, it seems that each tissue is represented homogeneously. However, taking a closer look reveals that it is not the case, as we mentioned above: our visual system is used to correct for this kind of luminance variations. A computer program is not able to compensate for these inhomogeneities; there is thus the need to correct for this lack of uniformity, which is unfortunately not only linked to the scanner and the sequence used (in which case measuring it once with an appropriate phantom would be sufficient to describe it) but is also subject dependent.

To compute an intensity correction, the BrainVISA algorithm is based on a model of the observed intensity:

$$O(x) = I(x)F(x) + N(x)$$

where :  $I$  is the intrinsic intensity of the tissue,  
 $F$  the spatial bias,  
 $N$  the acquisition noise,  
 $O$  the observed intensity.

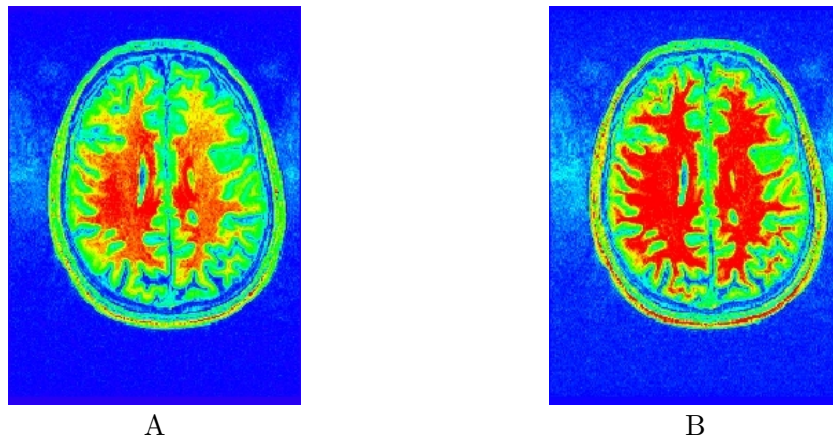


Figure 3.1: Bias correction of the anatomical image. Axial slice of an anatomical image before (A) and after (B) the bias correction. The latter provides a more uniform grey-level value for each tissue. The colormap used here, identical for both images, illustrates the intensity uniformization induced by the bias correction.

The aim is to best estimate the spatial bias  $F$ , supposed to be spatially smooth which is reasonable with regard to the MR acquisition process. The algorithm relies

on the minimization of the following energy  $U$ :

$$U(F) = k_S S(O) + k_R R(F) + k_M M(O)$$

where  $S(O)$  is the resulting image entropy,  $R(F)$  a function measuring the spatial smoothness of the correction field  $F$  and  $M(O)$  a measure of the discrepancy between the original image global mean and the corrected image global mean. This latter term prevents the algorithm to converge to a uniform grey level image. The constants  $k_S$ ,  $k_R$  and  $k_M$  weight each criterion of the energy. The optimization method implemented relies on a stochastic scheme. For a more detailed presentation of this method, see Mangin 2000 [142].

In order to judge the quality of the result after convergence, one compares visually the two images (original input image and the bias corrected output image) and especially checks for the homogeneity of the white matter grey level (see figure 3.1).

### 3.3.2 Grey level histogram analysis

Relying on the bias corrected image, the next step is to automatically compute a rough grey level evaluation of the different tissues of interest, here to distinguish mainly three classes: GM, WM and the other brain tissues (including CSF). As mentioned above, the latter values differ strongly across scanners, MR sequences and subjects.

The algorithm implemented in BrainVISA performs a grey level histogram analysis based on the scale-space theory (see for instance Koenderink 84,[123], Witkin 83 [244]) and relies on the two following invariant properties of T1 MR images:

- there are three peaks in this histogram: one for the background, one for the grey matter and one for the white matter, the order being always the latter;
- these peaks account for the largest amount of voxels.

We give an overview of the algorithm, detailed in [143]. Each tissue class should produce a specific mode in the image grey level histogram, and the modes order is constant across images. However, the detection of these modes is not always straightforward: as two neighboring modes, e.g. GM and WM modes, can be mixed, grey level histogram and first derivative extrema analysis are not sufficient. Starting from the study of scale-space images derived from a mixture of two Gaussian distributions, one notices a structure linking the trajectories of the order  $i$  derivatives extrema to those of the order  $i + 1$  derivatives. This structure is always present independently of the Gaussian parameters, taking a large enough order of derivatives depending upon the case. With MR images, the first two derivatives of the histogram are empirically sufficient for the two modes of interest (GM and WM). Assuming the modes to be relatively symmetric, the means are given by the minima of the

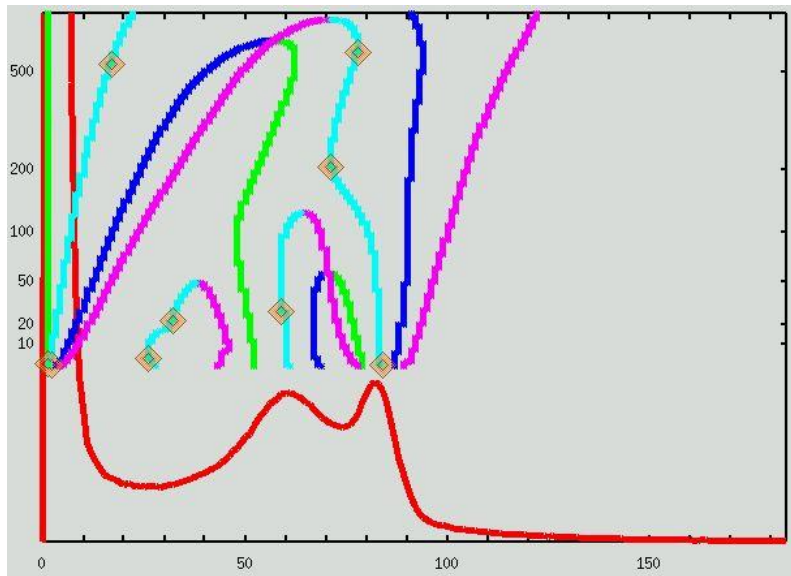


Figure 3.2: Histogram analysis based on the scale space theory. The grey levels are shown horizontally and the scales vertically (on a log-scale). The red curve is the grey level histogram of the image, the trajectories of the minima (m) and the maxima (M) of the first two derivatives are shown in dark blue, green, light blue and purple respectively. The diamonds are the results of the analysis used to identify the CSF, GM and WM tissues modes (mean and variance). Figure borrowed from <http://brainvisa.info>.

second order derivatives and the standard deviations correspond to the maxima of the closest first derivatives. The algorithm thus uses that information to group the trajectories using the notion of cascades and, after an automatic characterization of the sequence used to acquire the image (Inversion Recovery sequences show very distinct histograms for instance), the algorithm estimates the CSF, GM and WM modes. Figure 3.2 illustrates the result of the scale space analysis of the grey-level histogram for a given anatomical image.

### 3.3.3 Skull stripping

A first binary image of the brain is computed by thresholding the original image with the values found in the previous step; this new mask stands for the voxels corresponding to the white and grey matter (mask=1) and removes the other tissues voxels (mask=0). This is however insufficient, many other elements being kept (the eyes, meninx,...). A parameterized erosion process is simulated in order to whittle down this binary image. This erosion gives rise to different connected components, from which the largest one is kept as a brain seed. A dilation process is then applied to this seed to recover the brain. Figure 3.3 illustrates these different steps, referred as *skull stripping*.

As for the bias correction, the resulting mask should be checked visually against the

original image. For our retinotopic mapping studies for instance, we focused on the occipital lobes (at the back of the brain) where the low-level cortical visual areas are located.

### **3.3.4 Brain mask segmentation**

Our work mainly focuses on the low-level visual areas mostly located on the medial parts of the occipital cortex. The latter are facing each other very closely, which makes impossible the visualization on a single model of the whole cortical surface. A separation of both hemispheres is therefore required to allow an optimal display of the medial surfaces. The cerebellum is also included in the mask after the skull stripping. An algorithm based on Chamfer distances and a Voronoi graph computation allows to classify the mask into three distinct parts: the cerebellum, the left hemisphere and the right hemisphere. The final result is shown in figure 3.4.

## **3.4 Cortical surfaces extraction**

The cortical surface of a given hemisphere is modeled using the GM/WM and the GM/CSF (Cerebro Spinal Fluid) interfaces. To perform the tissue classification and the cortical surfaces extraction, we have two alternative approaches, both starting from the above hemisphere separation. We use either the BrainVISA or the ABSOLUt software algorithms, which are respectively described and finally compared in the following paragraphs. Note that, before ABSOLUt software was developed, we tried another algorithm also designed at the laboratory and described in [85], which can be seen as a special case of the ABSOLUt method and therefore led to lower quality results. Moreover, this method did not allow a tissue classification.

### **3.4.1 Algorithm 1: BrainVISA**

#### **Tissue classification**

Although not explicitly performed during the surfaces extraction (see below), the BrainVISA package also implements an algorithm dedicated to the GM and WM tissues labeling within the mask of each hemisphere. The method relies on the histogram analysis presented in paragraph 3.3.2, further refined with a Markovian regularization favoring a voxel to have the same label as its neighbors.

#### **Cortical surfaces extraction**

The approach implemented in BrainVISA is based on a combination of the Homotopic Deformable Region (HDR) method and mathematical morphology tools. We give the main steps of the method which is fully described in [144].

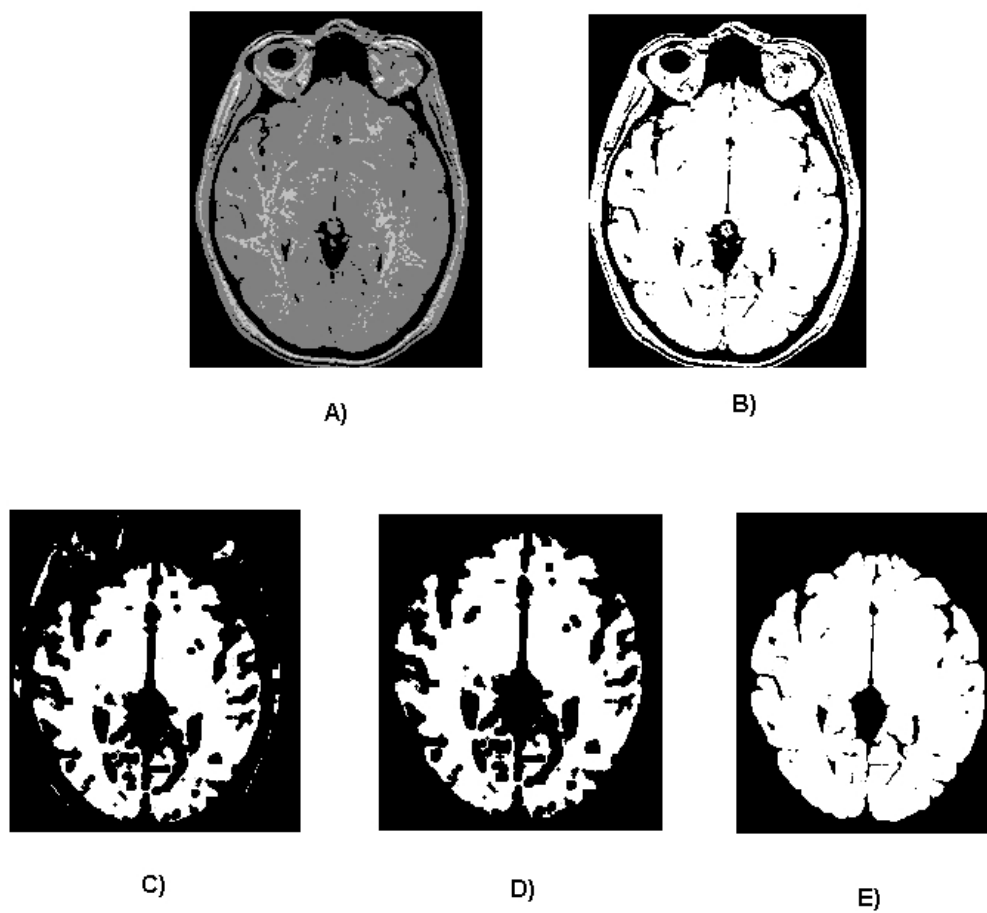


Figure 3.3: Illustration of the different steps for the brain mask computation. A: bias corrected anatomical image. B: thresholded image; the thresholds were automatically chosen based on the histogram analysis result. C: result after the first erosion on B. D: the largest connected component in C. E: final brain mask after dilation.



Figure 3.4: Brain mask segmentation, separating both hemispheres and the cerebellum

The following cortical surfaces detection is applied separately to both previously computed masks of each hemisphere. An initial empty parallelepipedic bounding box (hence homotopic to a sphere) of the hemisphere mask, noted  $O_0$ , is first deformed to the hemisphere mask border with a homotopically preserving deformation. This is performed in two steps:

- $O_0$  is iteratively dilated conditionally to the complement of the mask in  $O_0$  inside, leading to  $O$ ;  $O$  stands for a spherical topology outer part of the mask.
- $O_0$  outside is iteratively dilated conditionally to  $O$ , subject to the constraint that no connection between the inside and outside of  $O$  is allowed.

At the end of these steps,  $O$  corresponds to the estimated subset of voxels representing the thin layer outside the GM (the brain hull). Note that the conditional dilations are performed in a pyramid multiscale fashion, allowing faster computation.

The model  $O$  is then homotopically dilated conditionally to its original inside toward the GM/WM interface. The deformation comes down to adding to  $O$  each voxel that decreases the two terms energy  $E(O) = E_d(O) + E_r(O)$  where:

- $E_d$  is a data driven term, i.e. a sum of potentials for each voxel based on a K-means classification of GM or WM voxels with respect to their grey levels
- $E_r$  is a regularization term based on Ising models, i.e. minimizing the GM/WM interface length.

As the evolution of  $O$  is homotopically constrained, the GM/WM interface is therefore constrained to have a spherical topology. A topology-consistent marching cube algorithm is finally used to compute a mesh of the GM/WM (which holds the spherical topology) and the GM/CSF interface (which is a priori not topologically spherical). Finally, a decimation is applied to the meshes, including a smoothing to avoid artifacts due to the underlying discretization. The decimation strength depends on the trade-off between the final expected quality of the mesh with respect to the segmentation and the mesh size.

### 3.4.2 Algorithm 2: ABSOLUt

In this approach, a statistical classification method is used to provide a good initialization of deformable models that further evolve to the estimated GM/CSF and GM/WM interfaces. Constraints on the evolution guarantee topological properties of both meshes such as spherical topology, absence of self-intersections and mutual intersections. These two steps are performed on a masked version of the original anatomical image for each hemisphere. Note that we use dilated versions of the hemispheres masks computed with BrainVISA to include CSF voxels that are mandatory for a reliable tissue classification with the default implementation; a typical value for the dilation radius is 2 voxels.

#### Tissue classification

The tissue segmentation relies on a hidden Markov Random Field classification, coupled with an automatic estimation of the tissue distribution parameters and of the bias field with the expectation-maximization (EM) algorithm. Similarly to BrainVISA’s tissue segmentation method, the tissue distribution is modeled by a Markov Random Field (MRF) encouraging neighboring voxels to have the same class labels, while the observed intensity of each tissue class is modeled by a Gaussian distribution. The labels  $L$  of the voxels are estimated from the observed intensities  $I$  with a maximum a posteriori (MAP) criterion:

$$\hat{L} = \arg \max_L P(L|I) = \arg \max_L P(I|L) P(L).$$

The parameters of the tissue statistical model are the mean and the standard deviation of each tissue class, and a bias field accounting for the inhomogeneities in the image grey-level values. This bias is taken as affine with respect to intensities, smooth and non-parametric over space.

A rough initial estimate of CSF, GM and WM mean grey-levels is provided by the user, for instance using BrainVISA’s automatic histogram analysis (see paragraph

3.3.2). Then, iteratively, class labels are estimated by MAP and the tissue parameters and the bias field are then updated with the EM algorithm.

The different outputs of this step are:

- a labeling of image voxels,
- the mean and the standard deviation of each tissue class,
- a bias-corrected image.

Note that a bias-corrected image is once again computed in this approach, which is redundant with the bias field computation previously performed in BrainVISA during the hemisphere segmentation procedure. However, this bias correction step is intrinsic to the ABSOLUt software. The latter lacks an automatic hemisphere separation algorithm that must be performed with BrainVISA's method.

### 3.4.3 Cortical surfaces extraction

The hidden Markov Random Field classification is powerful for automatic parameter estimation but it is not sub-voxel accurate and disregards topology. Extracting an isosurface of the labeling would give a very coarse reconstruction with a lot of topological defects. Hence, the labeled image of the previous step is fed into a deformable model segmentation task with a topology preserving nested level set method based on [97] and refined as described in [175], section 3.2. More specifically, in order to obtain a close and topologically consistent initialization, a set of topology preserving nested level sets are fit to the labeling before starting a surface evolution. Later in the algorithm, the labels are no more taken into account, and the surfaces are homotopically evolved according to the intensities of the bias-corrected image. Since the image inhomogeneities have been removed in the latter, the boundaries between the different tissues can be found robustly with a Bayesian region-based evolution. Finally, the meshes can be computed by a topology-consistent marching cube algorithm.

### 3.4.4 Algorithms comparison

As we considered two alternative approaches for the final steps of the anatomical image processing, it is natural to compare their respective outcome, especially for the GM/WM interface we are mostly interested in.

We have carried out various qualitative comparisons on our normal human brain dataset images and also on macaque monkey brain MR images from Professor Orban's group, K.U. Leuven, Belgium. Note that these comparisons are always done on meshes of comparable size, a parameter that can roughly be tuned in both methods. The sheet-like parts of the GM/WM interface at the extremities of the gyri are

better recovered by the ABSOLUt method, which also avoids mis-reconstruction like splittings of connected parts or unexpected connections through CSF or ventricles, as illustrated in figures 3.5. Another interesting feature of the ABSOLUt software is the implicit representation, i.e. through levelset functions, of the surfaces produced as output. Such a representation is of particular interest for computationally efficient cortical surface based processing, such as the smoothing of fMRI data along the cortical geometry described in paragraph 4.1.5. Finally, the GM/CSF surface spherical topology as well as absence of intersections between inner and outer cortex surfaces are guaranteed by the ABSOLUt method, which is not the case with BrainVISA procedures.

Globally, we use the ABSOLUt software for the WM/GM interface extraction which, for a given mesh size, provides a finer estimate of the cortical surfaces than BrainVISA while guaranteeing better topological properties.

### 3.5 Cortical surface inflating

The cortical surface has complex geometry, mainly through its highly folded configuration, making the results visualization particularly awkward inside the sulci. Two different techniques, based on unfolding the cortical surface, are usually used to facilitate the visualization: flattening and inflating. Figure 3.6 illustrates both approaches. In both cases, distances and/or angular distortions are unavoidable. The flattening allows larger cortical surface portion visualization in a single view, but at the costs of losing spatial relationship at points where the surface is cut and operator dependent surface positioning of the latter.

In our studies, we used the second method, inflating the cortical surface of each cerebral hemisphere. The algorithm we used was implemented by Dr Olivier Coulon<sup>3</sup> and is available in the BrainVISA Package. It relies on an energy minimization allowing to compute an inflating force at each vertex of the mesh. This force is made of three components:

- a strictly speaking inflating component, along the current vertex normal,
- an “elastic” component, trying to maintain the distances between neighboring nodes,
- a smoothing component, moving each node toward its neighboring vertices.

---

<sup>3</sup>Olivier Coulon is currently at the Laboratoire des Sciences de l' Information et des Systmes, CNRS, Marseille, France.

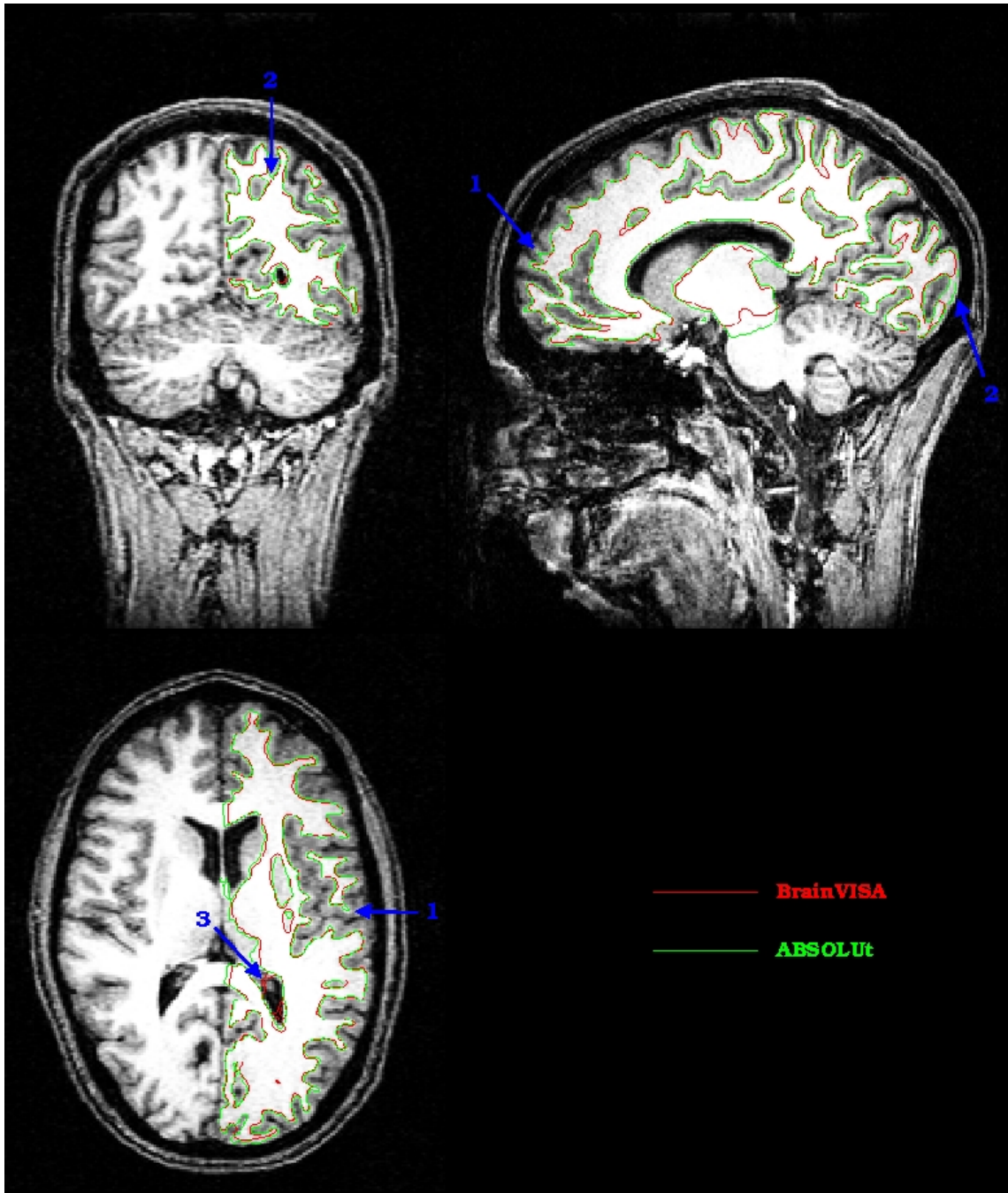


Figure 3.5: Comparison of BrainVISA and ABSOLUt GM/WM surface extraction. The red and green curves represent the intersection of the GM/WM interface mesh extracted with BrainVISA and ABSOLUt respectively and image slices of the original anatomical image. To fulfill an unbiased comparison with respect to the surface models resolutions, both meshes have a similar size, with 100822 and 99511 nodes respectively (1.3% relative difference). The meshes are mostly identical, though some important differences plead in favor of the ABSOLUt procedure: the blue arrows emphasize finer segmentations of sheet-like parts of the thinnest gyri (1) while avoiding the splitting of a connex white matter regions (2) and crossings through the ventricles or the CSF (3).

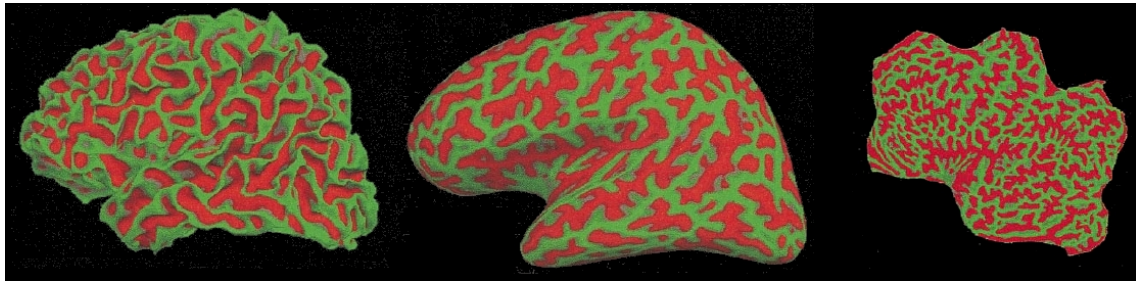


Figure 3.6: Representations of the fiducial cortical surface (left) either inflated (middle) or flattened (right). The sulci are represented in red, the light in green. Adapted from [71].

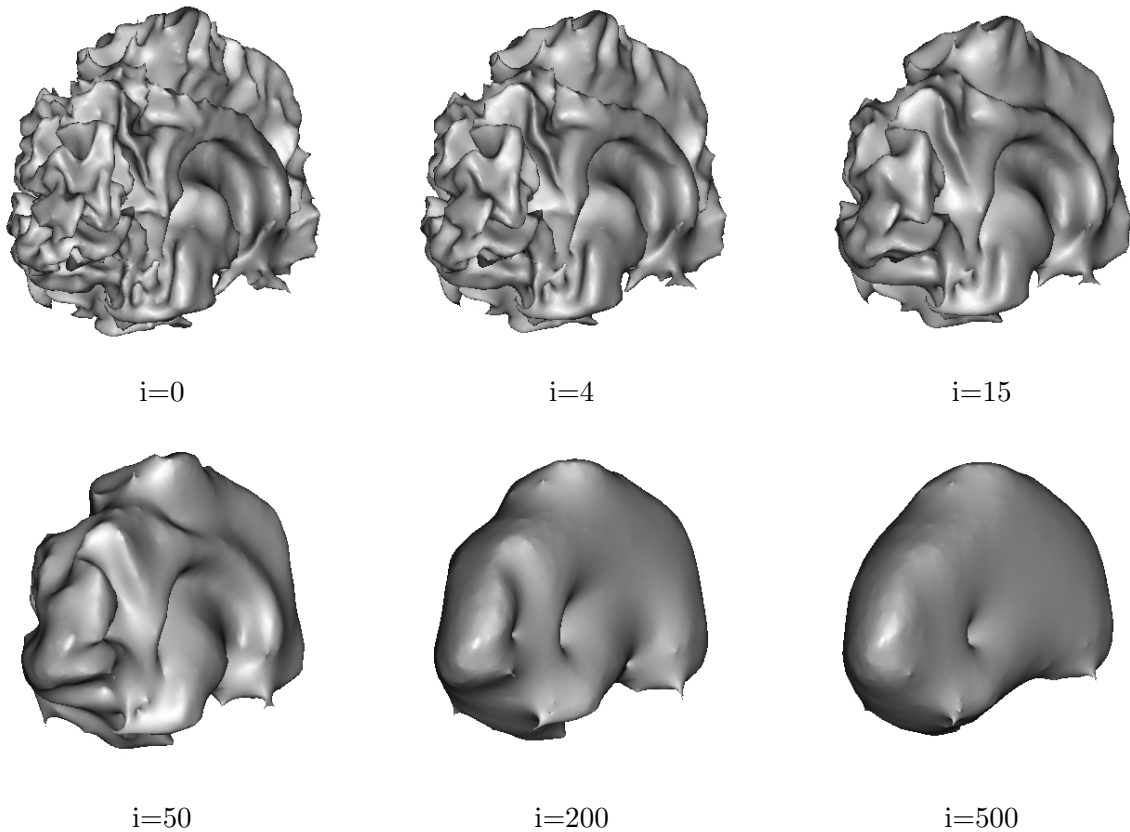


Figure 3.7: Different stages of the inflating algorithm on a given left cortical hemisphere,  $i$  indicates the iteration step.

The inflating is the result of a trade-off between these three components. Intermediate images can be saved during the energy minimization, thus allowing an easy tracking of the sulci and gyri along the process. The global result is satisfying, although perfectible notably when the curvature is locally large. Figure 3.7 presents some views of a left cortical surface at different stages of the inflating process.

### 3.6 Volumetric data projection

There are various ways to project volumetric information from a 3D image to a 2D surface. A typical application of such a projection is to overlay the statistical significance map coming from the functional images analysis on the cortical surface model. In the Anatomist software, which is the visualization software provided in the BrainVISA package, various projections methods are proposed. These methods can be separated in two consecutive steps: first the geometrical sampling, i.e. how the information to represent on each mesh vertex is searched in the 3D volume, and second the merging mode of these values, i.e. how to compute a single value per vertex when each vertex is related to multiple voxels by the geometrical sampling method chosen.

The geometrical sampling at each vertex can be done in the following ways:

- Point to vertex: only the information coming from the voxel encompassing the mesh vertex is used.
- Point to vertex with depth offset: only one voxel information is taken into account, but its position is shifted along the local normal to the mesh; the shift length and the shift direction, either inside or outside the mesh, can be tuned.
- Segment to vertex: information is taken along the normal line, both inside and outside the mesh, with a segment length and sampling step specified by appropriate parameters.
- Inside/outside segment to vertex: similar to the segment to point method but only one side of the mesh is considered.
- Sphere to vertex: voxels information is taken from voxels within a sphere centered at the current vertex; the sphere radius and sampling step can be tuned.

When the geometrical sampling method chosen implies multiple voxels for each vertex, different merging techniques can be applied to assign a single value per vertex. The most obvious way is to take the mean of the voxel values encountered at each sampling step. A more suitable mixing implemented in Anatomist discards the 3D image minimum value in the mean computation to avoid a blurring of the mapped values with, for instance, under threshold voxels. Finally, the maximum (or minimum) value of all the voxels within the sampled location can also be chosen. Changing the geometrical sampling and/or the merging methods can have dramatic effects on the final result. The choice should therefore depend on the 3D data considered. To overlay our statistical T maps or the retinotopic angular maps (see chapter 4), we employed the segment to vertex geometrical sampling, taking into account the voxels crossed along the local outer normal to the GM/WM interface at a distance up to 2.5mm from the current vertex and with a spatial step of 0.5mm.

Regarding the merging technique, we used the corrected mean for the retinotopic angular maps and the maximum for the statistical T-maps.

Some refinements might be envisaged to assign 3D values to a 2D surface, for instance taking into account the GM/CSF interface in the segment to vertex approach to restrict the integration segment in the sub-volume defined by the inner and outer cortical surfaces. However, regarding the large functional voxel size ( $2\text{mm}^3$ ) with respect to the cortical thickness (ranging between 1 and 4.5mm, with a mean of 2.5 [70]) and the currently imperfect coregistration between anatomical and EPI images, we speculate a finer approach should not improve dramatically our functional maps overlays.

\*\*\*

We have presented in this chapter various algorithms mainly based on image processing and computational geometry methods used to generate efficient segmentations of brain tissues and extractions of the cortical surface models. The overall process takes from 30 minutes to 1 hour for a given subject, including some manual editing of the masks whenever necessary. The results of this analysis of the anatomical information are further used to visualize fMRI activations over the cortical surface (chapter 5) but also as a base for anatomically constrained computations such as cortical surface based fMRI data smoothing (section 4.1.5) or DTI based fiber tracking restricted to the white matter tissue (chapter 7).

# Chapter 4

## Functional data analysis

### Contents

---

<b>4.1</b>	<b>Preprocessing</b>	<b>90</b>
4.1.1	Motion correction	91
4.1.2	Anatomical/Functional image alignment	92
4.1.3	Correction of the inter-slice gap or <i>slice-timing</i>	93
4.1.4	Isotropic spatial smoothing	94
4.1.5	Cortical surface constrained smoothing	94
4.1.6	Temporal filtering	99
<b>4.2</b>	<b>Statistical analysis of fMRI data</b>	<b>102</b>
4.2.1	Problem statement	102
4.2.2	Classification of methods	102
4.2.3	The General Linear Model	104
4.2.4	Non-parametric HRF estimation	109
4.2.5	Frequency domain analysis	112
4.2.6	Multivariate analysis methods	112

---

The indirect measurement of brain activations can be performed with BOLD signal images. A typical fMRI experiment consists in acquiring a set of consecutive images while the subject undergoes a stimulation and/or performs a cognitive task. At each voxel in the functional volume, we therefore record a time series of BOLD signal variations. In the following, the functional series will be viewed as 4D data (3 spatial dimensions + time). Each volume acquired within a given repetition time (RT) is seen as an image, and a set of volumes acquired in a row is called a run or a session.

A fMRI data analysis typically comprises the following steps:

- the pre-processing, which aims at correcting possible defects in the acquisition (head motion, acquisitions gaps between slices,...) and performs some spatial and temporal filtering of the data,
- the statistical analysis: it allows to assess the volume's elements whose activity are correlated with the experimental paradigm,
- results interpretation: confront quantitative statistical results to, among others, qualitative stimulus or task criteria.

Following this typical analysis process, we first describe various preprocessing methods common to most fMRI studies. We expose a methodological contribution regarding anatomically constrained spatial filtering of fMRI data. The second section deals with the statistical analysis. After a brief overview of the main approaches proposed in the literature, we detail a few of them, emphasizing on the methods we used to analyze our own experiment datasets. Although a specific section is not dedicated to the results interpretation, this topic is addressed in the description of each method.

## 4.1 Preprocessing

To begin the functional data analysis, it is preferable to apply different preprocessing steps; indeed, since only the BOLD signal is of interest to brain activation characterization, any other signal is thus considered as noise and should, as much as possible, be removed.

It is first necessary to discard the first images from the temporal series. We indeed always take a few images (typically 5 RT in our case, i.e. about 10 seconds) during the MR signal stabilization phase; the latter, depending on the scanner and the sequence used, is known to give rise to many artifacts in the images, which are mostly abnormal high level values in the signal. Naturally, no stimulation are presented during these few scans. We can then apply the following preprocessing steps to the remaining images.

### 4.1.1 Motion correction

The subject’s head motion during a scanning session is unavoidable and may induce artifacts, leading to a mislocalization or a loss of activation or, worst, to false positives, i.e. to voxels considered activated by the stimulation or task where they are actually not. All subsequent analysis or processing on series comprising motion can be invalid as the signal and the voxels cannot be properly identified.

The images realignment, i.e. an estimation followed by a correction of subject’s head motion, can be performed using the standard *realign* tool implemented in the SPM<sup>1</sup> software. A reference image  $I_R$  is designated by the user and the other images are registered to it using a rigid transformation  $T$ . A 3D rigid displacement can be described by 6 parameters: 3 for the translations in each direction of the 3D space and 3 for the rotations around each axis  $x$ ,  $y$  and  $z$  (called pitch, roll and yaw respectively). The error  $E$  between the reference image  $I_R$  and the image  $I_i$  to realign is the sum of the squares of the intensity differences at each voxel  $x$ :

$$E^2 = \sum_x (I_R(x) - I_i(T(x)))^2$$

$E$  is minimized with respect to  $T$  using a classical least squares technique. At the end of this step, we can visualize the corrections attached to each 3D image, and thus have an estimation of subject’s motion (see figure 4.1).

Following the work of Freire and Mangin [75] to more appropriately estimate head motion without creating spurious activations in fMRI time series, we actually used a different tool implemented in the INRIAAlign software<sup>2</sup>. This toolbox, interfaced with the SPM software, implements various similarity measures to avoid the difference of squares drawbacks, as proposed in SPM99 *realign* technique. We used the default algorithm relying on the Geman-McClure robust estimator which leads to the most reliable results in their validation study. See [76] for more details.

Note that many other motion correction softwares have been proposed in the literature. A very recent study [156] compared the most popular among them, namely AFNI, AIR, BrainVoyager, FSL, and SPM2, on phantom as well as on typical human studies data. Their conclusion is threefold: (i) although slight differences could be observed, no single software outperformed the others (ii) the parameter tuning for each method has very little impact on the final results (iii) they nonetheless warmly recommend the inclusion of the motion correction step in fMRI data analysis.

The global estimated motion was generally inferior to 1mm in each translation direction and to 1 degree around each rotation axis. In case of more important motion,

---

<sup>1</sup>We will often refer to the SPM software in the remainder of the thesis. It refers to a set of methods implemented in a popular software classically used for fMRI signal processing. The core of the SPM approach will be detailed in the next section.

<sup>2</sup>INRIAAlign, developed in the Épidaure Team, INRIA Sophia-Antipolis, France, is available at <http://www-sop.inria.fr/epidaure/software/INRIAAlign/>

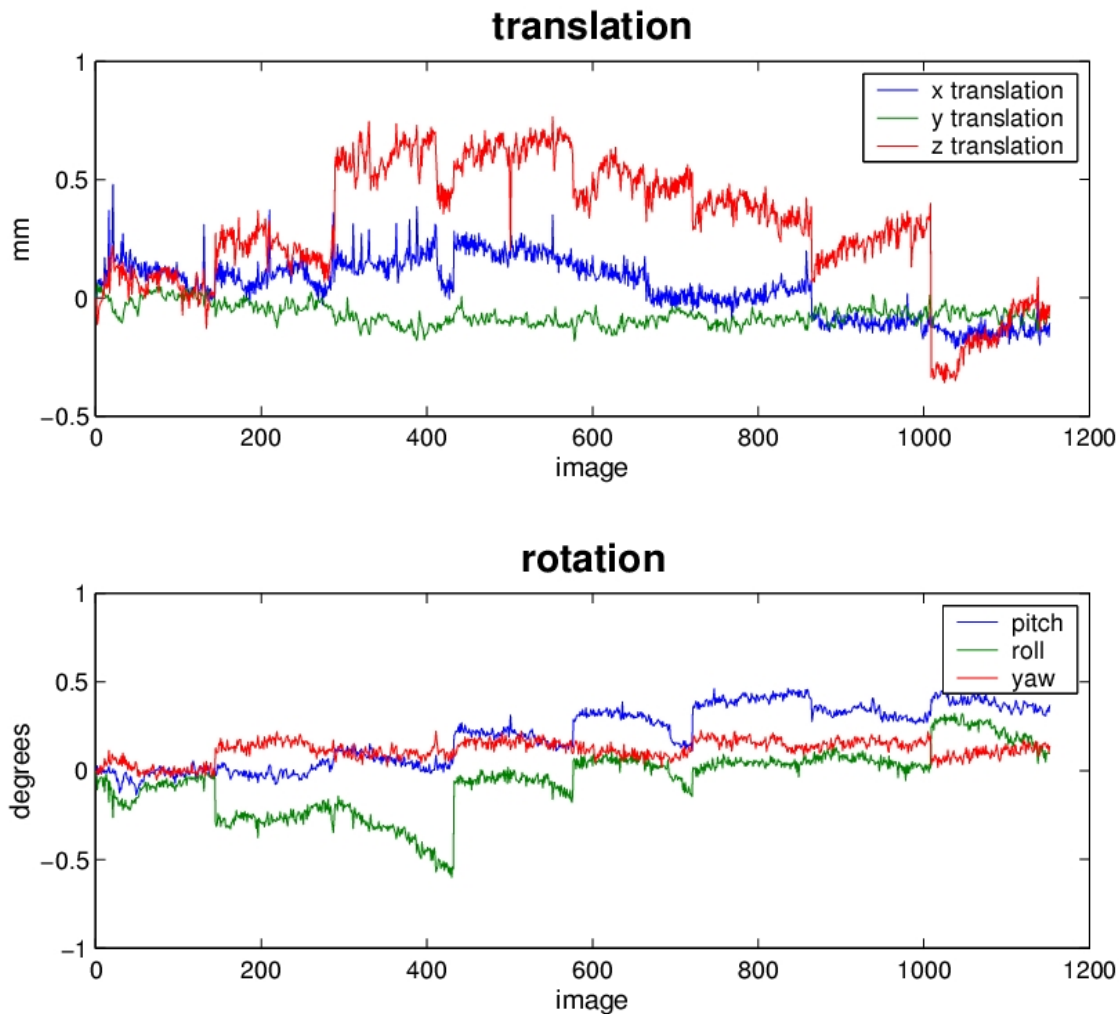


Figure 4.1: Typical output file produced by a motion correction of the fMRI time series. The upper graph shows the estimated values of the 3 coordinates of translation directions for each image with respect to the first, the lower one shows the 3 estimated coordinates values of the rotation motion computed. We notice that the motion is larger between each session of 144 images, corresponding to a single run, which seems consistent with a motion of the subject waiting between two runs. Note that this was not specified to the algorithm during the motion correction: the estimation seems reliable.

subject could be removed from the analysis.

#### 4.1.2 Anatomical/Functional image alignment

As we use information from the anatomical image to constraint computations on functional images such as cortical constrained filtering (see paragraph 4.1.5) or for the segmentation of retinotopic areas over the cortical surface (see paragraph 5.1.9), the alignment between functional and anatomical scans is crucial. There are two main sources for disalignment:

- the subject moved the head between the anatomical and the functional scans. Such a coregistration issue should be well corrected by a rigid deformation computation (rotation and translation).
- as it is often reported in high field Echo Planar Images (EPIs), there could be distortions in the functional images that might not be appropriately handled by a rigid deformation alone.

We addressed this coregistration issue using a non-rigid deformation algorithm, estimating a deformation field to be applied to the functional images. We used a software developed in the laboratory, MATCH, which is fully detailed in [26, 25]. Briefly, a dense deformation field is computed by composing small displacements minimizing a local correlation criterion. Such a local similarity measure allows to cope with nonstatic behaviors in the intensity profiles of images coming from different modalities. The estimated deformation field is finally regularized by a low-pass filtering.

Considering the coronal acquisition sequence used for our functional studies, the estimated dense deformation field was negligible with respect to voxel size, we therefore decided not to apply the non-rigid correction field. The coregistration was nonetheless performed by the classical SPM routine and the result was systematically assessed visually using SPM's `chek_reg` function.

A complementary solution is to rely on a specific measurement of the known Echo Planar Imaging (EPI) geometric distortions caused by magnetic field inhomogeneity [117]. This can be achieved by acquiring a phase map, i.e. an image mapping the spatial distribution of field inhomogeneities. A specific method is for instance proposed in a SPM interfaced toolbox<sup>3</sup>. However, the phase maps acquisition was only recently available at the centre IRMf de Marseille where we performed our experiments, so that we could only apply such a correction to the experiment described in 7.

#### 4.1.3 Correction of the inter-slice gap or *slice-timing*

A volume is made of different slices that are not acquired at the same time during the scanning process. Thus, in the case of the interlaced sequences as used in our experiments, a time discrepancy of the magnitude of half the RT can be present between two spatially adjacent slices of the same volume. A temporal analysis of the raw images should take into account these differences. A simple solution is to

---

<sup>3</sup>The Fieldmap toolbox can be freely downloaded at: [www.fil.ion.ucl.ac.uk/spm/toolbox/fieldmap](http://www.fil.ion.ucl.ac.uk/spm/toolbox/fieldmap)

correct for this discrepancy to be able to apply the same statistical analysis to each slice and consider them as acquired at the same point in time.

This pre-processing is performed by the *Slice-Timing* method of the SPM software, which moves slices in time to get a volume considered to be acquired at the same time. This correction relies on a temporal interpolation of the time series at each slice using an interpolation with a *sinc* function. The algorithm then realigns each slice by changing the phase of the signal taken in the Fourier space. Note that this method assumes there is no information of interest beyond the Nyquist frequency, i.e. the sampling frequency divided by two. The output of the algorithm is a temporal series of images where each slice would have been acquired at the same reference time point within the RT.

#### 4.1.4 Isotropic spatial smoothing

Although surprising at first, a spatial smoothing is commonly applied to fMRI images [79]. The main reason is to increase the signal to noise ratio (SNR), by reducing the effect of spatially uncorrelated noise. This smoothing also increases the validity of the assumptions used during the statistical analysis done by the SPM software, i.e. the residuals of the regression model can be treated as a Gaussian random field (see paragraph 4.2.3 below). Lastly, this also helps insuring a better spatial overlap between activations across different subjects in multi-subjects analysis.

The Gaussian kernel we typically use has a Full Width at Half Maximum (FWHM) equal to 1.5 times the voxel size. The FWHM is linked to the standard deviation  $\sigma$  of the Gaussian kernel by the formula:

$$FWHM = \sigma \sqrt{8 \ln(2)}$$

In our visual area mapping experiments, this smoothing step highly increases the quality of the resulting maps. However, such a 3D-smoothing is not optimal as it does not take into account the geometry of the cortical surface, thus mixing voxels from different tissues or remote cortical locations. We have therefore implemented another approach enabling an anisotropic smoothing along the cortical surface, presented in the following paragraph.

#### 4.1.5 Cortical surface constrained smoothing

As mentioned above, the typical spatial smoothing applied to fMRI data is usually 3D-isotropic, thus mixing voxels from different anatomical tissues (e.g. grey matter, white matter and CSF). This leads to undesirable averaging of signals at neighboring voxels, potentially affecting the analysis sensitivity. Furthermore, due to the highly convoluted geometry of the cortex, the "tissue-blindness" of this smoothing yields a mixing of signals across sulci at voxels close to each other in the volume but distant

on the cortical surface, reducing further the spatial discrimination power. Taking into account the cortical geometry in the smoothing process seems to be a natural way to avoid these drawbacks, as illustrated in figure 4.2.

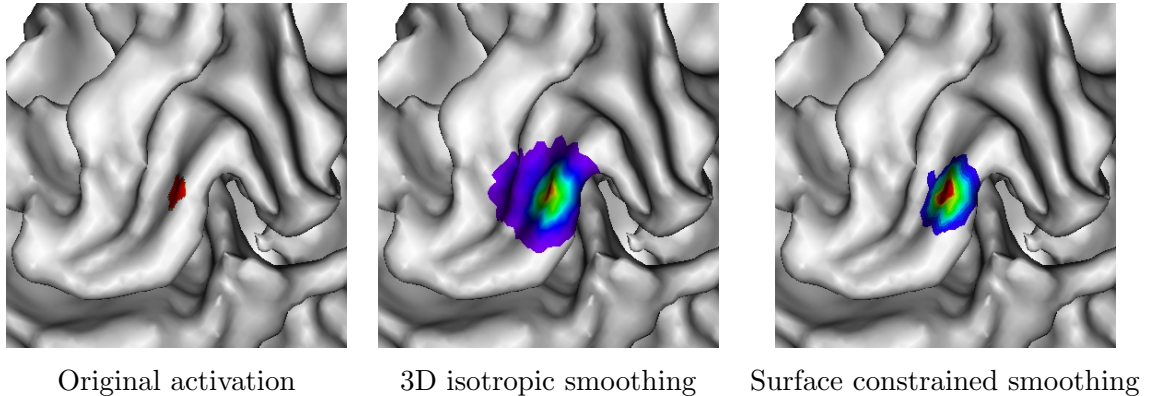


Figure 4.2: Synthetic illustration of the advantage of cortical surface based smoothing methods. Left: original activation; Middle: 3mm 3D isotropic smoothing, leading to false activation on the opposite bank of the sulcus; Right: 3mm Laplace-Beltrami smoothing.

We implemented and compared two algorithms for surface-based smoothing, one based on an explicit mesh scheme and the other on the level set framework. Both implementations solve the same problem: minimizing the variations of the scalar values  $u_0$  defined along the cortical surface  $S \subset \mathcal{R}^3$ ; in other words it consists in finding  $u$  that minimizes the energy  $E$ :

$$E = \int_S \|\nabla u\|^2 dx \quad (4.1)$$

As shown in [3, 30] for the mesh based approach and by [149] for the level set based approach, 4.1 is formally equivalent to solving the partial differential equation (PDE):

$$\begin{cases} \frac{\partial}{\partial t} u(x, t) = \Delta_S u(x, t) \\ u(x, 0) = u_0(x) \end{cases} \quad (4.2)$$

where  $\Delta_S u(x, t)$  is the Laplace-Beltrami operator. The equivalent Gaussian kernel FWHM is easily linked to the equation running time  $T$ :

$$FWHM = 4\sqrt{T \ln(2)}$$

Note that such a formulation could easily lead to a scale-space study of the smoothing influence over the data. The smoothing process is naturally bounded, since running equation 4.2 for a sufficiently long time  $\tau$  leads to a constant solution  $u_\tau = \bar{u}(1, \dots, 1)$

The cortical surface models, either represented as a mesh or a level set function, are obtained with the anatomical image analysis methods described in chapter 3. Note

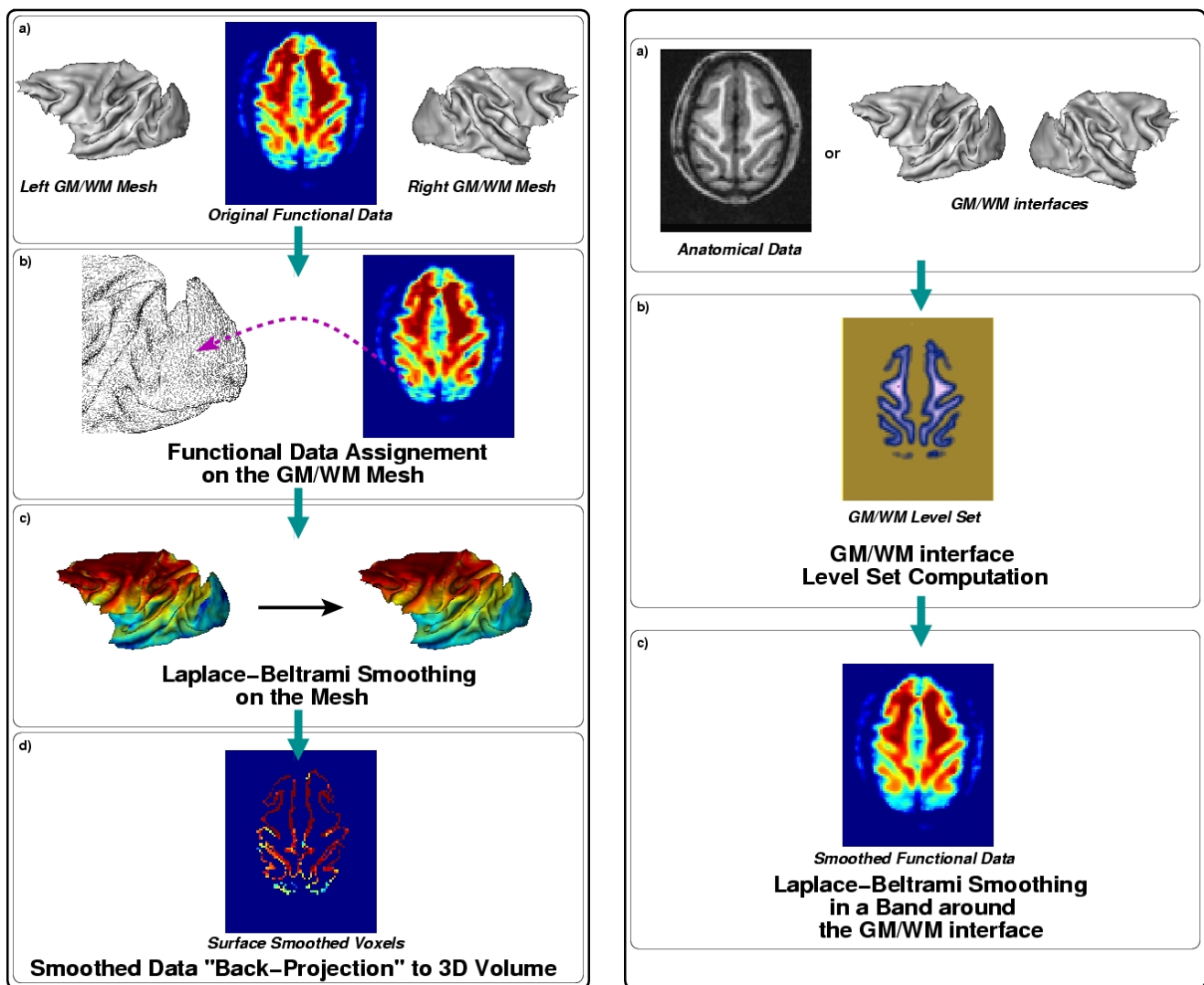
that an efficient algorithm implemented in the ABSOLUt package allows to switch from one representation to the other. Depending on the representation chosen, two alternative and non-equivalent approaches are performed.

### **The mesh-based approach**

The mesh-based approach, illustrated in figure 4.3-A) starts with a projection of the cortical voxels values from the functional image onto the GM/WM interface mesh. More specifically, we assign at each vertex of the mesh the scalar value of the voxel located at a distance  $d$  along the local outer normal to the surface. To insure the voxel chosen lies within the grey-matter tissue, possible values for  $d$  range between 0 and 3.5mm. We typically took  $d = 1.5mm$ . The PDE described in equation 4.2 is then ran on the assigned scalar values, leading to a smoothed scalar field over the mesh. Finally, a simple "back projection" replaces each node smoothed value to its original voxel in the 3D space. Getting back to the original image 3D space enables the direct use of the classical volumetric functional data analysis tools as SPM. Note that, considering the projection step from the 3D volume to the 2D surface, alternative techniques than the  $d$  mm-translated nearest neighbor projection can be used, as detailed previously in paragraph 3.6; nonetheless, assigning information from different voxels to a given node leads to a non-invertible operation during the back-projection to the 3D volume step. This method thus implies a compression of the information originally available in the cortical voxels. The procedure is repeated for each volume in the time series and the analysis is then performed classically over the whole time series. Nonetheless, while visualizing the results one has to keep in mind that only a subset of voxels was concerned by the anisotropic smoothing. Applying the same projection on the surface to the results images (such as T-contrasts) avoids any confusion between results coming from filtered and not filtered signals.

### **The level set approach**

The level set approach, illustrated in figure 4.3-B, relies on level set representation of the GM/WM interface, i.e. a 3D volume which intensities correspond to the signed Euclidean distance from this surface. The PDE is then solved directly in the functional volumes, in the vicinity of the zero level (which corresponds by definition to the GM/WM interface). The diffusion is therefore encouraged in directions parallel to this boundary and discouraged otherwise. We repeat the procedure for each volume, after what the analysis can be performed classically over the whole time series. Similarly to the mesh based approach, the analysis of the results has to be performed considering that only a subset of voxels was actually concerned by the filtering.



A) Mesh based approach

B) Level Set based approach

Figure 4.3: The different steps of the mesh based (A) and the level set based (B) smoothing approaches. Starting from the GM/WM interface meshes and the original functional data (A-a), the mesh based approach requires a projection of the functional data on the explicit cortical surface representations (A-b); the data are then smoothed on the mesh grid (A-c) before being back-projected to the original image to be further analyzed (A-d). Based either on GM/WM interface meshes or directly on the anatomical scan (B-a), the level set based approach first requires the computation of an implicit level set representation of the cortical surface (B-b). The Laplace-Beltrami anisotropic filtering is then performed directly in the image 3D space in the vicinity of the GM/WM interface, favoring diffusion in directions parallel to this boundary (B-c).

## Deriving global thresholds

Since only a subset of brain voxels is concerned by the smoothing procedure, it is necessary to take this restriction into account in subsequent statistical thresholding which classically end the activation detection analysis. Based on the framework of Gaussian Random Field Theory introduced by [248, 247], we derived a formula to adapt the threshold value for a T-test (see below paragraph 4.2.3) performed on cortical surface constrained smoothed data. Transforming the T variable to a Z variable using standard procedures, the corresponding z-map can be considered as a Gaussian Random Field of dimension 2 on a surface  $A$  (the cortical sheet) with a given smoothness. From the expected Euler-Poincaré characteristic  $\chi_t$  of the 2D-field once thresholded at level  $t$ , we have:

$$E(\chi_t) = A|\Lambda|^{\frac{1}{2}}(2\pi)^{-\frac{3}{2}}H_D(t)e^{-\frac{t^2}{2}}$$

where  $\Lambda$  is the covariance matrix of the field (basically, its smoothness) and  $H_D$  the Hermite polynomial of degree  $D$ . For a high value of  $t$ , the significance value (or p-value) of the z-map is related to the Euler-Poincaré characteristic:

$$P(z_{max} \geq t) \approx P(\chi_t = 1) \approx 1 - e^{-E(\chi_t)} \approx E(\chi_t)$$

The smoothness of the field can be expressed as:

$$A|\Lambda|^{\frac{1}{2}} = RESELS(4\log(2))$$

where  $RESELS$  is the number of resolution elements, a notion also introduced by Worsley, and given for the cortical surface by:

$$RESELS = \frac{A}{FWHM^2}$$

where  $FWHM$  corresponds to the Full Width at Half Maximum of the smoothing filter we applied. Finally, we thus have:

$$P(z \geq t) \approx \frac{A}{FWHM^2}(4\log(2))(2\pi)^{-\frac{3}{2}}\frac{e^{-\frac{t^2}{2}}}{t}$$

Note that Bonferroni correction or False Discovery Rate technique can also be applied to correctly derive appropriate thresholds.

Computing such a correction now allows us to compare the results of both methods with the standard volumetric SPM-smoothing at equivalent p-value.

## Methods comparison

We have performed comparisons on various datasets between the classical 3D-isotropic smoothing and both methods of cortical surface based anisotropic smoothing. Figure 4.4 illustrates the results on a dataset from a monkey visual speed motion

experiment. These data are courtesy of Prof. Orban laboratory, KUL, Leuven. Figure 4.5 show some results on the hMT+ complex localizer experiment described in 5.2. Globally, both anisotropic approaches lead to higher statistical values and to spatially more coherent activation foci as compared to the classical 3D-isotropic method. These results confirm the benefits of anatomical information introduction in fMRI signal pre-processing, as already stressed in [3].

Besides, this work is to our knowledge the first implementation of an fMRI smoothing method based on the level set framework. We find expected differences between both anisotropic methods that can be attributed to the use of different numerical schemes and, to a more important degree, to the fact that the mesh-based approach is restricted to projected voxels only whereas the level set based approach solves equation 4.2 continuously within a band around the GM/WM interface. This is an important argument that favors the level set based approach at different steps:

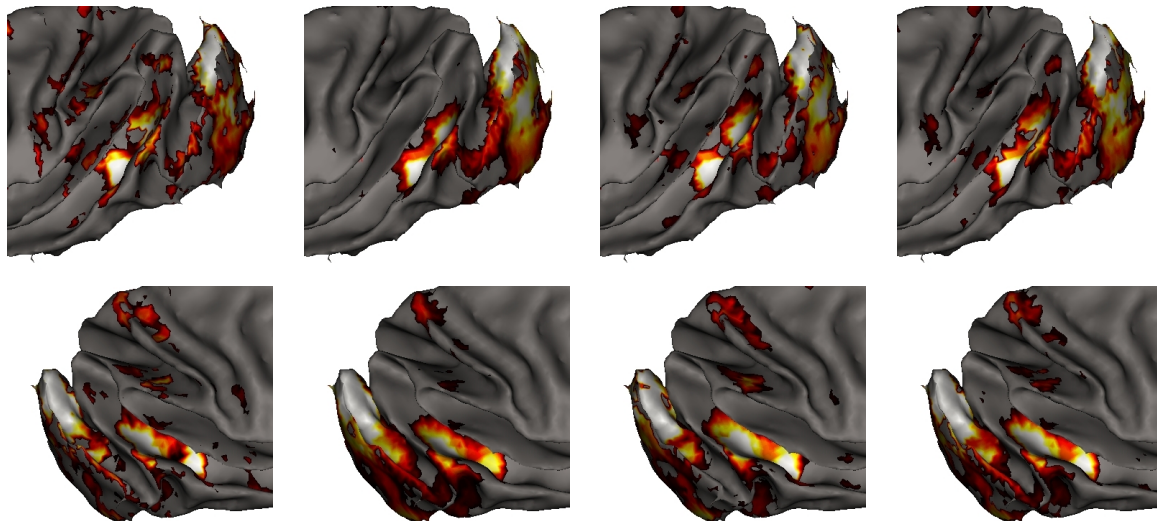
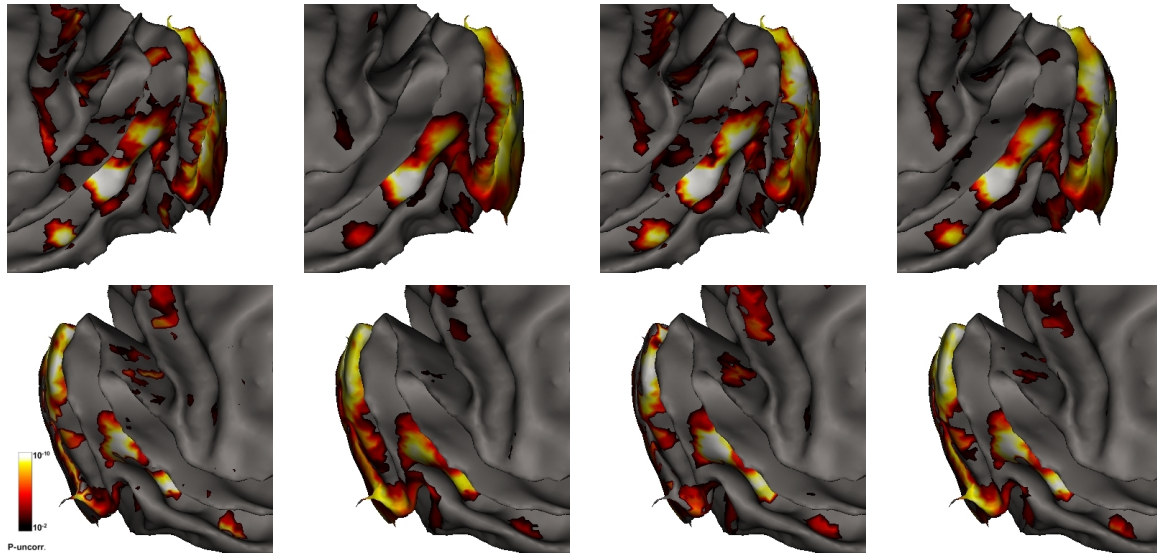
- the approach is independent of a method assigning functional data to the cortical surface,
- consequently, the choice of a projection method to visualize the statistical results on the cortical mesh can be made *a posteriori*,
- the implementation is more straightforward, avoiding intermediate surfacical data files and faster in terms of computation time.

Whenever a smoothing was envisaged to preprocess our data, we therefore systematically used the level set based anisotropic smoothing to pre-process our fMRI data. The core program to resolve the PDE was implemented by Jean-Philippe Pons in C++ within the ABSOLUt software library. We also developed a Matlab interface, based on SPM functions, to give ergonomic interactions with the user. The input cortical surface can be either in BrainVISA explicit mesh format (.tri or .mesh extension files) or directly in the implicit level set format. In the latter case, the level set image has obviously to be coregistered with functional data. If necessary, an automatic resampling of the level set image is performed to fit the functional images space. The desired filter FWHM is then entered and the programs estimates the appropriate running time  $T$  of the equation (more specifically an iteration time step  $\Delta t$  and a global iteration number  $n$ , with  $T = n\Delta t$ ).

#### 4.1.6 Temporal filtering

##### Correction of the scanner trend

Instabilities of some scanner equipments give rise to a trend in the signal baseline. Furthermore, aliased physiologically induced effects (cardiac, breathing,...) also introduce low frequency components in the signal. These confounds can easily be



**No spatial  
smoothing**

**SPM isotropic  
approach**

**mesh based  
approach**

**level set based  
approach**

Figure 4.4: Comparison of the different smoothing approaches on a monkey fMRI dataset. Each column corresponds to a smoothing approach, namely from left to right: non-smoothed data, SPM 3D-isotropic approach, mesh-based approach and finally levelset based approach. In each smoothing process, the FWHM of the Gaussian kernel was set to 3mm. The dataset belongs to a macaque vision study, where the animal passively viewed textures either static or moving at different velocity (1,2,8,16 deg/sec respectively). The experimental paradigm consists in randomly alternated presentation of 35.31sec epochs for each condition. The only task the monkey had to perform was to maintain gaze at the fixation point located at the center of the display. 9 scans of 154 volumes each were analyzed the classical GLM. Thresholded T-test p-values of two different contrasts between the conditions are shown on the reconstructions of the GM/WM interfaces for each hemisphere. We restricted the display to partial view of the occipital poles to focus on the low-level visual system. The first two rows represent p-values of a contrast between low velocities conditions (1 and 2 deg/sec) and the static condition. The last two rows represent p-values of a contrast between fast velocities conditions (8 and 16 deg/sec) and the static condition.

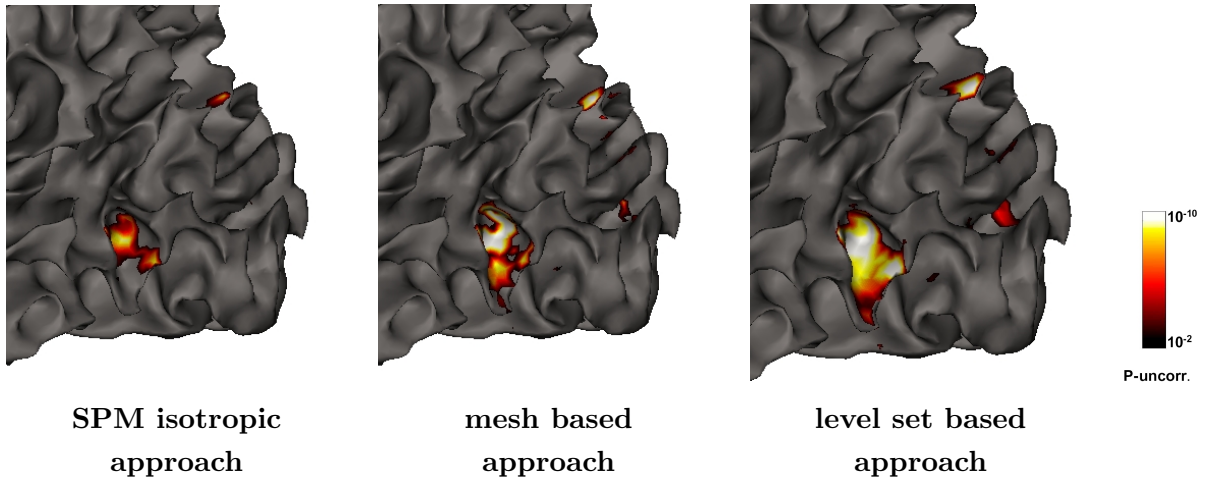


Figure 4.5: Comparison of the different smoothing approaches on a human fMRI data. Data were smoothed by a 3mm Gaussian kernel FWHM by the classical 3D isotropic method (left), the mesh based approach (middle) and the level set based approach (right). The dataset comes from the hMT+ localizer experiment, detailed in section 5.2.

removed applying a high-pass filter during the statistical analysis of the voxels time series. The cutting period (the inverse of the cutting frequency) is chosen to depend on the interval of time separating two equivalent stimulations in a given session. This interval is classically called the Stimulus Onset Asynchrony (SOA). We typically used 2.5 times this value (expressed in seconds) to remove every frequencies lower than  $\frac{1}{2.5SOA}$ .

### Low pass filtering

A temporal smoothing is classically performed on the data to consider as known the residual time series autocorrelations. This procedure insures better estimates of the statistical model parameters used in the analysis done at the next step (see section 4.2). We use a simple Gaussian temporal filtering on the data that will be taken into account in the statistical analysis.

We have given in the above paragraphs an overview of the main pre-processing steps that can be envisaged in the context of fMRI signal analysis. The final chain applied to a given dataset and the parameter tuning involved in each step can have dramatic impact on the results [47, 128]. Selecting the appropriate procedure depends strongly on the underlying experimental paradigm and the assumptions of the analysis method used to assess the data. We mention the assumptions made in the analysis methods of the next section and precise the specific preprocessing chain performed for our different experiments in their respective chapters.

## 4.2 Statistical analysis of fMRI data

This section summarizes the main approaches that have been proposed to analyze the pre-processed fMRI data. After a brief statement of the problem and a classification of the main methods that have been proposed to address this problem, we will describe the General Linear Model methodology widely used in fMRI literature. We then present a non-parametric approach we used to analyze our motion adaptation experiment, and mention frequency domain analysis often used in periodic paradigms as retinotopic mapping. We end this chapter with a rapid overview of the most popular multivariate methods.

### 4.2.1 Problem statement

The goal of fMRI data analysis is to extract relevant information from the spatio-temporal data recorded during the experiment, linking the experimental protocol to the presumed brain activity.

The statistical analysis of functional images is a complex task for various reasons. First, the amount of 4D data to be analyzed can restrict the choice of analysis technique. Indeed, a typical fMRI session recording generates several hundred megabytes of data for each subject which may not be computationally tractable by every method in terms of memory and computational time. Besides, the signal to noise ratio (SNR) of the BOLD effect is low, as the signal of interest is mixed with various artifacts: the respiratory and cardiac rhythms of the subject, subject motion which is only partially corrected by pre-processing methods, EPI spatial distortions created by inhomogeneities in the magnetic field, scanner artifacts such as signal drift and thermal noise. Last but not least, the link between the neural response and the BOLD effect is still not well understood [138, 137], limiting the results interpretation.

Beyond these important technical reasons, a fundamental question raises: what is the relevant information we want to extract? We generally wish to test between different hypotheses related to the experimental protocol and to derive statistical activation maps from them. The information of interest can then be the detection of response to the experimental protocol, but also the delay or the amplitude of the response. Another goal can be to build a more synthetic representation of the dynamics of the dataset. Various analysis methods have been proposed in the literature which can be classified given the questions they are able to address.

### 4.2.2 Classification of methods

Figure 4.6 gives an overview of the main existing methods. Following [212, 121], we will classify the methods in two categories: hypothesis-driven and exploratory.

Hypothesis driven methods rely on an explicit modeling of the response to the exper-

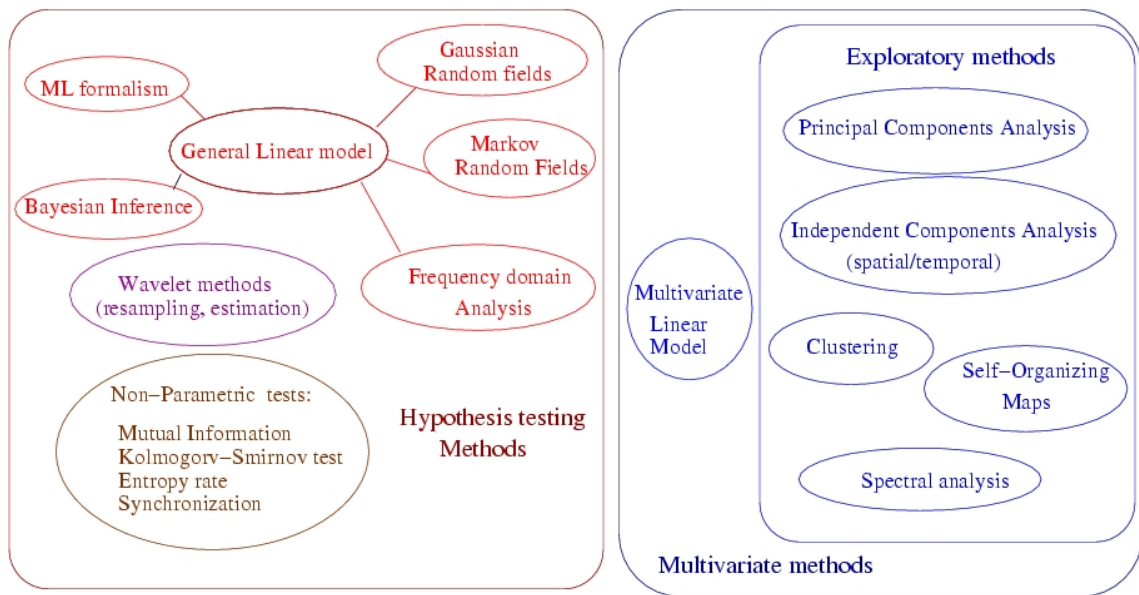


Figure 4.6: Overview of the main fMRI analysis methods. The main classification separates univariate and multivariate approaches. The figure is borrowed from [212].

imental paradigm. This leads to an estimation of the model parameters followed by statistical tests on the latter to assess the presence of an activation and comparisons between different experimental conditions. Most of these methods are univariate, in the sense that they consider each voxel as independent. The main weakness of these approaches is the more or less restrictive assumptions made on the response shape which may not fit actual responses. Their main advantage is the clear answer, with an estimated probability of confidence, they can give to particular questions such as: "which voxel's activity is strongly correlated with the stimulation?" or "what voxels are more activated in condition A than in condition B?". The methodological variations between hypothesis-driven methods can concern the signal modeling, the parameter estimation method employed or the framework on which statistical tests rely.

On the other hand, exploratory methods work directly on the functional data, often ignoring the experimental paradigm. The idea is to extract temporally and/or spatially structured patterns from the dataset. These approaches are called multivariate because they consider all voxels simultaneously. They try to give a general account of the data content which is particularly interesting when considering the complex and mixed sources of the data generation. Yet, the interpretation of the resulting patterns is often difficult. Exploratory methods can therefore be employed to identify some confounds that could be removed but also to identify possible response shapes that can further be used in univariate approaches. The methodological variations come from the way features are discriminated in the data: it can be the decorrela-

tion between the components (yielding to Principal Component Analysis -or PCA-methods), the independence (Independent Component Analysis) or a distance in a feature space (clustering approaches).

Note that this rough classification is not exclusive, as some methods such as the Multivariate Linear Models [249] are just between both categories.

### 4.2.3 The General Linear Model

The General Linear Model (GLM) is a standard statistical framework in data analysis on which is based the most popular analysis software used in the fMRI community: SPM<sup>4</sup>. Behind this acronym stands Statistical Parametric Mapping which is a kind of image from which functional activations are detected. By extension, the SPM methodology often refers to the processing chain offered by the SPM software, including some pre-processing tools we already mentioned in the previous section, SPM estimation and statistical inference tools. For a more comprehensive presentation of the methods implemented in SPM, one can refer to [79]<sup>5</sup>. Here we give a description of the model specification and the inference steps we relied on to analyze some of our datasets.

#### Model specification

The GLM is a voxel-based method, i.e. it addresses each voxel individually. In the following description, we therefore consider a single voxel time course. The observation at time  $t$  of a temporal signal  $Y = (y(t))_{t=t_1 \dots t_T}$  is modeled as the linear combination of  $C$  explicative variables  $\{x_i(t)\}_{i=1 \dots C}$ , called the *regressors*, and a noise term  $\epsilon(t)$ :

$$y(t) = \beta_1 x_1(t) + \beta_2 x_2(t) + \dots + \beta_C x_C(t) + \epsilon(t) = \sum_{i=1}^C \beta_i x_i(t) + \epsilon(t)$$

The  $(\beta_c)_{c=1 \dots C}$  are supposed to be time independent, leading to:

$$\begin{cases} y(t_1) = \beta_1 x_1(t_1) + \dots + \beta_C x_C(t_1) + \epsilon(t_1) \\ \vdots \\ y(t_T) = \beta_1 x_1(t_T) + \dots + \beta_C x_C(t_T) + \epsilon(t_T) \end{cases}$$

which can be written in matrix form:

$$Y = X\beta + \epsilon \quad \text{with} \quad \mathbb{E}(\epsilon) = 0 \quad \text{and} \quad \text{Var}(\epsilon) = \sigma^2 I$$

---

<sup>4</sup>SPM was developed at the Wellcome Department of Cognitive Neuroscience, Functional Imaging Laboratory, London, UK and is freely available at: [www.fil.ion.ucl.ac.uk/spm](http://www.fil.ion.ucl.ac.uk/spm)

<sup>5</sup>A comprehensive manual is freely available from the web page: <http://www.fil.ion.ucl.ac.uk/spm/doc/books/hbf2>

Assuming  $\mathbb{E}(\epsilon) = 0$  comes down to take a constant regressor  $x_1(t) = 1 \quad \forall t \in \{t_1, \dots, t_T\}$  or to consider the signal  $Y$  centered.

The  $T \times C$  matrix  $X$  is called the *design matrix* and is formed of each regressor in its column. The basic regressor corresponds to a convolution of the time  $P_c$  of a given condition  $c$  in the experimental paradigm with a canonical model of the hemodynamic response function (HRF) noted  $h$ :

$$x_c(t) = h(t) * P_c(t)$$

The typical HRF used in SPM is obtained with a difference of two Gamma functions, but other alternatives have been proposed. Such modeling is the consequence of the following assumptions:

- the response is linear with respect to the stimulation; in other words, if a stimulation leads to a BOLD response in a given voxel, then the same stimulation repeated over time will produce as a response the sum of the response at each stimulation,
- the response is time-invariant; a delay in the stimulation induces the same delay in the response,
- the response is causal; the output signal does not depend on future events.

The linearity of the BOLD response holds for stimulations sufficiently separated in time [84] and for block design experiments, but non linear effects were consistently revealed in various event-related studies [236, 84]. Non linearity of stimulus repetition is also the central assumption of fMR-adaptation experiments as will be presented in chapter 6.

Other regressors can also be introduced as explicative variables: first or second temporal derivatives of the HRF convoluted by the stimulation to model some variations in the response such as the delay, head motion estimates [82, 118] or low-frequency signals that behave as high-pass filters to model low-frequency variations (cardiac and respiratory effects, signal drift). Figure 4.7 shows two examples of design matrices used either in an event-related or in a block design experiment.

### Parameter estimation

The vector of parameters  $\beta = (\beta_c)_{c=1\dots C}$  can be estimated by the ordinary least squares method which comes down to minimizing the residual sum-of-squares, i.e.

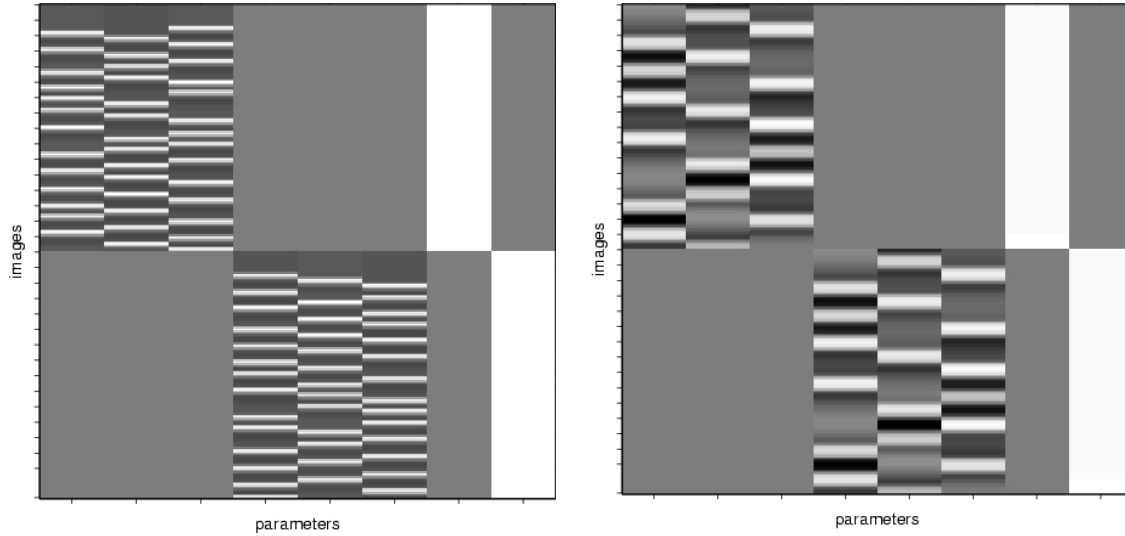


Figure 4.7: Examples of design matrices used in an event-related paradigm (left) or a block design paradigm (right) with two sessions in both case. In each matrix, the columns are the model regressors and the rows the temporal steps (i.e. the images).

the sum of the square differences between the actual and fitted values, noted  $\mathcal{E}$ :

$$\begin{aligned}\mathcal{E} &= \hat{\epsilon}^\top \hat{\epsilon} \\ &= (Y - X\hat{\beta})^\top (Y - X\hat{\beta}) \\ &= Y^\top Y - 2\hat{\beta}^\top X^\top Y + \hat{\beta}^\top X^\top X\hat{\beta}\end{aligned}$$

A necessary condition (and also sufficient as we are considering a quadratic positive definite form) for minimizing the error  $\mathcal{E}$  leads to the so called normal equations:

$$\frac{\partial \mathcal{E}}{\partial \beta} = 0 \Leftrightarrow X^\top Y = (X^\top X)\hat{\beta}$$

Thus,  $(X^\top X)$  being invertible (i.e. if the matrix  $X$  is of full rank<sup>6</sup>), the least square estimation of  $\beta$  is:

$$\hat{\beta} = (X^\top X)^{-1} X^\top Y$$

with the dispersion matrix:

$$Var(\hat{\beta}) = \Lambda_{\hat{\beta}} = \sigma^2 (X^\top X)^{-1}$$

Note that the least square solution can have a geometric interpretation in which estimating  $\beta$  comes down to project  $Y$  into the sub-space generated by the model regressors.

Under the assumption of Gaussianity for the residuals and also assuming their independence, this estimation is the one of maximum likelihood and also, in virtue of

<sup>6</sup>In cases where the design matrix is not of full rank, which should be avoided in general, pseudo-inverses such as Moore-Penrose can be used.

Gauss-Markov theorem, the best linear un-biased estimation of  $\beta$ . In other words, this means that among all estimators that are linear combinations of the data with a mean equal to the true value of the parameters ( $\mathbb{E}(\hat{\beta}) = \beta$ ), its variance is minimum. It is however known that fMRI noise is correlated, at least temporally, making the independence assumption incorrect. In case of colored noise:

$$\epsilon \sim \mathcal{N}(0, \Sigma) \quad \text{with} \quad \Sigma = \sigma^2 V$$

we can get the following estimations:

$$\begin{aligned} \hat{\beta} &= (X^\top V^{-1} X)^{-1} X^\top V^{-1} Y \\ \Lambda_{\hat{\beta}} &= \sigma^2 (X^\top X)^{-1} X^\top V X (X^\top X)^{-1} \end{aligned}$$

This estimator is once again the best linear un-biased estimation of  $\beta$ . However, it is necessary to have a precise estimation of  $\Sigma$  or  $V$ , which is in general unlikely. Two main solutions can be envisaged: whitening the noise or impose a known covariance matrix. Both can be seen as a temporal filtering of the data achieved through a convolution matrix  $K$ :

$$KY = KX\beta + K\epsilon$$

which give the following parameter estimation:

$$\begin{aligned} \hat{\beta} &= (X^\top K^\top K X)^{-1} X^\top K^\top K Y \\ \text{Var}(\hat{\beta}) &= \sigma^2 (X^\top K^\top K X)^{-1} X^\top K^\top K V K^\top K X (X^\top K^\top K X)^{-1} \end{aligned}$$

Whitening the noise consists in choosing  $K = V^{-\frac{1}{2}}$ , which also requires an estimation of the covariance matrix  $V$ . This can be done by imposing a certain structure to  $V$ , such as an auto-regressive model as proposed in [81, 246].

The alternative solution, called precoloring and implemented in SPM, is to impose a known correlation structure by applying a low-pass filter  $K$  so that:

$$\text{Var}(K\epsilon) = \sigma^2 K V K^\top \approx \sigma^2 K K^\top$$

In other words, a "strong" enough filter is applied in order to neglect the intrinsic data correlations.

As argued in [81], both techniques are biased but the precoloring appears more robust for a moderate loss of efficiency.

### Statistical inference

Based on the parameter estimation, we can now derive two kinds of statistical maps to test our hypotheses: T maps and F maps. We define contrasts  $\gamma$ , which are linear combination of the estimates  $\hat{\beta}$  related to a null hypothesis we wish to test:

$$H_0 : \gamma^\top \hat{\beta} = 0$$

It allows to test if the effects linked to a given subset  $A$  of experimental conditions led to greater or smaller effects than another subset of conditions  $B$ . The significance of the estimated response to the contrast  $\gamma$  is given by:

$$\frac{\gamma^\top \hat{\beta}}{\text{Var}(\gamma^\top \hat{\beta})} = \frac{\gamma \hat{\beta}}{\sqrt{\gamma^\top \Lambda_\beta \gamma}} \sim t_d$$

where  $t_d$  is the Student distribution with  $d$  degrees of freedom,  $d$  being derived from the design matrix  $X$  by standard methods detailed in [245]. We indeed find a Student distribution for the left handed term of the above equation under the null hypothesis and assuming the Gaussianity of the residual  $\epsilon$ . Note that the Student test is signed which allows to answer if an effect is smaller or greater than another. When the  $t$  scores are computed over all the voxels, we get a statistical  $t$  map. The  $t$  map can also be converted to a normal variable  $z$  map through standard procedures.

To assess if a given regressor subset "explains" well the observed signal, one can consider a set of contrasts  $\Gamma = \{\gamma_1, \dots, \gamma_g\}$  and derive a statistical score to assess the square norm of  $\Gamma\beta$  with respect to its dispersion:

$$\frac{\Gamma \hat{\beta}^\top \Gamma \hat{\beta} d_2}{\Gamma^\top \hat{\Lambda}_\beta \Gamma d_1} \sim \mathcal{F}_{d_1, d_2}$$

where  $\mathcal{F}_{d_1, d_2}$  is the Fisher distribution with  $d_1$  and  $d_2$  degrees of freedom of the numerator and the denominator respectively. The computation of the  $F$  scores over the brain leads to a statistical  $F$  map that can test for a subspace spanned by contrasts of the design matrix.

Note that in both kind of maps, the covariance matrix  $\Lambda_\beta$  is implied, emphasizing the importance of its estimation.

The inference finally consists in rejecting the null hypothesis given the statistical map. Knowing the distributions under the null hypothesis  $H_0$ , one can analytically derive the related threshold for a given significance value (or P-value). A voxel showing a higher statistical value than the threshold rejects the null hypothesis and is therefore declared as responding to the experimental paradigm.

### Map-wise threshold

The inference described above leads to a voxel-based threshold, which does not take into account the global map. A first solution to control the number of false positive voxels in the whole map is the Bonferroni correction: assuming the independence of the  $N$  voxels considered, the probability  $q$  that any voxel in the map has a  $z$  score above the threshold  $t_q$  under the null hypothesis is related to the same probability for a given voxel,  $p$ , by:

$$q = p^N$$

This method is particularly straightforward to apply, but the independence hypothesis simply ignores the spatial correlations within the data, specifically the fact that the activations we seek are more likely to be a subset of clustered voxels than just isolated ones. The Gaussian Random Field Theory was therefore introduced to take into account these spatial correlations and derive more appropriate thresholds. The general idea was already presented above in paragraph 4.1.5 (although in general, the map should be considered as a 3D Gaussian Random Field, implying slight modifications in the above formula). Note that this approach gives another justification for the spatial smoothing of the data, which makes the stationary Gaussian random field hypothesis more credible.

### **Alternative univariate approaches**

Various alternatives have been proposed to improve some aspects of the GLM framework in the perspective of univariate fMRI analysis. For instance, [80] have introduced non-linear terms in the GLM to model non-linearities of the BOLD response such as observed in rapid event-related paradigms; other frameworks have also been introduced to address the parameter estimation, such as Bayesian inference or Maximum Likelihood estimators. Making a detailed account of all these contributions is far beyond our purpose and we refer the reader to [212, 121] for more comprehensive reviews.

In the next two paragraphs, we will focus on two univariate approaches that are of particular interest for the analysis of our experiments data. We first describe a method allowing non parametric estimation of the BOLD response used to analyze our motion direction adaptation experiment dataset (chapter 6). We then quickly mention frequency domain based analysis that is used in most fMRI retinotopic mapping procedures.

#### **4.2.4 Non-parametric HRF estimation**

Parametric approaches such as the GLM may introduce a bias on the Hemodynamic Response Function (HRF) modeling. However, getting a precise modeling of this signal can be of interest for various purposes:

- compare its shape variations (regarding for instance the amplitude, delay or width) between experimental conditions in a given voxel or brain region,
- investigate the spatial variability across brain regions,
- retrieve a finer characterization of the BOLD signal, including its link with neuronal activity,
- ultimately allow a better understanding of cerebral activations.

Non-parametric models of the HRF could be achieved by considering each voxel (or brain region) as a system characterized by a Finite Impulse Response. The general idea is to introduce physiologically motivated temporal priors in the response model and, based on the Bayesian framework, to accurately estimate the HRF given these priors and the observed data. The first methods described in [88, 146] could only be used to estimate one HRF in response to a single condition of a periodic or synchronous event-related paradigm. Besides, these methods could only consider each session separately. A generalization of this approach was achieved in [35, 34, 147] and further implemented by Dr Philippe Ciuciu in a MATLAB toolbox interfaced with the SPM software: the HRF toolbox<sup>7</sup>. We give below an overview of the different steps and underlying assumptions of this method. It was applied to the analysis of our motion direction adaptation experiment data described in chapter 6.

In the following, we consider the observed signal  $y_v$  at a given brain voxel  $v$ . To lighten the notations, we drop the  $v$  index, so that  $y_v = y$ . For a given session  $s \in \{1, \dots, S\}$ , the voxel time course  $y_s = (y_s(n))_{n=1, \dots, N}$  is modeled as follows:

$$y_s = h * X_s + P_s l_s + \epsilon_s \quad (4.3)$$

where:

-  $h * X_s = \sum_{c=1}^C h_c * x_s^c$ , with  $x_s^c$  the binary vector with 1 at condition  $c$  onsets and 0 elsewhere and  $h_c$  the unknown HRF time course characterizing the voxel BOLD response to condition  $c$ . Note that it is implicitly assumed here that the different conditions HRFs add linearly. The method allows an interesting feature regarding asynchronous paradigms, in which stimulus onsets can occur at any time during the session: the HRFs can be estimated on a finer temporal grid than that induced by the scanner sampling period (i.e. the Repetition Time or TR) without oversampling the original data. Let  $\Delta t \leq TR$  be the sampling period of this refined temporal grid, we have:

$$h_c * x_s^c(t_n) = \sum_{k=0}^K h_c(k\Delta t) x_s^c(t_n - k\Delta t)$$

Such a temporal refinement procedure allows to estimate the HRF model with a precise temporal resolution, taking advantage of the asynchrony between the experimental paradigm and the scanning rate.

-  $P_s l_s$  is a nuisance term modeling the known low frequency fluctuations of the fMRI signal.  $P_s$  is a  $N \times Q_i$  matrix which consists of  $Q_i$  functions taken from an orthonormal basis modeling low frequencies (e.g. low order polynomial or 1-dimension discrete cosine transform).  $l_s \in \mathbb{R}^{Q_i}$  is the weighting coefficients of the

---

<sup>7</sup>The HRF toolbox can be freely downloaded at [www.madic.org/download/HRFTBx](http://www.madic.org/download/HRFTBx)

basis functions that has to be estimated by the method.

-  $\epsilon_s$  is the residual error, assumed to follow a  $\mathcal{N}(0, \sigma_i)$  distribution, further independent of  $h$ .

The model described in 4.3 is applied to each session of the experiment with the following hypothesis set:

- 1) The HRF time course  $h_c$  for each condition  $c \in \{1, \dots, C\}$  is assumed to remain constant across sessions.
- 2) The noise fluctuations across sessions are assumed to be mainly due to physiological variations, which leads to model the low frequency confounds in a session specific way while the residual variance  $\sigma_i^2$  is taken constant across sessions. Despite the known temporal correlation of fMRI time series, the authors argue that various noise correlation structures have little impact on the estimation performances.
- 3) Finally, based on physiologically plausible assumptions, each HRF temporal structure is constrained by the following priors: (a) its amplitude is close to zero at the first and end points. Note however that this constrained can be relaxed. (b) its variations are smoothed. This is achieved by the introduction of hyperparameters  $\theta$  which allow to minimize the discrete approximation of  $\|h_c\|$ . (c) the different HRFs be estimated show a prior statistical independence.

The estimation is achieved by a two step procedure:

- estimate the drift parameters  $l = (l_s)_{(s=1, \dots, S)}$  and the hyperparameters of the prior model  $\theta$ . This step is performed by computing the Maximum-Likelihood estimator with an Expectation Conditional Maximization (ECM), a variant of the classical Expectation Maximization (EM) algorithm.
- compute the Maximum A Posteriori (MAP) of  $p(h|y, l, \theta)$  based on Bayes rule.

This results in estimations of each HRF with relative error bars at each time point. These estimates are a trade-off between the information brought by the raw data and the prior constraints. The authors have demonstrated the robustness of the estimated HRFs with respect to various features on realistic simulations as well as real fMRI datasets. This includes departure from the hypothesis of equal noise variance across sessions, relevance of the temporal refinement procedure, validity of the HRF estimates error bars. They nonetheless precise the limits of their method regarding low signal to noise ratios or the selection of high dimension nuisance model (which should typically be:  $Q_i \leq 5$ ).

A useful feature of this method is the possibility to perform region-based HRF estimation. Considering each ROI as functionally homogeneous, the procedure uses all the available time series within the ROI to characterize the shape of the HRF

for each condition. The more straightforward approach is to estimate the HRFs from the ROI mean signal. Nonetheless, to avoid inaccurate estimation in case of inhomogeneous ROI (for instance due to partial volume effects), a preliminary outliers detection step can also be used to remove outlier voxels from the ROI. It is achieved using the least trimmed squares (LTS) method. Note that a rough estimation of the outliers proportion has to be given as input to the algorithm.

Finally, statistics can be computed over the estimated HRFs. This includes a rough activation detection, assessing if the estimated response is significantly different from a null time course, and, more interestingly, a comparison between two estimated HRFs. The latter allows to observe significant differences in the HRFs elicited by different experimental conditions, suggesting differences in the underlying neural processing. Such an application of this method is demonstrated in chapter 6.

#### 4.2.5 Frequency domain analysis

Another univariate method that can be used is frequency domain analysis. This approach allows to easily separate the different frequencies of the signal time course leading to less biased hypothesis testing due to the approximate independence of the Fourier coefficients. Although their use of has been limited as they are mainly restricted to periodic paradigms, this approach has shown to be useful for specific purposes. First, it is particularly appropriate when a selected feature in the stimulus is varied periodically. Based on the Fourier transform of the voxel time course, we analyze the component corresponding to the stimulus frequency. The amplitude is linked to the voxel neurons sensitivity to the feature while the phase indicates their preferred value for this feature. This procedure is classically used to analyze retinotopic mapping data [239], but has also been used to study functional sensibility to color [63], spatial frequency [216] or orientation [217]. Note however that a classical GLM approach can equivalently be used to analyze periodic stimulations, as we will show in section 5.1.

Note that frequency domain analysis can also be used to detect physiological confounds as shown in [98].

#### 4.2.6 Multivariate analysis methods

We give in the following paragraphs a brief overview of the main multivariate methods that have been proposed for an exploratory analysis of fMRI data. As opposed to univariate methods such as those presented above, these methods consider all the voxels simultaneously and generally do not rely on a specific model of the signal. If they do not lead to statistical inference, these approaches can help in designing appropriate regressors to build a model of the signal. Another important applica-

tion is also functional connectivity studies [78, 96] which aim at finding correlations between the temporal signals of spatially remote voxels. Multivariate methods are indeed particularly sensitive to temporal correlation between signals and where successfully applied to functional connectivity [5, 171]. Finally, they can be used to identify confounds in the raw data.

### Principal Components Analysis (PCA)

The Principal Component Analysis method relies on a Singular Value Decomposition (SVD) of the data matrix. The fMRI spatio-temporal signals are represented as a  $N \times T$  matrix  $Y$ ,  $N$  being the number of voxels considered and  $T$  the number of points in the time series. Applying the SVD technique, we get:

$$Y = U\Sigma V^T$$

with:

- $U$  a  $N \times N$  orthogonal matrix of *singular images* which diagonalizes  $YY^T$ ,
- $V$  a  $T \times T$  orthogonal matrix of *singular time series* which diagonalizes  $Y^TY$ ,
- $\Sigma$  a  $N \times T$  a diagonal matrix of the corresponding singular values  $(\sigma_i)_{(i=1,\dots,k)}$ .

Further constraining the ordering of  $\sigma_i$  to be decreasing, the decomposition is unique (up to a sign change between  $U$  and  $V$ ). Each component, orthogonal to the others, models a portion of the variability that can be observed in the data,

with  $\sigma_j / \sum_{i=1}^k \sigma_i$  the percent of total variance carried by the  $j$ -th component.

Applying a PCA to the raw data therefore separates different variations of the signals which can detect, without specifying any hypothesis on the paradigm, a temporal signal present in the data such as low frequency confounds. The GLM residuals can also be analyzed through a PCA to reveal variations modes that do not fulfill the Gaussian distribution hypothesis which are not modeled in the design matrix.

Various refinements have been proposed to project the data in a space of interest, such as introducing the design matrix  $X$  and performing the SVD of  $X^TY$ . These variations around the PCA are performed by applying distinct normalizations of the matrices  $X$  or  $Y$ .

### Independent Components Analysis (ICA)

Unlike the PCA which leads to orthogonal components both spatially and temporally, one may be interested in extracting statistically independent components from the data. This is the purpose of Independent Components Analysis (ICA)

techniques. However, such a decomposition has to be done separately for the spatial and the temporal domains. Considering spatial ICA for instance, the idea is to model our  $N \times T$  matrix  $Y$  (the dataset) as the superposition of  $M$  independent sources  $S$  plus a residual noise term  $\epsilon$ :

$$Y = AS + \epsilon$$

where  $A$ , called the *mixing matrix*, models the superposition of the sources. The problem is now to estimate the *unmixing matrix*  $B$ ,  $S$  and  $K$  such that:

$$S = B(X - \epsilon) \tag{4.4}$$

$B$  can be viewed as a generalized inverse of  $A$ . Solving equation 4.4 supposes to define an independence criterion for the sources and to choose the rank of the generative model  $K$ , which can appear to be arbitrary. Finally, the estimated source terms in  $S$  can be interpreted as independent activation maps standing for different effects present in the dataset [20].

To give an illustration, we have applied a spatial ACI technique to a retinotopic mapping dataset using the SICA toolbox developed at the U494 INSERM team laboratory, Paris, France. Figure 4.8 shows the two first spatial components extracted by the algorithm, without giving any prior about the experimental paradigm. It illustrates the possible advantages of the method to separate components consistent with the stimulation from confounds such as non-corrected head motion or physiological noise, as shown in [172].

### Clustering analysis

Clustering approaches allow to group a collection of objects into subsets (or clusters) based on a similarity measure between these objects. In the fMRI data analysis context, the time courses of voxels can be considered as a set of  $N$  features (our objects) belonging to a given feature space  $\mathcal{F}$ .

Some clustering methods rely on parametric models of the features distribution in  $\mathcal{F}$ : classifying the data into different subsets comes down to identifying the main modes of this distribution.

An important issue is the definition of the feature space  $\mathcal{F}$ ; this is related to the choice of the metric used to quantify the similarity between time courses. The Euclidean distance on the raw time courses has naturally been considered, but alternatives such as the Mahalanobis metric can also be used. Some authors proposed to apply clustering methods to various features extracted from the dataset: the cross-correlation coefficients between the time courses and an ideal response to the paradigm [87], or t-maps, finite impulse response filter model [86]. Using

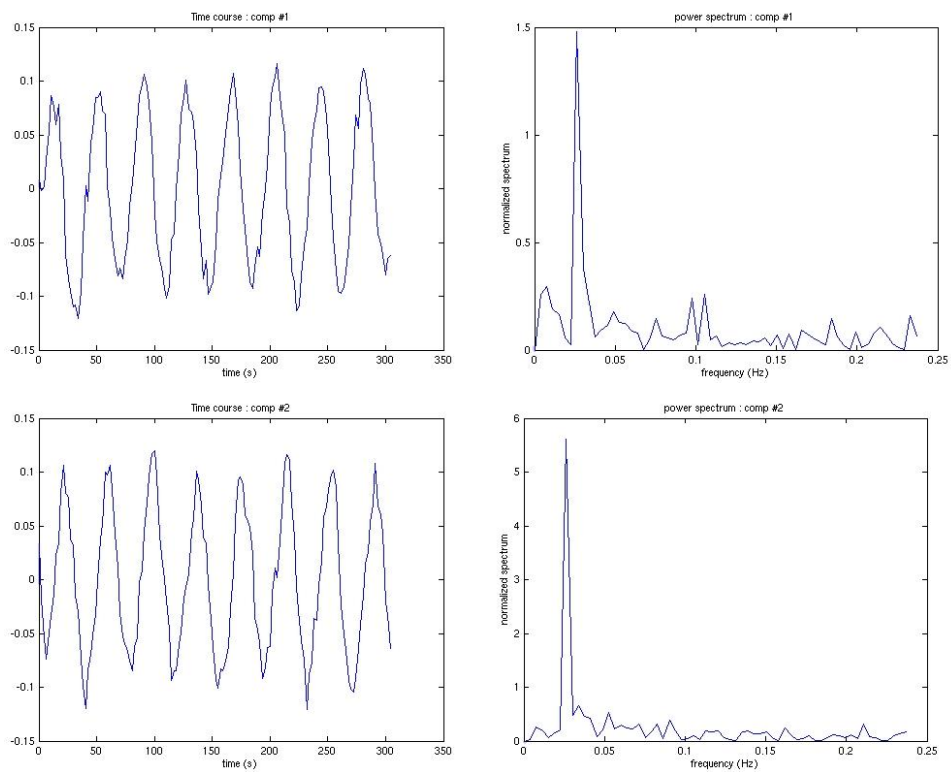


Figure 4.8: Illustration of the spatial ICA method on a retinotopic mapping dataset, as detailed in 5.1. Without any information regarding the experimental paradigm, the two first components extracted show a spectrum picked at the stimulation fundamental frequency (1/38 Hz)

these features can have several advantages: first it reduces the dimensionality of the time course to classify, thus improving the computational efficiency. This also introduces some knowledge about the paradigm in the analysis, leading to an easier interpretation of the final clusters. Finally, it allows to perform a meta-analysis that can separate activated voxels into different clusters [86].

Another problematic aspect of clustering is to choose the number of clusters which leads to a bias/variance trade-off. The main clustering algorithms, such as K-means or fuzzy C-means have been used to compute the final solution, yielding to similar results.

Another clustering method applied to fMRI in [29] is self-organizing maps, which are designed to map the input vectors onto a 1, 2 or 3D maps. This method has however received less attention since it is quite technical and relies on several non-interpretable parameters.

We have presented in this chapter the main methods we considered to pre-process and analyze our datasets. The specific processing chain we used for the experiments described in the remainder of the thesis will be detailed in their respective chapters.

# Chapter 5

## Visual areas mapping

### Contents

---

<b>5.1</b>	<b>Retinotopic areas mapping . . . . .</b>	<b>118</b>
5.1.1	The cortical retinotopic organization . . . . .	118
5.1.2	Experimental protocol . . . . .	124
5.1.3	Functional images preprocessing . . . . .	125
5.1.4	Statistical analysis . . . . .	126
5.1.5	Angular values computation . . . . .	133
5.1.6	Angle maps analysis . . . . .	135
5.1.7	Mapping reproducibility . . . . .	143
5.1.8	Mapping efficiency . . . . .	145
5.1.9	Area delineation . . . . .	149
5.1.10	Conclusion . . . . .	154
<b>5.2</b>	<b>Functional mapping of hMT+ . . . . .</b>	<b>155</b>
5.2.1	The hMT+ complex . . . . .	155
5.2.2	hMT+ localizer: previous work . . . . .	156
5.2.3	hMT+ optimal mapping . . . . .	156
5.2.4	Results . . . . .	159
5.2.5	Conclusion . . . . .	168

---

The general cortical architecture is globally consistent across subjects of a given species, that is the same type of area and the same amount are found in any non-pathological individual. However, the strong physiognomical variations of the cortex folds implies an important anatomical variability across individuals. Furthermore, studies of the cortical plasticity suggest that the anatomy-function correspondence can vary across time for a given subject. An individual identification of distinct areas can therefore be considered as a prerequisite to any study of the human visual cortex. This gives more information about the visual system organization over the cortical sheet, which can be compared to other species in an evolutionary perspective or between different populations to investigate pathologies or developmental mechanisms. Moreover, an objective area delineation can be used to define independent Regions of Interest (ROIs) that will be further characterized in subsequent experiments.

This chapter is divided into two parts, each one corresponding to a specific criterium we used to delineate low level visual areas. In the first part, we describe the fMRI retinotopic mapping procedure employed to delineate the early occipital retinotopic areas. In the second part, we present the functional mapping used to identify the hMT+ complex.

## **5.1 Retinotopic areas mapping**

### **5.1.1 The cortical retinotopic organization**

From the retina to the low level visual cortex, a perceptual element such as a retinal ganglion cell or a cortical neuron is only sensitive to a restricted portion of the visual field called its receptive field. Coarsely, the receptive field is “what the perceptual element sees”. More precisely, the visual receptive field of a cell generally corresponds to a small portion of surface in the fixation plane which, when a stimulation enters it, modifies the response of the cell. In our experiments, this fixation plane is the screen the subjects look at; the terms classically used to refer to different portions of the visual field are illustrated in figure 5.1.

Let us now state three fundamental properties of the visual areas that define their retinotopic organization:

- 1) The neurons from different layers of a given cortical column share the same receptive field [109, 111].
- 2) Two points close to each other in the visual field project closely on the retina. After various steps and following different paths, these close retinal stimuli

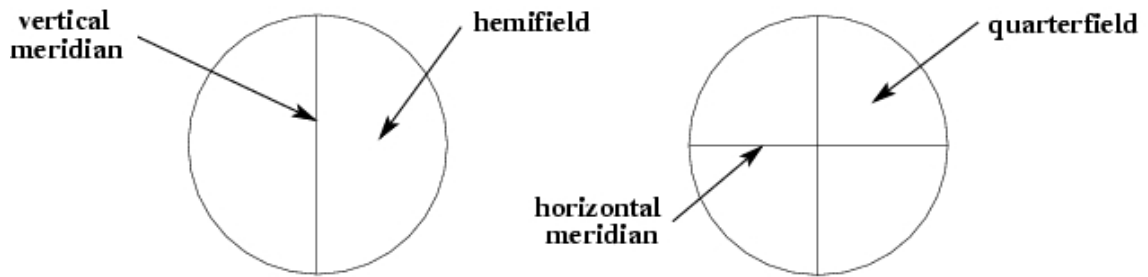


Figure 5.1: The visual field is split along the vertical meridian into two hemifields, each again split into two quarterfields along the horizontal meridian. The latter further splits the vertical meridian into its lower and upper parts.

will be analyzed, inside a given area, in neighboring regions of the cortex. Although the precise distances and angles are not preserved, the local topology is preserved from the visual field to the cortical surface of retinotopic areas. Figure 5.2 illustrates this property, showing the representation of the visual field in macaque monkey area V1.

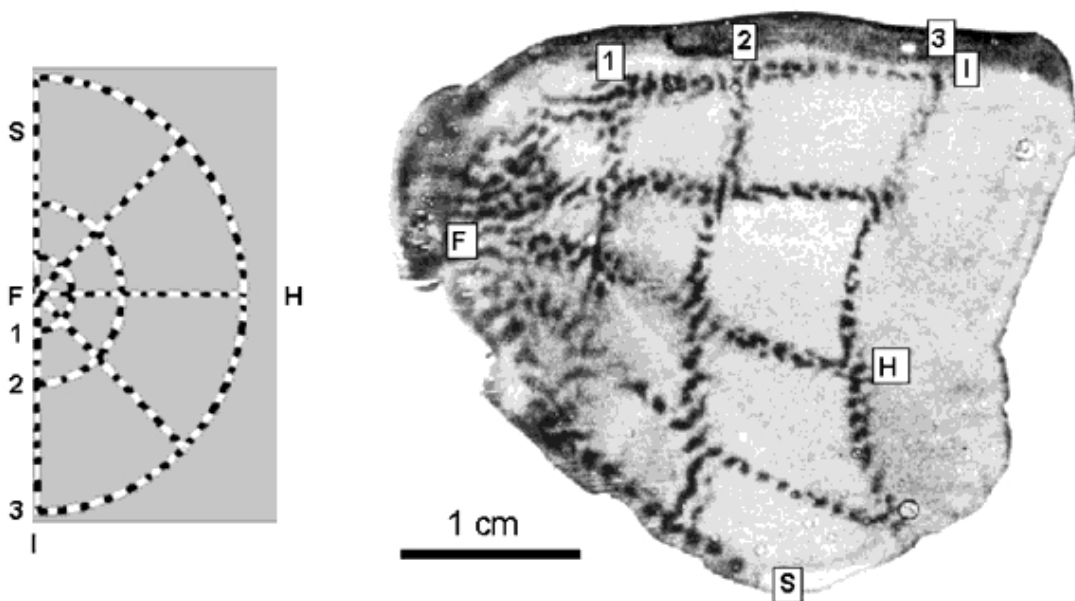


Figure 5.2: Retinotopy in macaque visual cortex: a flickering stimulus (left) and its retinotopic representation in a flattened view of layer 4C of area V1 (right), revealed through a  $^{14}\text{C}$ -2-deoxy-d-glucose (DG) autoradiography procedure. Reproduced from Tootell et al. [220]

For instance, the primary visual cortex in humans (V1), anatomically found in the occipital lobe around the calcarine sulcus, presents a retinotopic organization. The latter is approximately polar:

- when one moves along the cortical surface from a posterior to an anterior position in V1, the representation in the visual field moves smoothly from the center (fovea) to the surround. We say we vary the *eccentricity*.

- similarly, a displacement from the inferior limb of the calcarine to the superior limb results in a smooth variation of the representation from the superior vertical meridian of the visual field to the inferior part of this vertical meridian. We say we vary the *polar angle*.

This type of representation is found in various visual areas, implying that the visual cortex contains several maps of the visual field. The correspondence with polar coordinates has naturally led to define polar-coded stimuli as we will see below.

3) Two adjacent areas on the cortical surface (such as V1 and V2) differ with respect to their representation of the visual field. This is a crucial point for the differentiation of areas we are looking for. Indeed, some areas present a so called *reverse* or *mirror* representation, the visual field being projected on the cortical surface as if it was seen through a mirror, whereas others have a *normal* representation, consistent with the visual field spatial order. The representations change chirality<sup>1</sup> for two adjacent areas, a useful information we will take into account to detect the borders between them. We illustrate this property in the sketch of figure 5.3.

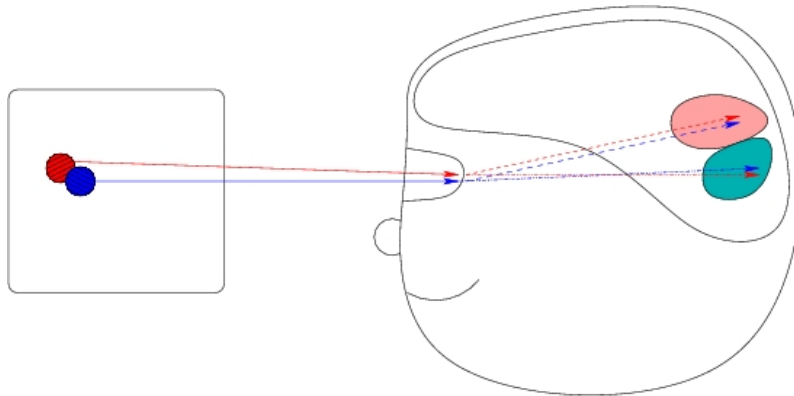


Figure 5.3: Schematic illustration of the retinotopic properties of the visual system in primates: continuity between the visual field and the cortical surface, inversion of the chirality between two adjacent areas.

---

<sup>1</sup>In geometry, a figure is chiral (and said to have chirality) if it is not identical to its mirror image, or more specifically can't be mapped to its mirror images by rotations and translations alone, i.e. both figures are related like our left and right hands.

## Previous work

The first studies of human cortical retinotopy were based on patients having focal occipital lesions [104, 105, 107, 106]. Non-human primates visual cortex was extensively studied over recent decades by invasive studies, mainly electrophysiology [46, 253, 230], resulting in a far more detailed understanding of retinotopic organization. More recently, the first human functional imaging studies appeared using TEP [73] and fMRI [190].

The periodic fMRI retinotopic mapping paradigm was introduced in [60], in which the authors used two expanding rings to measure the eccentricity map within the calcarine sulcus. The stimulation was subsequently completed with a rotating wedge to establish the polar angle coordinates [50, 192, 49]. This general procedure has since then been used in numerous studies, with some variations regarding various parameters such as:

- the number of simultaneous rings or wedges in the display [62, 233],
- the stimulus pattern which is often a black and white [192] or colored [222, 239] checkerboard, but also a moving dots pattern [112] or a video [196, 187],
- the stimulus pattern flicker frequency,
- the amount of complete cycles, the cycle duration, the number of averaged runs,
- the task performed by the subject, which can be a passive-viewing, central or peripheral attentional task.

We will come back to some of these differences below while comparing our choices to the literature.

Alternative approaches to retinotopic mapping have been proposed to reveal cortical visual field maps with fMRI. Some groups have used block designs with static stimulations of a limited spatial positions amount, such as a few eccentricity bands [95, 100] or the horizontal and vertical meridians only [101, 72]. These approaches naturally cannot give a detailed account of the visuotopic maps and may be prone to a poor spatial localization as mentioned in [238]. [83] evaluated the binary m-sequence paradigm for a retinotopic stimulus presentation which leads to comparable maps than those obtained with periodic paradigms but without lowering the acquisition duration. Two different groups recently investigated the feasibility of mapping a precise sub-region of the visual field using randomized block designs with spatially restricted localizers [127] or a multifocal mapping stimulation technique [235]; these approaches have the advantage to be faster and more precise than the classical procedure when only a task-relevant subsets of positions is mandatory.

From previous studies of the cortical retinotopy in humans, we can infer the

retinotopic structure classically found in the human occipital cortex. First, as the two hemifields (the vertical separation of the visual field) split at the level of the optical chiasm, each hemisphere is only concerned with the visual information of its opposite hemifield. Second, as found in animal studies, some areas are split into two parts at the representation of the horizontal meridian. Hence the limits between adjacent areas correspond to horizontal or vertical meridians. More specifically, most studies agree in the visual field representation and labeling as follows:

- V1-also called the “striate” cortex with respect to its markedly laminated anatomy and its 11 layers (rather than the customary 6 in other areas) and by opposition with the next “extrastriate” areas- has a complete contralateral hemifield representation, covering the calcarine sulcus. The horizontal meridian lies in the fundus of the latter and the representation smoothly changes to the superior vertical meridian in the ventral lip of the calcarine sulcus and to the lower vertical meridian in the dorsal lip of the calcarine sulcus respectively. These vertical meridians define the borders of V1 with the two distinct parts of V2. The representation in V1 is qualified of *mirror*, as the visual field is projected on the cortical surface as if seen through a mirror (see section 5.1.1).

- V2 is divided into two distinct quarter-field representations, the upper contralateral quadrant being located ventrally to V1 (V2v for V2 *ventral*) and the lower contralateral quadrant dorsally (V2d for V2*dorsal*). Unlike V1, the representation in V2 is *non-mirror*. In other words, the polar angle gradient along the surface is reversed with respect to V1. The borders of V2v and V2d with respectively V3v and V3d are defined along the horizontal meridian representations.

- V3, akin to V2, is split into two quadrants. V3d follows V2d as one moves dorsally and shows another lower quarter-field representation; V3v, also called VP for Ventral-Posterior because it was suspected to be distinct from V3d in monkeys studies, follows ventrally V2v and shows an upper visual field quadrant. We chose to call this portion of the cortex V3v instead of VP, as this separation between the two aim at being less and less supported in the monkey literature and as no evidence was presented to distinguish them in humans (for a more complete discussion, see Zeki’s paper about “improbable areas” [254]). The representation in both parts of V3 is reversed with respect to V2, thus mirror like V1.

- V3A, located dorsally to V3d, shows a complete contralateral hemifield non-mirror representation.

Figure 5.4 illustrates this description. Note however that beyond V3v ventrally and V3A dorsally, there is still no consensus in the actual visual field maps and consequently the areas labeling. We will discuss some of these issues when analyzing our results in paragraph 5.1.8. For now, we see how the knowledge about the visual field representation over the cortical sheet can be sufficient to delineate the low-level visual areas.

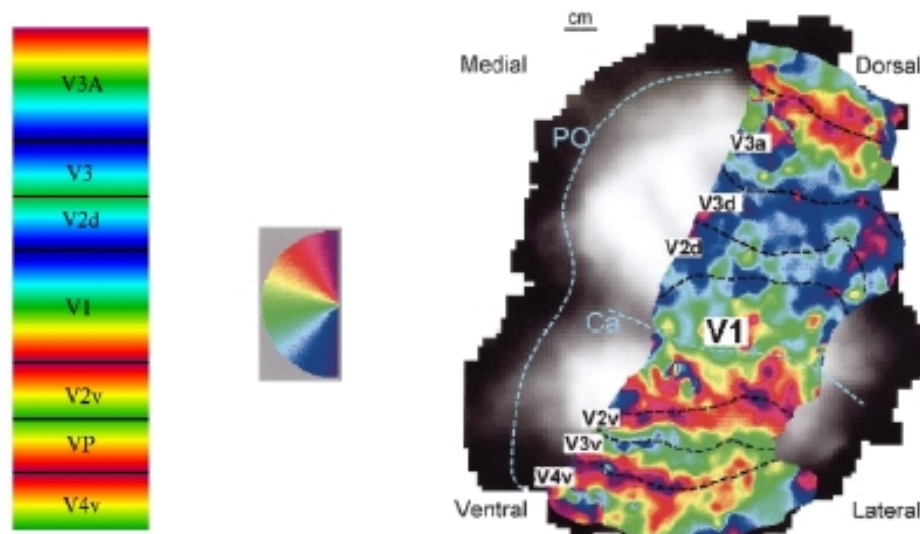


Figure 5.4: Polar angle retinotopy of the right hemisphere, i.e. the left visual hemifield. The left-hand side of the figure illustrates the spatial arrangement of different areas and their retinotopy, the hemi-circle at the center corresponding to the color code employed for each angle of the visual field (from Wandell [239]). The right-hand side of the figure shows results obtained from human fMRI on an unfolded cortical surface by Pr. Wandell's team, V3v and V3d respectively corresponding to V3 and VP in the text and on the left-hand side of the figure.

## Applications

fMRI retinotopic mapping is not only the main way to explore the organization of the visual field maps in humans but has also been applied to study many aspects of the early visual areas. This technique allowed quantitative estimation of parameters to characterize further the visual maps such as the cortical magnification factor [60, 192, 62], the receptive field size [203] or the cortical surface area for each visual area [53]. It can naturally be used in children [39], offering opportunities to developmental studies. Similarly, retinotopic mapping of patients allow to study the cortical representation of retinal diseases [210, 7, 103] and the presence or absence of a related cortical plasticity [201]. The method was also successfully applied to sub-cortical brain structures like the lateral geniculate nucleus [27, 189] or the superior colliculus [188] and to other species such as cat [160] and macaque [16], serving as a useful reference to study homologies and differences along the evolution [221, 163, 195]. From a methodological point of view, fMRI retinotopic maps can also be helpful to constraint the source localization in Electro-encephalography (EEG) or Magneto-encephalography (MEG) studies [51]

### 5.1.2 Experimental protocol

Taking into account the retinotopic properties of the visual cortex described above and building on previously published work on the subject, we now define our experimental paradigm and our stimuli. Let us recall that the aim is to uncover the mapping of the visual field over the cortical surface. This can be achieved by stimulating locally and periodically the visual field of the subject whose gaze stays fixated at the central point. The basic pattern of our stimuli is a radial checkerboard distributed in the radial and the polar dimensions, similar to those described in the literature (e.g. [192, 239]). To take into account the cortical magnification, the size of squares is increasing with the eccentricity.

#### The stimuli

We finally require two families of stimulus:

- The *wedge* is a 80 degrees wide conical sector rotating around the central fixation point. This stimulus moves in discrete 20 degrees steps in the visual field in a circular clockwise or anti-clockwise fashion, thus leading to 18 different positions for a complete 360 degrees rotation (see figure 5.5).



Figure 5.5: The “wedge” stimulus seen in different positions. It encodes the polar angle coordinate  $\theta$  of the visual field.

- The *ring* is an annulus centered at the fixation point, its size varying with respect to the eccentricity. Similarly to the *wedge*, it has two “directions of rotation”: either contraction or expansion; a complete rotation is achieved in 18 distinct steps. When the annulus reaches its maximal eccentricity (respectively minimal), it is replaced by an annulus at minimal (resp. maximal) eccentricity, with an intermediate position of coexistence (cf. the right image of figure 5.6). This wrapping around allows to have a close to continuous motion of the stimulus.

In terms of polar coordinates, the *wedge* stimulus encodes the polar angle component whereas the *ring* encodes the radial component. The complete visual field is then completely covered, and these two families of stimuli carry complementary information with respect to the simulation of the visual field.

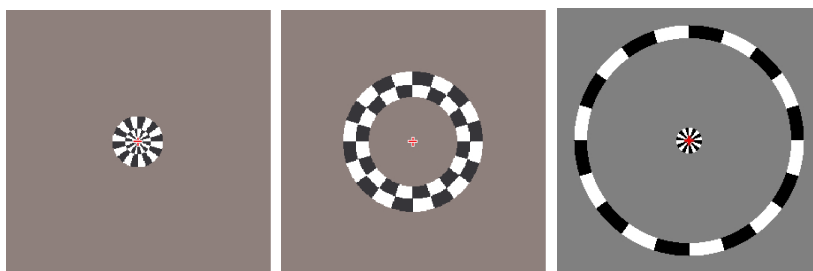


Figure 5.6: The “ring” stimulus at different positions. It encodes the eccentricity coordinate  $\rho$  of the visual field.

For each position of the stimulus, we scan a functional volume, yielding at the end of each stimulation a temporal series of images  $(Y_t)_{t=0,\dots,T-1}$ .

The checkerboard pattern of these stimuli flickers (at 9Hz in our setup, one cycle consisting of 1/18 sec black and 1/18 sec white) in order to insure a sustained neuronal response. Indeed, most of the receptive fields cells in the retina and the Lateral Geniculate Nucleus -the main inputs for the first visual cortical areas- consist of two antagonistic regions, the best response of the cells being obtained with a luminance local contrast between their center and surround. This checkerboard pattern is superimposed on a mid grey-level equiluminant background to let the cells whose receptive fields do not fall on the checkerboard at rest.

Let us recall that the display size of our videos and the experimental setup provide a 20.9x20.9 degrees display. The extent of the diameter reached by the stimuli circular aperture is 19.5 degrees, giving a maximum radial opening in the visual field of  $19.5/2=9.75$  degrees.

The stimuli we used were programmed in Matlab to generate a video sequence in avi format. A number of parameters were adjustable.

### Stimulus optimization

Our main goal is to design an experimental setup allowing a fast and reliable retinotopic mapping to accurately delineate the visual areas. We varied three different parameters of our stimulus: the number of sectors in the wedge, the number and the duration of complete rotations (or cycles). The results, presented in [252], are described below in paragraph 5.1.6.

#### 5.1.3 Functional images preprocessing

Our retinotopic mapping functional datasets are systematically preprocessed as follows:

- The motion correction step is run first, taking as reference functional image the closest to the anatomical scan in the acquisition order.
- We then apply the rigid coregistration step between the anatomical image and the functional scans.
- The data are then smoothed using either the classical 3D isotropic Gaussian kernel or the cortical surface based method<sup>2</sup> described in paragraph 4.1.5. In both cases, the filter FWHM is set to 1.5 the inplane voxel size.
- Finally, a temporal filtering is applied to the data. A high-pass filter is used to remove low-frequency confounds and a low-pass filter to roughly control the temporal auto-correlations.

#### 5.1.4 Statistical analysis

This stage aims at establishing which functional voxels are correlated to our stimulation. The method used is based on the General Linear Model (GLM) framework (see paragraph 4.2.3) and can be qualified as:

- univariate: the analysis is performed independently for each voxel (as opposed to multivariate analysis which considers all voxels simultaneously),
- differential: the inference answers to a binary question (a voxel is qualified either as activated or not activated),
- parametric: some assumptions are made about the linearity of the response with regard to the stimulation and about the structure of image noise.

We describe in this section the model specification followed by the definition and estimation of statistical tests used to reveal the activated voxels. Practically, our analysis is performed with the SPM99 software.

#### Specification of a linear statistical model

As mentioned above, a frequency analysis is classically used to analyze periodic paradigms such as the retinotopic mapping. However, we show below how this kind of paradigm can be viewed as a particular case of a linear model and therefore tackled with classical GLM analysis.

In the following description, we consider a given voxel  $v$  and a given session (e.g. *clockwise wedge*) of length  $T$ . Based on the retinotopic properties (paragraph 5.1.1) and our stimulus paradigm (paragraph 5.1.2), the voxel  $v$  should only show a correlated signal, if any, when the stimulus position overlaps the receptive fields of the neurons within this voxel. As our stimuli are moving periodically and as

---

<sup>2</sup>We have been systematically using the cortical surface based approach since it was validated.

far as the response is linear (which is reasonable if two consecutive stimulations are sufficiently separated in time), the observed signal time course  $(Y_v(t))_{t=0,\dots,T-1}$  should also be periodic, with a frequency equal to the stimulation frequency, denoted  $f_0$ . It is therefore natural to study the discrete Fourier transform of our time series:

$$Y_v(t) = \sum_{f=0}^{T-1} c_v(f) e^{\frac{2i\pi ft}{T}} \quad \forall t \in \{0, \dots, T-1\} \quad (5.1)$$

$$\text{where } c_v(k) = \frac{1}{T} \sum_{t=0}^{T-1} Y_v(t) e^{-\frac{2i\pi kt}{T}} \quad \forall k \in \{0, \dots, T-1\}$$

A simple relation links the stimulus frequency  $k_0$  to  $\omega_0$ , the stimulus pulsation<sup>3</sup>:

$$\omega_0 = \frac{2k_0\pi}{T}$$

We are interested in the part of the signal at the frequency  $k_0$ . According to the discrete Fourier transform properties, equation (5.1) can be written:

$$\forall t \in \{0, \dots, T-1\}, Y_v(t) = \beta_{v,0} + c_v(k_0) e^{\frac{2i\pi k_0 t}{T}} + c_v(T-k_0) e^{\frac{2i\pi(T-k_0)t}{T}} + \epsilon_v(t)$$

where  $\beta_{v,0}$  is the mean of the temporal signal and  $\epsilon_v(t)$  the signal components at frequencies different from  $k_0$ .

We have the following properties:

$$Y_v(t) \in \mathbb{R} \implies c_v(T-k_0) = \overline{c_v(k_0)}$$

$$t \in \mathbb{N} \implies e^{\frac{2i\pi T t}{T}} = e^{2i\pi t} = 1$$

so that  $\forall t \in \{0, \dots, T-1\}$ :

$$\begin{aligned} Y_v(t) &= \beta_{v,0} + c_v(k_0) e^{\frac{2i\pi k_0 t}{T}} + \overline{c_v(k_0)} e^{\frac{2i\pi(-k_0)t}{T}} + \epsilon_v(t) \\ &= \beta_{v,0} + 2\text{Re}(c_v(k_0) e^{\frac{2i\pi k_0 t}{T}}) + \epsilon_v(t) \\ &= \beta_{v,0} + 2\text{Re}(c_v(k_0)) \cos\left(\frac{2\pi k_0}{T} t\right) - 2\text{Im}(c_v(k_0)) \sin\left(\frac{2\pi k_0}{T} t\right) + \epsilon_v(t) \\ &= \beta_{v,0} + 2\text{Re}(c_v(k_0)) \cos(\omega_0 t) + 2\text{Im}(c_v(k_0)) \sin(\omega_0 t) + \epsilon_v(t) \\ &= \beta_{v,0} + \beta_{v,1} \cos(\omega_0 t) + \beta_{v,2} \sin(\omega_0 t) + \epsilon_v(t) \end{aligned}$$

Detailing the formulas, it yields:

$$\begin{cases} Y_v(0) &= \beta_{v,0} + \beta_{v,1} \cos(\omega_0 \times 0) + \beta_{v,2} \sin(\omega_0 \times 0) + \epsilon_v(0) \\ &\vdots \\ Y_v(T-1) &= \beta_{v,0} + \beta_{v,1} \cos(\omega_0 \times (T-1)) + \beta_{v,2} \sin(\omega_0 \times (T-1)) + \epsilon_v(T-1) \end{cases}$$

<sup>3</sup>The pulsation  $\omega_0$ , expressed in radian per second, is linked to the stimulation period  $T_0$ , expressed in seconds, by the simple relation:  $\omega_0 = \frac{2\pi}{T_0}$

We therefore define two temporal regressors:

$$X_1 = \begin{pmatrix} \cos(\omega_0 \times 0) \\ \cos(\omega_0 \times 1) \\ \vdots \\ \cos(\omega_0 \times (T - 1)) \end{pmatrix} \quad \text{and} \quad X_2 = \begin{pmatrix} \sin(\omega_0 \times 0) \\ \sin(\omega_0 \times 1) \\ \vdots \\ \sin(\omega_0 \times (T - 1)) \end{pmatrix} \quad (5.2)$$

so that:

$$Y_v = \beta_{v,0}X_0 + \beta_{v,1}X_1 + \beta_{v,2}X_2 + \mathcal{E}_v \quad (5.3)$$

- where :
- $X_0$  is the temporally constant regressor, i.e. a unity vector of dimension  $T$  (all coordinates equal to 1)
  - $\mathcal{E}_v \in \mathbb{R}^T$  is the residual error, i.e the part of the signal not explained by our model, corresponding to all frequencies different from  $k_0$ .

Equation (5.3) can be written in matrix form:

$$Y_v = XB_v + \mathcal{E}_v \quad (5.4)$$

The  $(\epsilon_v(t))_{t=0,\dots,T-1}$  are supposed to be independently and identically distributed (*iid*), following a  $\mathcal{N}(0, \sigma)$  law. This assumption is justified thanks to the high-pass temporal filter applied during the preprocessing step, which removes temporal autocorrelations.

The constant regressor does not play any special role in the remainder, it is just a way to center each session signal. The vectors  $X_1$  and  $X_2$  are decorrelated, as  $Cov(X_1, X_2) = 0$ . Furthermore, the regressors are decorrelated from one session to the other as they are not applied to the same data. Consequently, our design matrix  $X$  is of full rank.

We can get a graphical description of our model via SPM, as shown in figure 5.7, in particular with the correlations between the different model regressors  $X_i$ .

Lastly, within this model we will look closely at two parameters:

- $\|2c_v(k_0)\|^2 = \beta_{v,1}^2 + \beta_{v,2}^2$  coding the strength of the frequency  $k_0$  in the voxel time course,
- $\phi = \arctan\left(\frac{\beta_{v,2}}{\beta_{v,1}}\right)$  which is an estimator of the fMRI signal phase.

The same model is applied to each stimulus, so that for each subject we define 4 models (formally similar) with 2 regressors each (ignoring the constant regressors).

### Statistical analysis: Design orthogonality

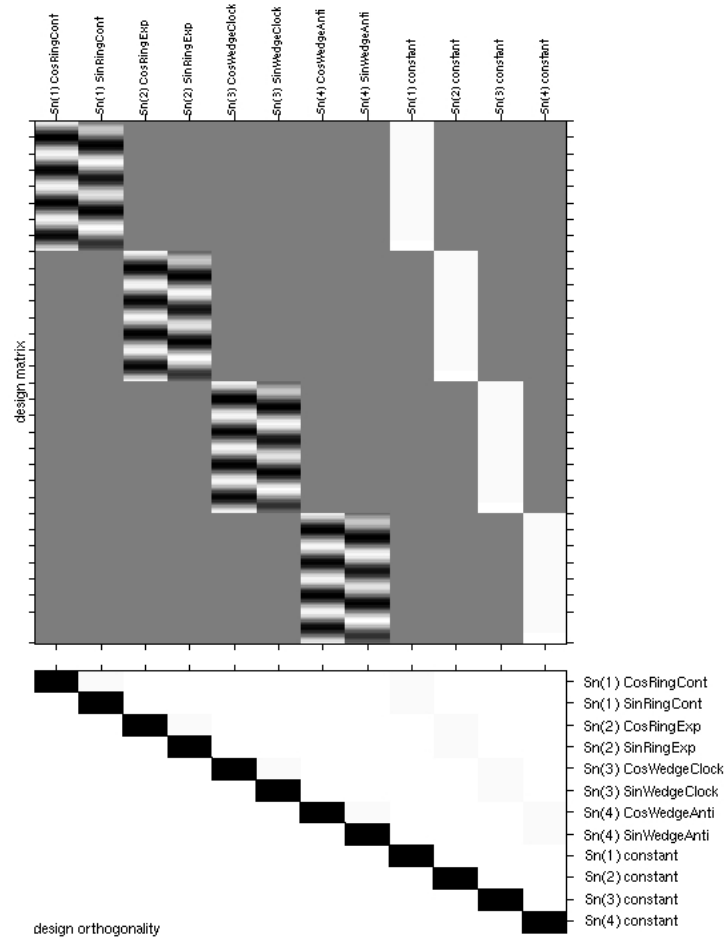


Figure 5.7: Graphical description of the statistical model used in retinotopic data analysis. The upper graph represents the SPM design matrix, in which each column corresponds to the values of a given regressor across scans. The four right columns are the constant regressors. The lower graphic shows the orthogonality of the design matrix, i.e. the correlation between the regressors of our model. They all appear to be decorrelated as expected (represented by the white color), implying that our design matrix is of full rank.

The regressors coefficients  $\beta_{v,i}$  estimation is performed with the classical least-square technique, as detailed in paragraph 4.2.3. Let us recall that under the assumption of Gaussianity for the residuals and also assuming their independence, this estimation is the one of maximum likelihood and also the best linear un-biased estimation of our regressors.

### Statistical tests

The next step consists in producing statistical tests on the parameters  $\beta_{v,i}$  in order to decide whether a given voxel signal variations is explained or not by our model. It naturally leads to an F-test on these coefficients. We will deduce from this test a mask of the voxels considered as activated in the final step.

In our study, we defined two slightly different tests that can be applied to every voxel: the global test can be used when we acquire both polar angle and eccentricity maps, whereas the specific test is applied to a single stimulation type. To lighten the notations, we drop the  $v$  index in the remainder.

### Global test

The first test, allows to answer the question: “is our set of regressors accounting well for the signal variations at the voxel considered?”. It is called “effect of interest” in the SPM language. The constant regressors being excluded, we test for the null hypothesis:

$$(H_0) : \beta_1^s = 0 \text{ and } \beta_2^s = 0 \quad \forall s \in S = \{wc, wa, re, rc\}$$

where  $wc$ ,  $wa$  and  $re$ ,  $rc$  are respectively notations for *wedge clockwise* or *anti-clockwise* and *ring expansion* or *contraction*. The null hypothesis ( $H_0$ ) is equivalent to the nullity of  $\|c_v(k_0)\|$ , implying that no signal contains any significant energy at the fundamental frequency of the stimulus.

The alternative hypothesis is:

$$(\overline{H_0}) : \exists (i, s) \in \{1, 2\} \times S \quad / \quad \beta_i^s \neq 0$$

meaning that our model “explains” at least a significant part of the signal, or from a frequential point of view, that a significant part of the signal contains energy at the stimulation fundamental frequency.

To be able to perform a statistical test, we need an additional assumption on the  $\beta_i^s$ : they are supposed to follow a Gaussian law  $\mathcal{N}(0, \sigma')$ . They are therefore all independent (as they come from Fourier decompositions) and Gaussian. Then:

$$\sum_{i=1}^2 \sum_{s \in S} (\beta_i^s)^2 \rightsquigarrow (\sigma')^2 \chi^2(8)$$

The global model residuals variance is estimated with the sum of the residuals divided by their degrees of freedom. By assumption,  $\epsilon_t \rightsquigarrow \mathcal{N}(0, \sigma)$  and are independent, we then have:

$$\frac{1}{T-q} \sum_{t=0}^{T-1} \epsilon_t^2 = \frac{\mathcal{E}^\top \mathcal{E}}{T-q} \rightsquigarrow \sigma^2 \frac{\chi_{T-q}^2}{T-q}$$

where  $T-q$  is the number of degrees of freedom remaining in  $\epsilon$ . Here,  $q = 12$  (the eight  $\beta_i^s$  plus the four constant regressors).

The respective variances of the residuals and the  $\beta_i^s$  are identical ( $\sigma = \sigma'$ ), as they correspond to the global variance of the signal  $Y_v$ . Moreover, the residuals and the  $\beta$  are independent thanks to the Fourier decomposition of the signal (equation 5.1).

The statistical test thus relies on:

$$\hat{F} = \frac{\frac{1}{8} \sum_{i=1}^2 \sum_{s \in S} (\beta_i^s)^2}{\frac{\mathcal{E}^\top \mathcal{E}}{T-12}} \rightsquigarrow \mathcal{F}(8, T-12)$$

where  $\mathcal{F}(x, y)$  is the Fisher law with  $x$  and  $y$  degrees of freedom. This ratio is estimated and then compared to the p-value  $f$  of the corresponding Fisher law<sup>4</sup> at each voxel. We typically take  $p = 10e^{-3}$ . Any voxel verifying  $\hat{F} > f$  (unilateral right test) does not follow ( $H_0$ ), so its signal is partly explained by our model. Such a voxel will be part of the “effect of interest” mask.

### Specific tests

The other contrast we defined can be considered as more specific in the sense that it is linked to only one family of stimulus (*wedge* or *ring*). It allows to test one of the two assumptions:

$$(H_1^w) : \beta_1^{wc} = 0 \text{ and } \beta_2^{wc} = 0 \text{ and } \beta_1^{wa} = 0 \text{ and } \beta_2^{wa} = 0$$

or

$$(H_1^r) : \beta_1^{re} = 0 \text{ and } \beta_2^{re} = 0 \text{ and } \beta_1^{rc} = 0 \text{ and } \beta_2^{rc} = 0$$

The corresponding statistical tests are derived as before, leading to a  $\mathcal{F}(4, T-6)$  law. Specific “wedge” and “ring” masks can thus be derived. This specific test

---

<sup>4</sup>It shall be noted that the way SPM computes the degrees of freedom is slightly more complicated because it takes into account the high-pass and low pass filtering applied by SPM; this leads to non integer values for these degrees of freedom, but the used here is sufficient, the threshold values computed being very close to the theoretical values.

allows to check if the respective model of each type of stimulus explains well the observed signal, or can also be used when only one stimulus type is used. Figure 5.8 presents typical  $\hat{F}$  values of a specific test for the *wedge* stimulus.

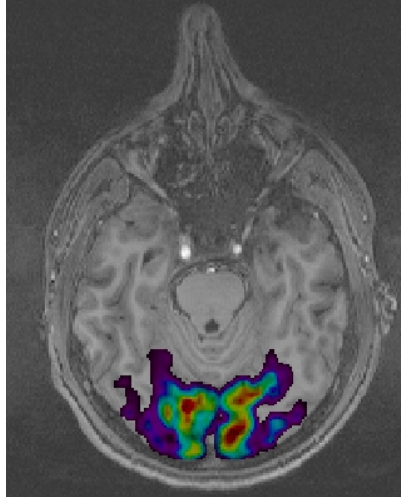


Figure 5.8: An axial slice of the values of the statistics  $\hat{F}$  for the *wedge* stimulus. The values under the theoretical p-value computed for  $p = 0.001$  are discarded. The colored voxels are those considered as activated and kept in the analysis.

Globally, even when we acquire both polar angle and eccentricity data, we prefer to analyze our results with each specific mask separately, as the two families of stimuli can be viewed as independent. We however considered the global mask as neurons activated by one family of stimulus (e.g. the "wedge") should also be activated by the other (e.g. the "ring"), the portion of the visual field globally covered by both stimuli being strictly identical. The difference in the final activated voxel masks derived either from a global or two specific tests has shown to be negligible in practice.

We wrote a series of scripts ("batches" in the SPM99 vocabulary) to automate this computing steps using SPM99, since defining the model by hand is time consuming and repetitive when analyzing many datasets. Those scripts define the model and the contrasts leading to our F-test, then call the appropriate SPM99 function used for the regression step and the statistics estimation. Note that the temporal filtering parameters are also driven with this script and applied before the model parameters estimation. Various parameters can be easily changed to fit, among others, with the session's duration, the stimulus fundamental frequency, the TR duration, etc.

### 5.1.5 Angular values computation

The last step in the analysis of retinotopic data consists in recovering the phase of the signal for each voxel included in the statistical mask computed previously. The latter is linked to the stimulus position that induced the voxel's response.

According to our paradigm and the construction of our model, this would be relatively straightforward without the hemodynamic filtering. Indeed, as seen previously,  $\phi = \arctan(\frac{\beta_2}{\beta_1})$  is an estimator of the signal phase, corresponding to a unique stimulus position in the visual field. But the response we are faced with is filtered and delayed by the hemodynamic response, making the underlying position estimation more difficult. Taking advantage of the two directions of rotation for each family of stimulus nonetheless allows to estimate, *for each voxel*, this hemodynamic delay.

Let us consider a given supra-threshold voxel  $v$ , and define the following notations:

- $\theta^+$  (respectively  $\theta^-$ ) is the *angle* coding for the position of the stimulus rotating positively (resp. negatively) in the visual field.
- $\phi^+$  (resp.  $\phi^-$ ) is the periodic signal estimated *phase* for the stimulus in positive (resp. negative) rotation.
- $\tau^+$  (resp.  $\tau^-$ ) is the “expected” signal phase, i.e. the delay of the neuronal response (close to zero at our temporal scale), linked with the position  $\theta^+$  (resp.  $\theta^-$ ) of the stimulus by the relation  $\theta^+ = \tau^+\omega_0$  (resp.  $\theta^- = \tau^-\omega_0$ ) where  $\omega_0$  is the stimulus pulsation. We have the relation  $\tau^+ = 2\pi - \tau^-$ .
- $t_h$  is a delay in the recorded BOLD response, i.e. the hemodynamic delay at the voxel  $v$  plus the acquisition delay linked to the corresponding slice in the volume. We assume that this delay is identical for the two directions of rotations of the same stimulus, which appears to be reasonable<sup>5</sup>. Similarly, this delay could also comprise some physiological aspects as lateral propagation effects which could reasonably be assumed to be identical in both directions of rotation.

---

<sup>5</sup>Note that this assumption is valid concerning the slice acquisition delay because our stimulus time course is precisely synchronized with the volume's acquisition, making each slice acquired with the same delay with respect to the stimulus change of position in both directions of rotation.

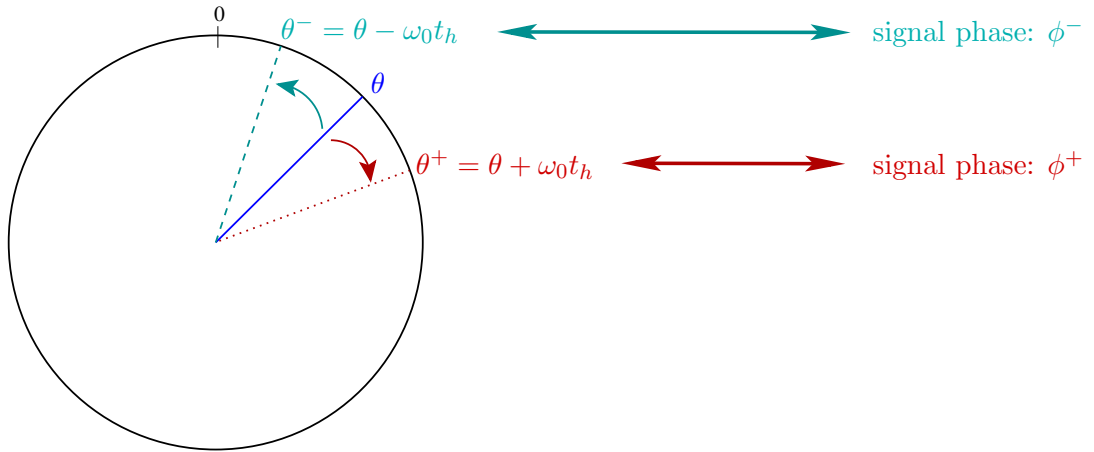


Figure 5.9: Description of the stimulus positions in the visual field linked to the periodic signal measured phases. This sketch refers to the *wedge* stimulus. The red and green color correspond to a positive and negative rotation respectively.  $\theta$  is the *angle* corresponding to the stimulus position in the visual field inducing a simulation of the neurons included in the voxel considered,  $t_h$  is mainly due to the hemodynamic delay of this voxel,  $\omega_0$  the stimulus pulsation. The conjunction of the estimated *phases* in the periodical signals,  $\phi^+$  and  $\phi^-$ , allows to evaluate the values of  $\theta$  and  $t_h$ .

We thus have :

$$\begin{aligned}\phi^+ &= \tau^+ + t_h \\ &= \frac{\theta^+}{\omega_0} + t_h\end{aligned}$$

$$\begin{aligned}\phi^- &= \tau^- + t_h \\ &= 2\pi - \tau^+ + t_h \\ &= 2\pi - \frac{\theta^-}{\omega_0} + t_h\end{aligned}$$

We can remove the term  $2\pi$ , useless here as our results will in fine be defined modulo  $2\pi$ . It leads to:

$$t_h = \frac{\phi^+ + \phi^-}{2} \quad (5.5)$$

$$\theta^+ = \frac{\omega_0(\tau^+ - \tau^-)}{2} \quad (5.6)$$

The hemodynamic delay is defined modulo  $\pi$  by equation (5.5), but the ambiguity is removed by the fact that the stimulus frequency is chosen low enough to allow the hemodynamic delay value to be, expressed in terms of stimulus position angle, between 0 and  $\pi$  (modulo  $2\pi$ ).

At the end of this step, we are thus able to evaluate at each voxel concerned by our stimulus the value of the angle (thus the underlying position) of the stimulus giving rise to its activity.

As for the statistical model definition and the estimation of parameters, this

phase estimation step was automated using a Matlab program. It leans on the SPM interface to select the images (i.e. the  $\beta$  images and the F-values image).

### 5.1.6 Angle maps analysis

We can now analyze the angular maps obtained through the functional processing and the statistical analysis described above. In the following paragraphs, after a first rapid verification of the results, we discuss the qualitative aspects of our visual field maps and compare our results to the literature. We also study the polar angle maps we obtained while varying some stimulus parameters, leading to an optimal stimulation paradigm. Finally, we address both the intra- and inter-subject reproducibility of our approach.

#### First verification

The first point to address is whether the angle values found are properly located according to anatomo-functional a priori knowledge. As mentioned in paragraph 5.1.1, the eccentricity maps around the calcarine fissure should show increasing values from the occipital pole to more anterior brain regions, while polar angle maps should reveal the visual field splitting, each hemifield projecting on the contralateral hemisphere. We also check for both angular maps smoothness along the cortical surface. This rough verification can be performed on 2D slices showing the angular maps overlaid on the subject anatomical image, as illustrated in figure 5.10.

A more appropriate way to assess the results is to render the eccentricity and the polar angle maps on the subject's cortical surfaces, using the construction of cortical geometry models with methods detailed in chapter 3. From these surfacical maps, we can also address some debated issues regarding the organization of human occipital visual field maps.

#### Eccentricity maps

**General results** The ring stimulus is used to get the phase-encoded eccentricity map, mapping the cortical responses to a ring located at various eccentricities. Our stimulus extends radially up to a maximum of 9.75 degrees of visual angle.

As a general qualitative result, we find, for every subject tested, the classical pattern in which a large foveal representation lies at the occipital poles around the calcarine fissure and as eccentricity increases, the corresponding representations appear more anterior and medial.

In [237], Wade and colleagues reported an isolated foveal representation ventrally and anteriorly to the V1/V2v/V3v areas. We confirm the presence of this foveal representation in our maps for every hemispheres analyzed. In the dorsal surface,

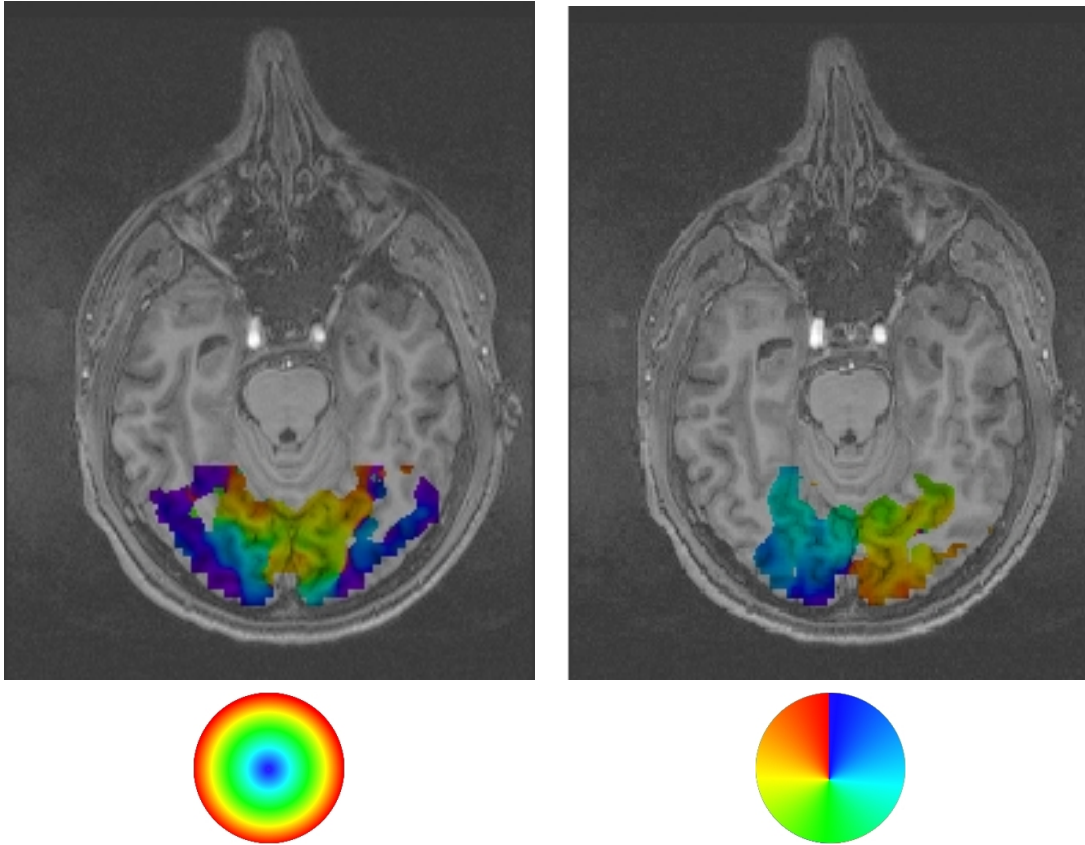


Figure 5.10: Eccentricity (left) and polar angle (right) maps obtained for a given subject, overlaid on an axial slice of the anatomical image. Both maps appear reasonably smooth along the cortical surface of the occipital lobe. Furthermore, well-known global properties of human retinotopic maps are verified: the angles corresponding to low eccentricity values (foveal) are close to the occipital lobe, and we move further anteriorly as the eccentricity increases; in the polar angle map, each visual hemifield projects respectively to the contralateral hemisphere.

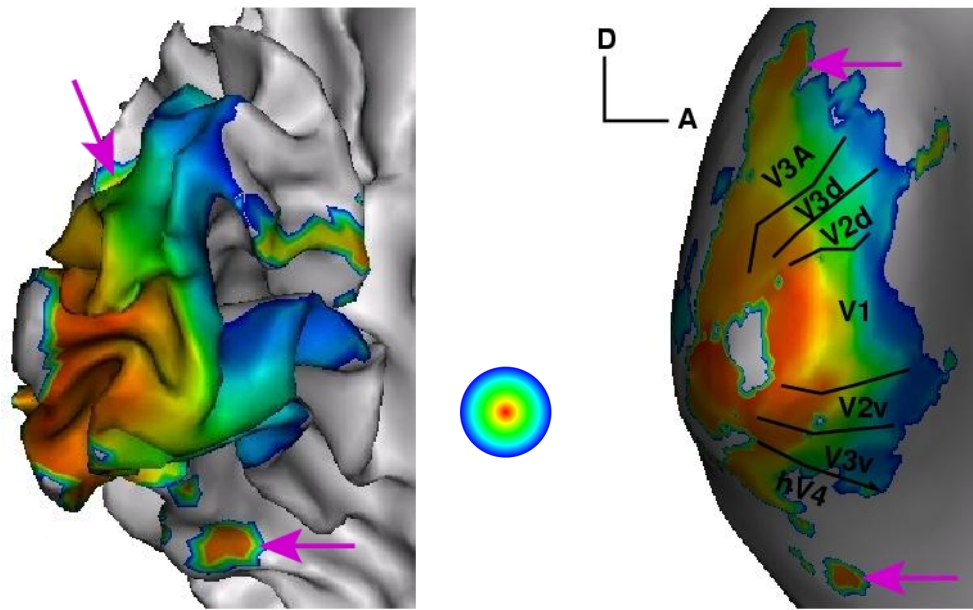


Figure 5.11: Example of the eccentricity map in a medial view of the left occipital lobe of subject JK. The left figure shows the original surface and the right one an inflated view. We can clearly see the isolated ventral foveal activation reported by Wade et al. (lower arrow) [237], located ventrally beyond the V1-V2v-V3v confluent foveal region. The areas borders are defined using the subject's polar angle map (see below). The upper arrow designate a dorsal foveal representation lying clearly beyond V3d. The color gradient going to blue at the border of the map does not correspond to an angular representation but is actually an Open GL interpolation that cannot be removed under the current version of the Anatomist visualization software.

extending from the posterior portion of the intraparietal sulcus, the same group also reported two distinct foveal representations [177]. We can observe a clear foveal activation in some subjects but can not reliably distinguish two distinct representations. Figure 5.11 shows an eccentricity map overlaid on the subject's left hemisphere, where both a ventral and a dorsal activations to low eccentricities are found.

**Foveal sensitivity** The eccentricity maps on the cortical surface are smooth and qualitatively match what we expected to see from other studies. However, the extreme occipital pole is not fully covered of angular values, whereas we can expect here a foveal representation. We wondered if the periodic stimulation paradigm used was sensitive enough to foveal stimulus position. To answer this question, we tested in one subject a classical block design to contrast a 5 degrees eccentricity stimulation with a uniform grey field fixation (see figure 5.12). Each condition was presented 10 times, each block lasting 8 TR (or 16,888 s).

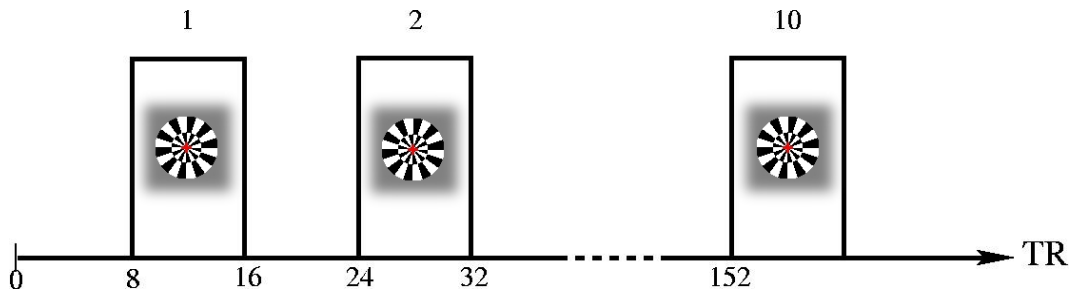


Figure 5.12: The block design used to map the foveal representations in the occipital cortex. Between two foveal stimulation blocks, the baseline condition is a uniform mid-grey field with the red fixation cross.

The analysis was performed classically with a linear regression of the box car function representing the stimulation (1 during foveal presentation, 0 otherwise) convoluted with a classical hemodynamic response model from SPM. No spatial smoothing was performed on the data, to prevent any blurring effect. We show in figure 5.13 the comparison between the t-map drawn from this block design experiment thresholded at  $p < 0.001$  uncorrected and the angular values computed from 4 cycles (contracting and expanding) of the ring stimulus. We compared directly the results in slices of the 3D volume to avoid any mismatch that could arise from the cortical surface extraction or the projection of the functional data onto it. The comparison is presented here for a single axial slice, but the result is qualitatively equivalent for any slice of the volume: there is a strong overlap between any value in the eccentricity map coding for a foveal ring position and supra-threshold t-values from the block design foveal stimulation. This is in particular the case in the ventral foveal representation, located ventrally beyond area V3v, as already mentioned above. At the very pole of the occipital lobe, we do not find any significant t-value with our block paradigm, consistent with our eccentricity maps. This lack of signal at this precise anatomical location is also found in most figures of the literature showing eccentricity maps, though this point is generally not addressed. It is nonetheless quickly discussed in a footnote in [192]. One reason could be small eye movements can affect the signal to noise ratio in the macula, where the receptive fields size is smallest. Another source for this missing signal may be attributed to echo-planar geometric distortions inducing a compression in the occipital pole. For technical reasons, we could not record the appropriate field maps to estimate and correct these distortions. Finally, a lack of power in the measurements and the different analysis processes could also explain this missing “center of gaze” representation.

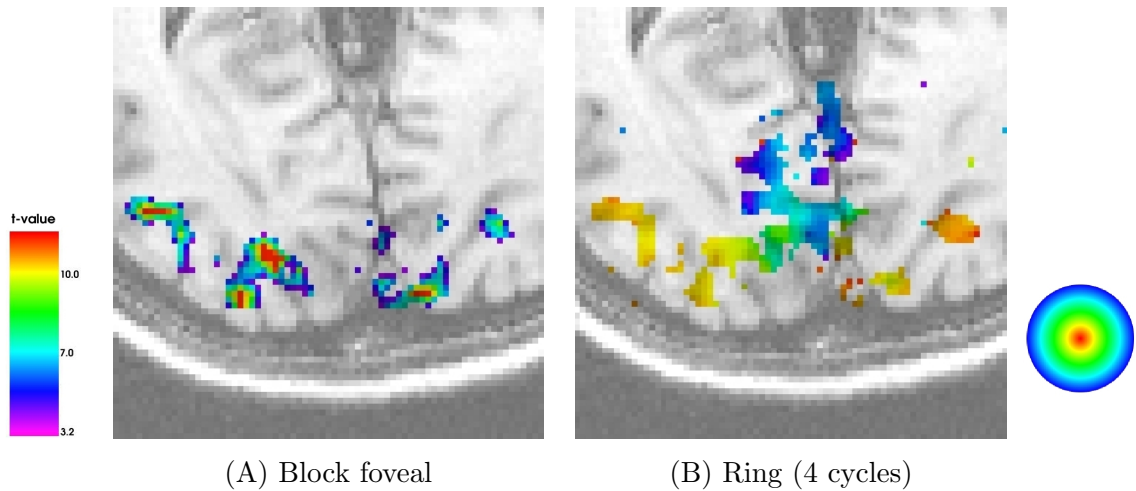


Figure 5.13: Comparison between (A) the t-map, contrasting foveal stimulation blocks versus uniform grey field fixation blocks (3.2 is the t-value for  $p=0.001$  uncorrected) and (B) the eccentricity map derived from the 4 cycles ring stimulus, in an axial slice. The t values above the statistical threshold in (A) systematically match the low angular values in (B).

### Polar angle maps

**General results** Stimulating a subject using the wedge stimulus allows to get his polar angle map, mapping the cortical activity implied by a cone located at different positions around the center of gaze. From previous neurophysiological studies, it appears that the boundaries of early retinotopically organized visual areas are defined by reversals in the representation of the polar angle. This stimulus is thus sufficient to segment the first retinotopic visual areas.

As for the eccentricity maps, the general pattern of representation of the visual field on the cortical surface is smooth, accordingly to the basic principles of the retinotopy. Based on the literature agreements, we can reliably identify areas V1, V2v, V2d, V3v, V3d and V3A in every subject scanned. Figure 5.14 shows the polar angle patterns generally found in human fMRI retinotopic mapping reports overlaid both on the original and an inflated version of the GM/WM interface.

**Wedge stimulation optimization** We tested different conditions for the wedge stimulus in order to optimize our stimulation process. Following [239, 200], we tried a bifield wedge stimulus instead of the unifield wedge, for two main reasons:

- the stimulus being symmetrical with respect to the fixation point, the subject would be helped maintaining its gaze in the center of the display,
- the stimulation could run up to twice quicker.

The main drawback of  $n$ -wedges stimulus ( $n \geq 2$  being the number of simultaneous

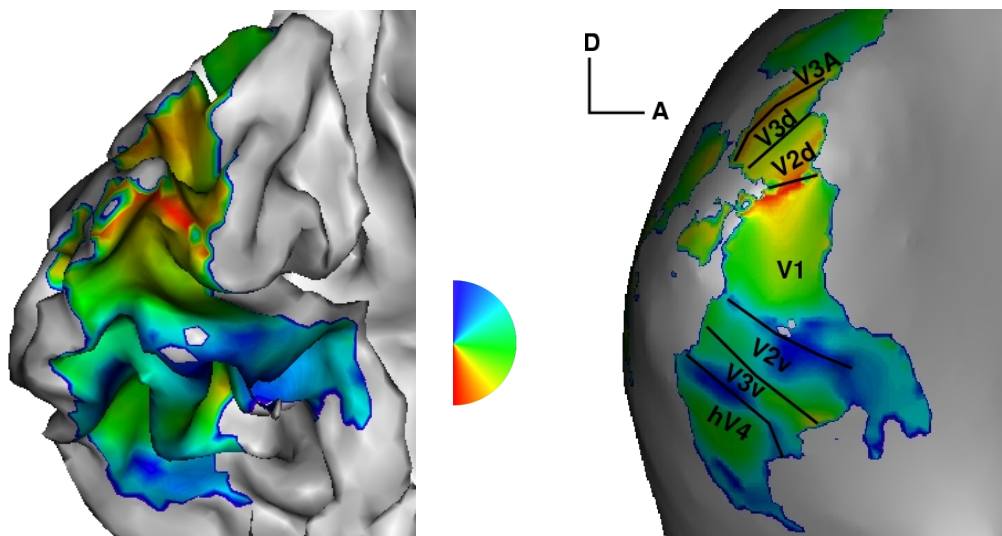


Figure 5.14: Polar angle map overlaid on subject's left hemisphere either folded (left) or inflated (right). We find the general angular values pattern all investigators are agreed upon in the literature for areas V1, V2v, V2d, V3v, V3d and V3A. The boundaries between the above mentioned areas are manually drawn.

sectors) stems from the more difficult signal phase interpretation than in the unifold wedge case. Indeed, with multiple wedges stimuli, the analysis globally remains the same, but the results show a phase ambiguity: a given value of the BOLD response phase corresponds to  $n$  locations in the visual field. When  $n = 2$ , the prior knowledge about the hemisphere/hemifield specialization implies this ambiguity only appears for the vertical positions, other positions being uniquely defined in each hemifield, thus in each hemisphere. The vertical position can then be disambiguated taking into account the expected local smoothness of the maps. An alternative was proposed in [200] in which the authors proposed to split vertically the bifield wedge stimulus while it spans the vertical meridian to avoid this phase ambiguity (see their figure 1). For  $n \geq 3$ , the phase ambiguity becomes more problematic and a priori knowledge may not be sufficient to resolve the latter. We tested a bifield wedge stimulation in comparison to the classical unifold wedge, also varying the spatial extent of the sectors (see figure 5.15) and the rotation velocity for the bifield stimulus.

### Different velocities

We first compared on 3 subjects the final maps obtained with (i) the classical 80 degree unifold wedge, (ii) a 40 degree bifield wedge and (iii) a 80 degree bifield wedge, as illustrated in figure 5.15.

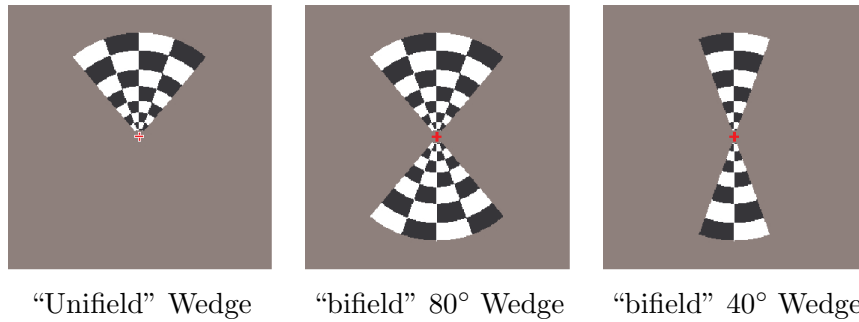


Figure 5.15: The different wedge stimuli tested.

In the 6 hemispheres we analyzed, we observed a lower signal in both bifield wedges conditions, leading to less supra-threshold voxels (see table 5.1) and therefore less comprehensive maps than the unifield wedge as illustrated in figure 5.16.

Subject	Unifield 80°	Bifield 40°	Bifield 80°
CG	31106	19287	20195
GR	50473	23282	21711
SR	49154	25774	24683

Table 5.1: Number of supra-threshold voxels ( $p=10e^{-3}$  uncorrected) for different stimulus pattern rotating at different velocities, the bifield wedges stimuli rotating twice quicker than the unifield wedge.

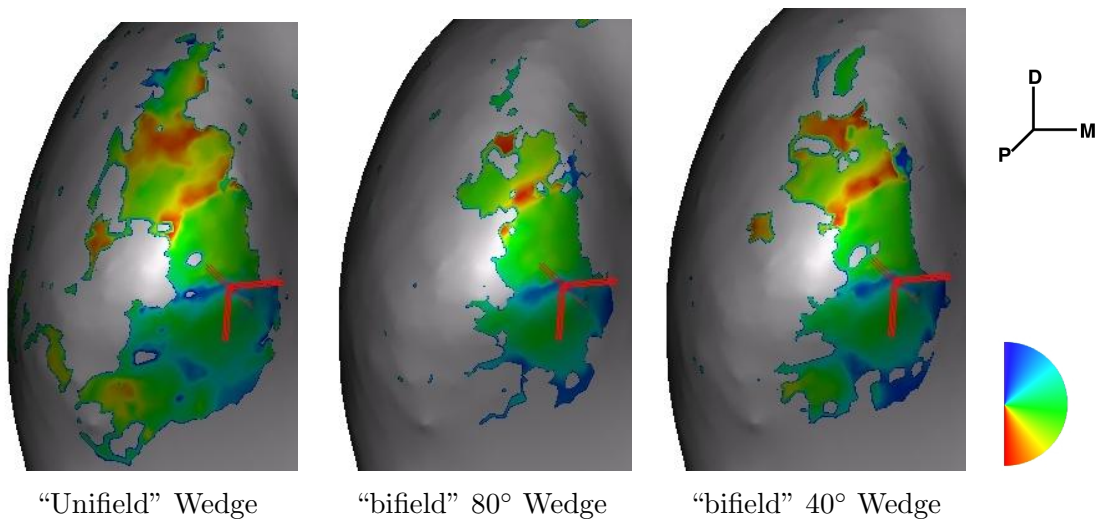


Figure 5.16: Comparison of polar angle maps projected on the inflated left hemisphere with respect to different stimulations (subject CG). The unifield stimulus clearly leads to more signal, thus angular values, than the bifield, rotating at twice the unifield wedge velocity.

These results might appear in contradiction with the study of Slotnick and Yantis [200] at first sight, but having a closer look at their figure 3 suggests a comparable signal loss with the bifield wedge as compared to the unifield wedge. The rotation velocity, which for the bifield wedges was twice that of the unifield wedge, might account for this important signal loss. Indeed, if the stimulation frequency is too high, the low pass filter of the hemodynamic response affects these high frequencies, including the fundamental stimulation frequency, in many voxels. Moreover, the higher quality achieved with the 40 degree bifield wedge than with the 80 degree also probably comes from the hemodynamic response low-pass filter, preventing the signal to return to its baseline between two consecutive stimulations with the larger wedge. This phenomenon is supposed to occur twice as much with the 80 degree wedge than with the 40 degree.

### Same velocity

To strictly isolate the bifield versus the unifield wedge comparison, we performed a subsequent experiment on 3 different subjects, using the same rotation velocity for each stimulus. Maps qualitatively look much closer to each other in this comparison than in the previous one. However, the amount of supra-threshold voxels is still higher for the unifield stimulus (see table 5.2). Figure 5.17 shows a qualitative comparison on a representative hemisphere.

Subject	Unifield 80°	Bifield 40°	Bifield 80°
LQ	60902	46151	42570
CV	45197	37310	34494
IH	64413	51070	42671

Table 5.2: Number of supra-threshold voxels ( $p=10e^{-3}$  uncorrected) for different stimulus pattern rotating at the same velocity.

Eye movements could be a reason responsible for this difference between unifield and bifield wedge maps. Eye movements are indeed twice more likely to lead to unexpected stimulation with the bifield than with the unifield stimulus. The resulting signal is thus more likely to be inconsistent with respect to the stimulus frequency and consequently considered as noise. However, as we were not yet able to measure eye movements during the experiments, we could not quantitatively confirm this assumption.

As a result of these multiple comparisons with the wedge stimulus, the unifield wedge with a rotation frequency of 1/38 Hz was kept for its higher accuracy.

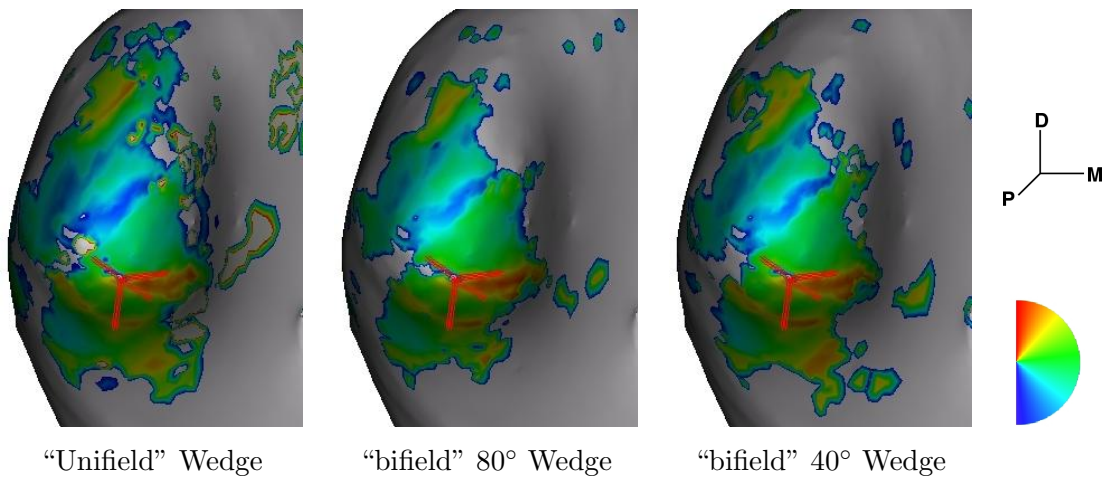


Figure 5.17: Comparison of polar angle maps projected on an inflated left hemisphere with respect to different stimulations. The unifield stimulus leads to more activations than the bifield, even if rotating at the same velocity (subject LQ).

### 5.1.7 Mapping reproducibility

Beyond the confrontation of our maps with the results from other labs, one way to assess the robustness of our retinotopic mapping procedure is to study its reproducibility for different subjects (inter-subjects reproducibility) but also for a single subject in different scanning sessions (intra-subject reproducibility).

#### Inter-subjects reproducibility

As already discussed in paragraph 5.1.6, our maps show a high agreement across subjects, as we globally find the same patterns of angular values representations, at least in the systematically mapped cortical region comprising V1, V2v, V2d, V3v, V3d and V3A.

#### Intra-subject reproducibility

**Intra-session** The stimulus optimization previously detailed allows us to check for the reproducibility of the polar angle map in a given subject within the same scanning session. Figures 5.16 and 5.17 illustrate this intra-session reproducibility of a given subject, using different stimulus parameters. The red crosses are linked for each image, showing the high quality alignment of area borders (here the lower boundary of V1) found in each map. The differences in the maps result mainly in a lack of significant signal at some voxels. This is to be mainly linked with the changes in stimulation as discussed in the previous paragraph.

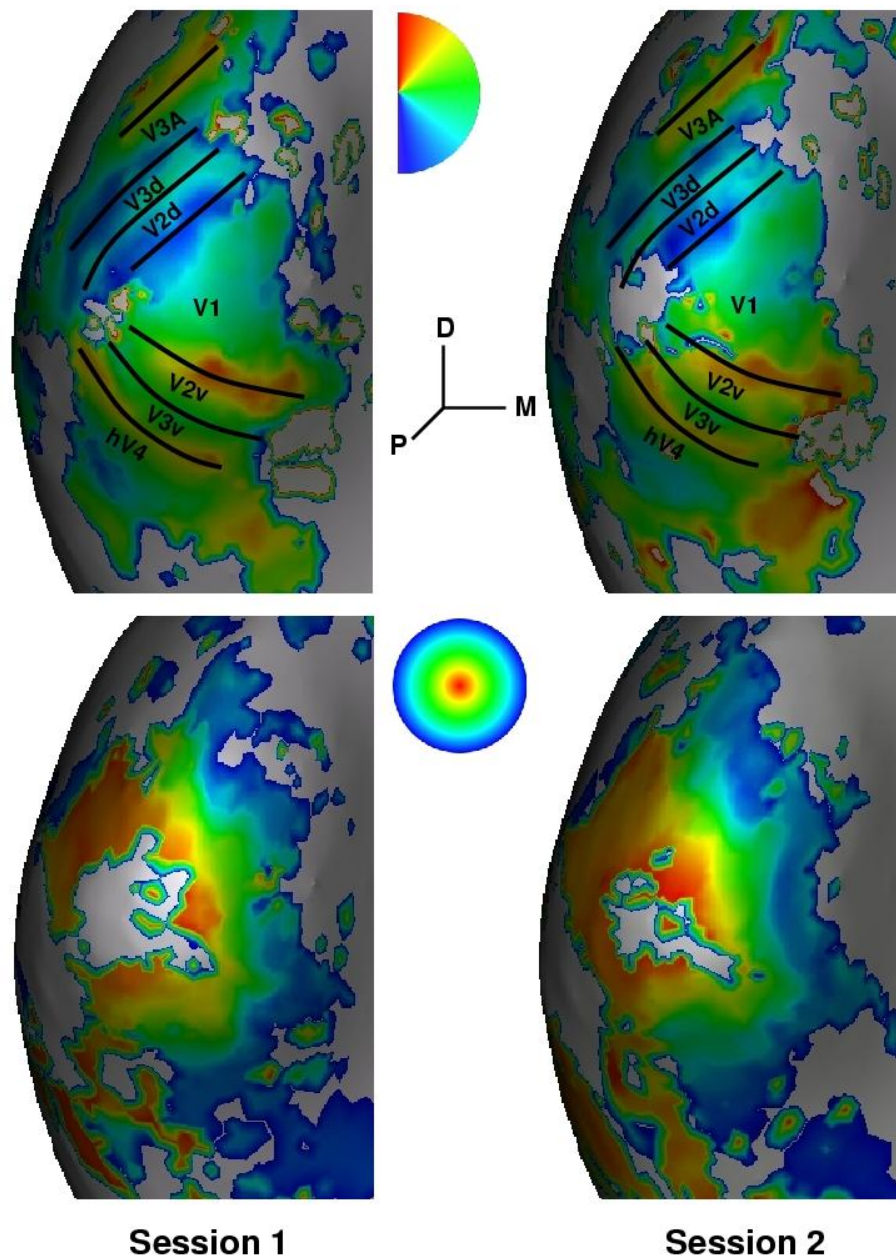


Figure 5.18: Intra-subject inter-sessions reproducibility (subject LQ). The data from session 2 were realigned in session 1 coordinate system using the anatomical images coregistration transformation. The maps are qualitatively identical, showing the high reproducibility of the whole procedure. Specifically, the areas borders based on the polar angle map from session 1, depicted by the black lines in the top images, fit accurately the polar angle map derived from session 2 data.

**Inter-session** The reproducibility of the maps derived from a given subject through different scanning sessions was also assessed for two different subjects. The results for one of them are shown in figure 5.18. The different maps are computed independently for each session. The realignment between different structural T1 images acquired at each session is done using the standard SPM2 coregistration algorithm, registering each session anatomical scan on that of an arbitrary chosen reference session. The transformations estimated are then applied to the respective functional images and the preprocessing and analysis are applied independently to each functional dataset. Resulting independent phase maps are finally displayed on the inflated mesh of the GM/WM interface extracted from the reference session anatomical scan. Both eccentricities and polar angle maps show a strong overlapping as well as the areas segmentation that can be obtained from these maps. This inter-session reproducibility was found in both hemispheres of the two subjects analyzed. These results prove the high intra-subject and inter-session reproducibility of the whole procedure implemented.

### 5.1.8 Mapping efficiency

Following the validation of our method, we now compare our approach with the literature, first in terms of the overall experiment duration and second regarding cutting edge issues about the cortical visual field representations.

#### Experiment duration

Our initial goal was to accurately identify the low-level retinotopic areas within a minimum scanning duration. The experimental and image analysis procedure we have designed allows to precisely map the occipital visual field representations consensually reported in the literature based on a 15 minutes functional scanning experiment. This rapid method compares favorably to the different procedures reported in the literature, as summarized in table 5.3. Note that although Slotnik and Yantis claim a very low duration of just over 4min, they do not perform eccentricity maps measurements and only use a single rotation direction for the polar angle stimulus. The latter point, also explicitly notified in [49, 62, 39], implies the use of a constant hemodynamic response delay over the voxels, which might significantly bias the resulting phase map. Considering similar limitations, our procedure is actually comparable to that of Slotnik and Yantis as we require 5mn30s to acquire a complete set of the wedge rotating in a single direction and globally faster than the other groups. As we already mentioned above, this rapid acquisition might explain the lower signal obtained dorsally and ventrally.

Reference	#Cycles /run	Averaging	Eccentricity mapping	Polar Angle mapping
Sereno et al. [192]	n.s.	n.s.	n.s.	n.s.
DeYoe et al. [49]	n.s.	2-4	n.s.	n.s.
Engel et al. [62]	4-6	n.s.	n.s.	n.s.
Tootell et al. [222, 95]	n.s.	4-12	4-12x8mn32s ≈20mn-1hr	4-12x8mn32s ≈20mn-1hr
Smith et al. [203]	4	2	4x216sec≈14mn	4x216sec≈14mn
Wade et al. [237]	6-8	2-4	n.s.	n.s.
Warnking et al. [240]	14	none	2x7mn16≈14mn30s	2x7mn16≈14mn30s
Dumoulin et al. [57]	10	3-4	3-4x6.5mn≈22mn	3-4x6.5mn≈22mn
Slotnik et al. [200]	6	none	none	4mn30
Conner et al. [39]	8	2	2x8mn32≈17mn	2x8mn32≈17mn
Brewer et al. [15]	25	n.s.	25x24sec≈10mn	25x24sec≈10mn
Our method	4-8	none	2x2mn32s≈5mn	2x5mn04s≈10mn

Table 5.3: Comparison of the retinotopic mapping methods reported in the literature with respect to the number of complete cycles by run, the number of identical runs averaged and the functional images acquisition duration for each phase map type. "n.s."=non specified

### Beyond the “great agreement zone”

Beyond V3A dorsally and V3v ventrally, maps and conclusions are getting less consensual in the human fMRI retinotopic mapping literature.

#### *Dorsal maps*

In the dorsal occipital region, another quarterfield representation labeled V3B was reported by Smith et al. [202]. Regarding its location, it was suggested to be similar to area KO previously identified by Van Oostende et al. [233] on the basis of strong responses to kinetic boundaries. A complete hemifield representation was afterwards reported by Wandell’s group in [177] at the same location (following Smith and colleagues, they labeled it V3B). Tootell’s group also reported in [217] and [216] another area abutting dorsally the V3A/V3B region, labeled V7 and supporting an upper quarter-field representation. Yet, Press et al. later reported in [177] a complete hemifield representation in this area V7.

Our results in this portion of the cortical surface are less reproducible from subject to subject and often lack signal, probably because we reach the accuracy of our method which performs retinotopic map acquisitions too fast to provide enough signal (only 8 complete cycles for each rotation direction of the wedge, without any additional averaging of runs). These issues should be resolved with a more

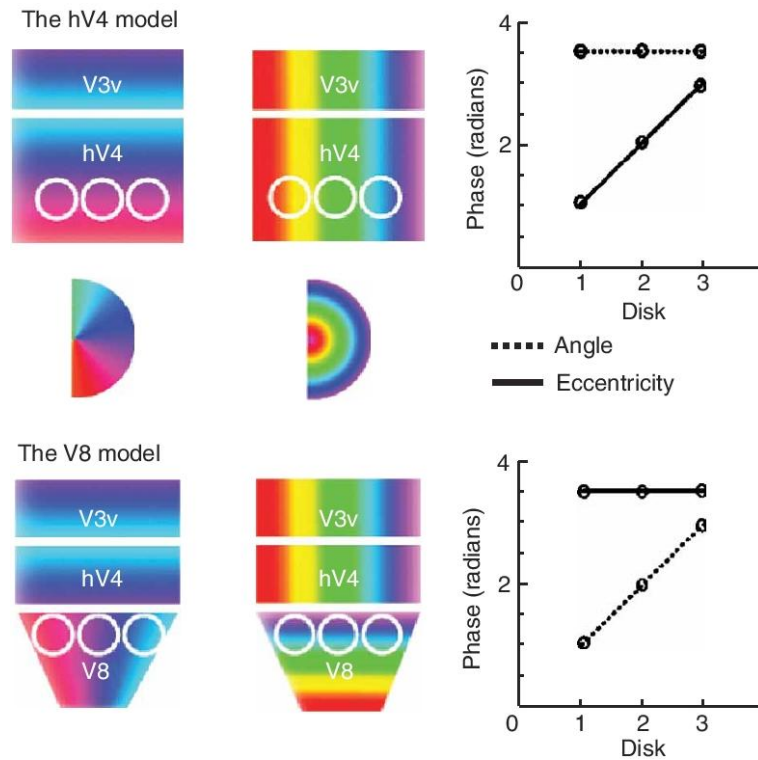


Figure 5.19: Concurrent scenarii for the ventral occipital visual field maps beyond V3v. The hV4 model proposed by Wandell’s group assigns a complete hemifield representation parallel to V3v upper vertical meridian representation. On the other hand, the V8 model proposed by Tootell’s group suggests a parallel quarterfield representation labeled V4v followed by perpendicular complete hemifield representation labeled V8. The values from the white circles show the expected polar angle and eccentricity values close to V3v ventral border by both models. Figures are adapted and modified from [15].

sensitive data acquisition (for instance using a surface coil), with more cycles in the stimulus presentation or an averaging of signals across different acquisition sessions and maybe with further improvements in the data processing.

### *Ventral maps*

Moving ventrally beyond V3v, we also find some retinotopic signal, but the visual field representation and the labeling is once again not in agreement here. Hadjikhani et al. reported in [95] a quarterfield representation, labeled V4v, followed by a complete representation they called V8 (supposed to be a color sensitive area). But the authors only show one dataset with a V8 fovea, whereas later publications from this group (see for instance [222]) show retinotopic maps not always consistent with this interpretation. On the other hand, Brewer et al. recently reported in [15] three complete hemifield representations located ventrally to the vertical meridian representation of area V3v. Figure 5.19 summarizes the concurrent labeling in the

ventral occipital cortex.

According to our data, our conclusions are closer to those from Wandell's group, as shown in figure 5.20. In particular, the V8 assumption seems invalidated by the absence of foveal representation for each polar angle values in this portion of cortex beyond V3v. But similarly to the dorsal occipital region, more reliable signal is required in this ventral region of the occipital cortex to draw a solid conclusion and to confirm or infirm the VO model further suggested by Wandell's group. For instance, finer measurements should be obtained using more specific stimuli patterns such as chromatic contrast, as high selectivity to color stimuli was reported in this part of the visual cortex [148, 237].

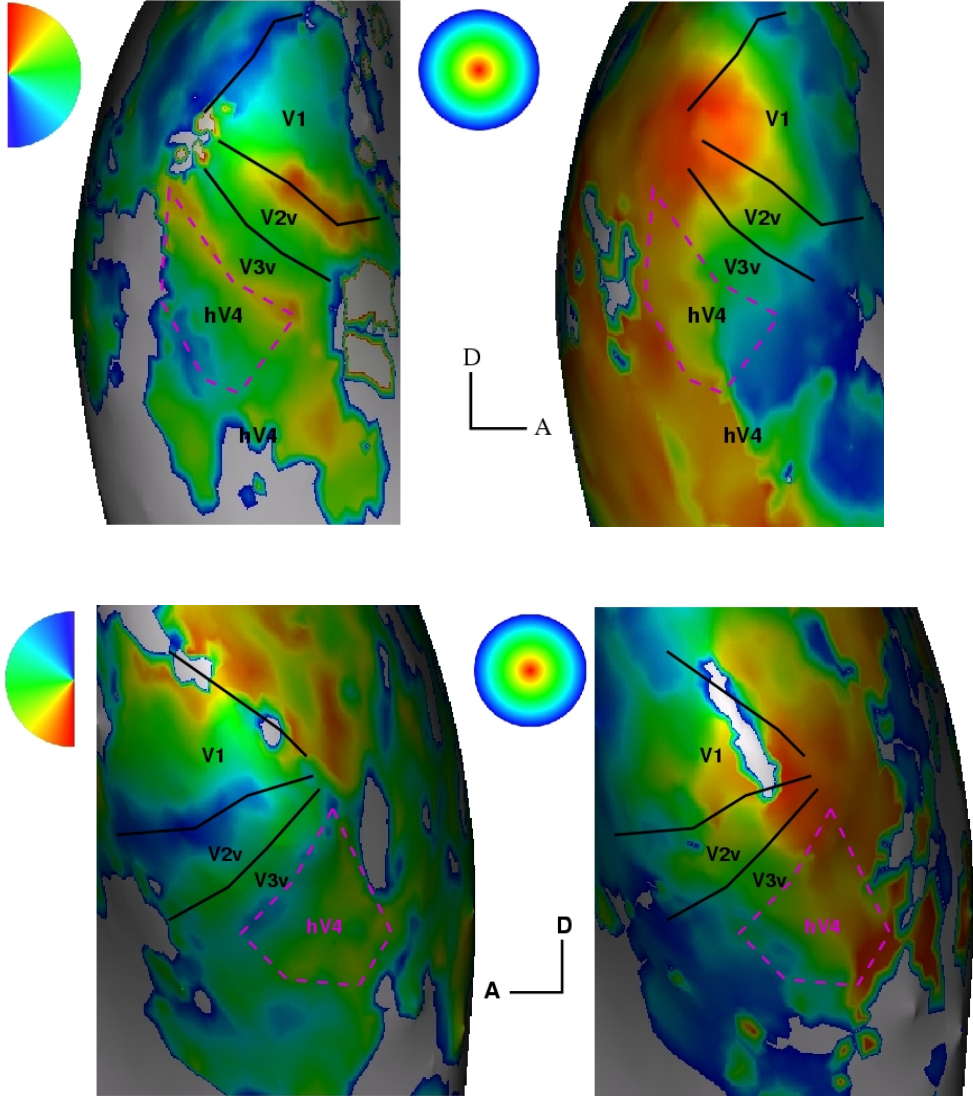


Figure 5.20: Example of hV4 polar angle and eccentricity maps (subject LQ). These results are consistent with a complete hemifield representation beyond V3v.

### 5.1.9 Area delineation

Beyond the characterization of the visual field representations over the cortical surface, the retinotopic mapping allows to delineate the different retinotopic areas revealed. One can then extract the subset of cortical voxels corresponding to each area identified, thereby building coherent Regions Of Interest (ROIs) that can be used in subsequent analysis. We first present below the Visual Field Sign method tested on our data and then quickly describe a manual procedure we can alternatively use to properly delineate the visual areas.

#### Visual Field Sign maps

In [193], Sereno et al. introduced an automatic method combining the eccentricity and polar angle maps to construct the Visual Field Sign (VFS) map, allowing a direct delineation of the retinotopic cortical areas from electro-physiological data. The technique was then applied to fMRI retinotopic maps in [192] and [239], and further implemented in a volumetric fashion in Dumoulin et al. [57].

The Visual Field Sign is built to indicate the orientation of the representation of the visual field, either mirror or non-mirror, on the cortical surface. It is given by:

$$VFS = \text{sign}(\det(\partial\psi))$$

where  $\psi : (x, y) \in \mathbb{R}^2 \mapsto (\rho, \theta) \in \mathbb{R}^+ \times [-\pi; \pi[$  is the function mapping, for each point  $(x, y)$  on the cortical surface, its preferred position  $(\rho, \theta)$  in the visual field, as illustrated in figure 5.21.

The VFS computation therefore involves the local gradients of the eccentricity (noted  $\vec{\nabla}\rho$ ) and the polar angle (noted  $\vec{\nabla}\theta$ ) maps, leading to the equivalent formulation:

$$VFS = \text{sign}(\det(\vec{\nabla}\rho, \vec{\nabla}\theta, \vec{N}))$$

where  $\vec{N}$  is the exterior normal to the cortical surface. According to the retinotopic properties of the visual cortex, this sign will change between two neighboring areas, allowing us to easily delineate them.

The gradient directions of both functions  $\vec{\nabla}\rho$  and  $\vec{\nabla}\theta$  (defined on the cortical surface) are estimated at each vertex of the underlying mesh with a least square method, using the current vertex neighborhood information. Formally, we look for the vector  $\hat{V}$  verifying:

$$\hat{V} = \underset{V}{\text{Min}} \quad \|\delta F - V\delta X\|$$

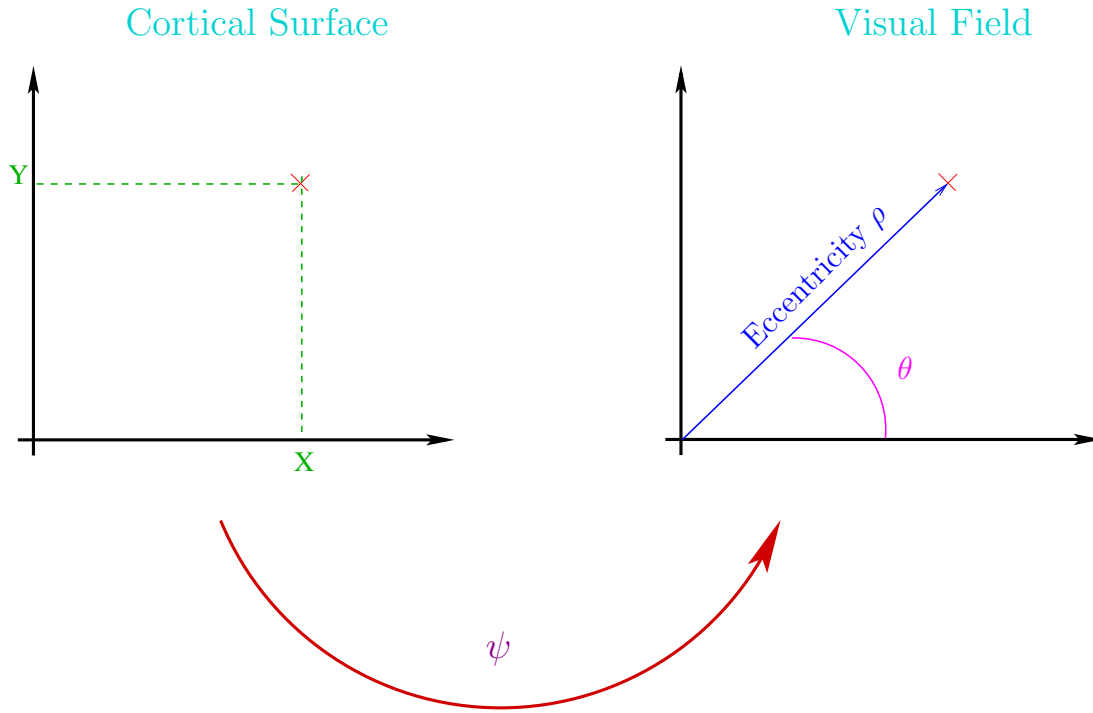


Figure 5.21: Schematic representation of the  $\psi$  function, linking points defined on the cortical surface to the corresponding preferred position - supposed to be the center of an ideal voxel's receptive field - in the visual field.

Where: -  $F$  is the function  $\rho$  or  $\theta$ ,  $\delta F$  a local variation of  $F$ ,  
-  $\delta X$  is a local variation of the cortical surface coordinates.

By definition of the gradient:

$$\begin{aligned} dF &= \nabla F dX \\ \Rightarrow dF^T &= dX^T \nabla F^T \\ \Rightarrow \nabla F^T &= (dX dX^T)^{-1} dX dF^T \end{aligned}$$

This computation is done at each vertex of the mesh, directly on the cortical surface, modeling it locally as a plane orthogonal to the normal  $\vec{N}$ . We perform this computation on the inflated surface, avoiding problems with locally high curvature values (where the local plane approximation of the surface would not be valid anymore).

The first problem we encountered with this computation was many gradients close to zero. The cortical mesh is much more precise than the original volume of the functional data. Consequently, the original angular maps are oversampled on the mesh, often giving rise to close to null variations between two neighboring vertices. To solve this problem, we considered a higher order neighborhood. For instance, the 2nd order neighborhood of a vertice  $v$  is made of the neighbors of the

neighbors of  $v$ , without its first order neighborhood and  $v$  itself. Depending on the degree of the mesh precision (increasing the latter globally decreases the distance between neighboring vertices), it was found to be useful to use a third or even higher order neighborhood to have a more reliable estimation of these gradients. This indeed solves the problem that leads to null gradients at many vertices. However, an important issue remained: the VFS map obtained was still noisy with respect to the ideal delineation expected (see figure 5.22-B). Two techniques were envisaged to improve the VFS maps. We first tried to smooth the ring and wedge phase maps defined over the cortical surface using an appropriate surface-constrained smoothing method developed by Rachid Deriche et al. in the laboratory [205]. It is actually the same algorithm employed in the mesh based smoothing approach described in 4.1.5. The local gradients estimation followed by the VFS computation are then performed classically. Although this technique removes most unexpected VFS reversal while preserving the sought borders, it actually does not enhance sufficiently the results to allow a straightforward area segmentation (see figure 5.22-C). In a second attempt, we performed a filtering directly on both surfacical gradient fields  $\overrightarrow{\nabla\rho}$  and  $\overrightarrow{\nabla\theta}$ . Each original vector field is independently smoothed with an appropriate method also developed by Lucero Lopez and colleagues. Details about this method can be found in [139, 198]. This 3D vector field smoothing step is followed by the classical VFS computation. The resulting VFS maps are once again far less noisy than the classical ones and also better than that obtained with the phase maps surfacical smoothing, especially preserving better the stripes shape of V2 and V3 (see figure 5.22-D). Nonetheless, the final maps are not accurate enough to allow a fully automatic identification of the occipital retinotopic areas.

A closer look at the data over the cortical surface reveals that our angular maps were not as regular as they are supposed to be with respect to electrophysiological data, explaining the problems we encounter with this VFS computation. Besides, personal communications with other laboratories applying the retinotopic mapping techniques and trying the VFS lead us to the conclusion that this method is not robust enough for fast retinotopic map acquisition. Let us recall that our technique allows the acquisition of these maps (eccentricity and polar angle) within 15 minutes of functional scans, which is significantly less than what is usually reported in the literature. Last but not least, a closer inspection of the results shown in the literature using the VFS computation often reveals the same noisiness in their VFS maps, (e.g. figure 3 in [192], figures 7 and 8 in [57]). This review led us to look for an alternative way to segment our retinotopic areas.

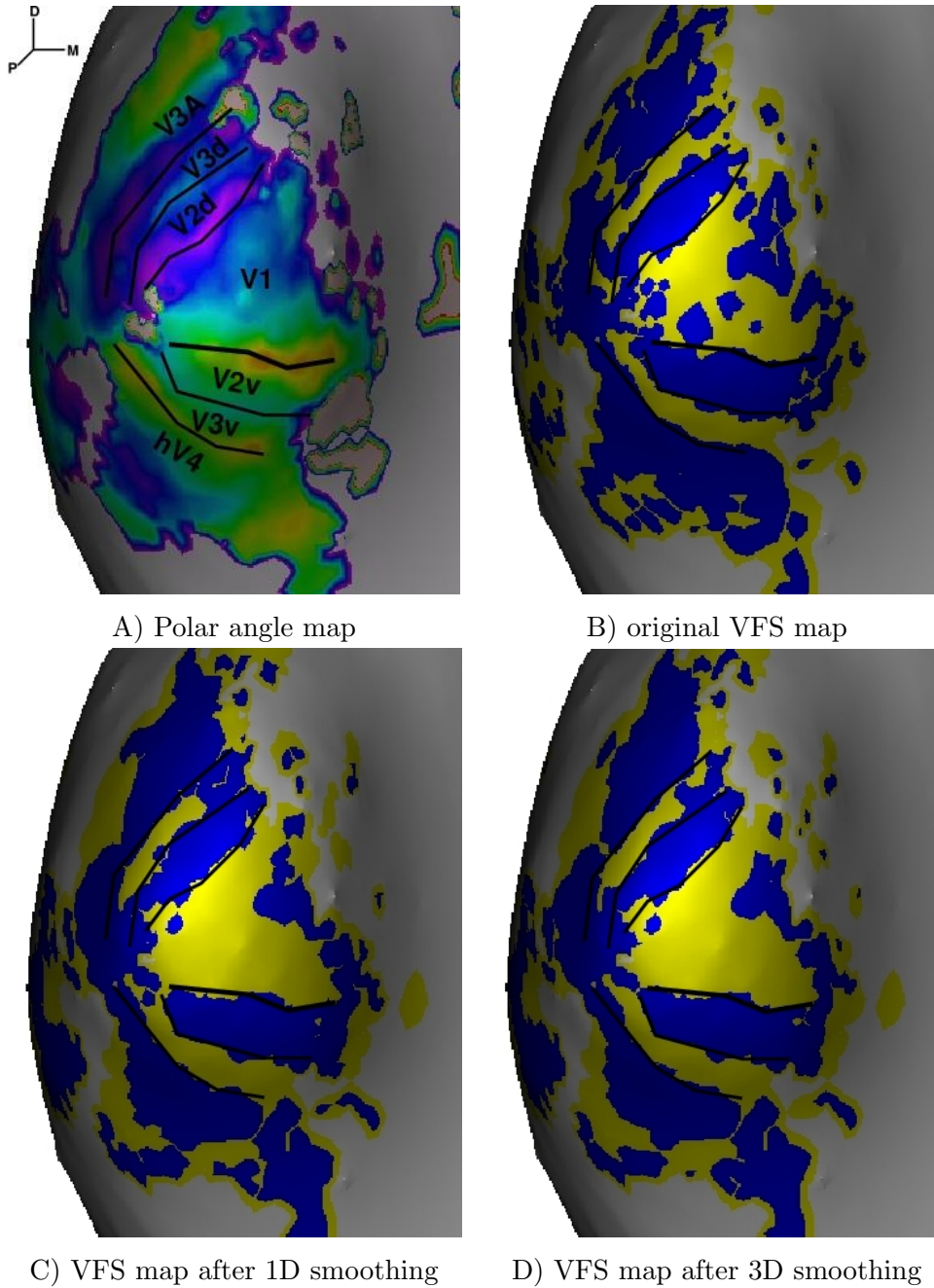


Figure 5.22: Visual Field Sign maps (see text). A) Polar angle map overlaid on the inflated left occipital cortex. The areas boundaries were drawn by hand, based on the angular variations pattern. The VFS results based on B) the original polar angle and eccentricity maps, C) the surface-based smoothing of the angular maps (equivalent Gaussian kernel with  $\sigma = 3\text{mm}$ ) and D) the surface-based angular gradients field smoothed along the cortical geometry. Yellow (blue) indicates a locally mirror (non-mirror) visual field representation.

### Manual area delineation

In order to get a correct delineation of our visual retinotopic areas, we can use a manual area definition, mainly based on the polar angle map of the subject. As we already mentioned above, this map gives the information of angle reversion needed to properly delineate the first retinotopic areas.

This method allows us to correct for the noise found in our VFS maps -which can nonetheless be used as a starting point. Most importantly, it can also be used to completely delineate the retinotopic areas solely based on the polar angle values, allowing faster functional scanning session to identify low-level visual areas.

We adapted the SUMA<sup>6</sup> software to our needs, allowing to draw directly on the inflated cortical surface and to save the 3D vertices coordinates from the original (non inflated) surface. This adaptation mainly involved data format and coordinate system conversions between the different softwares we used. Figure 5.23 illustrates the delineation obtained with this procedure.

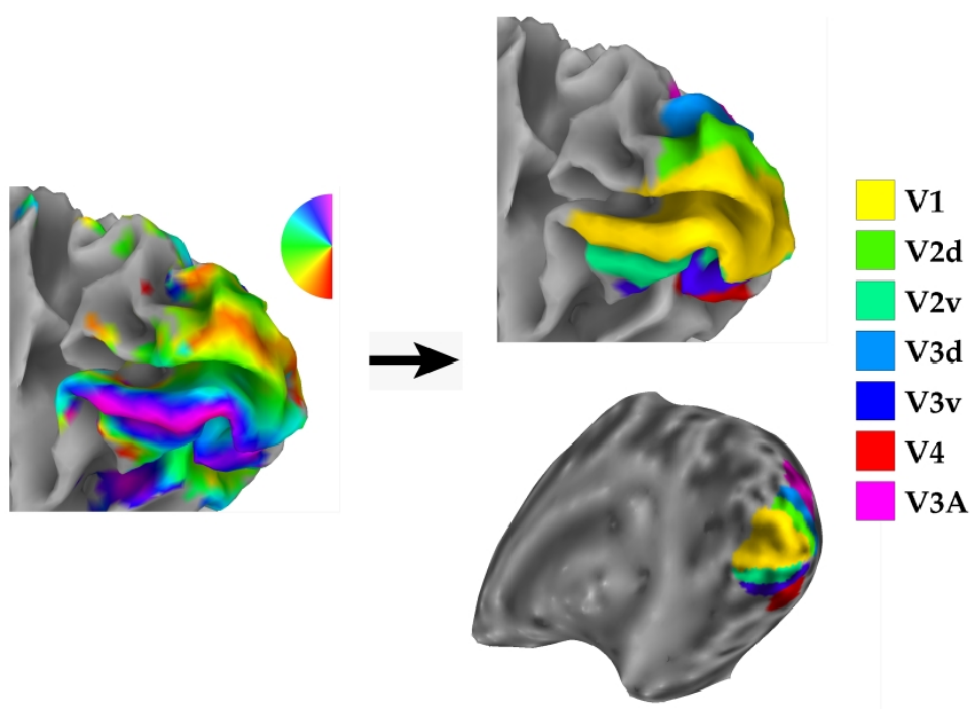


Figure 5.23: The subject's polar angle map projected on a mesh of the GM/WM interface (left) allows to delineate various occipital retinotopic areas as shown on the original mesh (top-right) and on the inflated surface (bottom-right).

Using the manual area delineation procedure, we are able to delineate low-level retinotopic areas of any given subject based on 15 minutes functional scans plus the anatomical image acquisition time. However, our approach is time consuming

<sup>6</sup>Surface MAPPING software, developed by Saad and Cox at the NIMH, NIH; documentation and binaries are freely available at [http://afni.nimh.nih.gov/sscc/staff/ziad/SUMA/SUMA\\_doc.htm](http://afni.nimh.nih.gov/sscc/staff/ziad/SUMA/SUMA_doc.htm)

and manual editing is somewhat less reproducible than a completely automatic delineation. We might further try other approaches like [53], using a model for each phase map and warping these models onto the actual measurements, or in [57], allowing a volumetric visual field sign computation (even if the resulting VFS maps of the latter technique are not as accurate as ideally expected).

### **Volumetric definition of ROIs**

The visual area segmentation technique described above can be used to derive volumic Regions Of Interest (ROIs) from surface-based defined regions, for instance the subset of voxels representing V1. Starting from the surfacical area labeling, we perform a “back-projection” consisting in the attribution, for each labeled vertex, of a subset of voxels in the original volume, according to the projection technique used to map the functional values on the cortical surface. We typically use an integration (averaging) of the values at different voxels from the vertex considered (lying on the GM/WM interface) to a certain distance along the local normal to the surface; this distance is supposed to match the cortex thickness, typically 3mm. These ROIs can then be used for any further experiment characterizing more precisely these retinotopic visual areas.

#### **5.1.10 Conclusion**

The retinotopic maps we obtained are globally in agreement with the related literature and our results confirm some cutting edge questions, as the presence of a ventral fovea representation beyond area V3v. Our general procedure is also currently applied by the INCM team in Marseille in a clinical study of the cortical organization in patients suffering from retinal diseases such as visual scotomas. Preliminary results were presented at two ophtalmology conferences [103, 102]. Beyond this mapping aspects, we can derive within 10 minutes of functional scans surfacic or volumic ROIs that can be used in other experiments exploring the human cortical visual system. As our acquisitions are fast, complementary MRI scans such as functional or diffusion tensor images can be acquired within the same scanning session.

Various aspects may nonetheless be addressed in future work. First, using complementary stimuli patterns, we can expect to clarify visual field representations beyond what we have called “the great agreement zone”. Second, the scan duration required to get retinotopic maps might be further lowered not only with technical imaging advances but also with judicious stimulation tricks. For instance, it might be possible to simultaneously map the polar angle and eccentricity coordinates using two distinct frequencies, each specific to one dimension. Finally, a fully and reliable automatic method to delineate the different visual field maps would be of great interest to facilitate this tedious and expert-dependent task.

## 5.2 Functional mapping of hMT+

This section is dedicated to the functional mapping of area hMT+. We first recall the main contributions in the neuroimaging literature to identify this portion of the visual cortex before describing our choices and experimental results.

### 5.2.1 The hMT+ complex

The functional specialization of human cerebral cortex has first been demonstrated with neuroimaging by Zeki and colleagues [257]. Using PET, they reported two extrastriate regions, one in the ventral lingual and fusiform gyrus specially activated by color stimuli, the other in the temporo-parieto-occipital junction activated by motion stimuli. The latter is classically referred to as hMT/V5+ (i.e. the human MT/V5 complex, we will refer to as hMT+ in the remainder), because it was originally thought to be the human equivalent to macaque's MT, MST and adjacent areas. Several other evidences later supported and precised this broad homology. Using both PET and fMRI, [241] reported the consistent localization of hMT+ at the junction of the ascending limb of the inferior temporal sulcus (ALITS) and the lateral occipital sulcus (LO). This localization was further refined in [56]. These findings had to be linked with anatomical studies which showed the particularly dense myelination of this region in humans [37, 223, 4], which is characteristic of macaque MT/V5 area [232]. Moreover, various studies improved the functional characterization of hMT+. Tootell and colleagues precised its functional selectivity, showing its response to various moving patterns and also incoherent flicker, its high sensitivity to low contrasts and its lower activity elicited by isoluminant color stimuli [218]. They also suggested in [219], later followed by others [43], the implication of hMT+ in the Motion After-Effect (MAE)<sup>7</sup>. This result was actually infirmed by Huk and colleagues who later showed that the activation was only due to attentional effects [113]. The latter group demonstrated the presence of pattern motion cells in this complex [114].

Some efforts were finally made to distinguish subregions within the hMT+ complex, based on putative homologies with non-human (especially macaque) motion sensitive areas. [55] subdivided hMT+ into area MT responding to contralateral visual field only, area MSTd showing ipsilateral peripheral selectivity and area MSTl based on non-visually driven pursuit eye movement. These results were partially confirmed by [112] who distinguished the putative MT homologue relying on its retinotopic property and the putative MST homologue based on its functional selectivity to

---

<sup>7</sup>The Motion After-Effect refers to a famous optical illusion which involves the apparent motion of a stationary stimulus in the opposite direction to a previously observed one. It is also called the waterfall illusion as staring for a few tens of seconds to a waterfall before looking at a fixed object aside produces a MAE.

peripheral and ipsilateral stimuli. However, such tentative subdivisions of this motion selective region require many specific scans and need a more precise characterization, explaining the reference to the hMT+ complex in most neuroimaging literature.

### 5.2.2 hMT+ localizer: previous work

We present an overview of the different stimulation paradigms used in fMRI to functionally identify the hMT+ region. This review does not pretend to be exhaustive but rather accounts for the main approaches proposed so far.

In most fMRI experiments to localize hMT+, subjects undergo a passive viewing task with blocks of either a motion condition or a control condition. Beyond this general and rather natural principle, the methods differ between groups with respect to different parameters:

- the stimulus pattern: random black and white checkerboard (also called a random texture pattern or RTP), random dots pattern (RDP), sinusoidal gratings, concentric rings,
- the type of motion presented: simple translation (vertical or in any direction), expansion/contraction (alternating or not), incoherent motion (flicker),
- the control condition: a static or a flickering presentation of the stimulus pattern.

Other less crucial parameters may also differ across studies. For instance, the block duration and number of blocks used should impact the final t-maps observed, which is obviously linked to the amount of signal available. Stimulus size has shown to have little effect on hMT+ activations [209], although increasing the stimulus extent should naturally lead to larger activation focus since MT has a crude retinotopy. When a flicker condition is included, it seems that the flickering rate does not have much influence on the final results in area hMT+ [209]. Similarly, [14] reported a weak difference in hMT+ activations to different velocities they tested (5 and 20 deg.s<sup>-1</sup>).

Table 5.4 summarizes the different combinations employed in some representative studies regarding the main stimulation parameters.

### 5.2.3 hMT+ optimal mapping

#### Stimuli

As various stimuli are described in the literature to reveal the hMT+ complex using neuroimaging, it was not obvious to decide which stimulus configuration would

Reference	Pattern	Coherent motion	Flicker
Tootell et al. 1995 [218]	random dots squares/rectangles sinusoidal grating	expansion or contraction translation translation	2-3 Hz
Van Oostende et al. 1997 [233]	random checkerboard	translation	30 Hz
Smith et al. 1998 [202]	concentric rings with various patterns	1.2 Hz expansion/contraction	-
Sunaert et al. 1999 [209]	random checkerboard	translation	6 or 15 Hz
Dumoulin et al. 2000 [56]	random checkerboard	-	2 Hz
Braddick et al. 2001 [14]	random checkerboard	vertical translation	50 Hz
Huk et al. 2002 [114]	random dots	1Hz alternating expansion/contraction	-

Table 5.4: Overview of the main stimulation configuration used in the literature to reveal the hMT+ complex.

optimally drive hMT+ activations. We tested the influence of two parameters: the control condition and the stimulus pattern.

### Control condition

We tried a contrast between coherent motion (COH) and non-coherent motion, i.e. a randomly flickering pattern (FLI). Even if hMT+ was shown to be responsive to flicker [218, 233], we can expect a significant difference with the coherent motion condition as shown in [14]. The use of such a contrast is justified by three theoretical reasons:

- it should only drive “coherent motion” sensitive neurons,
- neurons only sensitive to high spatial frequencies would thus be avoided,
- it could help discriminating local and global motion processing neurons.

We also presented blocks with a static image presentation (STA) of the same pattern, which allowed us to compare the different contrasts used in the literature: coherent minus incoherent motion (COH-FLI), coherent motion minus a static stimulus (COH-STA) and incoherent motion minus a static stimulus (FLI-STA).

### Stimulus pattern

We tried two different kinds of stimulus pattern:

- (1) a black and white RDP on a mid-grey background with a  $10.28 \text{ dots.deg}^{-2}$  density, similar to [114]. For this stimulus, the coherent motion blocks consist in inward and outward radial motion with a velocity of  $7.53 \text{ deg.s}^{-1}$ , alternating every 500ms; this alternated motion prevents adaptation effects. In this radial motion, dots leaving the mask were replaced through a radial wrap-around constrained to

keep the dots density constant. The flicker condition is randomly drawn patterns at 18Hz.

(2) a rectangular black and white checkerboard, similar to that used in Orban's group [209]. The coherent motion condition is a global translation at  $7.53 \text{ deg.s}^{-1}$  in a randomly selected axis changing every second; the translation direction along the same axis is further reverted every 500ms. The flicker condition is a randomly drawn pattern at 18Hz.

Both stimuli were presented within a circular aperture, as illustrated in figure 5.24.

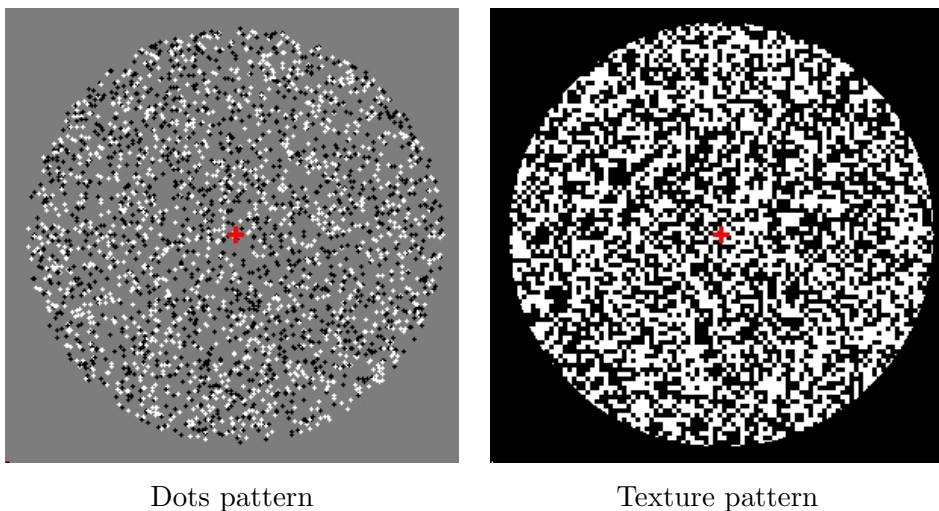


Figure 5.24: The two kinds of pattern tried for our motion localizers. The circular aperture diameter subtended 19.5 degree.

## Imaging

We tested both stimuli patterns (RDP and RTP) and the 3 conditions (COH, FLI and STA) in 4 subjects. Both patterns were presented in separate runs. We used a typical block design, in which each of the 3 modes of stimulation was presented during blocks of 8 RT (16.888sec). A run started with 5 scans with only the fixation cross (MR signal stabilization), followed by 6 repetitions of each of the 3 block types shuffled in a pseudo-random fashion and ended with 2 fixation cross scans to allow slice-timing correction, hence leading to a total of 151 scans ( $\approx 5\text{mn}20\text{sec}$ ).

Each functional image spans 20 coronal slices 3mm thick and  $2 \times 2 \text{mm}^2$  in plane resolution, approximately orthogonal to the calcarine sulcus covering the occipital retinotopic areas and extending ventrally to confidently include the expected hMT+ location. A high resolution anatomical image was also acquired from which an individual model of the cortical surface was extracted with methods described in

chapter 3, enabling to smooth the functional images along the cortical geometry and to visualize the activation maps.

### **Data analysis**

The time courses were slice-timing corrected, motion corrected, coregistered to the anatomical image and smoothed with our cortical surface based method (FWHM=3mm). For more details about each preprocessing steps, refer to section 4.1. Each voxel time courses were then analyzed under the classical GLM implemented through SPM99 custom designed batches, each stimulation condition being modeled by a box-car convolved with the standard HRF model, as detailed in section 4.2. T-maps contrasting two conditions of stimulation were finally estimated and thresholded at  $p=10^{-3}$  uncorrected to reveal the voxels considered as significantly more activated in a condition compared to another.

### **5.2.4 Results**

#### ***hMT+ activations***

Figures 5.25 to 5.28 show the estimated activations for the different contrasts and pattern we tested in a lateral view of the GM/WM interface. This point of view was particularly appropriate to show the expected location of area hMT+. We do not show inflated surfaces to avoid important areal changes that occurred at the highly folded location of hMT+ activations.

The COH-STA contrast systematically reveals an activation focus in the inferior temporal sulcus of the 8 hemispheres analyzed, either with the RDP or the RTP stimuli. We note however that the RTP led to a smaller activation extent in one hemisphere of subject GG (figure 5.27).

The same result was found with the COH-FLI contrast, also leading to significant activations at the expected location in the 8 hemispheres considered, with also a smaller activation extent in one hemisphere of another subject for the RTP stimulus (subject HR in figure 5.25). Interestingly, within the expected location of hMT+, the COH-FLI activation patch was systematically included in that of the COH-STA contrast and the p-values were systematically smaller in the former as compared to that in the latter, independently of the pattern used. This result confirms the higher functional selectivity of the COH-FLI contrast with respect to the COH-STA contrast. Furthermore, when the COH-FLI activation area was strictly smaller, it was always located in the most dorsal part of the COH-STA activation patch.

We relate this result with previous fMRI attempts to subdivide hMT+, [55, 112] which distinguished putative human homologues of macaque MT and MST located in posterior-ventral and anterior-dorsal parts of hMT+ respectively. We therefore hypothesize that the subregion revealed by the COH-FLI contrast can be the human homologue of macaque MST. Further experiments to map complementary information such as retinotopic organization, receptive fields size or functional selectivity to pursuit eye movements in hMT+ would be needed to confirm this hypothesis.

The FLI-STA contrast elicited more erratic activations in the hMT+ region, with only 3/8 hemispheres showing a clear hMT+ activation with the RDP and 4/8 with the RTP. This result suggests the sub-optimality of a comparison between incoherent motion and a static condition to reveal the hMT complex. This is to be related with the report in [56], who found no significant responses in 33% of the cases (5 subjects out of 15 in their study).

We thus discourage the use of an incoherent motion minus a static condition contrast (FLI-STA) to reveal the human MT complex. On the other hand, choosing the more appropriate control condition to be compared with coherent motion is less clear for this identification purpose. At this point, we cannot reliably label the sub-region revealed by the COH-FLI contrast. We prefer to consider the COH-STA contrast and label the inferior temporal sulcus differential activation as the hMT+ region.

Regarding the stimulus pattern, our RDP led to higher p-values and larger activation patches as compared to the RTP. This might be due to the density of stimulus elements bringing motion information which are lower in the RTP, in which only the square corners and the edges non parallel to the motion direction carry motion signal, with respect to our RDP stimulus, in which every dot provides a motion signal. Further experiments are nonetheless required to study the correlation between motion signal energy and hMT+ activation.

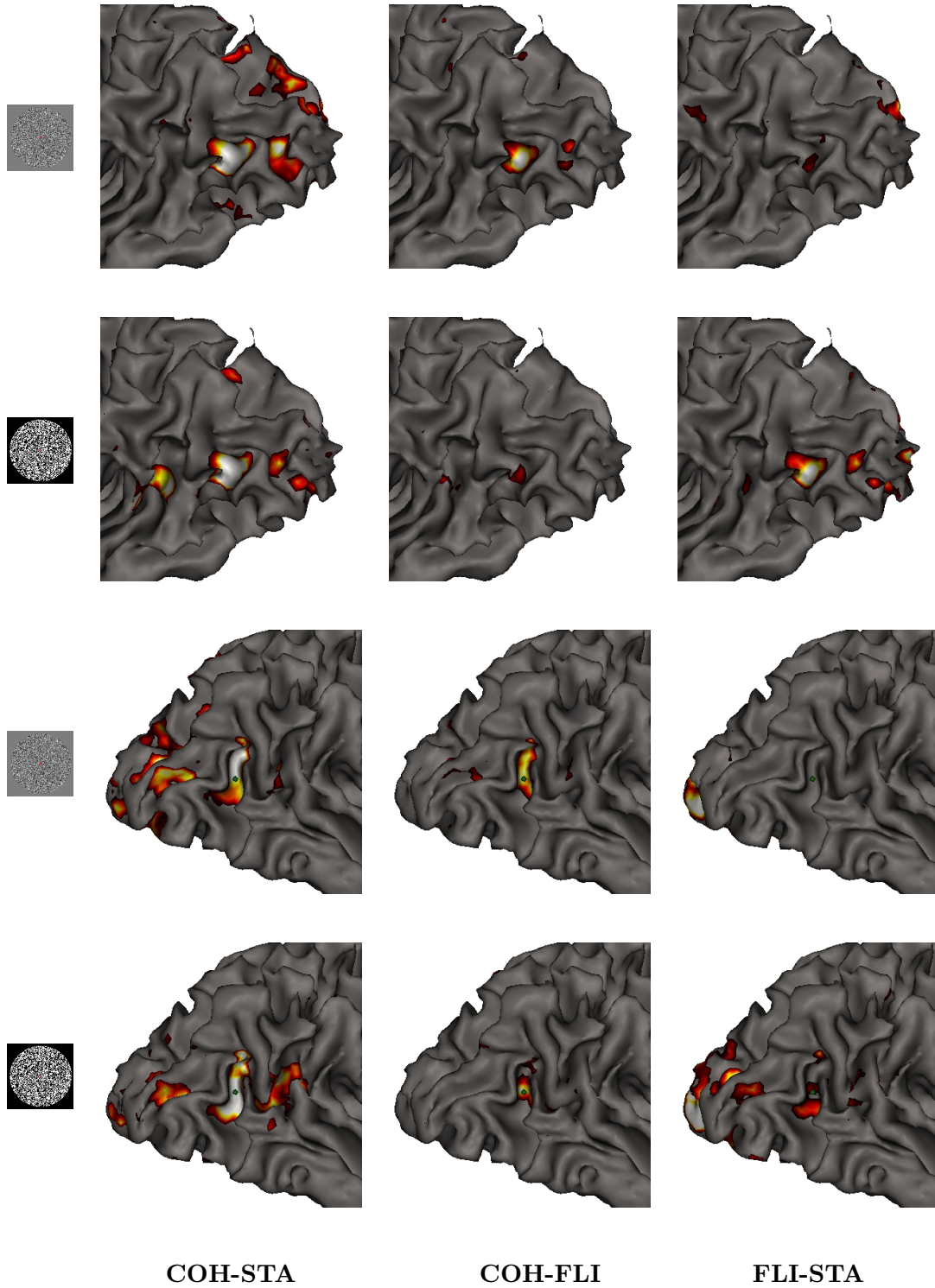


Figure 5.25: hMT+ localizer, for different stimulus pattern and contrasts (subject HR)

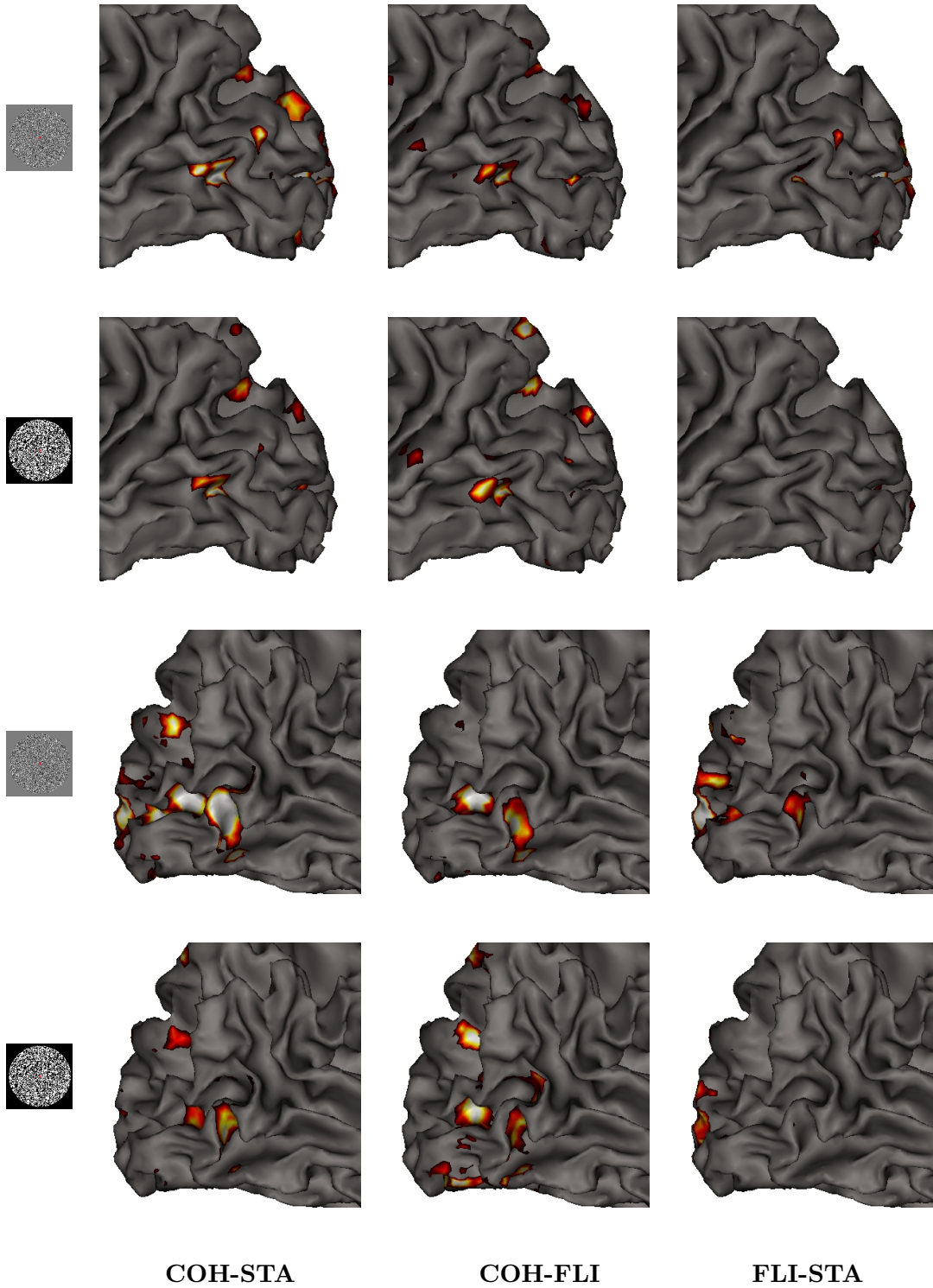


Figure 5.26: hMT+ localizer, for different stimulus pattern and contrasts (subject GM)

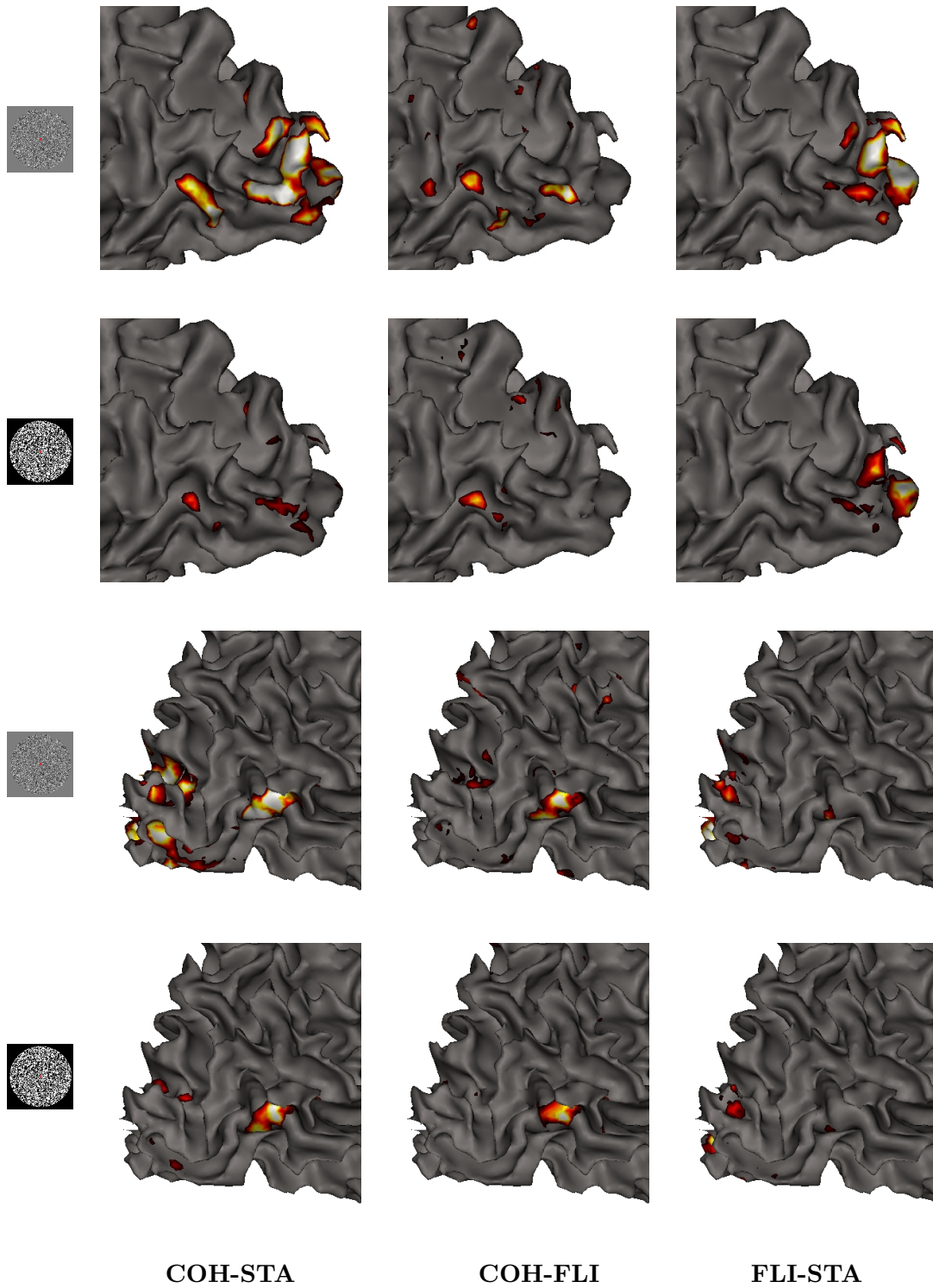


Figure 5.27: hMT+ localizer, for different stimulus pattern and contrasts (subject GG)

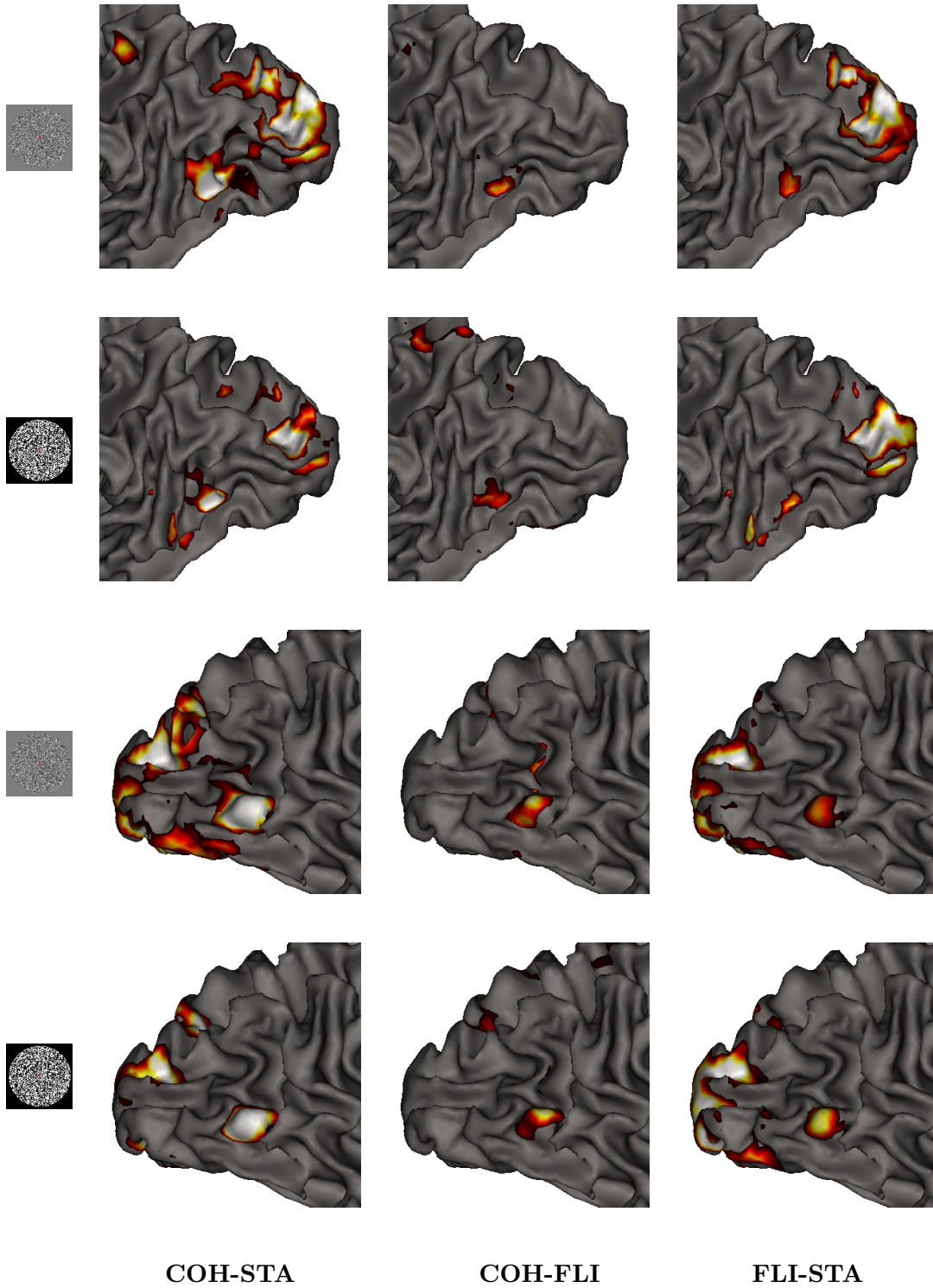


Figure 5.28: hMT+ localizer, for different stimulus pattern and contrasts (subject LH)

### Intra-subject reproducibility

We checked the intra-subject reproducibility of the hMT+ functional mapping by analyzing data from the same subject in distinct scanning sessions. The scans from both sessions were coregistered on a arbitrary defined reference session through the high resolution anatomical images using SPM2 coregistration algorithm. We globally found a good overlap across sessions, as illustrated qualitatively in figure 5.29.

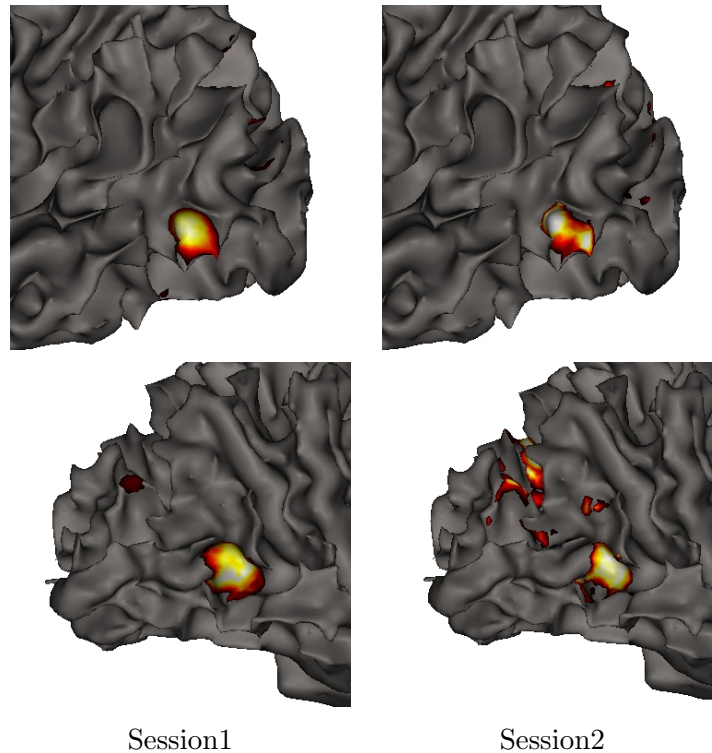


Figure 5.29: Intra-subject multi-session reproducibility of hMT+ mapping with the RDP stimulus and COH-FLI contrast,  $p = 10^{-3}$  uncorrected (subject EC).

### Occipital cortex activations

Even if our main goal was to individually localize the hMT+ complex, we could also observe some significant activations in the occipital cortex depending on the contrast and pattern considered.

The COH-FLI contrast elicited no activation in the occipital cortex around the calcarine sulcus in every hemisphere we analyzed. On the other hand, this region was significantly more activated by flicker than by a static stimulus (FLI-STA), as illustrated in the first two columns of figure 5.30. This preference for flickering as compared to static stimuli is not surprising, as recent studies confirmed that human V1 and surrounding extrastriate areas comprise direction selective cells ([113] and next chapter in this thesis). More interestingly, we also found that the flicker condition elicited a greater response than a coherent motion stimulation within the

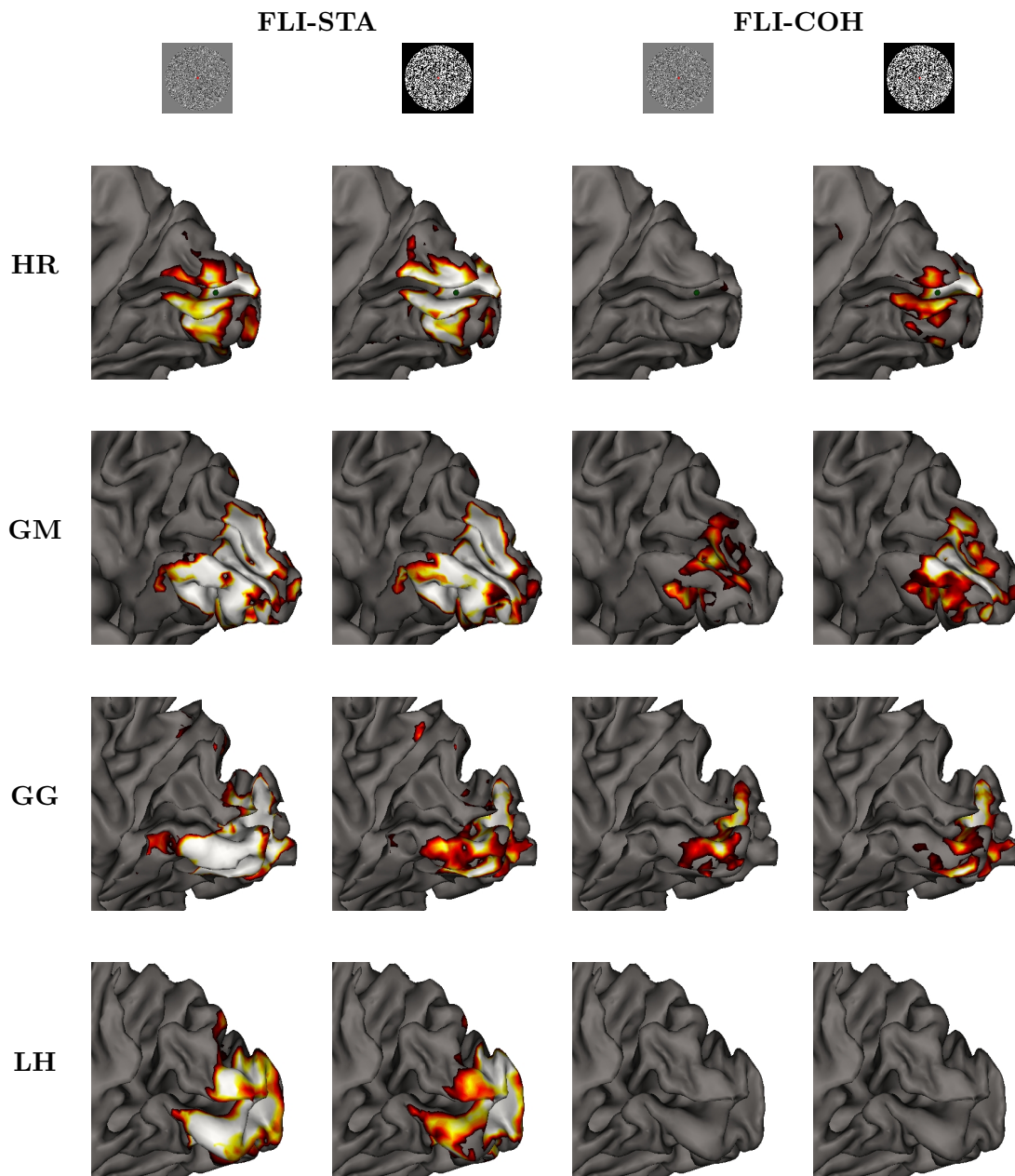


Figure 5.30: Relative activations in the occipital pole when contrasting FLI-STA or FLI-COH for both stimuli patterns. Each subject's right hemisphere is presented in a row corresponding to different contrasts between conditions and stimulus pattern.

occipital pole in various hemispheres (4/8 for the RDP, 5/8 for the RTP), as illustrated in both right rows of figure 5.30. This result confirms a previously reported observation [14]. Such a relative activation in V1 suggests the involvement of more cells stimulated by incoherent motion than the amount of cells stimulated on their preferred direction by the coherent stimulus in area V1. This observation should be linked to the receptive field size: direction selective neurons with small receptive

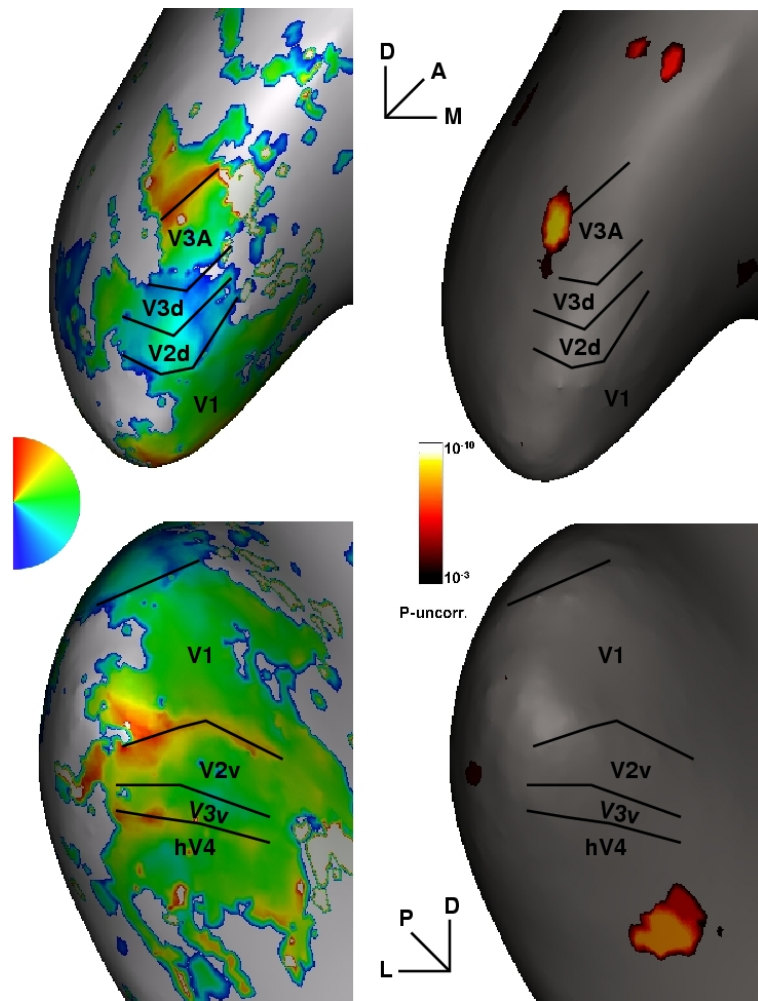


Figure 5.31: Dorsal and ventral activations revealed with the RDP stimulus and COH-FLI contrast and the corresponding polar angle maps (subject LH).

fields should not be disrupted by incoherent direction information that does not fall inside their receptive fields. On the other hand, direction selective cells with large receptive fields will respond less to incoherent motion signals. Interestingly, receptive field size was shown to be smallest in V1 as compared to other extrastriate areas [203].

Further away from the occipital pole, we also systematically found a stronger response to coherent motion than flicker (COH-FLI) in regions located both dorsally and ventrally. Based on retinotopic angular maps also acquired in the same subjects, the dorsal locations seem to correspond to V3A-V3B and even more dorsal cortical regions which could include V7 [177], while the ventral activations extends to ventral regions beyond putative hV4. Figure 5.31 shows these activated areas and the corresponding polar angle maps observed on the inflated hemisphere of a representative subject.

### 5.2.5 Conclusion

Based on an analysis of the experiments described in the literature, we tested different stimulus patterns and contrasts between conditions to decide the most reliable procedure to identify the hMT+ complex. We finally decided to use a random dot pattern and a contrast between coherent motion and a static condition which systematically led to highly significant and reproducible activations at the expected cortical location.

Our data also opened different perspectives. First and foremost, the systematic inclusion of the COH-FLI activation within the COH-STA activation suggests a possible functional subdivision of the hMT+ complex. This assumption should be confirmed with complementary criteria such as precise visual field mapping or studies of anatomical connectivity. Addressing these issues is of particular interest to study the possible homologies with non-human primates and better characterize visual motion processing taking place in this cortical region [163, 195]. Secondly, we found distinct activation profiles in the occipital cortex when comparing coherent or incoherent motion with a stationary stimulation, consistent with previous reports of similar subdivisions [209, 14]. This characterization of motion responsive regions needs to be further investigated, for instance with a more continuous variation of the motion stimulus coherence and performing complementary parametric measurements of functional selectivity as shown in the next chapter.

\*\*\*

We described in this chapter two techniques developed to accurately identify various visual areas in any subject within 30 minutes of functional scans. The next two chapters build on these individual mapping to further characterize the low-level visual cortex, first functionally by revealing distinct direction selectivity and second structurally by studying the anatomical connectivity among them.

# Chapter 6

## fMR-adaptation of direction selectivity

### Contents

---

<b>6.1</b>	<b>Introduction</b>	<b>170</b>
6.1.1	Problem statement	170
6.1.2	fMR-adaptation: principle and previous work	170
6.1.3	Direction selectivity and fMR-adaptation	173
<b>6.2</b>	<b>Experimental procedure</b>	<b>173</b>
6.2.1	Subjects	173
6.2.2	MRI data acquisition.	173
6.2.3	Visual stimuli.	174
6.2.4	Defining the visual areas.	174
6.2.5	The adaptation stimulus.	174
6.2.6	Attentional measurements.	176
<b>6.3</b>	<b>fMRI data analysis.</b>	<b>177</b>
6.3.1	Visual areas identification experiment	177
6.3.2	Adaptation experiment	177
<b>6.4</b>	<b>Results</b>	<b>178</b>
6.4.1	BOLD signal adaptation	179
6.4.2	Direction selectivity	179
6.4.3	Quantitative comparisons between areas	181
6.4.4	Responses to stimulus transient	184
<b>6.5</b>	<b>Discussion</b>	<b>185</b>
6.5.1	Motion direction selectivity	185
6.5.2	Macaque/human homologies in V1 and MT	187
6.5.3	Attention, adaptation and direction tuning	187
6.5.4	fMR-adaptation methodology	188
<b>6.6</b>	<b>Conclusion</b>	<b>189</b>

---

## 6.1 Introduction

### 6.1.1 Problem statement

The low-level visual cortex has been extensively studied using invasive techniques in non-human primates. In each area, functional selectivity was characterized with respect to various stimulus dimensions such as orientation or direction. Especially, the tuning bandwidths of visual motion direction selective neurons are known to be area specific in monkeys, as shown in various electrophysiological and imaging studies (e.g. [151, 52]). A similar knowledge is missing in humans.

The major goal of our study is to estimate the motion direction selectivity of different human visual areas with fMRI. A classical subtraction paradigm, comparing the BOLD signals recorded in response to different stimulation conditions, is not sufficient to assess neuronal selectivity to a particular stimulus dimension such as motion direction. Indeed, a single fMRI voxel contains several neuronal sub-populations, with a priori the same proportions of neurons preferentially tuned for any direction. The BOLD signals elicited by two different directions would therefore be equal, leading to a null contrast between both stimulation conditions. Fortunately, a fundamental property of neurons, neural adaptation, can be used in fMRI as a tool for inferring neural sensitivities.

### 6.1.2 fMR-adaptation: principle and previous work

The firing rate of a stimulated neuron decreases when the same stimulation is repeatedly presented: this is neural adaptation. Figure 6.1 illustrates this property in a typical neuron found in macaque MT.

This general feature can also be observed using fMRI, in which a sustained presentation of the same stimulus leads to a decrease of the BOLD signal. The fMR-adaptation paradigm takes advantage of this property to allow inferences about the functional selectivity of neuronal populations within a voxel [90]. The basic idea is to proceed in two steps. First, the neural population is adapted using a repeated presentation of a single stimulus, leading to a significant reduction of the fMRI signal. Second, a given stimulation parameter (e.g. the direction of motion) is changed and two situations can appear: either the signal remains at the same adapted level, suggesting the neuronal invariance to the stimulation change; or the signal recovers a higher level, suggesting the neurons sensitivity to the stimulus feature varied.

We review here some work that have used fMR-adaptation paradigm in human or macaque studies, with an emphasis on the experimental designs employed. Table 6.1 summarizes this overview. We distinguish 2 main subsets of fMR-adaptation paradigm: block and event-related.

The fMR-adaptation block design was first introduced in [89] to study the visual per-

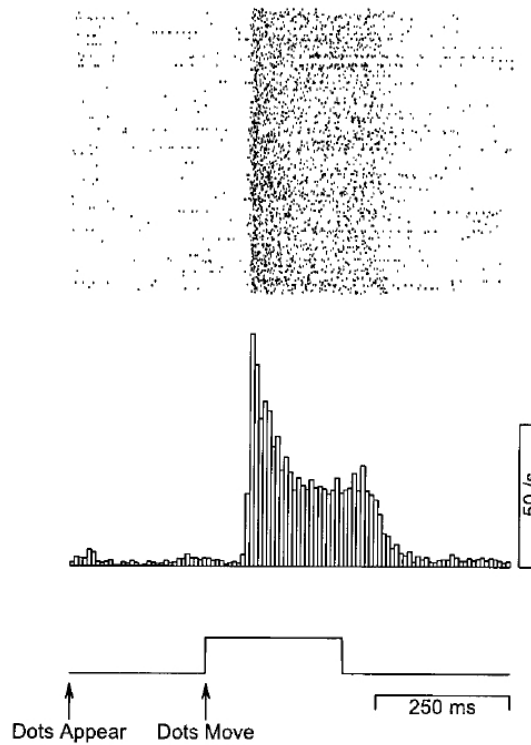


Figure 6.1: Neural adaptation of a typical macaque MT neuron. The upper part shows the neuron response to 256 repetitions of the same stimulus. The histogram gives the mean over the different repetitions. Below is shown the stimulation time course. From [178].

ception of objects and faces under various presentation conditions. Within a block, a succession of  $n$  stimuli (e.g. images of objects) either identical or different with respect to a given feature of interest (e.g. the object size) is presented. The degree of dissimilarity between the  $n$  stimuli is varied across the blocks, from the block with a single stimulus presented repeatedly to the block containing  $n$  different stimuli. The analysis then consists in comparing the mean fMRI signal over the block types. The typical prediction is a lowest mean signal in the identical blocks and a highest mean signal in the all different blocks. The block design adaptation paradigm was applied to investigate the presence of pattern-motion cells in hMT+ [114] or the cortical specialization for inanimate objects and places in the visual cortex [65]. A similar paradigm to that of Grill-Spector and colleagues was recently used by [184] to compare human's and macaque's object adaptation in shape-sensitive regions. Event-related fMR-adaptation is more widely used, mainly because it is faster and allows an estimation of the hemodynamic response function shape. In this paradigm, a trial is generally a pair of stimuli separated by a blank. Both stimuli in a trial are either identical or distinct regarding a feature under study. The stimuli presentation duration and the Inter-Stimulus-Interval (also called the blank period) between

them are variable across studies but are generally on the order of a few hundreds milliseconds each. The BOLD response to each trial type (either similar or different paired stimulations) are then compared to assess the influence of a stimulation variation in a given cortical region. This paradigm was applied in various studies to characterize object priming sensitive regions [18], object shape processing [126], orientation selectivity [13], attentional processes [154], face perception [59], numerosity [173], form analysis [125].

A few event-related fMR-adaptation experiments were conducted differently, revealing different assumptions and interpretation of the underlying neural processes. In a study often misleadingly referred to as a block design fMR-adaptation experiment, Tootell and colleagues investigated orientation selectivity in human V1 [217]. They presented black and white gratings with similar orientations within each 40 seconds block and measured the signal increase occurring at each block transition. Rather this experiment can be considered as event-related since the signal of interest is mainly the transients between two blocks.

To prevent possible strategy changes when the subject becomes aware of the repetition paradigm, Naccache and Dehaene suggested the use of subliminal presentation of the first stimulus and demonstrated its efficiency in a number representation study [155].

<b>Reference</b>	<b>Purpose</b>	<b>Design</b>
Buchner et al. 98 [18]	Orientation priming	E-R
Tootell et al. 98 [217]	V1 orientation selectivity	E-R
Grill-Spector et al. 99 [89]	Object/Face processing in LOC	Block
Kourtzi et al. 00 [126]	Object shape processing in LOC	E-R
Huk et al. 01 [113]	Direction selectivity	E-R
Huk et al. 02 [114]	Pattern motion in hMT+	Block
Boynton et al. 03 [13]	Orientation selectivity	E-R
Murray et al. 04 [154]	Attention in LOC	E-R
Eger et al. 04 [59]	Invariant face perception	E-R
Piazza et al. 04 [173]	Numerosity	E-R
Ewbank et al. 05 [65]	Object and places selectivity	Block
Kourtzi et al. 05 [125]	Form analysis	E-R
Sawamura et al. 05 [184]	Shape processing	Block

Table 6.1: Overview of the human fMR-adaptation literature. E-R:=event-related.

### 6.1.3 Direction selectivity and fMR-adaptation

Single-unit electrophysiology experiments of short-term motion adaptation in macaque area MT have shown that the tuning of the adaptation is similar to the tuning of the neuron to direction [179, 178]. fMR-adaptation data on visual motion tuning would therefore help define more accurately the functional properties of different visual areas.

Our study complements a recent work which investigated direction selectivity defined as the imbalance between opposite directions of motion ([113]). The new aspects introduced in our work are the following: we use an event-related paradigm to allow more than two opposite directions to be presented within a run, so that estimates of direction tuning and proportions of functional population types with respect to this feature can be assessed. We also address the attentional issue raised by Huk and colleagues in a different way. To control attention, Huk et al. used a speed-discrimination task which requires highly-trained observers who also have to perform extensive pilot experiments outside the scanner. This stringent control is necessary because these authors have shown that the increased activity observed during a Motion After-Effect or MAE (e.g. [219]) arises because of attention to this after-effect. This is actually a concern when using block designs where test durations are long enough to elicit an MAE. We anticipated however that this problem would be highly minimized by using an event-related paradigm with short test durations which do not elicit MAEs. We therefore simplified the attentional control task to allow the inclusion in our study of non psychophysically-trained observers.

## 6.2 Experimental procedure

### 6.2.1 Subjects

Four subjects (1 female, age 28-40 years) with normal or corrected-to-normal visual acuity participated in the study.

### 6.2.2 MRI data acquisition.

Subjects participated in two separate 1 hour long scanning sessions: one to identify the retinotopic areas and hMT+, the other to measure motion direction adaptation. A scanning session started with a fast low-resolution anatomical localizer to appropriately set the subsequent functional scans slices location, followed by 8 functional scans and ended with a T1-weighted image acquisition. These high resolution anatomical scans were used as references to coregister the different sessions.

During each functional scan, 151 Echo Planar Images were acquired over 5mn19sec using our coronal sequence (see paragraph 2.4.4). Each functional image spans 20

coronal slices 3mm thick and  $2 \times 2 \text{mm}^2$  in plane resolution, approximately orthogonal to the calcarine sulcus covering the occipital retinotopic areas and extending ventrally to hMT+. The first five images (10.555secs) were systematically discarded to avoid magnetic saturation effects. The following 144 images correspond to the visual stimulus per se. The last two images were taken to allow slice-timing correction preprocessing.

### 6.2.3 Visual stimuli.

Stimuli were generated under Matlab 6.1 using the Image Processing Toolbox (Matlab, The Mathworks), providing an avi file with eighteen  $300 \times 300$  pixels frames per second and lasting 5mn04sec. The stimulation was presented through our classical setup, leading to a display subtending a visual angle of  $20.9^\circ \times 20.9^\circ$ . The stimuli are all presented within a circular aperture of  $19.5^\circ$  in diameter. During the first 5 and last 2 scans, a mid grey-level image with the  $0.5^\circ$  red fixation cross was shown to the subjects.

### 6.2.4 Defining the visual areas.

#### Occipital areas

Low-level retinotopic areas were identified and delineated using the method described in the previous chapter. V2v and V2d (respectively V3v and V3d) were merged as one area V2 (respectively V3). Lacking the eccentricity maps to accurately separate V3A from V3B [202, 177], we considered the most medial hemifield representation that abuts the dorsal border of V3d, considering it as V3A.

#### hMT+

The human mid-temporal complex, hMT+, was revealed with the block design method detailed in the previous chapter. The clusters were found either with the COH-FLI contrast or with the COH-STA contrast and were always within or close to the inferior temporal sulcus (cf.[56]). As already noticed in our preliminary mapping experiments, the (COH-FLI) contrast gave systematically a smaller cluster always included in the (COH-STA) cluster. We also considered the cluster defined by the (COH-FLI) contrast as the hMT+ ROI in our adaptation data analysis.

### 6.2.5 The adaptation stimulus.

We used a black and white random dots pattern (RDP) on a mid-grey background with a  $10.28 \text{ dots.deg}^{-2}$  density, which was similar to the hMT+ localizer stimulus except for the contrast. In [211], adaptation was indeed reduced for large visual stimuli while using a high contrast as compared to a low contrast. We therefore

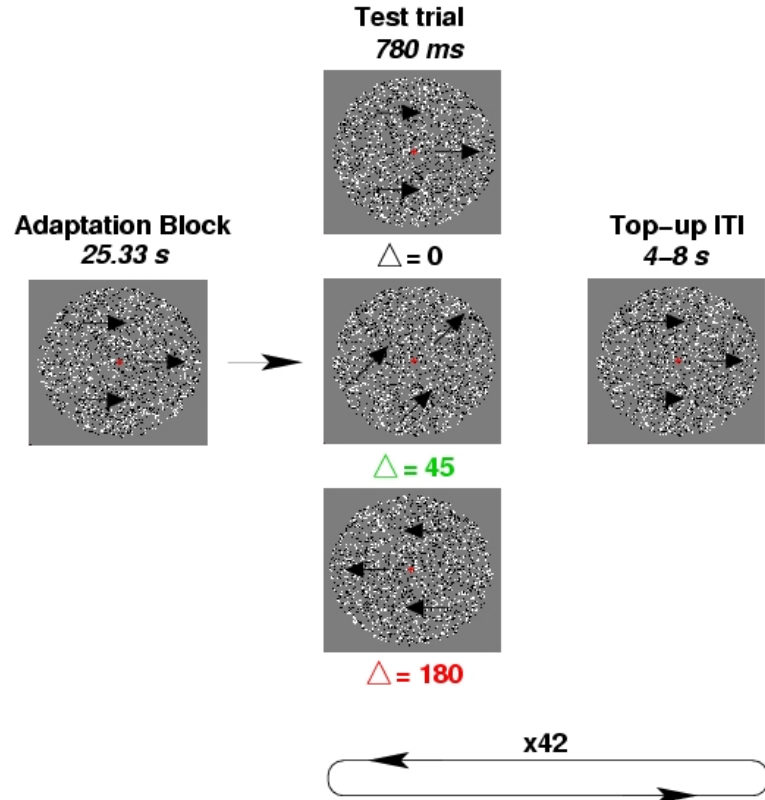


Figure 6.2: Stimulation design diagram in the adaptation experiment. After a 25.33sec *adaptation epoch* (direction chosen for each run between rightward -as in the figure-, leftward, downward or upward), 42 *test trials* lasting 780ms each were presented in a pseudo random-fashion. A test trial consisted in either no change in the motion direction ( $\Delta_0$  condition) or a motion direction change of 45 or 180 degrees (The  $\Delta_{45}$  and  $\Delta_{180}$  conditions respectively). The Inter-Trials Intervals (ITI) between two test trials consisted in a return to the *adaptation direction* or top-up adaptation. The duration of each ITI was drawn from a truncated gamma distribution, mean 5sec, sigma 1sec, min 4sec, max 8sec. The random dot pattern was systematically redrawn at each condition transition, i.e. at each test trial onset and each top-up adaptation onset. Subjects made a size discrimination task at the fixation cross.

reduced the contrast to 20%, still centered around the mid-grey level. In each condition, the RDP drifted coherently at  $7.53 \text{ deg.s}^{-1}$ . The time course of the stimulus started with a 12 RT (25.33sec) *adaptation epoch* in the randomly chosen adaptation direction (either left, down, right or up, fixed for the whole run but randomly changed across runs to avoid any directionality bias), followed by 42 test trials of 780ms where the direction of motion was changed by an angle  $\Delta X$  with respect to the adaptation direction ( $\Delta X = 0, 45$  or  $180$ ) (see figure 6.2). A run thus contained 14 test trials for each  $\Delta X$  value tested; the trials were presented in a pseudo random fashion to equalize the trials apparition order (two successive trials with identical  $\Delta X$  values were not allowed). Note that the  $\Delta 45$  test condition evenly led to a clockwise (+45 degrees) or counterclockwise (-45 degrees) direction change with respect to the adaptation direction. Between two test trials, the Inter-Trial Intervals (ITI) consisted of a *top-up adaptation* in which the dots shifted back to the adaptation direction. The ITI distribution follows a gamma law  $\Gamma(5, 1)$  truncated for values outside [4sec,8sec]. This top-up adaptation allowed to keep the adaptation state relatively constant along the run. Note that we did not add any blank between the trials and the top-up adaptation ITI, in contrast to other event-related adaptation paradigms. Nonetheless, the random dot pattern was redrawn at each condition transition, namely at each test event onset and each top-up adaptation onset. This resetting led to a brief visual transient that could result in a non-specific alerting effect (see the discussion below). Note that a similar stimulation was used at the same time in a recently published study investigating orientation selectivity [66].

### 6.2.6 Attentional measurements.

To control subject's attention, a simple attentional task was performed during each functional scan (localizer and adaptation sessions). Subjects were instructed to fixate a central red cross ( $0.5^\circ$ ) and to click when the cross size increased to  $0.77^\circ$  during 167msec. Concerning the localizers, attentional events followed a uniform distribution between 2 and 6 sec, mainly used to help and check fixation. For the adaptation experiment, where the attention is far more crucial for the results interpretation, attentional events were systematically placed within a test trial and also during the adaptation block starting each run and the inter-trial adaptation periods, globally following a uniform distribution between 2 and 6 secs. More importantly, we stressed that this attentional task was always irrelevant with the random dots pattern motion, either during the adaptation epoch, the inter-trial top-up adaptation or the test trials. This attentional task could not influence the motion direction perception, nor should it have modified dramatically the tuning properties of motion direction sensitive neurons (see *Discussion*). Responses were analyzed off-line. Over

all the adaptation sessions, we observed a mean hit rate of 81.91% correct (ranging from 60.61% to 97.53% correct across subjects and runs), thus reliably above chance. No significant differences were found across the analyzed subjects (respective mean across runs of 76.99%, 84.12% and 83.99%).

## 6.3 fMRI data analysis.

### 6.3.1 Visual areas identification experiment

The functional images for the retinotopic and hMT+ mapping were first realigned with the INRIAlign toolbox and coregistered with the anatomical image with SPM2, then smoothed through a method taking into account the cortical geometry, with a 3mm equivalent Gaussian filter FWHM. A high-pass and a low-pass filtering were also performed on the time-courses to respectively remove low-frequency signal drifts and high frequency noise. Finally, subsets of connected voxels were extracted for each area and further used as ROIs for the adaptation experiment (see paragraph 6.2.4).

### 6.3.2 Adaptation experiment

The datasets were slice-timing corrected, realigned using the SPM INRIAlign toolbox and coregistered with the reference anatomical scan. No spatial smoothing was applied. Datasets were then analyzed independently for each ROI using the HRF approach detailed in paragraph 4.2.4. We used the region-based HRF estimation method that considers each ROI as functionally homogeneous and then uses all the available time series within the ROI to characterize the shape of the HRF for each trial type. A preliminary outlier detection step can be used to remove outlier voxels. The underlying model is non-parametric in the sense that no prior shape of the HRF is assumed in advance, and this technique provides robust HRF estimates since smoothness constraints are introduced within the Bayesian framework (for more details, see [35, 34, 147]). Importantly, the subtle though statistically significant effects we observed using this appropriate analysis framework were totally absent when we processed our data through a classical General Linear Model analysis.

To compare the results across the different conditions and ROIs considered, we defined an adaptation rebound index as the following ratio:

$$I_{X-Y} = \frac{\overline{hrf(\Delta_X)} - \overline{hrf(\Delta_Y)}}{\overline{hrf(\Delta_0)} - \overline{hrf(Adapted)}} \quad \text{where } (X, Y) \in \{(180, 0), (45, 0), (180, 45)\}$$

$\overline{hrf(\Delta_X)}$  is the estimated HRF mean computed as the mean signal at three time points centered at the peak of the estimated HRF (mostly observed at  $t \simeq 6sec$ ) for  $\Delta_X$  ( $X = 0, 45$  or  $180$ ) test trials. In other words, if the HRF pick was observed

at  $t = t_0$ , then  $\overline{hrf(\Delta_X)} = (hrf(\Delta_X)(t_0 - 1) + hrf(\Delta_X)(t_0) + hrf(\Delta_X)(t_0 + 1))/3$ . The Adapted response was taken as the HRF mean estimated during the last 10sec of the 25sec adaptation epoch starting each run, i.e. when the signal was maximally adapted. The numerator of  $I_{X-Y}$  is the difference in the response means to two trial types ( $\Delta_X$  and  $\Delta_Y$ ). The denominator is the difference between the estimated response mean for  $\Delta_0$  trials and the estimated adapted signal baseline, therefore representing the subject and ROI specific responsivity. This normalization minimizes possible differences in the BOLD response gain due to any confound irrelevant with the motion direction changes such as the stimulus transient occurring at each test trial onset. Provided the denominator is positive, which was systematically the case in our data, we have:

- $I_{X-0}$  ( $X \in \{45, 180\}$ ) approximately equal to zero indicates that no non-adapted neurons responded to the direction change, whereas a high value indicates the recruitment of an important proportion of non-adapted neurons
- $I_{180-45}$  approximately equal to zero indicates no differences in the BOLD signals elicited by  $\Delta_{180}$  and  $\Delta_{45}$  trials, suggesting identical cells proportion recruited by both direction changes, whereas high value indicates a strong difference in both elicited signals, suggesting a difference in the proportion of non-adapted cells recruited by both direction conditions. We assume that this difference is directly related to the population of broadly tuned neurons, since a similar proportion of narrowly tuned neurons, though with distinct preferred direction, is involved in the  $\Delta_{180}$  and in the  $\Delta_{45}$  trials.

We therefore considered the following indices: (A)  $I_{180-0}$ , i.e. comparing  $\Delta_{180}$  with  $\Delta_0$ , (B)  $I_{45-0}$ , i.e. comparing  $\Delta_{45}$  with  $\Delta_0$  and (C)  $I_{180-45}$ , i.e. comparing  $\Delta_{180}$  with  $\Delta_{45}$ . We assume that these comparisons are related respectively to (A) the global population of direction selective cells, irrespective of their directional tuning bandwidth, (B) a population of relatively narrowly-tuned cells which have a differential response to a 45 degree change in motion direction and (C) a population of relatively broadly-tuned cells which have a large differential response to a direction change of 180 degree but a small (or inexistent) differential response to a 45 degree change. Consequently, the ratios  $\frac{I_{180-45}}{I_{180-0}}$  and  $\frac{I_{45-0}}{I_{180-0}}$  respectively give a rough estimate of the proportion of broad-band and narrow-band cells within the motion direction selective population of each area.

## 6.4 Results

Out of four subjects scanned, three were kept in our final analysis as one was discarded because of important head motion ( $>3\text{mm}$ ). We analyzed the time course of the BOLD signal during the motion adaptation stimulation separately in each retinotopically or functionally defined ROI.

### 6.4.1 BOLD signal adaptation

Each run started with a first 25.33s (12 TR) adaptation epoch, where dots all move coherently in the randomly chosen adaptation direction. This stimulation led to the expected signal decrease in every subject and area considered, supposed to be correlated with neuronal adaptation. Figure 6.3 illustrates the mean signal decrease in area hMT+ of subject S1 during the adaptation epoch. Similar result were systematically observed, though with various degrees, in each area and subject considered.

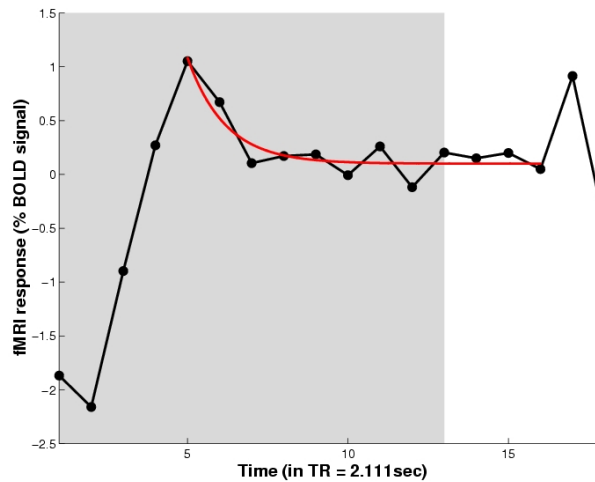


Figure 6.3: Time course of the adaptation epoch (subject LQ) and fitted exponential decay. The grey period corresponds to the adaptation epoch, in which the same motion direction is continuously presented. The black curve shows the averaged time course from hMT+ voxels and over 8 scans acquired within the same session. The red curve is an exponential fit of the adaptation time course.

### 6.4.2 Direction selectivity

Following the adaptation block, the runs consisted of several test trials in which the direction of motion was changed with respect to the adaptation direction for a duration of 780ms. The angle difference between adaptation and test direction is noted  $\Delta_X$ , and we tested the values 0 (direction unchanged), 45 and 180 (opposite directions) degrees. According to the adaptation paradigm, two situations can appear at any voxel during a test trial:

- (1) every neuron in the voxel is insensitive to the motion direction change, therefore the voxel mean BOLD signal remains adapted,
- or
- (2) a sub-population of neurons in the voxel is sensitive to the motion direction change, the responses of which induce a BOLD signal increase (or rebound).

We also predict that the HRF rebound will increase with the  $\Delta_X$  value. Indeed, if a rebound occurs for  $\Delta_{45}$  trials, this suggests the presence of narrowly tuned neurons with preferred direction centered around the 45 degrees direction relatively to the adaptation direction. On the other hand, possible broadly tuned neurons centered at the relative 45 degree direction should remain adapted, since the direction difference between the adaptation and 45 degree test trial does not impact significantly their responsivity. In the case of  $\Delta_{180}$  trials, a similar proportion of narrowly tuned neurons as in the  $\Delta_{45}$  condition should also respond, specifically the narrowly tuned neurons with preferred direction centered around the relative 180 degrees direction. Additionally, the population of broadly tuned neurons centered around the relative 180 degrees condition that were not adapted by the adaptation direction will also be activated by the relative 180 direction, leading to an additional BOLD signal increase. Hence, the rebound observed for  $\Delta_{180}$  trials should be superior (or at least of equal value if no broadly tuned neurons are involved) as that of the  $\Delta_{45}$  trials.

We computed the responses to each  $\Delta_X$  value we tested through the HRF-toolbox over all ROIs and all runs (see *fMRI data analysis*). Figure 6.4 shows the estimated hemodynamic response function (HRF) of each identified areas for one representative subject (LQ).

First of all, the estimated curves are always ordered as expected, showing higher rebounds with increasing difference between the adapting and the test directions. In other words, as we predicted, the bigger  $\Delta_X$  is, the larger the BOLD signal rebound should be as more neurons respond to the stimulus changes. Every functionally defined area studied showed this ordered rebound effect, although with varying degrees.

To further precise this observation, statistical T-test p-values shown in table 6.2 provide evidence for (1) the significance in the activation for each estimated curve, i.e. a difference between the latter and a null vector signal (first 3 columns) and (2) a statistical difference in the estimated signals between two test conditions (last 3 columns). The statistical tests are performed on the subset of 4 time points between 2 and 9 sec, thus centered around the maximum of the response typically found at the fourth time point ( $t=6.333\text{sec}$ ) and take into account the relative variances at each estimated time point. The differences between each pair of estimated curves were significant ( $p<0.0015$ ) for all 3 subjects in areas hMT+, V1 and V2 and relatively less consensual for areas V3 (though  $p<10^{-4}$  for 2 subjects) and V3A ( $p<0.0075$  for 2 subjects). V4v curves were statistically not different from one another ( $p>0.3$ ) for 2 subjects, revealing a less robust signal than that found in the other visual areas.

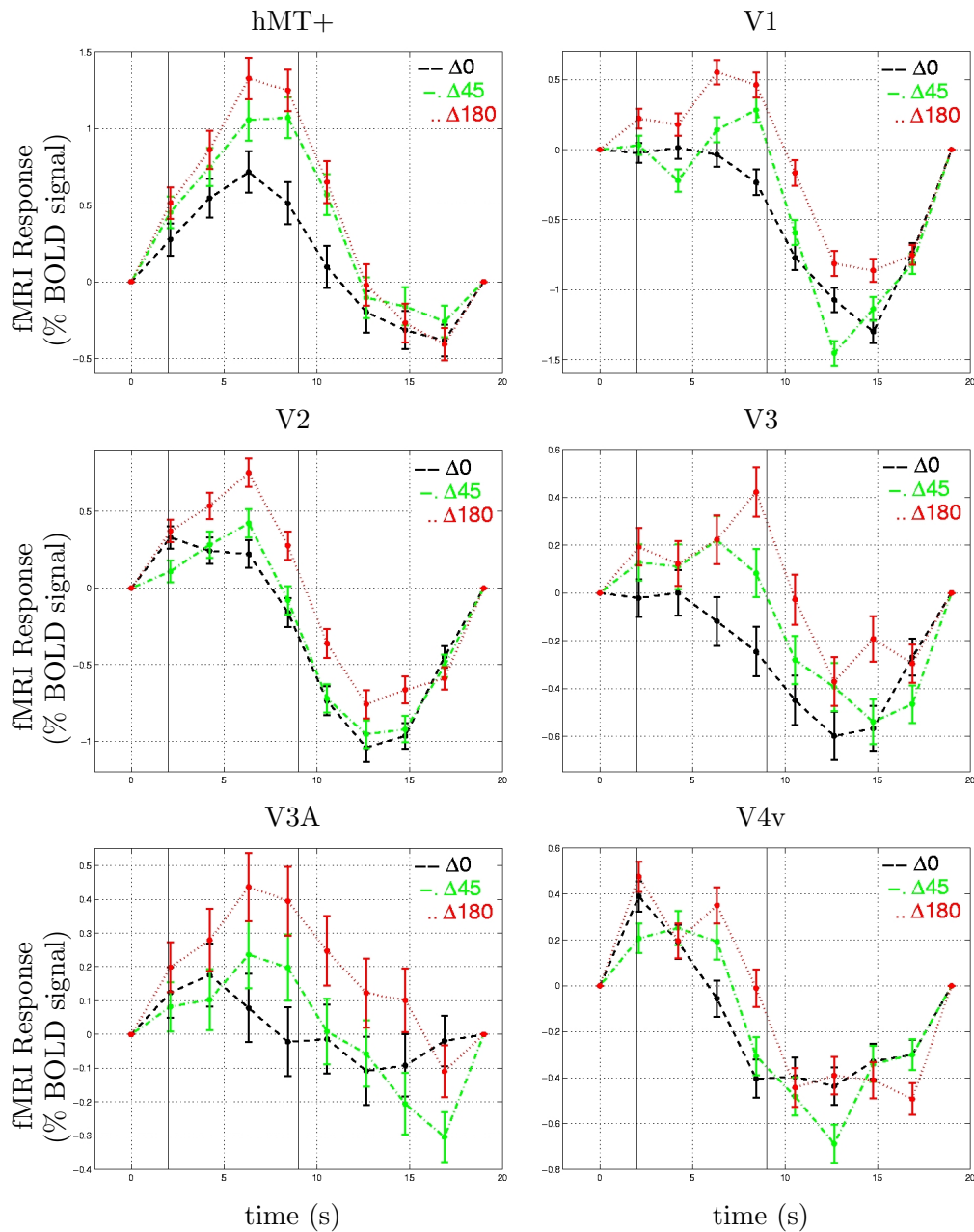


Figure 6.4: Typical BOLD signal time courses for each condition and area estimated using the HRF toolbox (subject LQ). BOLD signals increased with increasing angular difference between adaptation and test direction ( $\Delta$  value), suggesting sub-populations recruitment elicited by the direction change. Error bars correspond to  $\pm 1$  SEM across repeated trials and voxels in each ROI.

### 6.4.3 Quantitative comparisons between areas

To further quantitatively characterize the motion direction selectivity, we computed a normalized adaptation rebound index (see paragraph 6.3). The latter allows to perform comparisons in the BOLD signal responses elicited by changes in the direc-

Area	$\Delta_0$	$\Delta_{45}$	$\Delta_{180}$	$\Delta_{45} - \Delta_0$	$\Delta_{180} - \Delta_0$	$\Delta_{180} - \Delta_{45}$
<b>HR</b>						
hMT+	$< 10^{-4}$	$< 10^{-4}$	$< 10^{-4}$	$< 10^{-4}$	$< 10^{-4}$	$< 10^{-4}$
V1	$< 10^{-4}$	$< 10^{-4}$	$< 10^{-4}$	0.0001	$< 10^{-4}$	$< 10^{-4}$
V2	$< 10^{-4}$	$< 10^{-4}$	$< 10^{-4}$	$< 10^{-4}$	$< 10^{-4}$	$< 10^{-4}$
V3	0.3614	0.0028	$< 10^{-4}$	0.8518	0.2893	$< 10^{-4}$
V3A	0.2810	0.0089	0.0004	0.6494	0.1614	0.0010
V4v	0.0450	0.2223	0.0518	0.4002	0.3782	0.3009
<b>GM</b>						
hMT+	0.0209	0.0009	0.0003	0.0012	$< 10^{-4}$	$< 10^{-4}$
V1	$< 10^{-4}$	$< 10^{-4}$	$< 10^{-4}$	$< 10^{-4}$	$< 10^{-4}$	$< 10^{-4}$
V2	$< 10^{-4}$	$< 10^{-4}$	0.0093	$< 10^{-4}$	$< 10^{-4}$	0.0001
V3	$< 10^{-4}$	$< 10^{-4}$	0.0001	$< 10^{-4}$	$< 10^{-4}$	$< 10^{-4}$
V3A	0.0015	$< 10^{-4}$	$< 10^{-4}$	$< 10^{-4}$	0.0013	$< 10^{-4}$
V4v	$< 10^{-4}$	$< 10^{-4}$	$< 10^{-4}$	$< 10^{-4}$	$< 10^{-4}$	$< 10^{-4}$
<b>GG</b>						
hMT+	0.0005	0.0011	$< 10^{-4}$	0.0015	$< 10^{-4}$	$< 10^{-4}$
V1	$< 10^{-4}$	$< 10^{-4}$	$< 10^{-4}$	$< 10^{-4}$	0.0003	$< 10^{-4}$
V2	$< 10^{-4}$	$< 10^{-4}$	$< 10^{-4}$	$< 10^{-4}$	$< 10^{-4}$	$< 10^{-4}$
V3	$< 10^{-4}$	$< 10^{-4}$	$< 10^{-4}$	$< 10^{-4}$	$< 10^{-4}$	$< 10^{-4}$
V3A	0.0037	0.0050	0.0064	0.0075	0.0062	0.0021
V4v	0.5761	0.4312	0.0010	0.8939	0.9753	0.9986

Table 6.2: Statistical significance (T-tests) for each estimated BOLD responses and their differences by pair. The first 3 columns show the p-values for each estimated response to be different from zero, the last 3 represent the p-values regarding the differences between the estimated responses.

tion of motion across visual areas. Figure 6.5 shows the mean over the three subjects of the indices when considering (A)  $I_{180-0}$ , i.e. comparing  $\Delta_{180}$  with  $\Delta_0$ , (B)  $I_{45-0}$ , i.e. comparing  $\Delta_{45}$  with  $\Delta_0$  and (C)  $I_{180-45}$ , i.e. comparing  $\Delta_{180}$  with  $\Delta_{45}$ . We recall that these indices are related respectively to (see 6.3):

(A) the global population of direction selective cells, irrespective of their directional tuning bandwidth,

(B) a population of relatively narrowly-tuned cells which have a differential response to a 45 degree change in motion direction

(C) a population of relatively broadly-tuned cells which have a large differential response to a direction change of 180 degree but a small (or inexistent) differential response to a 45 degree change.

Furthermore, the ratios  $\frac{I_{180-45}}{I_{180-0}}$  and  $\frac{I_{45-0}}{I_{180-0}}$  respectively give a rough estimate of the

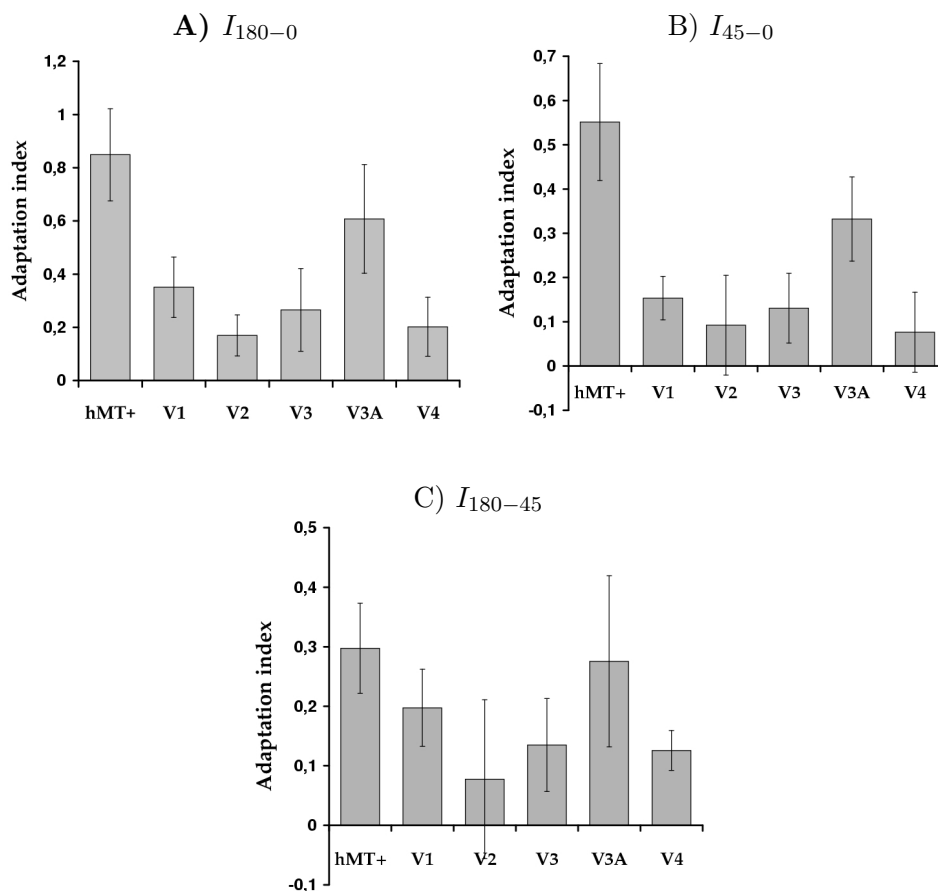


Figure 6.5: Direction selectivity indices averaged across 3 subjects for each visual area. (A) represents the  $I_{180-0}$  mean, which quantifies the normalized difference between  $\Delta_{180}$  and  $\Delta_0$  estimated BOLD responses, presumably proportionally related to the global population of direction selective cells; (B) represents  $I_{45-0}$  related to narrowly tuned direction selective neurons; (C) represents  $I_{180-45}$ , related to broadly tuned direction selective neurons. Error bars correspond to  $\pm 1$  SEM across subjects.

proportion of broad-band and narrow-band cells within the motion direction selective population of each area. The estimated sub-population proportions are presented in figure 6.6.

As shown in figure 6.5, hMT+ clearly appears as the most direction selective area, having the highest values for each index computed, specifically 0.85 for opposite directions ( $I_{180-0}$ ), 0.55 for a smaller angular difference ( $I_{45-0}$ ) and 0.30 for rather high angular difference (i.e. strictly over 45 degree) ( $I_{180-45}$ ). Our result clearly confirms the important proportion of direction selective neurons in this region of the human cortex. We can further derive an estimated proportion of 35% (0.30/0.85) of broadly-tuned versus 65% of narrowly-tuned neurons within the motion direction selective population in hMT+. V3A shows the second most important difference between the estimated responses for  $\Delta_{180}$  and  $\Delta_0$  ( $I_{180-0} = 0.6077$ ), also

suggesting a relatively important proportion of direction selective cells. The estimated proportion of broadly-tuned neurons is 45.4% (0.2756/0.6077) versus 54.6% (0.3321/0.6077) for narrowly-tuned neurons in V3A. V1 also shows significant positive values for our three indices, implying the presence of direction selective neurons as well. However, the index  $I_{180-45}$ , standing for the difference between  $\Delta_{180}$  and  $\Delta_{45}$ , is surprisingly high with respect to  $I_{180-0}$  with respective values of 0.1973 and 0.3508, suggesting an unlikely important broadly-tuned cells proportion of 56.2%. This result is discussed below in the discussion. The  $I_{180-0}$  values of areas V3, V4v and V2, though lower, also suggest the presence of motion direction selective cells but with various sub-population proportions. More specifically, V3 indices suggest a rather equal proportion of narrow and broad neurons (0.1307/0.2655=49.2% and 0.1348/0.2655=50.8% respectively) while V4v direction selective population seems to be more predominantly broad with an estimated proportion of broadly tuned cells of 62.2% (0.1258/0.2021). Note that the HRF estimations for  $\Delta_0$  and  $\Delta_{45}$  had important variances in area V4v, leading to less reliable index values and sub-population proportion estimations. This lack of robustness was also mentioned in the macaque monkey fMRI study of [214]. Nonetheless, the  $\Delta_{180}$  estimated response is significantly positive in the 3 subjects (p=.0518, p<1e-4 and p=0.001 respectively), clearly arguing for direction selectivity in V4v. Finally, V2 shows the smallest  $I_{180-0}$  and  $I_{180-45}$  index values, suggesting a lower proportion of motion selective cells in this area relative to the other areas considered.

#### 6.4.4 Responses to stimulus transient

At each transition between adaptation and test direction, the random dot pattern was reset, leading to a brief noticeable transient. Considering the  $\Delta_0$  estimated BOLD response allows to assess the sensitivity of each area to such a transient only, as every other stimulus parameter (especially the direction of motion) remained constant. The first column of table 6.2. shows the p-value of the T-test comparing the  $\Delta_0$  estimated response and the null vector. We found highly significant p-values (< 10e-4) for areas V1 and V2 in the three subjects. The same observation also holds in V3 and hMT+, but on two subjects respectively, whereas it is less clear in V3A and V4v that the estimated response to a stimulus transient statistically differs from zero. These results reveal the differences of response to a stimulus transient in the above areas, suggesting a veridical representation of the retinal stimulus in V1, V2 and a cruder representation in higher level areas such as V3A and V4v [13]. Note that these differences support the way we defined our index to quantitatively compare the areas sensitivity to motion direction changes.

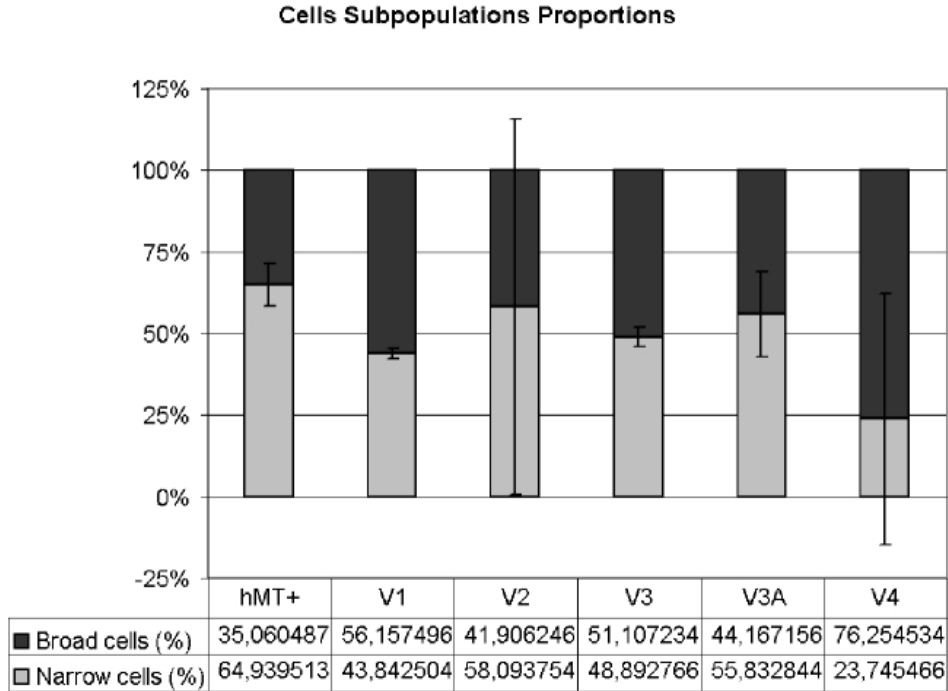


Figure 6.6: Estimated proportions of motion direction selective sub-populations computed from indices ratios. Error bars correspond to  $\pm 1$  SEM across subjects.

## 6.5 Discussion

### 6.5.1 Motion direction selectivity

Our study extends the work of [113]. Regarding hMT+ and V3A, we replicated their results when comparing opposite test direction with respect to adaptation direction (our  $\Delta_{180}$  condition). But we further added a test condition to a lower angular difference of 45 degrees (our  $\Delta_{45}$  condition), a precise BOLD response estimation for each test direction and area considered and statistically relevant comparisons between them, therefore providing a firmer characterization of the motion direction selectivity.

hMT+, directly followed by V3A, are the two areas showing highest indices about their direction selectivity. This general result about the involvement of hMT+ and V3A in motion direction processing is consistent with various reports in the neuroimaging literature [257, 219, 224, 202, 41], see [44] for a review. V3 is also characterized by a significant, though at least twice smaller than in hMT+ and V3A, direction selectivity. These results support the difference for areas V3 and V3A between humans and macaques, as mentioned for instance in [234, 161, 224]. In macaque, V3 is moderately motion and direction selective, but V3A is not. In humans, however, this relationship is reversed: V3A is much more motion selective

than V3. We found the same characterization in the present fMR-adaptation experiment. V2, though direction selective, appears last in our motion direction selectivity hierarchy with the weakest values for our three indices; this result is in line with Huk and colleagues study where V2 appears last with V1.

In V1 and V4v however, our results differ from those from Huk and colleagues. On the one hand, relative to other areas, V4v is weakly direction sensitive in our study, whereas it stands right after V3A in Huk et al. (their figure 4D, p.167). We have stressed above that our V4v datasets were not as robust as in the other areas but also note that the proportion of direction selective cells should not be that different than in V1 according to single cell studies, namely about 25% ([186, 162, 93] estimations are 35%, 27% and 23% respectively). Note also that human area V4 definition is still subject to controversy [222, 254, 15], which might explain the differences observed between both studies.

Regarding our V1 results, the estimated proportion of broad-band cells is at least as large as the estimated proportion of narrow band cells, which stands in contradiction with single cells studies. A possible explanation to this mismatch could be that proposed by Tolia and colleagues who faced the same inconsistency when comparing their macaque fMR-adaptation estimations with electro-physiological data. To explain this discrepancy, they first hypothesized in [214] that V1 and V4 direction selectivity could be increased due to feedback from higher areas such as MT, leading normally non-selective neurons to acquire direction selectivity after adaptation. They very recently published in [213] results from an electrophysiology study that clearly demonstrated this hypothesis in macaque V4, showing classically nondirectional V4 neurons that developed direction selectivity after adaptation. We suggest that this high indices we observed in V1, as well as the high estimated proportion of broad cells in V1 could result from a modulation of selectivity inherited from adapted neurons in higher areas.

Furthermore, it was recently shown in [124], which presents a macaque MT electrophysiology study, that adaptation could change the direction tuning of neurons, at least for sub-populations with preferred direction close to the adaptation direction. Similarly, considering object processing in the macaque Infero-Temporal (IT) cortex, Sawamura and colleagues [185] demonstrated a difference between stimulus selectivity of neuronal adaptation and stimulus selectivity of the neuron.

Taking into account these results from electrophysiological studies, the direction tuning we can infer from our BOLD signal rebound estimations might not be quantitatively linked to actual direction tuning curves of underlying neuronal populations in classical (i.e. non adapted) conditions. We nonetheless claim to show a reliable hierarchy of low-level visual areas, mostly in agreement with the literature. Our study extends the results of Huk and colleagues, and allows us to give a more precise motion direction selectivity hierarchy with hMT+ and V3A

ahead, followed by V1 then V3, V4v and finally V2.

### 6.5.2 Macaque/human homologies in V1 and MT

We note that our  $I_{180-0}$  index values shown in figure 6.5 and the directionality index values from [214] are strikingly comparable in humans and macaques areas MT and V1 respectively. Even if both indices are calculated in a different manner, they are both meant to quantify the BOLD signal rebound when presenting opposite adaptation and test directions. We found 0.85 in hMT+ compared to their 0.84 in macaque MT, and 0.35 in V1 compared to their 0.33 in macaque V1. This similarity may claim for the functional homology between the two species in these areas systematically found in all primates. This similarity is however not as marked in the remaining areas (V2: 0.17 vs 0.35; V3: 0.26 vs 0.37; V3A: 0.61 vs 0.42; V4v: 0.20 vs 1.0). One of the reason might be the specy differences in these areas: various evidences indeed suggest that V3 and V3A differ functionally between macaque and humans [161]; similarly, the homology between human V4v region and macaque V4 is still a subject of controversy as recently revived in [15]. Note also the important difference between the experimental procedure used in both studies: the animals were anesthetized in the study of Tolia and colleagues [214], while our human subjects were awake.

### 6.5.3 Attention, adaptation and direction tuning

The importance of controlling attention in fMRI experiments was clearly demonstrated in [113], which led them to reconsider previous Motion After-Effect (MAE) studies. The authors further emphasized the need to "employ the most similar tasks possible" across blocks or trials. We therefore implemented a rather simple attentional task at the central fixation cross, systematically present at each trial but also between trials (top-up adaptation), enabling us to control both the attention and the fixation of the subject. However, in contrast to Huk et al., our attentional task was not done on the motion signal itself, which was meant to minimize the attentional effects on direction tuning, as shown in [154]. The latter study indeed suggests that paying attention to a given feature (in their study the orientation of objects) increases the functional selectivity of the neural population involved in processing for this feature (in their study in the LOC -Lateral Occipital Cortex-, a region of the human brain involved in object shape processing). Our attentional task was thought to minimize this selectivity changes as it is not linked with any motion estimation judgment.

On the other hand, a first study [182] on V5/hMT+ further refined by [191] in the retinotopic areas have shown that performing an attentional task at the central fix-

ation impacts the peripheral visual field signals, leading to a signal decrease in the peripheral visual field with increasing attentional load. Our task was a low load task, thus minimizing this effect and our data nonetheless mostly show statistically significant differences between the three test conditions. However, how attention modifies the neuronal signals and consequently the BOLD signal is still poorly understood [12] and is thought to be a combination of enhancement in the neuronal response (gain) and a sharpening of the selectivity. We claim that the adaptation index we computed minimizes this attentional bias thanks to our normalization used to get rid of the attentional task effects (see paragraph 6.3).

Our simple task at the fixation cross is therefore a trade-off between attentional control, central visual field fixation control, neural selectivity changes and BOLD signal decrease in the peripheral visual field. We claim that our attentional control as such leads to a minimally biased characterization of post-adaptation motion direction selectivity in different low-level visual areas, leading to a reliable hierarchy among the latter.

#### **6.5.4 fMR-adaptation methodology**

fMR-adaptation is a relatively recent paradigm enabling the measurement of functional neuronal populations properties. It is therefore still necessary to develop and study the methodological aspects of this tool.

Our study brings another proof of the efficiency of event-related adaptation paradigms as a tool to examine the functional selectivity of cortical areas to a special feature, here the direction of visual motion. Most fMR-adaptation studies have been performed on high-level processing (objects, face, numbers representation), our results confirm that low-level processing issues can also be tackled with this paradigm.

In addition, our paradigm is minimally constraining. We do not use surface coils which increase the installation time of the subject; our attentional task is easily understood by the subjects and can reliably be performed; only a single, one hour acquisition session per subject is needed for the adaptation experiment, as compared to hours of scanning usually averaged in most adaptation studies. It is thus a straightforward experimental setup leading to reliable measures as proved by our error bars, which could be an important point for a use of the adaptation paradigm in a more constrained environment such as clinical. It is crucial to stress the contribution of accurate and unconstrained analysis tools such as the HRF toolbox which, combined with imaging technical improvements will help in detecting and characterizing subtle signals while alleviating scanning setup and durations.

Importantly, we want to address a typical aspect of fMR-adaptation paradigms

not discussed in the literature. To our knowledge, every event-related adaptation paradigm published so far includes a short blank period between the adaptation and the test stimuli. This appears rather counter-intuitive as this blank period may imply a decrease in the adaptation signal, therefore inducing a bias in the measured rebounds. The only justification for a blank period could come from [13] who studied the effect of the Stimulus Onset Asynchrony on the adaptation effect. However, their psychophysical results claim for  $\approx 2$ sec SOA (their figure 7) rather than 1.125sec (the smallest they tested); this result does not fit with SOA of less than 1 sec as mostly found in event-related fMR-adaptation studies. Another possible explanation for this blank could be to set a stimulus transient at the onset of the test trial in order to increase the neurons responses. We decided to avoid this blank period in our paradigm, thus setting the test trials just after the adaptation stimulation to keep neurons adapted all along the run except during the test trials. Doing so, we obtained reliable results leading to conclusions mostly in line with previous characterization of direction processing in human low-level visual areas. We conclude that this blank period was empirical in the first studies and remained in the next ones, without justification or discussion, although it actually does not appear necessary and is rather counter-intuitive.

## 6.6 Conclusion

Our study has shown that motion direction selectivity is area specific in low-level visual cortex. We achieved finer measurements of this particular feature with a minimally constraining adaptation paradigm. The global hierarchy among the different visual areas puts hMT+ and V3A as the most direction selective, followed by V1, V3, V4v and V2. This ordering further supports the classical Ventral-Dorsal classification. We interestingly found similar direction indices in V1 and hMT+ as Tolia and colleagues [214] previously showed in macaque V1 and MT, which might further support homologies in both species. We also found in human V1 and V4 a comparable adaptation induced selectivity effect recently demonstrated in the macaque by the same group, reviving the notion of context-dependent neuronal tuning. Last but not least, we have designed a relatively fast and unconstrained adaptation paradigm that could inspire further studies to characterize normal subjects and patients visual areas responses to various visual features, nonetheless keeping in mind the modulation of selectivity induced by adaptation and attention.

To confirm the functional segregation we found, future work may imply high resolution anatomical studies to identify the local cytoarchitecture underlying each area. A mathematical model of neuronal adaptation in the different neural populations and visual areas may also help to clarify the origin of the BOLD signal rebound ob-

served and its possible link to directionally tuned sub-populations activity. Finally, revealing the underlying distributed connectivity network among the above areas may also be achieved using Diffusion weighted MRI. We address this question in the next chapter.

# Chapter 7

## Anatomical connectivity in the low-level visual cortex

### Contents

---

<b>7.1</b>	<b>DTI connectivity mapping and the human visual brain: state of the art</b>	<b>192</b>
7.1.1	DTI connectivity mapping techniques	192
7.1.2	Human visual cortex connectivity: previous work	193
<b>7.2</b>	<b>Methods</b>	<b>195</b>
7.2.1	MR data acquisition	195
7.2.2	Processing pipeline	196
7.2.3	Connectivity maps and fiber tracts computation	200
7.2.4	Seed voxels placement	203
<b>7.3</b>	<b>Results</b>	<b>205</b>
7.3.1	Optic radiations	205
7.3.2	Callosal connections	208
7.3.3	hMT+ intra-hemispheric connectivity	209
<b>7.4</b>	<b>Discussion</b>	<b>210</b>
7.4.1	Visual cortex connectivity	211
7.4.2	Methodological issues	214
<b>7.5</b>	<b>Conclusion</b>	<b>216</b>

---

Understanding the relationship between anatomical structure and function is a key objective in neuroscience. In the last decades, neuroimaging advances have been providing ever more promising means to non-invasively address this fundamental issue, thus opening the possibility to investigate in vivo normal and patients cerebral architecture and activity. This is especially true for MRI, which allows to combine anatomical (structural MRI), functional (functional MRI) and white matter connectivity (diffusion MRI) information at a spatial resolution of a few millimeters. We showed in chapters 5 and 6 how anatomical and functional images could be jointly used to identify various visual areas and functionally characterize them. In this chapter, we propose to refine our knowledge of the human visual cortex by studying anatomical connections using a recently developed framework to analyze Diffusion Tensor Images. Using a Riemannian-geometry based connectivity mapping approach, we first identified the optic radiations connecting the LGN to area V1. We then studied interhemispheric connectivity, estimating the white matter connectivity between low-level visual areas and the splenium. Finally, we investigated intrahemispheric connectivity between hMT+ and occipital retinotopic areas.

## **7.1 DTI connectivity mapping and the human visual brain: state of the art**

In this section, we first give an overview of the different approaches used to estimate the anatomical connectivity of the human brain from DTI. We then review their main applications to the human visual cortex.

### **7.1.1 DTI connectivity mapping techniques**

Diffusion Tensor Imaging (DTI) models the probability density function of the three-dimensional water molecules motion, at each voxel of a DT image, by a local Gaussian process whose covariance matrix is given by the diffusion tensor [8]. Among other applications including the characterization of local tissue anisotropy, DTI can be used to estimate the anatomical connectivity across remote brain regions. Various approaches have been proposed to tackle this problem. They can be divided into three main classes: local, stochastic and geometric approaches.

Local approaches, based on line propagation techniques, rely on the fact that the eigenvector of the diffusion tensor associated with the major eigenvalue provides a relatively accurate estimate of the orientation of fiber bundles at each voxel. These methods may be refined to incorporate some natural constraints such as regularity or local uncertainty and to avoid being stopped in regions of low anisotropy [153, 130]. All these efforts aim to overcome the intrinsic ambiguity of diffusion tensor data arising from partial volume effects at locations of fiber merging, kissing or crossing.

If they can provide relatively accurate models of the main white matter macroscopic bundles, these methods are sensitive to noise and partial volume effects and cannot give a quantitative measure to evaluate the degree of connectivity between brain locations.

Stochastic tractography algorithms were introduced by modeling the uncertainty of the local fiber orientation [10, 77]. Through uncertainty propagation, they provide a powerful means to evaluate the probability of connection between remote points of the white matter. However, the intrinsic drawback of these methods is their computational complexity since it is necessary to resort to Markov Chain Monte Carlo methods or to evaluate probability density functions at enough locations of the space of interest.

Geometric methods use either Level Set methods [157, 134, 116], Fast Marching methods [169] or iterative sweeping techniques [115] to evolve a front on the basis of the diffusion tensor directional information. Although more naturally able to exploit the whole tensor information in the connectivity estimation, these approaches are usually prone to interpolation errors at the boundary of the evolution domain, which may lead to erroneous connections in highly convoluted areas. Besides, this class of methods suffers from a high computational complexity like the stochastic algorithms. Finally, most implementations work directly on the whole DT image, which can lead to anatomically impossible connections across non white matter tissue.

### **7.1.2 Human visual cortex connectivity: previous work**

DTI based connectivity mapping of the human visual cortex has been addressed by various groups with different protocols and methods. Using a classical streamline tractography with smooth interpolation of the tensor field [153], [40] could reconstruct various bundles including visual pathway fibers. They showed fibers passing through the splenium, with a specific topology: anterior splenium fibers head to the parietal lobe while dorsal splenium fibers progress toward the occipital cortex. However, although the distinction between these two bundles is clear, the fibers they show fail to reach any precisely defined target on the grey matter and callosal-occipital fibers seem to rapidly converge to a single path (see figure 1 in [40]). They could, more convincingly, show a topology within the geniculo-occipital fibers, where medial (respectively lateral) LGN fibers terminate in a more superior (resp. inferior) part of the occipital cortex. Using a similar streamline tractography algorithm, [22] have identified in a single subject different visual fiber bundles including occipito-frontal and occipito-temporal fibers. In a subsequent study, [23] have identified different visual fiber bundles: (i) the optic tract from the chiasm to the LGN; (ii) the optic radiations from the LGN to the occipital cortex, which can be further divided into a ventro-temporal bundle ending in the lower lip of the

calcarine sulcus and a dorsal bundle terminating in the upper lip of the calcarine sulcus; (iii) a splenium bundle connecting both occipital poles; (iv) U-shaped occipito-temporal fibers; (v) the controversial Inferior Longitudinal Fasciculus (ILF) directly connecting the extrastriate occipital cortex and temporal lobes. Despite these interesting findings, no functionally defined areas were used and data were mainly analyzed on a single mean DT image obtained through the averaging of different subjects, hence diminishing the possible interpretations of their findings when one considers the strong anatomico-functional variance across subjects.

The group of Ciccarelli, Toosy and colleagues used the Fast Marching Tractography (FMT) technique [167] to investigate 3 fiber bundles: the pyramidal tract, anterior callosal fibers and, more interestingly for our study, the optic radiations. They first concentrated on methodological issues, demonstrating the inter-subject reproducibility [33] as well as the inter-observer reproducibility [31] of the reconstructed tracts. More recently, they applied this technique to study changes in the optic radiation of patients affected by a specific optic nerve injury optic neuritis [32]. Note that the FMT method has been partly validated in a combined study on macaques and humans, showing a part of the cortico-spinal tract and the optic radiations in both species [168]. Note however that the authors acknowledge the currently limited spatial resolution in DTI which prevents reliable tractography in macaques and therefore a true validation.

As of today, only a few studies have combined fMRI and DTI to study the visual cortex. In the above mentioned study, [40] used fMRI activation maps to roughly identify the LGN and the occipital visual cortex. [242] demonstrated that the fractional anisotropy was lower in the activated occipital cortex than in the optic radiations. This is consistent with the known relative isotropy of grey-matter voxels as compared with white-matter voxels [174]. Using a probabilistic tractography method, [215] completed this work, showing a correlation between the estimated optic tracts mean FA values and the degree of fMRI activity within the visual cortex but, like the former, they did not functionally identify the occipital visual areas they were considering. To our knowledge, the most complete and precise study in the literature was done by [54] at Stanford. They combined a classical streamline tractography method with a functional identification of occipital retinotopic areas to recover occipital fiber tracts passing through the splenium. They demonstrated a good spatial matching in the splenium of independently estimated fibers starting from left and right occipital poles. More specifically, they found a topology in these tracts in which (i) dorsal (respectively ventral) cortical regions project dorsally (resp. ventrally) into the splenium, in agreement with a macaque autoradiography study, (ii) a foveal-periphery gradient can be found in the anterior-posterior direction of the splenium.

In the present study, we used a Riemannian geometry based connectivity mapping technique proposed in [133] and a recently introduced Fast Marching implementation [176] to assess the anatomical connectivity across individually identified areas in the low level visual cortex. The method estimates the anatomical connections of the white matter as geodesics in  $\mathbb{R}^3$  equipped with a Riemannian metric derived from the diffusion tensor. Besides its robustness and efficiency, this approach naturally restricts the estimation within the white matter voxels and further provides statistics of a local connectivity measure along each estimated fiber. We first validate this methodology by recovering typically known fiber tracts before addressing new issues regarding intra-hemisphere connectivity in the occipital visual cortex.

## 7.2 Methods

### 7.2.1 MR data acquisition

Subjects participated in two separate scanning sessions. A scanning session systematically starts with a fast low-resolution anatomical localizer to appropriately set the subsequent scans slices location, followed by the functional and/or diffusion scans, then the phase map acquisition is done before ending with a T1-weighted image acquisition. These high resolution anatomical scans were used as references to coregister the different sessions.

In the first session, the functional scans, later used to identify the retinotopic areas and the hMT+ complex, and diffusion weighted images were acquired. However, due to an acquisition problem, the phase map could not be reconstructed which is particularly problematic considering the important geometric distortions of the echo-planar diffusion weighted images (see below). As soon as this problem was solved, we acquired in a second session new diffusion weighted images and the corresponding phase map for the same subjects. As we were not acquiring functional images, we took advantage of the saved time to increase the number of repetitions for each direction, thus increasing the diffusion-weighted images signal to noise ratio. We also acquired a T1-weighted image to coregister data from both sessions.

### fMRI

During each functional scan, 151 Echo Planar Images were acquired over 5 mn 19 s using our coronal sequence (see paragraph 2.4.4). Each functional image spans 20 coronal slices 3mm thick and  $2 \times 2 \text{mm}^2$  in plane resolution, approximately orthogonal to the calcarine sulcus covering the occipital retinotopic areas and extending anteriorly to confidently include hMT+ region [56]. The first five images (10.555 s) were systematically discarded to avoid magnetic saturation effects. The 144 following

images correspond to the visual stimulus per se. The last two images were taken to allow slice-timing correction preprocessing.

### Diffusion Tensor Imaging

As mentioned in paragraph 2.4.4, we first tried different acquisition parameters to obtain the best diffusion weighted images. We finally used 12 diffusion directions for  $b=1000 \text{ s.mm}^{-2}$ , which is consistent with other studies [99] and allowed us to increase the number of repetitions to achieve a better SNR. Each gradient directions was repeated 6 (first session) or 12 times (second session). The other useful parameters are  $TR=10000\text{ms}$ ,  $TE=86\text{ms}$  and the voxel size  $2\times 2\times 2 \text{ mm}^3$ .

#### 7.2.2 Processing pipeline

Each dataset was analyzed on a subject basis to avoid undesirable normalizing effects such as the strong smoothing implied by this procedure. [242] showed it was possible to obtain geometrically matched fMRI and DWI with appropriate acquisition sequences, therefore avoiding various distortions correction steps. However, these images are not coregistered with the anatomical image and this procedure supposes to acquire data with the same volume prescriptions. In this study, as we considered complementary information from 3 different MRI modalities (anatomical, functional and diffusion-weighted images), acquired two distinct sessions for each subject and used different slice prescriptions for the different modalities, a reference space had to be chosen to coregister all these images together. We used the mean T2-weighted image (i.e. obtained without diffusion sensitization or  $b=0 \text{ s.mm}^{-2}$ ) further corrected for EPI geometric distortions (see below) as reference image. We note *umean T2* this reference image. This choice minimized the deformations and interpolations of the diffusion-weighted images acquired within the same run using a similar sequence. Each type of image received specific processings detailed in the following paragraphs and the extracted useful information was finally coregistered to the *umean T2* reference image. Figure 7.1 summarizes the overall processing pipeline used in this study.

#### Anatomical image.

High resolution anatomical images acquired in both sessions allowed precise inter-session coregistration using SPM2 algorithm. We note  $M1$  the estimated transformation mapping anatomical image from session1 to anatomical image from session2. The latter was further coregistered with the *umean T2* reference image by transformation  $M2$ . Besides, structural information was extracted from both anatomical scans. Using the methods described in chapter 3, models of GM/WM interfaces required to segment the retinotopic areas (see chapter 5) were obtained from session1

Session 1: Visual Areas Mapping

Session 2: Anatomical Connectivity

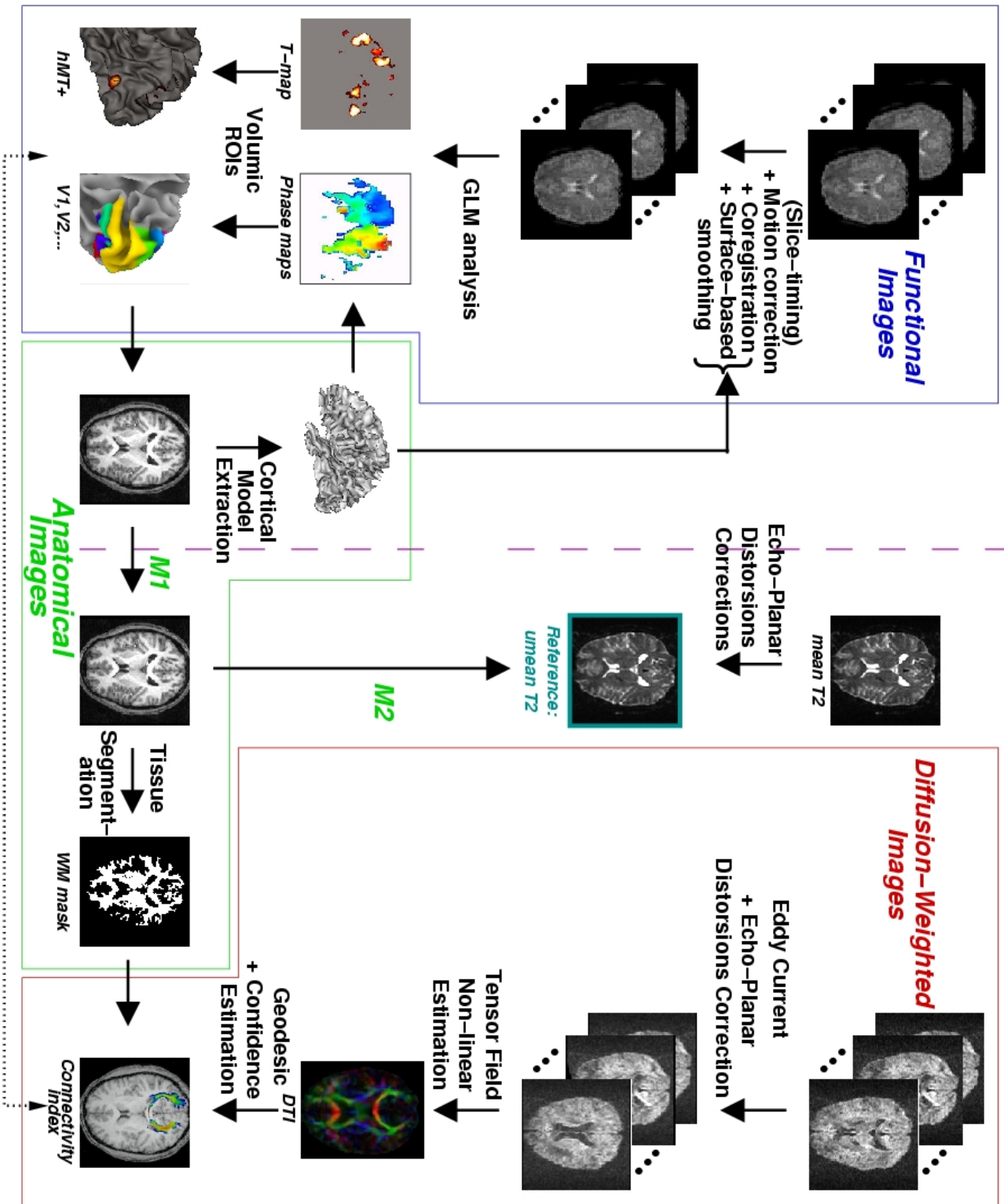


Figure 7.1: The image processings pipeline. See text for details.

anatomical image. A segmentation of session2 anatomical image was performed to obtain a white matter tissue mask in which the connectivity mapping computations were constrained.

### **Visual areas functional definition.**

Functional images for the retinotopic and hMT+ mapping were first realigned with the INRIAalign toolbox [76] and coregistered with the anatomical image with SPM2, then smoothed through the cortical surface based smoothing method described in chapter 3, with a 3mm equivalent Gaussian filter FWHM. A high-pass and a low-pass filtering were also performed on the time-courses to respectively remove low-frequency signal drifts and high frequency noise. Subsets of connected voxels were extracted for each area using the method described in chapter 5 and further used as ROIs in the connectivity analysis. However, diffusion anisotropy is relatively low in grey matter voxels [174], such as in the visual cortex [242], thus considerably limiting the directional information provided by DTI to evaluate the anatomical connectivity between grey matter regions. We therefore defined white matter ROIs, considering the white matter voxels closest to the cortical ROIs. Specifically, the hMT+ volumic ROIs were manually drawn based on the activation maps, selecting the white matter voxels closest to suprathreshold cortical voxels in the expected location of hMT+; the retinotopic areas volumic ROIs were automatically computed from their identification on the GM/WM interface by projecting the respective surface-based labels along the surface normal inside the white matter voxels. Each ROI voxels subset was then coregistered to the *umean T2* reference image by the transformation  $M1 \circ M2$  and further masked to solely lie within the white-matter mask extracted from the high resolution anatomical image. Possible intersections between each pair of ROIs were also removed from the analysis.

### **Diffusion weighted images.**

**T2 image:** the 8 T2-weighted images were motion corrected using INRIAalign before being averaged. The resulting mean T2 image was then processed to correct geometric EPI distortions caused by magnetic susceptibility inhomogeneities, i.e. magnetic field inhomogeneities particularly found at the interfaces between different tissues [117]. Based on the phase map acquired during session2, i.e. an image mapping the spatial distribution of field inhomogeneities, we used the SPM interfaced toolbox "Fieldmap" to compute and apply a voxel displacement map accounting for these susceptibility artefacts. As mentioned above, the resulting *umean T2* image served as reference image for connectivity maps computation.

**Diffusion-weighted images (DWI):** DWI data were first preprocessed to minimize the distortions induced by eddy-currents and related to the large diffusion-sensitizing gradients. We used the algorithm proposed by [145] and implemented within the BrainVisa package. Briefly, this method uses a 2D image registration technique to realign each DWI slice with its corresponding standard T2-weighted slice. A scale factor, a translation and a shearing are the parameters for the slice and image dependent affine transformation searched. The mutual information is used as a similarity measure to estimate the transformation parameters. We then applied to the resulting images the EPI geometric distortions correction algorithm used for the mean T2 image.

**Diffusion Tensor Image computation:** once the DWI are coregistered with our reference image, we can estimate the diffusion tensor image (DTI), i.e. a field of 3x3 real symmetric positive-definite tensors along the image domain  $V$ . This is done using the Stejskal-Tanner equation [206] for anisotropic diffusion, which relates the magnetic resonance signal attenuation to the diffusion tensor  $D(v)$  and the sequence parameters:

$$S_k(v) = S_0(v) \exp(-bg_k^T D(v) g_k) \quad \forall v \in V, k = 1, \dots, M$$

where  $(g_k)_{k=1, \dots, M}$  are the  $M$  normalized non-colinear gradient directions corresponding to each DWI  $(S_k)_{k=1, \dots, M}$  and  $b$  is the diffusion weighting factor. In our protocol,  $M = 12$  and  $b = 1000 \text{ s.mm}^{-2}$ .

The classical technique usually applied to compute the diffusion tensor field  $D$  from DWI relies on a least square estimations of its coefficients at each voxel  $v$ . It boils down to searching the optimal  $D \in S^+$ , the set of 3x3 real symmetric positive-definite matrices, minimizing the objective functional:

$$\mathcal{E}(S_0, \dots, S_M) = \sum_{k=1}^M \psi\left(\frac{1}{b} \ln \frac{S_k}{S_0} + g_k^T D g_k\right)$$

where  $\psi : \mathbb{R} \rightarrow \mathbb{R}$  is the classical squared residual  $\psi(x) = x^2$ . Although computationally efficient, this approach cannot strictly ensure the expected positive definiteness of each diffusion tensor. Alternative algorithms have been proposed to overcome this drawback, e.g. [243, 145, 225]. Here, we used a non-linear robust gradient method proposed in [135] which naturally evolves in  $S^+$ , therefore systematically leading to symmetric and positive definite solutions for  $D$ . The Huber's M-estimator was chosen for the  $\psi$  function with the tuning constant  $k = 1.2107$ , which allows to achieve an asymptotic efficiency of 95% on the standard normal distribution:

$$\psi(x) = \begin{cases} x^2 & \text{for } |x| \leq k \\ k(|x| - \frac{k}{2}) & \text{for } |x| > k \end{cases}$$

We have observed particularly significant differences between the two estimation methods in highly anisotropic regions, such as the corpus callosum, where the least square method could lead to nonpositive tensors. In such cases, the nonpositive eigenvalues are artificially set to a very small non-null value, leading to unreliable, highly planar (with a null eigenvalue) or linear (with a single positive eigenvalue) anisotropic tensors and possibly to numerical instabilities in subsequent tensor based computations. This situation, naturally, never occurs with the intrinsic gradient descent method as the solution necessarily belongs to  $S^+$ . Figure 7.2 illustrates these differences with a close up of an axial slice containing the splenium of the corpus callosum.

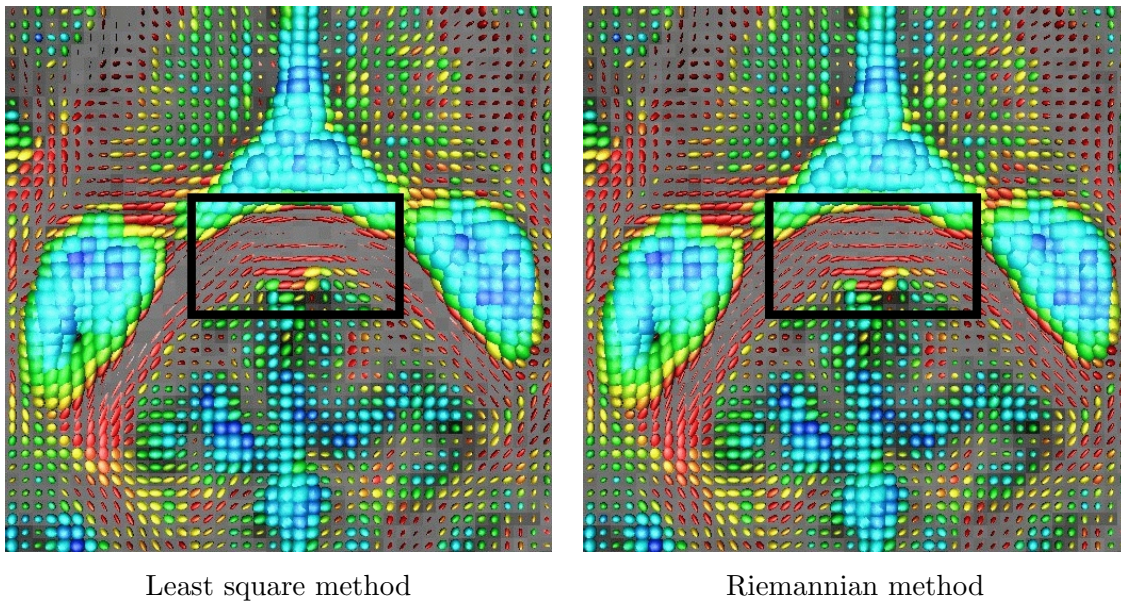


Figure 7.2: Estimation of Diffusion Tensors: comparison between classical least square (left) and gradient descent in  $S^+$ , the set of symmetric positive definite 3x3 matrices (right). (Blue: low anisotropy; Red: high anisotropy). Notice the difficulty to represent tensors in the middle of the corpus callosum with the least square approach, suggesting degenerate cigar-shaped tensors in this region.

### 7.2.3 Connectivity maps and fiber tracts computation

#### The Riemannian geometry framework applied to DTI

We used an approach based on a Riemannian geometric framework to compute (i) a distance function to a given point of interest (or *seed point*)  $x_0$ , (ii) the putative fiber path linking any voxel of a given brain region  $V$  to  $x_0$  and (iii) a connectivity map, i.e. a confidence measure associated with each fiber. In this geometrical formulation of DTI connectivity mapping, the DTI is modeled as a Riemannian manifold  $M$  whose metric is directly related to the diffusion tensor  $D$  modeling the

local diffusion properties of water molecules. As shown in [133, 157], the metric  $G$  of  $M$  is given by  $G = D^{-1}$ . From this metric, a distance function  $u(x_0, x)$  between a given seed point  $x_0$  and any other location  $x$  of the brain mask  $V$  can be evaluated as the solution of the following initial value problem:

$$\begin{cases} \|\nabla u(x_0, x)\|_G = 1 & \forall x \in V \setminus \{x_0\} \\ u(x_0, x_0) = 0 \end{cases} \quad (7.1)$$

This is the well-known Eikonal equation on the Riemannian manifold  $(M, D)$ . The solution  $u$  at any voxel  $x \in V$  can be interpreted as the minimum time  $t \geq 0$  to reach  $x_0$  starting from  $x$  on the manifold  $M$ . Considering the low anisotropy in the grey matter tissue, we consider for  $V$  the set of white matter voxels obtained from a segmentation of the anatomical image (see methods).

The geodesics of  $M$ , which can be derived from a continuous gradient descent over  $u$  along the direction given by  $-\nabla u$ , are considered as putative white matter bundles linking any voxel  $x \in V$  to  $x_0$ . As such, a geodesic connecting any voxel  $x \in V$  to the seed voxel  $x_0$  always exists. If an actual white matter fiber connects  $x$  and  $x_0$ , the associated geodesic coincides with the fiber. However, for any  $x \in V$ , the associated geodesic does not necessarily coincide with an *actual* white matter fiber. It is indeed highly unlikely from an anatomical point of view that a given brain locus could be directly connected to *every* other brain location. To overcome this issue, connectivity measures along each geodesic can be estimated, enabling to discriminate likely and unlikely white matter connections. In this study, we considered for each estimated geodesic statistics of the following local confidence measure:

$$C(x) = \|\nabla u(x)\|_E$$

We claim that  $C$  is a natural local measure of connectivity since, as we will see shortly, it can also be interpreted as the solution of an optimal control problem and measures the local "speed" of water molecules propagation in the white matter tissue. From this local connectivity index, we compute its first and second order statistics along the geodesic:

$$\mu(x) = \mathbb{E}[C(x)] \quad \text{and} \quad \sigma(x) = \sqrt{\mathbb{E}[C(x)^2] - \mathbb{E}[C(x)]^2}$$

An ideal fiber linking  $x$  to  $x_0$  will typically have a large mean value  $\mu(x)$  and a small standard deviation  $\sigma(x)$ . This connectivity measure provides a means to distinguish likely and unlikely fibers. Since each voxel  $x$  in  $V$  can be assigned a geodesic reaching  $x_0$ , we have a couple  $(\mu(x), \sigma(x))$  at each voxel. In the remainder, we note  $\mu$ -map and  $\sigma$ -map the respective images of  $\mu$  and  $\sigma$  values.

## Numerical resolution methods

Regarding the numerical resolution of equation (7.1) and the computation of geodesics and connectivity measures, we used two different methods respectively

based on the level set framework and a control theory formulation. If both interpretations are mathematically equivalent, they focus on different aspects of the problem. In the level set (or dynamic) approach, the emphasis is on the description of the manifold geometry, while in the optimal control point of view (or static) approach, the emphasis is on the optimal dynamics, which coincides with the intrinsic gradient of the distance function. We give below an overview of both methods.

#### *Level set method*

We first used the level set method described in [133, 134] and implemented in C++ by Christophe Lenglet at the Odyssee Laboratory. As shown e.g. in [164, 197], equation (7.1) can be reformulated in the level set perspective. This is achieved by introducing a new function  $\psi$  such that the evolving function  $u_t$  is a level set of  $\psi$ :

$$u_t = \{x \in V : u(x) = t\} = \{x \in V : \psi(x, t) = 0\}$$

Then, it can be shown [164] that finding  $u$  satisfying equation (7.1) is equivalent to solving the Partial Differential Equation (PDE):

$$\begin{cases} \psi_t + \|\nabla\psi\|_G = 0 & \forall t > 0 \\ \psi(x, 0) = \psi_0(x) \end{cases} \quad (7.2)$$

Where  $\|\nabla\psi\|_G = \sqrt{D\psi^\top G^{-1}D\psi}$ .

Starting from  $x_0$ , the rate at which the front propagates is given by the local diffusion tensor  $D$ . The larger the local tensor eigenvalues are, the faster the local front propagation will be in the associated eigenvector directions. Hence, evolution is fastest along white matter paths. The front arrival time at each voxel generates the distance function to  $x_0$ . Geodesics are then obtained by back-propagating along the function  $u$  gradient field from any voxel  $x \in V$  towards the origin  $x_0$ . The related connectivity measures  $\mu(x)$  and  $\sigma(x)$  are finally estimated during the computation of this optimal pathway linking  $x$  to  $x_0$ , by integration of the local criterion  $C$  along the entire geodesic.

#### **Fast Marching Tractography method**

Facing two major limitations of the level set approach, namely the high algorithmic complexity leading to relatively long computational time and, more importantly, numerical difficulties to properly deal with the white matter mask boundaries, we then used a very recently proposed formulation of the problem. By recasting problem (7.1) into the optimal control theory framework and numerically solving it with Fast Marching Method (FMM), its authors could propose a considerable computational improvement to evaluate the quantities of interest. The theoretical issues as well as the C++ implementation were developed in a collaboration between the Odyssee laboratory and the UCLA vision Laboratory. We refer the

reader to [176] for an indepth study of the approach and its contributions. Briefly, in this formulation, the problem comes down to estimating the optimal vector field  $f^*$  (optimal dynamics) corresponding to the field of the geodesics velocity in  $M$  (which also coincides with  $-\nabla u$ ). This is achieved using a Fast Marching based algorithm. Starting the front from an initial seed position  $x_0$ , the Fast Marching Method (FMM) systematically marches the front outwards one grid point at a time, by always locating the proper grid points configuration (the optimal simplex) yielding the smallest update value of the distance function  $u$ , a principle named causality. FMM thus constructs the optimal dynamics  $f^*$  by propagating the information "one way", requiring one single pass over the domain  $V$ . The distance function  $u$  is now a byproduct of the algorithm, no longer necessary for subsequent computations. Besides, the connectivity statistics maps  $\mu$  and  $\sigma$  are computed "on the fly". Indeed, based on the optimal simplex, one only needs to compute the local value for  $C$  and  $C^2$  and then build on previous values to derive  $\mu$  and  $\sigma$  associated to the geodesic linking  $x_0$  to the current voxel. If needed for visualization purposes for instance, the geodesic paths can be straightforwardly reconstructed by following the optimal dynamics  $f^*$ .

The Fast Marching Tractography (FMT) approach detailed above offers many advantages over existing work, including the level set method we first used:

- the method is efficient since it computes simultaneously the optimal dynamics and the statistics of our local connectivity measure; besides, the explicit computation of the geodesics is not mandatory to get the connectivity measure maps,
- the computation time is dramatically improved, from 20 minutes to get the distance function with the level set formulation to 7 seconds with the FM algorithm,
- the method naturally handles the constrained computation within highly convoluted regions such as in the occipital cortex white matter (figure 7.3),
- the algorithm exhibits a higher robustness with respect to noise over the level set implementation, as validated by numerical experiments on synthetic datasets.

The results we present below were systematically obtained with the FMT algorithm. Notice however that the level set method led to qualitatively similar results, although the computation time was by far higher and the numerical issues mentioned above could lead to anatomically impossible front propagation (figure 7.3), requiring iterative manual modifications of the white matter mask.

#### 7.2.4 Seed voxels placement

A crucial aspect for any fiber tracking method is the location of the initial seed. The seeds for the FMT algorithm were selected depending on the considered tracts.

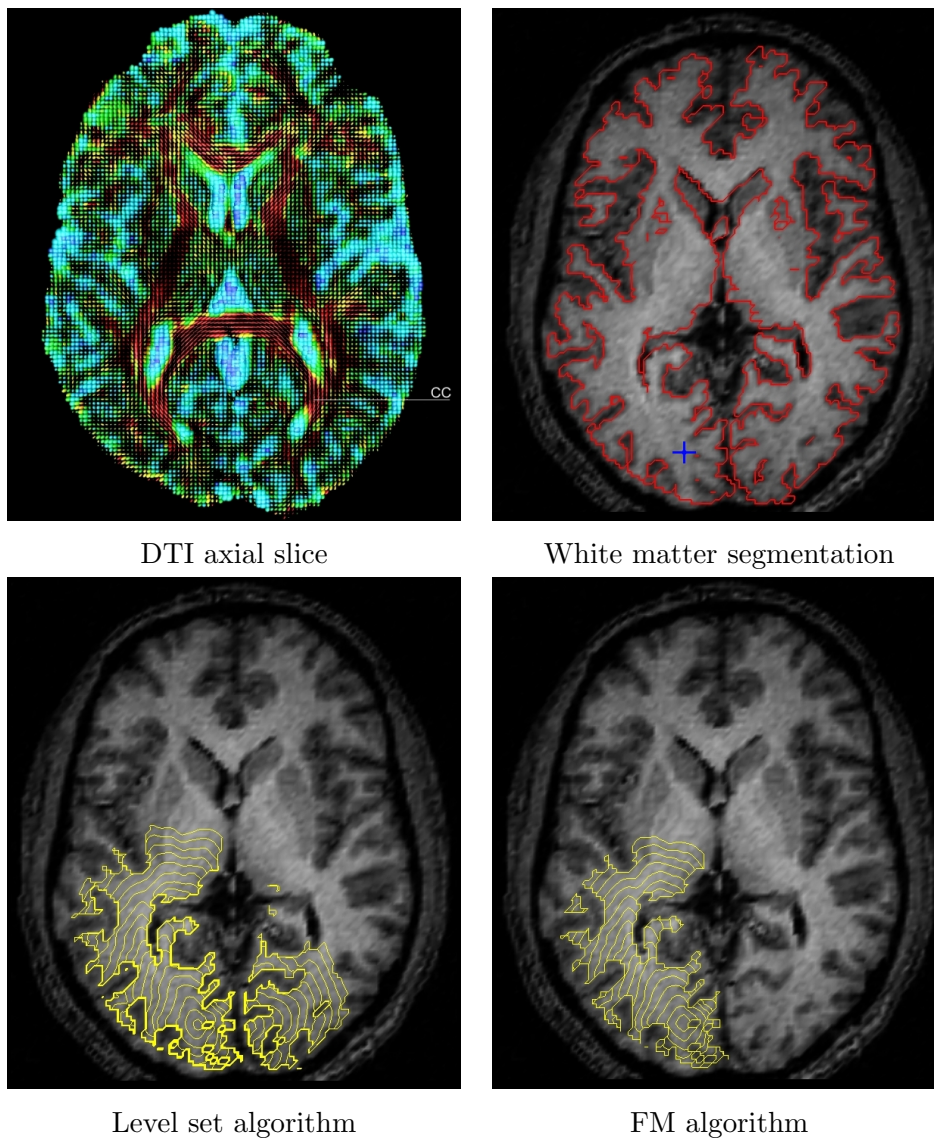


Figure 7.3: Distance function computed from DTI data (a) to an occipital seed voxel, the blue cross in (b) in a white matter mask (red line in (b)). Yellow lines depict distance function isovalues in the range  $[0;1500]$ , computed through the level set (c) or the Fast Marching (d) algorithms. Front diffusion of the level set method does not necessarily respect the white matter mask topology, leading to anatomically impossible connections through CSF voxels (c). This numerical problem is avoided in the Fast Marching method which naturally respects the mask topology (d).

#### *LGN seed voxels identification*

Lacking a precise functional localization of the LGN, we first identified LGN seeds voxels with a classical streamline technique. To do so, we manually selected in each hemisphere a rough thalamus sub-region which obviously included the expected

LGN location. More specifically, based on both anatomical and diffusion tensor image prior information, the initial region was identified anterior to the lateral ventricles and only voxels with a relatively high anisotropy ( $FA \geq 0.15$ ) were kept. Diffusion tracts starting from each selected voxel were estimated with a classical streamline tractography technique [130] and further automatically filtered to keep the fibers heading to the ipsilateral retinotopically identified area V1. Only fibers reaching a 3 voxels wide band around the functionally defined V1 region were kept. This approach is very similar to that of Conturo and colleagues [40], although we did not oversample the DTI data, thus getting less fibers than the latter work. The starting voxels of the remaining fibers were finally labeled as the LGN voxels. We typically found a region of 5 connected voxels in each hemisphere, consistent with the reported LGN size both in previous anatomical [108] and fMRI studies [27]. Beyond yielding an anatomical connectivity based delineation of the LGN, the reproduction of the well-known visual pathway as well as the likely extent and location of the LGN ROIs validates our diffusion-weighted images quality as well as our image processing pipeline.

#### *Other tracts*

For connectivity mapping starting from the functionally identified visual areas, we simply used the white-matter ROIs defined with the procedure previously detailed.

## **7.3 Results**

We first validated our protocol and connectivity mapping technique on the previously characterized optic radiation tracts before investigating callosal connectivity and intra-cortical connectivity across the functionally identified visual areas.

### **7.3.1 Optic radiations**

As one can notice from the above literature overview, the optic radiations were often reconstructed in diffusion tractography studies. We therefore decided to validate our fiber tracking approach by considering this well characterized fiber bundle, which links the Lateral Geniculate Nucleus (LGN) to area V1 in the occipital cortex.

Starting from each previously identified LGN voxels (see methods), we computed the connectivity index maps with the FMT technique. As we were not concerned here with inter-hemispheric connections, the FMT computation was restricted to the ipsi-lateral hemisphere of the seed voxel. Figure 7.4 shows two  $\mu$ -maps, one per hemisphere, in two subjects. As each map is restricted to its respective hemisphere, we merged them in a single image and overlaid the result on an axial slice of subjects' anatomical image. The seed voxel of each  $\mu$ -map is shown

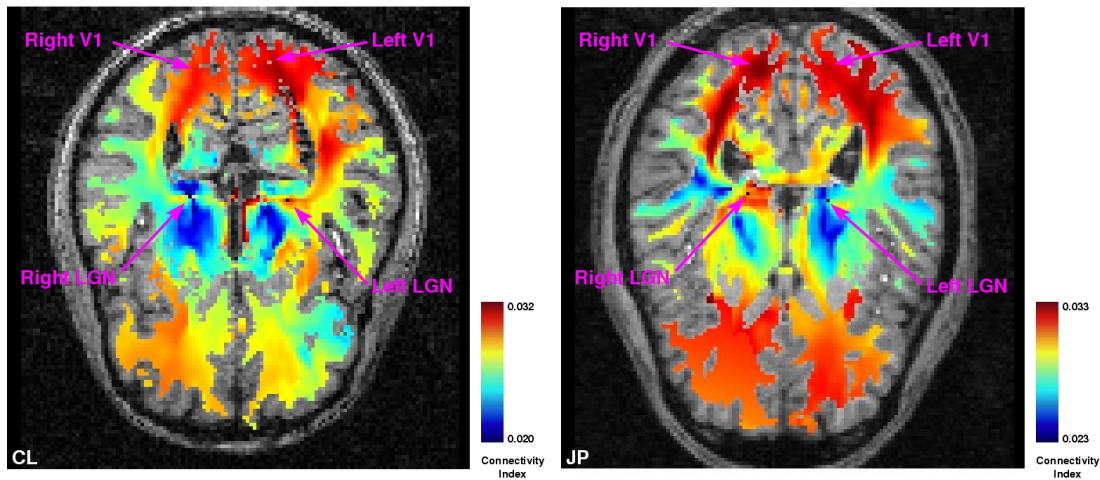


Figure 7.4: Connectivity  $\mu$ -maps obtained in two subjects with the FMT technique estimated from one LGN seed voxel (in black) for each hemisphere. The highest connectivity index values are found along the putative optic radiations paths, with the maximum value within area V1.

in black. The highest connectivity index values (dark red) are systematically found within the typical path of the optic radiations. Besides, highest values were found in the retinotopically identified V1 region. These results were found for each seed voxel in all subjects.

Finally, for each connectivity maps, the voxel with maximum connectivity mapping index (which lay in area V1) was identified and the geodesic linking that voxel and the seed point was traced. Figure 7.5 shows the reconstructed fiber bundles obtained with both methods. Although the thalamo-occipital fibers estimated with streamline and geodesic methods qualitatively match and are consistent with known anatomy, we noted some differences between reconstructed tracts.

As can be seen in figure 7.5, most fibers estimated by streamline propagation fail to reach the V1 white matter ROI, unexpectedly heading in a ventral direction a few millimeters before reaching the V1 region. We attribute this unexpected trajectory ending to an improbable connection with another fiber bundle crossing the thalamo-occipital track. This observation led us to use a relaxed constraint to filter the fibers passing closely to V1, as mentioned in the above description of the LGN seed voxel identification procedure. Note that [40] also used a 1cm band within the white matter, laterally located to the activated occipital cortex to filter their thalamo-occipital fibers (see [40], figure 3). Besides, other DTI tractography works showing this bundle do not exhibit an actual connection with a accurately defined V1 ROI, letting open the question of the fibers termination location.

On the other hand, FMT estimated tracts systematically reach our white matter V1 region, which illustrates an important advantage of the geometric front propagation method over local approaches. However, FMT fibers tend to converge rapidly after leaving the seed voxels, which denotes the less local characteristic of the method (see discussion).

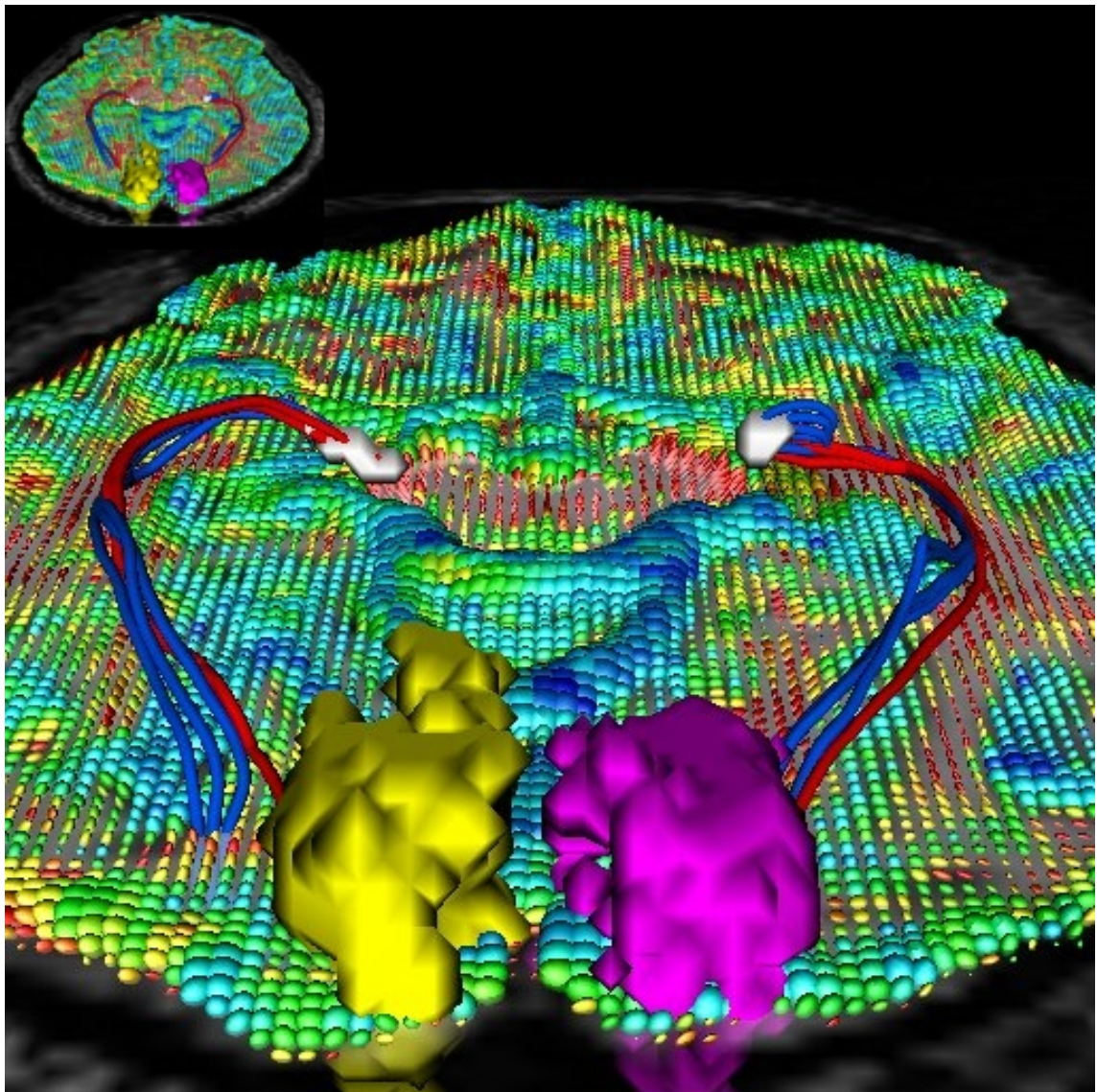


Figure 7.5: Optic radiation tracts estimated with a classical streamline method (blue) and with the FMT technique (red). The LGN seeds voxels (green), Left V1 (yellow), right V1 (purple) and an axial slice of the DTI are also represented.

### 7.3.2 Callosal connections

For each hemisphere, the low-level visual areas represent and analyze only one half of the visual field, i.e. their respective contralateral hemifield. Nonetheless, homologue areas of both sides, such as left and right V1, have been shown to be connected, at least for the vertical meridian representations, through the splenium, a portion of the corpus callosum [37]. Following [54], we studied the FMT estimated connectivity maps of our functionally defined areas. We were interested in looking at the capability of our FMT method to replicate the broad connection topology that Dougherty and colleagues reported in the region of the splenium.

We analyzed connectivity maps in the splenium voxels, starting from our retinotopically (or functionally for hMT+) defined ROIs. Each ROI was considered separately. We note  $X = (x_i)_{i=1,\dots,n}$  a specific  $n$  voxels seed ROI (e.g. left hemisphere V1) and  $Y = (y_j)_{j=1,\dots,m}$  the  $m$  splenium voxels identified on a mid-sagittal slice. For each seed voxel  $x_i$ , the corresponding  $\mu$ -map and  $\sigma$ -map were computed with the FMT method. We therefore have the mean and sigma values for each optimal path  $\gamma_{i,j}$  linking  $x_i$  to  $y_j$ . We then filter these maps to remove the highest variance paths and compute a single mean  $\mu$ -map in the splenium. Specifically, for each splenium voxel  $y_{j_0}$ , we have  $n$  putative paths  $\gamma_{i,j_0}$ . We discard a given proportion  $p$  of these  $n$  connectivity paths, removing paths with highest variance  $\sigma$ . The mean connectivity indices of the remaining putative fibers are then averaged, leading to a single mean value  $\mu$  at voxel  $y_{j_0}$ . The procedure is repeated for each  $y_j, j = 1, \dots, m$ . The resulting  $\mu$  map is interpreted as the mean connectivity between area  $X$  and the splenium.

Figure 7.6 shows the resulting mean  $\mu$ -maps for visual areas hMT+, V1, V3A and V4 respectively taken as starting ROIs in a mid-sagittal section of the brain for each subject.  $p$  was arbitrarily set to 10%. We do not represent here the mean  $\mu$ -maps for areas V2v, V2d, V3v and V3d, as they do not significantly differ from their closest neighboring areas on the cortical surface, i.e. V1v, V1d, V4 and V3A respectively (see discussion below).

Connectivity values are ordered similarly for each areas, with a smooth gradient from lowest values in the postero/dorsal portion of the splenium to highest values in its antero/ventral portion. Comparing the different origin areas, lowest values were systematically found for hMT+. Regarding areas V1, V3A and V4, values are not consistent enough across subjects to infer a systematic topology in the occipito-callosal connections. However, V3A connectivity is higher than for V4 in 4 out of 6 hemispheres, suggesting a stronger callosal connectivity for dorsal with respect to ventral areas. Finally, we observed a systematic asymmetry between the maps associated to each hemisphere. The highest values were found for putative connections originating from the left hemisphere. Figure 7.7 represents the most probable fibers

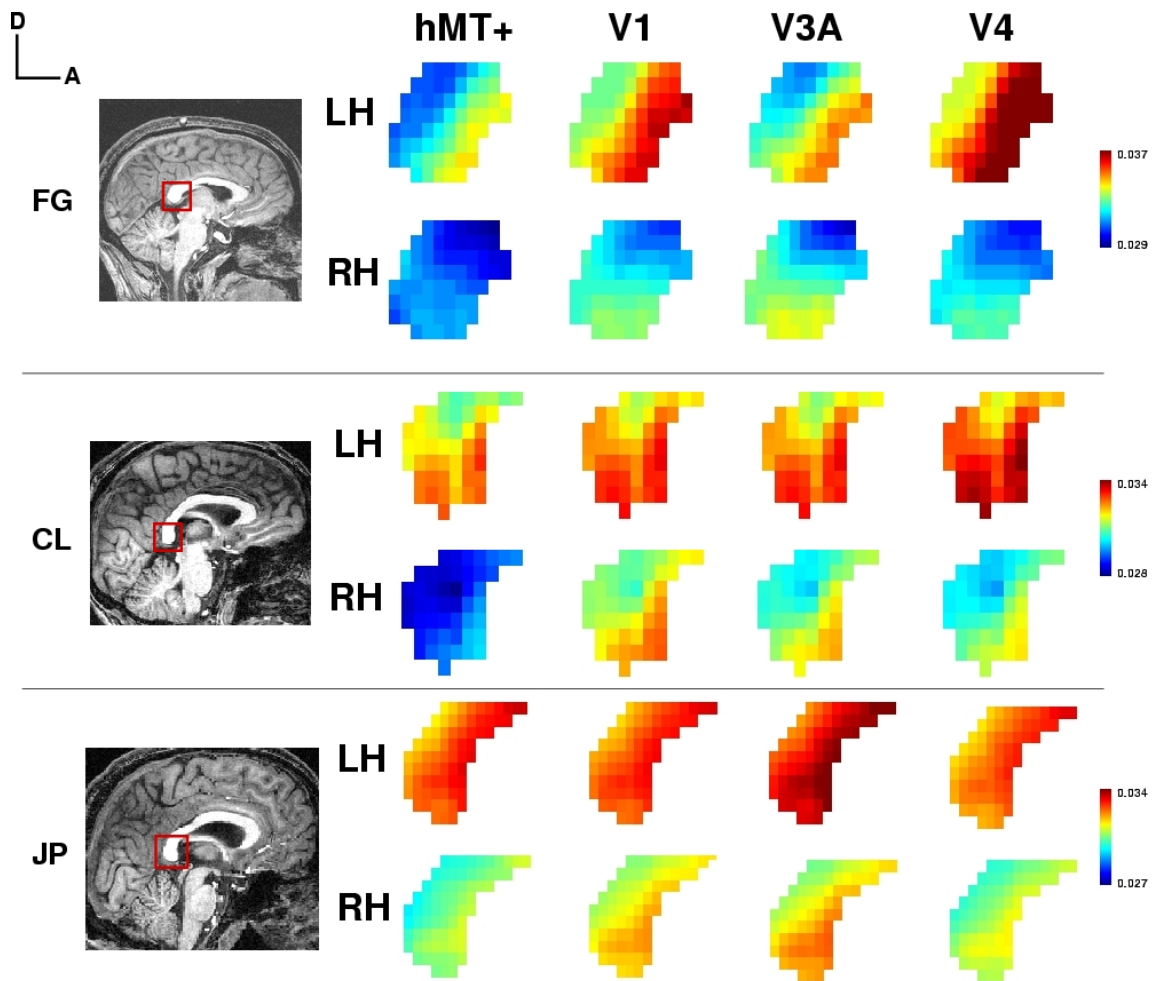


Figure 7.6: Mean connectivity indices from distinct visual areas to the splenium voxels. The mean connectivity values show a smooth gradient from postero/dorsal to antero/ventral splenium portions. Lowest connectivity values in the splenium are systematically found for hMT+.

linking each hMT+ voxel from both hemispheres to the splenium. We employed a similar method to that used to obtain the optic radiations fibers. More specifically, for each hMT+ voxel considered as a seed, we computed the related connectivity index maps. We then identified the splenium voxel with highest connectivity index and constructed the related geodesic. The estimated fiber tracts from the two hemispheres show a great spatial agreement.

### 7.3.3 hMT+ intra-hemispheric connectivity

Using a similar approach, we finally studied the FMT-connectivity of the human MT complex with the ipsilateral occipital retinotopic areas. The most probable connections were identified as follows. Taking as seeds each hMT+ voxel  $(x_i)_{i=1,\dots,n}$ ,

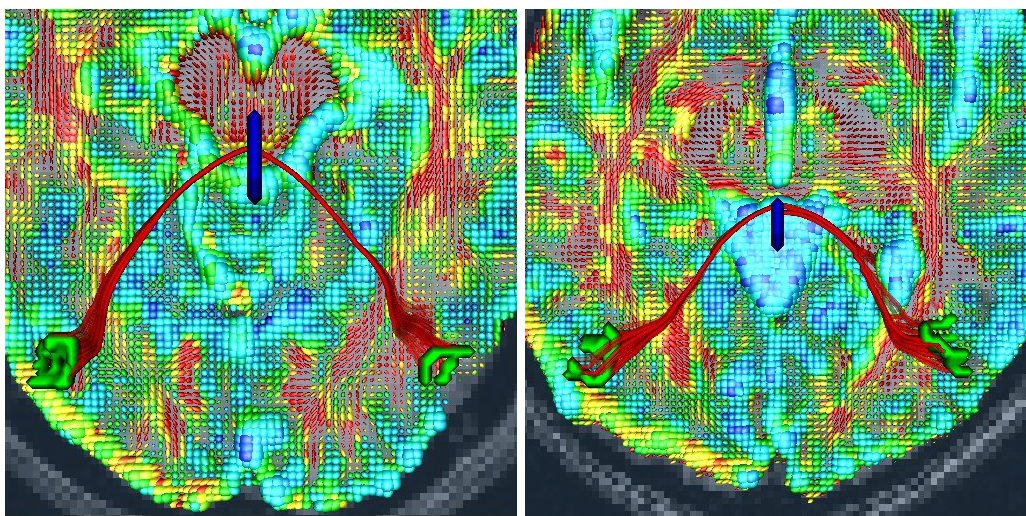


Figure 7.7: Independently estimated most probable fibers linking left and right hMT+ (in green) to the splenium (in blue) from two subjects (left CL and right JP).

we compute the  $\mu$  and  $\sigma$  maps with the FMT method. For each  $x_i$ , we then identify a given proportion  $p$  of paths with the highest  $\sigma$  values among the  $m$  paths linking target ROI voxels  $(y_j)_{j=1,\dots,m}$  to  $x_i$ . The mean  $\mu$  value of the remaining paths is then computed and assigned to voxel  $x_i$ . We end up with a mean connectivity value at each hMT+ voxel and for each retinotopically defined target ROI.

Figure 7.8 shows a box plot of the mean connectivity values distribution for the different seed voxels of hMT+ across areas. The boxes edges depict the values of the first quartile, the median and the third quartile. Values outside this box are also shown to completely represent the distribution dispersion.

V1 and V2 systematically showed the highest connectivity values, suggesting highly probable connections with hMT+. V1 and V2 can hardly be distinguished, which can be attributed to their very close anatomical locations given our voxel size (see discussion). On the other hand, V4 systematically showed the lowest connectivity values, suggesting a weak direct anatomical connection with hMT+. It is more difficult to clearly distinguish the remaining areas V3v, V3d and V3A.

Similarly to the splenium data analysis, we clearly found higher connectivity values for the left hemisphere as compared to the right, regardless of the area considered (see the values range on the vertical axes).

## 7.4 Discussion

We have combined informations from 3 different MR modalities to study connectivity within the human low-level visual brain. To date, only a few studies used functionally defined ROIs to characterize white matter connectivity in this part of the brain. We

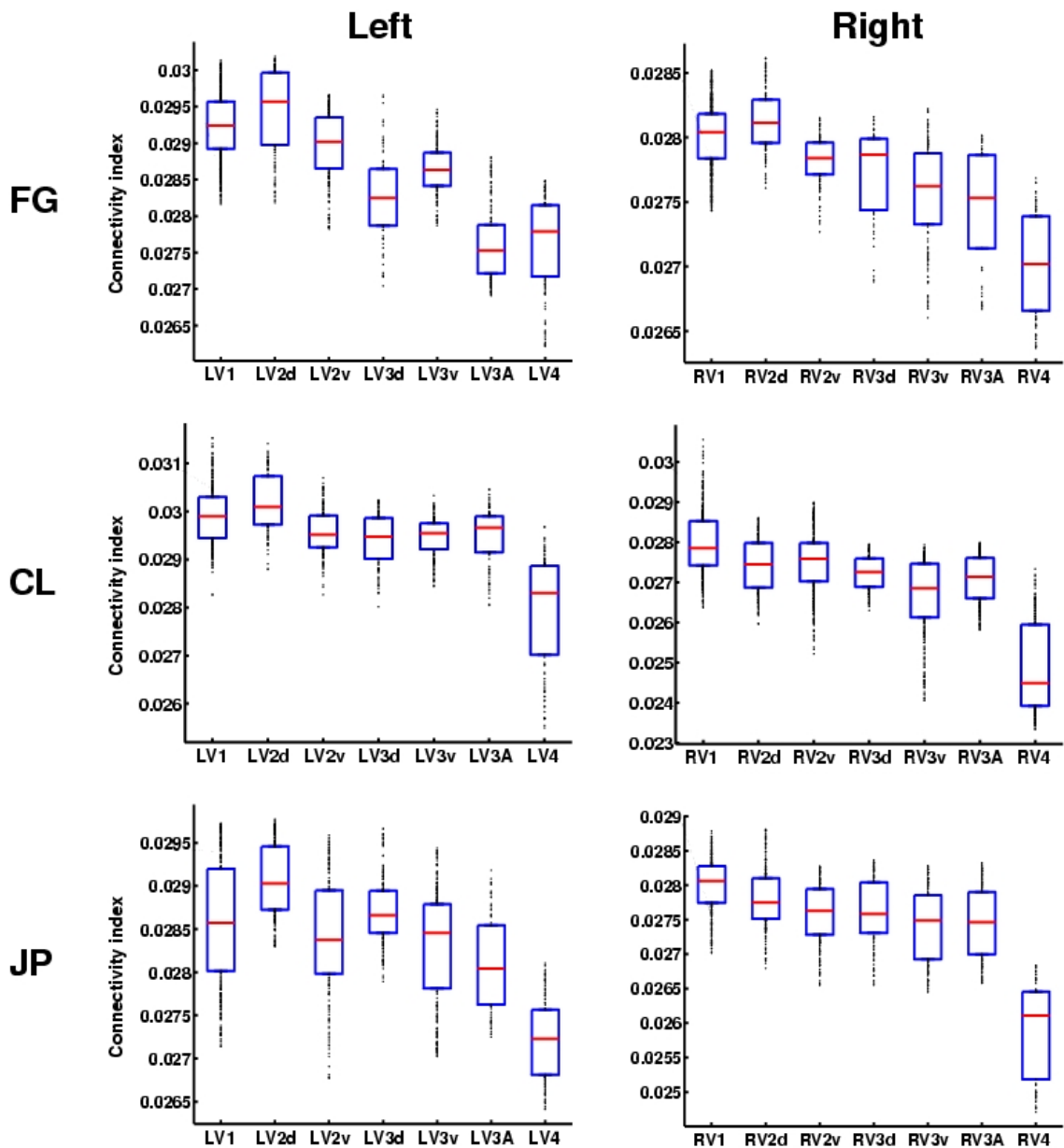


Figure 7.8: Occipital-hMT+ connectivity

have shown that it is possible to determine various connectivity patterns with our Riemannian geometric approach. We shall first discuss the results regarding current knowledge on the human visual brain connectivity and then address methodological issues regarding DTI based tractography.

#### 7.4.1 Visual cortex connectivity

*Thalamo-occipital fibres* We first reproduced tracking of the thalamo-occipital fibers bundle connecting the LGN and V1. This fiber bundle was identified in various

DTI tractography work, either with a deterministic streamline [40, 23] or a Fast Marching Tractography [33, 31] method. Although our methodology to identify the LGN seed voxels might appear biased as it is already based on DTI information, we stress that the estimated LGN location and extent consistently fits previous reports and known anatomy. Furthermore, this method is not prone to operator dependent seed selection. The successful identification of the well-characterized thalamo-occipital connection therefore validated our Riemannian FMT method. These results also illustrate the lower local sensitivity than in the case of a classical streamline approach, since spatially close seeds lead to relatively similar connectivity maps, hence to close fibers tracks (figure 7.5). This can be an advantage over classical streamline approaches as it is less prone to noise, but might also mask local topology across spatially close fibers, such as those shown by Conturo *et al.* in the thalamo-occipital fiber bundle [40].

#### *Splenium fibers*

We investigated the topology of callosal fibers with respect to their origin in the low level visual cortex. We could reproduce with our FMT method the antero-ventral localization of fibers linking occipital retinotopic areas to the corpus callosum (figure 7.6), as found by Dougherty *et al.* [54] using a classical streamline approach. Our results also suggest higher connectivity values for V3A when compared to V4, which is consistent with [54]. We could not however identify the precise topological organization of connections within the splenium they observed, neither with our FMT approach nor with a streamline technique similar to the one they used. A lower quality in our diffusion-weighted images may be responsible for this discrepancy.

We found the lowest connectivity values in the splenium for hMT+ when compared to occipital retinotopic areas (figure 7.6). This result should be related to a clinical study demonstrating that visual motion perception, strongly correlated with hMT+ activity, is not affected by posterior callosal destruction [36]. On the other hand, a weaker activation during bilateral visual field stimulation was found in the patient left hemisphere calcarine region compared to 20 normal subjects, correlated with severely impaired reading and colour naming performances. These findings suggested other, probably parallel, pathways conveying interhemispheric visual motion information. Possible candidates proposed by the authors for the alternative routes include anterior part of the corpus callosum, anterior commissure and subcortical (via the superior colliculus, the intercollicular commissure and the pulvinar) connections. Future work will shortly assess these alternative interhemispheric connections for hMT+.

#### *hMT+ and occipital areas connectivity*

We studied the connectivity between hMT+ and various low-level retinotopic areas. To the best of our knowledge, this is the first DTI connectivity study considering this cornerstone of the visual motion pathway. V1 systematically showed the highest connectivity index values with hMT+ (figure 7.8), consistent with the known highly myelinated white matter fiber bundles linking both areas [232]. Besides, lowest connectivity values between the retinotopic areas and hMT+ were systematically found for area V4. This result should be related to the previous chapter of the current thesis and with the work of Tolias and colleagues in macaques [214, 213]. This connectivity mapping result may suggest that acquired direction selectivity in area V4 might rather be mediated by V1 than by direct connections with hMT+, further supporting the famous distinction between ventral and dorsal streams [228]. This issue should be addressed in future work, e.g. reproducing the study of [213] after hMT+ resection or by using cortical cooling techniques in macaque MT region.

We also found similar hMT+ connectivity values for V3d and V3v, despite their relatively important distance along the cortical sheet. This observation could be an other evidence to consider V3d and V3v as the two quarterfields representation of a single area V3, as also demonstrated with anatomical connectivity studies in various species of monkeys [140, 141].

#### *Anatomical geometry and sampling constraints*

As mentioned above, we could hardly distinguish mean connectivity maps for areas V1 and V2. Although surprising at first sight, this result can actually find a simple explanation when considering together the anatomical layout of these areas and the current spatial resolution of DTI. Areas V1d and V2d (and similarly V1v and V2v) respectively lie on the opposite banks of the same gyrus<sup>1</sup>. The white matter tissue separating the latter is therefore relatively thin, especially with 2mm isotropic voxels. Thus we cannot expect to easily distinguish the connectivity maps obtained with two opposite voxels in this gyrus. Improvement of the spatial resolution appears as the only way to solve this problem. Although still to be considered for the areas couples V3d/V3A dorsally and V3v/V4 ventrally, this gyral proximity is less pronounced since these areas borders appear less constrained by the sulco-gyral pattern than for V1 and V2 borders.

#### *Hemisphere asymmetry*

Our results suggested a significant asymmetry in our connectivity maps between the two hemispheres. The left hemisphere exhibits higher connectivity values than its right counterpart. A similar result was also reported in [54], where more occipito-

---

<sup>1</sup>Note that Van Essen proposed an interesting mechanical tension-based theory to explain this particular folding pattern [231].

callosal fibers could be reconstructed in the left than in the right hemisphere by the employed streamline algorithm. The authors suggested a bias in the hemispheres respective size may account for this difference. Note that such an asymmetry between both hemispheres was also reported in the motor system [94] and could possibly be attributed to handedness. We suggest an alternative hypothesis, based on a perhaps more straightforward brain observation: hemispheric functional specialization. Undoubtedly, the hemispheres are functionally asymmetric and this should imply a different, asymmetrical wiring within each hemisphere. This may in particular be the case in the occipital cortex, the right lobe possibly presenting more fiber crossings than its left counterpart. As a consequence, the local diffusion tensors would not be equivalently anisotropic in both sides, leading to more difficult fiber tracking for streamline methods or lower connectivity values for our FMT algorithm.

As future directions, besides those mentioned above, we consider the work of Behrens and Johansen-Berg as a particularly promising application of DTI information to study the visual cortex. Based on remote cortical connectivity patterns, they could successfully segment the thalamus into anatomically consistent subregions [9]. A similar approach may be applied to uncover the different compartments of regions such as hMT+ or the Lateral Occipital Cortex. Cortico-cortical connectivity information may also be of great interest to clarify cutting-edge visual areas identification issues, both dorsally (V7, KO, ...) and ventrally (V4v-V8 vs. hV4 models, newly reported Ventral Occipital maps).

These issues will certainly be successfully addressed in the near future, provided necessary methodological advances regarding both data acquisition and tractography algorithms.

## 7.4.2 Methodological issues

### *Riemannian DTI connectivity: validity and limitations*

The current study provides a validation of the Riemannian approach to estimate DTI based connectivity mapping in the visual system. With its other application to the human motor system [132], this Riemannian geometrical approach, using the full tensor information, appears very useful to study anatomical connectivity in various cognitive systems. Geometrical tractography methods, such as the current Riemannian FMT used in our study, have three main advantages over other tractography approaches. First they provide a connectivity measure between any pair of points within the white matter. This information can be used to build connectivity matrices over the whole brain or to rank putative connections pathways in the white matter. Then, geometrical approaches can deal with locally isotropic tensors occurring at fibers kissing or crossing. This is not the case with deterministic

or probabilistic approaches where a FA threshold condition is often necessary to avoid unreliable fibers. Finally, these methods are less sensitive to acquisition noise, since they take advantage of the complete tensor information and of the less local behavior of the algorithm by comparison with streamline or stochastic approaches. Although previous implementations turned out to be computationally intensive [133], the recently developed FM method allows a very fast estimation of connectivity maps and geodesic path construction, as well as an improved robustness to noise. Besides, this approach naturally deals with the convoluted geometry of the white matter mask, avoiding anatomically impossible tracts passing through CSF voxels (figure 7.3).

There are however limitations both due DTI by itself and to the geometrical connectivity mapping framework. First and foremost, the relatively poor spatial resolution of DTI (typically a few  $\text{mm}^3$ ) when compared to actual white matter fibers diameter (between 0.2 and 20  $\mu\text{m}$ ) has important implications. (i) Only white matter "highways" may be properly recovered, which hardly represent every cortico-cortical connections; false negative connections are thus unavoidable. Improvements in image acquisition protocols, such as parallel imaging, may overcome this limitation, but a precise physical lower bound is still to be estimated. (ii) The tensor model cannot handle properly fibers crossings or kissings that may occur within a voxel. Emerging approaches using higher order models based on High Angular Resolution Diffusion Imaging (HARDI) [74, 226, 165, 21, 48] may provide an answer to this issue.

An intrinsic problem of the geometrical connectivity mapping approach used here comes from the absence of absolute threshold to confidently estimate fiber tracts from the connectivity maps [168]. Depending on the threshold choice (the  $p$  proportion, arbitrarily set to 10% here), false positive or false negative connections may arise. Combination of complementary connectivity indices associated with each geodesics may prove to minimize this limitation. Furthermore, most tractography methods to date, including ours, are not symmetrical in the sense that putative paths reaching a position  $y$  while starting from  $x$  may not necessarily coincide with those linking  $x$  when starting from  $y$ . Tracking within GM, although theoretically possible with geometrical approaches like the one we employed, still leads to difficult interpretations of the reconstructed connectivity maps and related tracts as the diffusion signal is poor in the cortical tissue. Last but not least, a direct validation of DTI based methods is still missing. Although reconstructed tracts such as the optic radiations in the current study or the motor pathway found in [132] are consistent with known anatomy, a quantitative validation could indicate the advantages and weaknesses of DTI based tractography methods. Ultimately, an animal study comparing the different tractography approaches with invasively identified connections would be of great interest to

demonstrate their respective advantages and current DTI based tractography limits.

#### *Combined fMRI and DTI*

The fMRI areas identification confidently constrained our analysis into known brain regions. We thus avoided possible operator-dependent bias in seed placement or rough anatomically based inference. No obvious false-positive connections were found in our study.

## **7.5 Conclusion**

We combined anatomical, functional and diffusion-weighted images information and a newly introduced Riemannian DTI analysis framework to study the anatomical connectivity in the low-level visual brain. We could successfully reconstruct the well-known optic radiations connecting the LGN and V1 with our fast connectivity mapping method. We also showed a plausible topology of occipito-callosal connections in the splenium, consistent with previous works. Finally, we assessed the anatomical connectivity between hMT+ and occipital retinotopic areas, supporting the view of parallel ventral and dorsal processing streams. With both image acquisition and methodological improvements, diffusion MRI should provide a new means to uncover the architecture of the visual system and further relate it to its functional characterization.

## Chapter 8

# Conclusion and perspectives



### 8.1 Summary of our contributions

We introduced a new approach to the cortical surface-based smoothing of fMRI data. We demonstrated its advantages over (i) classical 3D isotropic methods which ignore the complex cortical surface geometry and (ii) mesh-based implementations which require a preliminary projection of the functional data on the cortex model. A Matlab interface was implemented for the smoothing program and to allow the automatic computation of a level set representation of the cortical surface meshes. The core programs were implemented in C++ by Jean-Philippe Pons during his PhD at the Odyssee Laboratory.

We developed a complete procedure of retinotopic mapping allowing the identification of various low-level visual areas on a subject basis. We tested different stimuli parameters to optimize the resulting angular maps, yielding to reliable visual field maps acquired in 20 minutes. Programs to automate the different steps of the analysis were implemented in Matlab, including anatomical and functional images processing. Manual segmentation is nonetheless required for the visual areas delineation based on the angular maps, since the Visual Field Sign computation ends with unsatisfactory results, even after various attempts of post-processing corrections. The complete method is routinely used in the laboratory and at the centre IRMf de la Timone. It was also transferred to the DyVA team and is currently used for the study of the cortical organization in patients suffering from retinal diseases.

A functional identification procedure of the human MT complex (hMT+) was also developed. We identified the optimal stimulus parameters among different stimulus patterns and contrasts between conditions to obtain reliable activations in the expected zone.

Building on these visual areas identification procedure, we have characterized

the low-level areas functional sensitivity to motion direction. Based on an event-related fMR-adaptation paradigm combined with a powerful non-parametric hemodynamic response function estimation method, we can estimate the direction selectivity of each area and infer possible sub-populations proportions with respect to their tuning bandwidth type. We found the highest direction selectivity in areas hMT+ followed by V3A, confirming their involvement in motion processing. Unexpectedly high direction selectivity was also observed in areas V1 and V4v and a possible explanation in terms of context-dependent neural tuning was proposed.

Finally, we combined the retinotopic mapping method and the functional localization of the hMT+ with Diffusion Tensor Images to study the anatomical connectivity across the low-level visual areas. A complete processing pipeline was developed to analyze the different information in a common reference frame. Based on a Riemannian geometry connectivity mapping approach, we could reconstruct the optic radiations linking the LGN and V1. The topology of connections between the two hemispheres visual areas was studied in the splenium and confirmed a previous report. We finally show the estimated anatomical connectivity between hMT+ and the different occipital retinotopic areas, supporting the existence of two anatomically segregated pathways.

## 8.2 Perspectives

Naturally, this work opens more perspectives than it answers questions.

The retinotopic mapping procedure can be further improved in many respects. First, the acquisition time may be lowered by the use of a simultaneous polar angle and eccentricity stimulation, each coordinate having its own frequency. Although already suggested by others (e.g. [239]), this possible stimulation improvement has not been tested so far. Second, expanding the range of patterns used in the stimuli as well as the type of task performed by the subjects may broaden the scope of retinotopic mapping. Beyond providing a higher signal in the regions currently disputed, it could help unveiling new retinotopic maps as already shown by some groups (e.g. [194]). Third, the segmentation of the retinotopic areas is still manual in our procedure. Warping a model of the typical pattern onto a flat representation of the cortical surface, as proposed by [53], appears an appropriate solution to automate this last step. We will address this issue shortly in a collaboration with the DyVA team.

The fMR-adaptation experiment suggests several future works. First, increasing the number of motion direction could lead to tuning curves measurements

closer to those typically shown by electrophysiologists, hence yielding to finer functional sub-population characterization. However the non-linear relation between neural activity and the BOLD signal certainly restricts the sampling resolution along the stimulus dimension (here the direction of motion) that can ultimately be obtained. It would nonetheless be interesting to have an estimation of this limitation. Second, a mathematical model of neuronal adaptation in the different neural populations and visual areas would be of great interest to clarify the possible origins of the BOLD signal observed. Third, a similar approach combining our experimental fMR-adaptation paradigm and appropriate fMRI data analysis methods as the HRF toolbox can be straightforwardly applied to other stimulus dimensions such as motion velocity or color contrasts. Such experiments would bring a better characterization of functional selectivity in the human low-level visual areas. Finally, the results of this experiment attracted our attention on the important relations between (visual) perceptions and subject's state, including attention (precisely!) and stimulation history but also perhaps more global state parameters such as the emotional state. Improving our understanding of these complex inter-dependencies appears to us as an exciting direction for future research.

Exploring non-invasively the white matter connectivity within the visual brain has an enormous potential. First it could clarify the definition and labeling of visual areas currently under disputes or help in the segmentation of complex of areas such as hMT+. Additionally, anatomical connectivity is a complementary information to allow comparisons across species such as macaque and humans and better understand the biological evolution. Ultimately, diffusion-weighted imaging may reveal the anatomical structure of the human visual system that will have to be further related with its functional architecture. However, we have stressed some important limitations of inferences based on DTI. More sophisticated water diffusion models based on High Angular Resolution Diffusion Imaging (HARDI) and appropriate connectivity mapping methods constitute a promising direction to overcome these limitations. This issue will be addressed shortly in the laboratory on the occipital visual cortex using algorithms currently under study [48].



# Conclusion et perspectives



## Résumés des contributions

Nous avons introduit une nouvelle approche de lissage des données d'IRMf contraint à la surface corticale. Nous avons démontré ses avantages sur (i) la méthode classique de filtrage 3D isotrope qui ignore la géométrie complexe de la surface corticale et (ii) des procédés de régularisation sur une représentation explicite de la surface corticale (i.e. un maillage) qui nécessitent une projection préalable des données fonctionnelles sur un modèle du cortex. Une interface Matlab a été développée pour ce programme de lissage ainsi que pour calculer automatiquement une représentation implicite (i.e. par un ensemble de niveaux ou level set), à partir de maillages des surfaces corticales. Le programme de lissage a été implanté en C++ par Jean-Philippe Pons durant sa thèse au laboratoire Odyssee.

Une procédure complète de cartographie par rétinotopie permettant l'identification individuelle de différentes aires visuelles de bas-niveau a été développée. Différentes configurations des stimuli ont été testées en vue d'optimiser la qualité des cartes du champs visuel ainsi obtenues. Le paradigme ainsi retenu conduit à des résultats fiables en 20 minutes d'acquisitions fonctionnelles. Des programmes automatisant les différentes étapes de l'analyse et incluant des traitements des données anatomiques et fonctionnelles ont été implantés en Matlab. Toutefois, étant donné que le calcul du signe du champs visuel a conduit à des résultats insatisfaisants, et ce malgré différentes tentatives de post-traitements des données, une délimitation manuelle se fondant sur les cartes angulaires obtenues est nécessaire. La méthode complète est désormais utilisée en routine au laboratoire Odyssee et au centre IRMf de la Timone. De plus, elle a fait l'objet d'un transfert auprès de l'équipe DyVA et est actuellement utilisée pour étudier l'organisation corticale de patients souffrant de pathologies rétiniennes.

Une procédure d'identification fonctionnelle du complexe MT chez l'homme (hMT+) a également été développée. À l'instar de la cartographie rétinotopique, nous avons identifié la configuration de stimuli optimale parmi différents motifs et

contrastes entre conditions de stimulation afin d'obtenir des activations robustes dans la zone corticale présumée. La chaîne de traitements des images a également été automatisée.

En se fondant sur ces procédures d'identification de différentes aires visuelles, nous avons ensuite caractérisé la sensibilité fonctionnelle de celles-ci par rapport à la direction du mouvement. Une expérience d'IRMf d'adaptation événementielle couplée à une méthode non-paramétrique d'estimation de la réponse hémodynamique ont permis d'estimer la sélectivité à la direction propre à chaque aire et d'en inférer des proportions relatives de sous-populations cellulaires selon leur profil de sélectivité. Nous avons trouvé une sélectivité plus forte dans hMT+ suivi par l'aire V3A, confirmant leur implication forte dans le traitement du mouvement visuel. Une sélectivité singulièrement élevée a également été observée dans les aires V1 et V4v. Une explication plausible en terme de sélectivité fonctionnelle dépendant du contexte a été proposée pour rendre compte de ce phénomène.

Enfin, nous avons combiné les procédures de cartographie des aires visuelles avec des images du tenseur de diffusion pour étudier la connectivité anatomique entre les différentes aires visuelles de bas-niveau. Une chaîne de traitement complète a été développée afin d'analyser dans un même référentiel les informations complémentaires fournies par les différentes modalités d'IRM. En se fondant sur une approche de géométrie Riemannienne de cartographie de la connectivité anatomique, nous avons pu reconstruire les radiations optiques reliant le Corps Genouillé Latéral à l'aire V1. La topologie des connections entre les deux hémisphères des aires visuelles a également été étudiée au niveau du splenium et confirme des résultats publiés récemment. Enfin, nous avons estimé la connectivité anatomique entre hMT+ et les différentes aires rétinotopiques, corroborant l'existence de deux voies parallèles liées au traitement cortical de l'information visuelle.

## Perspectives

Naturellement, ce travail ouvre davantage de perspectives qu'il ne résoud de questions.

La procédure de cartographie rétinotopique peut être améliorée en différents points. Tout d'abord, le temps d'acquisition pourrait être réduit en présentant simultanément les stimuli codant respectivement pour l'angle polaire et l'excentricité, chaque coordonnée ayant sa propre fréquence fondamentale. Bien que déjà suggérée par d'autres auteurs (par exemple [239]), cette amélioration supposée de la stimulation n'a jusqu'alors jamais été testée directement. Par ailleurs,

accroître le type de motif utilisé dans les stimuli ainsi que la tâche réalisée par le sujet durant l'expérience devrait élargir le champ d'application de la cartographie rétinotopique. En plus de permettre l'enregistrement d'un meilleur signal dans des régions actuellement débattues, de telles améliorations pourraient révéler de nouvelles cartes rétinotopiques, comme cela a déjà pu être réalisé auparavant par d'autres groupes (voir par exemple [194]). Enfin, la segmentation finale des aires rétinotopiques est une étape manuelle dans notre procédure. Déformer un modèle des cartes angulaires typiques sur les données expérimentales projetées sur une représentation plane de la surface corticale, comme proposé récemment dans [53], semble une approche prometteuse. Nous allons implanter une telle procédure à court terme, en collaboration avec l'équipe DyVA.

L'expérience d'IRMf d'adaptation ouvre de nombreuses perspectives. Dans un premier temps, il serait souhaitable d'accroître le nombre de directions différentes du mouvement afin d'obtenir une mesure plus précise des courbes de sélectivité à cet attribut. Cependant, les relations non-linéaires entre l'activité neuronale et le signal BOLD limitent certainement la résolution de l'échantillonnage d'une sélectivité à une dimension du stimulus (ici la direction du mouvement) que l'on peut obtenir par cette méthode. Il serait souhaitable d'avoir une estimation quantitative de cette limitation. Deuxièmement, il serait particulièrement intéressant de développer un modèle mathématique de l'adaptation neuronale dans les différentes aires et populations neuronales. Cela pourrait contribuer à mieux cerner l'origine du signal BOLD mesuré dans les expériences d'adaptation. Troisièmement, une approche similaire, i.e. combinant notre paradigme d'IRMf d'adaptation et des méthodes appropriées d'analyse des données IRMf comparables à l'outil HRF utilisé ici, peut être directement appliquée à d'autres dimensions de stimuli comme la vitesse du mouvement ou la couleur. De telles expériences conduiraient à une meilleure caractérisation de la sélectivité fonctionnelle dans le cortex visuel de l'homme. Enfin, les résultats de cette expérience ont attiré notre attention sur les relations importantes entre perception (visuelle) et l'état général du sujet, que ce soit les processus attentionnels sous-jacents, l'historique de la stimulation présentée au sujet mais peut-être également des paramètres plus globaux comme son état émotionnel. Accroître notre compréhension de ces inter-dépendances complexes nous apparaît comme de passionnantes directions de recherche pour l'avenir.

L'exploration non-invasive des fibres de matière blanche dans le système visuel présente également un potentiel considérable. Tout d'abord, cela permettrait de clarifier la définition et l'étiquetage d'aires visuelles actuellement sujettes à de vigoureux débats dans la communauté. Cette information contribuerait aussi à segmenter des complexes d'aires tel que hMT+ en différentes sous-structures. En

outre, la connectivité anatomique fournit une information supplémentaire dans l'optique d'établir des analogies entre espèces telles que le macaque ou l'homme et ainsi de mieux comprendre l'évolution biologique. Finalement, l'imagerie de diffusion pourrait révéler l'architecture anatomique du système visuel cortical de l'homme qui sera alors à relier à son architecture fonctionnelle. Nous avons néanmoins souligné les limitations inhérentes aux inférences plausibles à partir d'images du tenseur de diffusion. Des modèles plus sophistiqués de la diffusion des molécules d'eau, fondées sur des données de diffusion à haute résolution angulaire assorties de méthodes de cartographie des connectivités appropriées représentent une direction prometteuse pour dépasser ces limitations. Cette direction sera prochainement examinée dans le cortex visuel occipital grâce à des algorithmes en cours de développement au sein du laboratoire Odyssee [48].

# Bibliography

- [1] G. K. Aguirre, E. Zarahn, and M. D’Esposito. A critique of the use of the Kolmogorov-Smirnov (KS) statistic for the analysis of BOLD fMRI data. *Magnetic Resonance Medicine*, 39:500–505, 1998.
- [2] T.D. Albright and R. Desimone. Local precision of visuotopic organization in the middle temporal area (MT) of the macaque. *Experimental Brain Research*, 65(3):582–592, 1987.
- [3] A. Andrade, F. Kherif, J.-F. Mangin, K. Worsley, A.-L. Paradis, O. Simon, S. Dehaene, D. Le Bihan, and J.-B. Poline. Detection of fMRI activation using Cortical Surface Mapping. *Human Brain Mapping*, 12(2):79–93, February 2001.
- [4] J. Annese, M.S. Gazzaniga, and A.W. Toga. Localization of the human cortical visual area MT based on computer aided histological analysis. *Cerebral Cortex*, 15(7):1044–1053, July 2005.
- [5] K. Arfanakis, D. Cordes, V. M. Haughton, C. H. Moritz, M. A. Quigley, and M.E. Meyerand. Combining independent component analysis and correlational analysis to probe interregional connectivity in fMRI task activation data sets. *Magnetic Resonance Imaging*, 18:921–930, 2000.
- [6] A. Aubert, R. Costalat, and Valabrègue. Modelling of the coupling between brain electrical activity and metabolism. *Acta Biotheoretica*, 49:301–326, 2001.
- [7] C.I. Baker, E. Peli, N. Knouf, and N.G. Kanwisher. Reorganization of visual processing in macular degeneration. *Journal of Neuroscience*, 25(3):614–618, January 2005.
- [8] P.J. Basser, J. Mattiello, and D. LeBihan. MR diffusion tensor spectroscopy and imaging. *Biophysical Journal*, 66(1):259–267, 1994.
- [9] T.E.J. Behrens, H. Johansen-Berg, M.W. Woolrich, S.M. Smith, C.A.M. Wheeler-Kingshott, P.A. Boulby, G.J. Barker, E.L. Sillery, K. Sheehan, O. Ciccarelli, A.J. Thompson, J.M. Brady, and P.M. Matthews. Non-invasive map-

- ping of connections between human thalamus and cortex using diffusion imaging. *Nature Neuroscience*, 6(7):750–757, 2003.
- [10] T.E.J. Behrens, M.W. Woolrich, M. Jenkinson, H. Johansen-Berg, R.G. Nunes, S. Clare, P.M. Matthews, J.M. Brady, and S.M. Smith. Characterization and propagation of uncertainty in Diffusion-Weighted MR Imaging. *Magnetic Resonance in Medicine*, 50:1077–1088, 2003.
- [11] R.T. Born and D.C. Bradley. Structure and function of visual area MT. *Annu. Rev. Neurosci*, 28:157–189, 2005.
- [12] G.M. Boynton. Adaptation and attentional selection. *Nature Neuroscience*, 7(1):8–10, January 2004.
- [13] G.M. Boynton and E.M. Finney. Orientation-specific adaptation in human visual cortex. *The Journal of Neuroscience*, 23(25):8781–8787, September 2003.
- [14] O. Braddick, J. O’Brien, J. Wattam-Bell, J. Atkinson, and T. Hartley. Brain areas sensitive to coherent visual motion. *Perception*, 30:61–72, 2001.
- [15] A. Brewer, J. Liu, A. Wade, and B. Wandell. Visual field maps and stimulus selectivity in human ventral occipital cortex. *Nature Neuroscience*, 8(8):1102–1109, August 2005.
- [16] A. Brewer, W. Press, N.K. Logothetis, and B.A. Wandell. Visual areas in macaque cortex measured using fMRI. *The Journal of Neuroscience*, 22:10416–10426, December 2002.
- [17] K. Brodmann. *Vergleichende Lokalisationslehre der Grobhirnrinde*. J.A.Barth, Leipzig, 1909.
- [18] R.L. Buckner, J. Goodman, M. Burock, M. Rotte, W. Koutstaal, D. Schacter, B. Rosen, and A.M. Dale. Functional-anatomic correlates of object priming in humans revealed by rapid presentation event-related fMRI. *Neuron*, 20(2):285–296, 1998.
- [19] R.B. Buxton, E.C. Wong, and L.R. Frank. Dynamics of Blood Flow and Oxygen Metabolism During Brain Activation: the Balloon Model. *Magnetic Resonance Medicine*, 39:855–864, 1998.
- [20] V.D. Calhoun, T. Adali, L.K. Hansen, J. Larsen, and J.J. Pekar. ICA of Functional MRI Data: an Overview. In *4th international symposium on Independent Component Analysis and Blind Signal Separation (ICA2003)*, Nara, Japon, 2003.

- [21] J.S.W. Campbell, K. Siddiqi, V.V. Rymar, A. Sadikot, and B.G. Pike. Flow-based fiber tracking with diffusion tensor q-ball data: Validation and comparison to principal diffusion direction techniques. *NeuroImage*, 27(4):725–736, October 2005.
- [22] M. Catani, R.J. Howard, S. Pajevic, and D.K. Jones. Virtual in vivo interactive dissection of white matter fasciculi in the human brain. *Neuroimage*, 17:77–94, 2002.
- [23] M. Catani, D.K. Jones, R. Donato, and D. H. ffytche. Occipito-temporal connections in the human brain. *Brain*, 126(9):2093–2107, September 2003.
- [24] L. M. Chalupa and J.S. Werner, editors. *The visual neurosciences*. MIT Press, 2004.
- [25] C. Chefd’hotel. *Geometric methods in computer vision and image processings: contributions and applications*. PhD thesis, École Normale Supérieure de Cachan, April 2005.
- [26] C. Chefd’hotel, G. Hermosillo, and O. Faugeras. Flows of diffeomorphisms for multimodal image registration. In *International Symposium on Biomedical Imaging*. IEEE, 2002.
- [27] W. Chen, X. Zhu, et al. Retinotopic mapping of lateral geniculate nucleus in humans using functional magnetic resonance imaging. *Proc. Natl. Acad. Sci. USA*, 96:2430–2434, March 1999.
- [28] K. Cheng, R. A. Waggoner, and K. Tanaka. Human ocular dominance columns as revealed by high-field functional Magnetic Resonance Imaging. *Neuron*, 32:359–374, 2001.
- [29] K.-H. Chuang, M.-J. Chiu, C.-C. Lin, and J.-H. Chen. Model-free functional MRI analysis using Kohonen clustering neural network and fuzzy C-means. *IEEE Transactions on Medical Imaging*, 18(12):1117–1128, 1999.
- [30] M.K. Chung and J. Taylor. Diffusion smoothing on brain surface via finite element method. In *Proceedings of ISBI*, pages 432–435. IEEE, 2004.
- [31] O. Ciccarelli, G.J.M. Parker, A.T. Toosy, C.A.M. Wheeler-Kingshott, G.J. Barker, P.A. Boulby, D.H. Miller, and A.J. Thompson. From diffusion tractography to quantitative white matter tract measures: a reproducibility study. *NeuroImage*, 18(2):348–359, February 2003.
- [32] O. Ciccarelli, A.T. Toosy, S.J. Hickman, G.J.M. Parker, C.A.M. Wheeler-Kingshott, D.H. Miller, and A.J. Thompson. Optic radiation changes after

- optic neuritis detected by tractography-based group mapping. *Human Brain Mapping*, 25(3):308–316, 2005.
- [33] O. Ciccarelli, A.T. Toosy, G.J.M. Parker, C.A.M. Wheeler-Kingshott, G.J. Barker, D.H. Miller, and A.J. Thompson. Diffusion tractography based group mapping of major white-matter pathways in the human brain. *NeuroImage*, 19(4):1545–1555, August 2003.
- [34] P. Ciuciu, J. Idier, A. Roche, and C. Pallier. Outlier detection for robust region-based estimation of the hemodynamic response function in event-related fMRI. In *2th Proc. IEEE ISBI*, pages 392–395, Arlington, VA, April 2004.
- [35] P. Ciuciu, J-B. Poline, G. Marrelec, J. Idier, C. Pallier, and H. Benali. Un-supervised robust nonparametric estimation of the hemodynamic response function for any fMRI experiment. *IEEE Transactions on Medical Imaging*, 22(10):1235–1251, October 2003.
- [36] S. Clarke, P. Maeder, R. Meuli, F. Staub, A. Bellmann, L. Regli, N. de Tribolet, and Assal G. Interhemispheric transfer of visual motion information after a posterior callosal lesion: a neuropsychological and fMRI study. *Experimental Brain Research*, 132(1):127–133, 2000.
- [37] S. Clarke and J. Miklossy. Occipital cortex in man: Organization of callosal connections, related myelo- and cytoarchitecture, and putative boundaries of functional visual areas. *The Journal of Comparative Neurology*, 298(2):188–214, 1990.
- [38] Y. Cointepas, J.-F. Mangin, Line Garnero, J.-B. Poline, and H. Benali. Brain-VISA: Software platform for visualization and analysis of multi-modality brain data. In *Proc. 7th HBM*, page S98, Brighton, United Kingdom, 2001.
- [39] I.P. Conner, S. Sharma, S.K. Lemieux, and J.D. Mendola. Retinotopic organization in children measured with fMRI. *Journal of Vision*, 4:509–523, 2004.
- [40] T.E. Conturo, N.F. Lori, T.S. Cull, E. Akbudak, A.Z. Snyder, J.S. Shimony, R.C. McKinstry, H. Burton, and M.E. Raichle. Tracking neuronal fiber pathways in the living human brain. *Proceedings of the National Academy of Sciences*, 96:10422–10427, August 1999.
- [41] L. Cornette, P. Dupont, A. Rosier, S. Sunaert, P. Van Hecke, J. Michiels, L. Mortelmans, and Orban G. Human brain regions involved in direction discrimination. *Journal of Neurophysiology*, 79:2749–2765, 1998.

- [42] J.C. Culham, S.A. Brandt, P. Cavanagh, N.G. Kanwisher, A.M. Dale, and R.B.H. Tootell. Cortical fMRI activation produced by attentive tracking of moving targets. *Journal of Neurophysiology*, 80:2657–2670, 1998.
- [43] J.C. Culham, S.P. Dukelow, T. Vilis, F.A. Hassard, J.S. Gati, R.S. Menon, and M.A. Goodale. Recovery of motion area MT following storage of the motion aftereffect. *Journal of Neurophysiology*, 81:388–393, 1999.
- [44] J.C. Culham, S. He, F.A.J. Verstraten, and S.P. Dukelow. Visual motion and the human brain: what has neuroimaging told us? *Acta Psychologica*, 107:69–94, 2001.
- [45] A.M. Dale, B. Fischl, and M.I. Sereno. Cortical surface-based analysis I: Segmentation and surface reconstruction. *NeuroImage*, 9:179–194, 1999.
- [46] P.M. Daniel and D. Whitteridge. The representation of the visual field on the cerebral cortex in monkeys. *Journal of Neurophysiology*, 159:203–221, 1961.
- [47] V. Della-Maggiore, W. Chau, P.R. Peres-Neto, and A.R. McIntosh. An empirical comparison of SPM preprocessing parameters to the analysis of fMRI data. *NeuroImage*, 17(1):19–28, 2002.
- [48] M. Descoteaux, E. Angelino, S. Fitzgibbons, and R. Deriche. A linear and regularized odf estimation algorithm to recover multiple fibers in q-ball imaging. Technical Report 5768, INRIA, November 2005.
- [49] E. DeYoe, G. Carman, P. Bandettini, S. Glickman, J. Wieser, R. Cox, D. Miller, and J. Neitz. Mapping striate and extrastriate visual areas in human cerebral cortex. *Neurobiology*, 93:2382–2386, March 1996.
- [50] E.A. DeYoe, P. Bandettini, J. Neitz, D. Miller, and P. Winans. Functional Magnetic Resonance Imaging (fMRI) of the human brain. *Journal Neuroscience Methods*, 54(2):171–187, October 1994.
- [51] F. Di Russo, F. Martinez, M.I. Sereno, S. Pitzalis, and S.A. Hillyard. Cortical sources of the early components of the visual evoked potential. *Human Brain Mapping*, 15(2):95–111, 2002.
- [52] A.C.M. Diogo, J.G.M. Soares, T.D. Albright, and R. Gattass. Two-dimensional map of direction selectivity in cortical visual area MT of cebus monkey. *Annals of the Brazilian Academy of Sciences*, 74(3):463–476, 2002.
- [53] R. Dougherty, V. Koch, A. Brewer, B. Fischer, J. Modersitzki, and B. Wandell. Visual field representations and locations of visual areas v1/2/3 in human visual cortex. *Journal of Vision*, 3:586–598, October 2003.

- [54] R.F. Dougherty, M. Ben-Shachar, R. Bammer, A.A. Brewer, and B.A. Wandell. Functional organization of human occipital-callosal fiber tracts. *Proceedings of the National Academy of Science*, 102(20):7350–7355, May 2005.
- [55] S.P. Dukelow, J.F.X. DeSouza, J.C. Culham, A.V. Van Den Berg, R. Menon, and T. Vilis. Distinguishing subregions of the human MT+ complex using visual fields and pursuit eye movements. *Journal of Neurophysiology*, 86(4):1991–2000, October 2001.
- [56] S. Dumoulin, R. Bittar, N.J. Kabani, C.L. Baker, G. Le Goualher, G.B. Pike, and A.C. Evans. A new anatomical landmark for reliable identification of human area V5/MT: a quantitative analysis of sulcal patterning. *Cerebral Cortex*, 10:454–463, May 2000.
- [57] S. Dumoulin, R. Hoge, C. Baker, R. Hess, R. Achtman, and A. Evans. Automatic volumetric segmentation of human visual retinotopic cortex. *NeuroImage*, 18(3):576–587, 2003.
- [58] H.M. Duvernoy, P. Bourgouin, E.A. Cabanis, E.A. Cattin, J. Guyot, M.T. Iba-Zizen, P. Maeder, B. Parratte, L. Tatu, and F. Vuillier. *The Human brain: surface, three-dimensional sectional anatomy with MRI, and blood supply*. Springer, 1999.
- [59] E. Eger, P. Schyns, and A. Kleinschmidt. Scale invariant adaptation in fusiform face-responsive regions. *NeuroImage*, 22:232–242, 2004.
- [60] S. Engel, D. Rumelhart, B. Wandell, A. Lee, G. Glover, E-J. Chichilnisky, and M. Shadlen. fMRI of human visual cortex. *Nature*, 369:525–529, June 1994.
- [61] S. A. Engel and C. S. Furmanski. Selective adaptation to color contrast in human primary visual cortex. *Journal of Neuroscience*, 21:3949–3954, 2001.
- [62] S.A. Engel, G.H. Glover, and B.A. Wandell. Retinotopic organization in human visual cortex and the spatial precision of functional MRI. *Cerebral Cortex*, 7:181–192, 1997.
- [63] S.A. Engel, X. Zhang, and B.A. Wandell. Colour tuning in human visual cortex measured with functional Magnetic Resonance Imaging. *Nature*, 388:68–71, 1997.
- [64] R. Epstein and N. Kanwisher. A cortical representation of the local visual environment. *Nature*, 392:598–601, 1998.
- [65] M.P. Ewbank, D. Schluppeck, and T.J. Andrews. fMR-adaptation reveals a distributed representation of inanimate objects and places in human visual cortex. *NeuroImage*, 28:268–279, 2005.

- [66] F. Fang, S.O. Murray, D. Kersten, and S. He. Orientation-tuned fMRI adaptation in human visual cortex. *Journal of Neurophysiology*, 94:4188–4195, August 2005.
- [67] O. Faugeras, G. Adde, G. Charpiat, C. Chefd’Hotel, M. Clerc, T. Deneux, R. Deriche, G. Hermosillo, R. Keriven, P. Kornprobst, J. Kybic, C. Lenglet, L. Lopez-Perez, T. Papadopoulo, J.-P. Pons, F. Ségonne, B. Thirion, D. Tschumperlé, T. Viéville, and N. Wotawa. Variational, geometric, and statistical methods for modeling brain anatomy and function. *NeuroImage*, 23S1:S46–S55, 2004. Special issue: Mathematics in Brain Imaging - Edited by P.M. Thompson, M.I. Miller, T. Ratnanather, R.A. Poldrack and T.E. Nichols.
- [68] D.J. Felleman and D.C. Van Essen. Distributed hierarchical processing in the primate cerebral cortex. *Cereb Cortex*, 1:1–47, 1991.
- [69] D.H. ffytche and R.J. Howard. The perceptual consequences of visual loss: ‘positive’ pathologies of vision. *Brain*, 122(7):1247–1260, July 1999.
- [70] B. Fischl and A.M. Dale. Measuring the thickness of the human cerebral cortex from Magnetic Resonance Images. *Proceedings of the National Academy of Sciences*, 97(20):11050–11055, September 2000.
- [71] B. Fischl, M.I. Sereno, and A.M. Dale. Cortical surface-based analysis II : Inflation, flattening, and a surface-based coordinate system. *Neuroimage*, 9(2):195–207, 1999.
- [72] D. Fize, W. Vanduffel, K. Nelissen, K. Denys, C. Chef d’Hotel, O. Faugeras, and G.A. Orban. The retinotopic organization of primate dorsal V4 and surrounding areas: A functional magnetic resonance imaging study in awake monkeys. *Journal of Neuroscience*, 23:7395–7406, 2003.
- [73] P.T. Fox, F.M. Miezin, J.M. Allman, D.C. Van Essen, and M.E. Raichle. Retinotopic organization of human visual cortex mapped with Positron-Emission Tomography. *Journal of Neuroscience*, 7(3):913–922, 1987.
- [74] L.R. Frank. Anisotropy in high angular resolution diffusion-weighted mri. *Magnetic Resonance in Medicine*, 45:935–939, 2001.
- [75] L. Freire and J.-F. Mangin. Motion correction algorithms may create spurious brain activations in the absence of subject motion. *Neuroimage*, 14(3):709–722, 2001.
- [76] L. Freire, A. Roche, and J.F. Mangin. What is the best similarity measure for motion correction in fMRI time series? *IEEE Transactions on Medical Imaging*, 21(5):470–484, May 2002.

- [77] O. Friman and C.F. Westin. Uncertainty in white matter fiber tractography. In *Proceedings of MICCAI*, pages 107–114. springer-verlag, 2005.
- [78] K. J. Friston. Functional and effective connectivity in neuroimaging: a synthesis. *Human Brain Mapping*, 2:56–78, 1994.
- [79] K.J. Friston, J. Ashburner, et al. *SPM 97 course notes*. Wellcome Department of Cognitive Neurology, University College london, 1997.
- [80] K.J. Friston, O. Josephs, G. Rees, and R. Turner. Nonlinear Event-Related Responses in fMRI. *Magnetic Resonance in Medicine*, 39(1):41–52, 1998.
- [81] K.J. Friston, O. Josephs, E. Zarahn, A. Holmes, S. Rouquette, and Poline J.-B. To Smooth or not to Smooth ? Bias and Efficiency in fMRI Time-Series Analysis. *NeuroImage*, 12:196–208, 2000.
- [82] K.J. Friston, S. Williams, R. Howard, R.S. Frackowiak, and R. Turner. Movement Related Effects in fMRI Time-Series. *Magn Res Med*, 35:346–355, 1996.
- [83] M. Fukunaga, P. van Gelderen, J.A. de Zwart, M. Jansma, and J.H. Duyn. Retinotopic fMRI mapping with pseudo-random stimulus presentation using the m-sequence paradigm. In *NeuroImage (HBM'04)*, 2004.
- [84] G.H. Glover. Deconvolution of impulse response in event-related BOLD fMRI. *NeuroImage*, 9:416–429, 1999.
- [85] J. Gomes and O. Faugeras. Reconciling distance functions and level sets. *Journal of Visual Communication and Image Representation*, 11(2):209–223, 2000.
- [86] C. Goutte, L. K. Hansen, M. G. Liptrot, and E. Rostrup. Feature-space clustering for fMRI meta-analysis. *Human Brain Mapping*, 13(3):165–183, 2001.
- [87] C. Goutte, P. Troft, E. Rostrup, A. Nielsen, and L.K. Hansen. On clustering fMRI time series. *NeuroImage*, 9(3):298–310, 1998.
- [88] Cyril Goutte, Finn Arup Nielsen, and Lars Kai Hansen. Modeling the haemodynamic response in fMRI using smooth FIR filters. *IEEE Transactions on Medical Imaging*, 19(12):1188–1201, 2000.
- [89] K. Grill-Spector, T. Kushnir, S. Edelman, G. Avidan, Y. Itzhak, and R. Malach. Differential processing of objects under various viewing conditions in the human lateral occipital cortex. *Neuron*, 24:187–203, September 1999.

- [90] K. Grill-Spector and R. Malach. fMR-adaptation : a tool for studying the functional properties of human cortical neurons. *Acta Psychologica*, 107:293–321, 2001.
- [91] K. Grill-Spector and R. Malach. The human visual cortex. *Annual Reviews Neuroscience*, 27:649–677, 2004.
- [92] E. Grossman and R. Blake. Brain areas active during visual perception of biological motion. *Neuron*, 35:1167–1176, 2002.
- [93] M. Gur, I. Kagan, and D.M. Snodderly. Orientation and direction selectivity of neurons in V1 of alert monkeys: Functional relationships and laminar distributions. *Cerebral Cortex*, 15(8):1207–1221, 2005.
- [94] M. Guye, G. J.M. Parker, M. Symms, P. Boulby, C.A.M. Wheeler-Kingshott, A. Salek-Haddadi, G.J. Barker, and J.S. Duncana. Combined functional MRI and tractography to demonstrate the connectivity of the human primary motor cortex in vivo. *NeuroImage*, 19:1349–1360, 2003.
- [95] N. Hadjikhani, A. Liu, A. Dale, P. Cavanagh, and R. Tootell. Retinotopy and color sensitivity in human cortical area V8. *Nature Neuroscience*, 1(3):235–241, July 1998.
- [96] M. Hampson, B. S. Peterson, P. Skudlarski, J.C. Gatenby, and J. C. Gore. Detection of functional connectivity using temporal correlations in MR images. *Human Brain Mapping*, 15:247–262, 2002.
- [97] X. Han, C. Xu, and J.L. Prince. A topology preserving level set method for geometric deformable models. *IEEE Transactions on Pattern Analysis and Machine Intelligence*, 25(6):755–768, 2003.
- [98] L.K. Hansen, F.A. Nielsen, and J. Larsen. Exploring fMRI data for periodic signal components. *Artificial Intelligence in Medicine*, 25(1):35–44, 2002.
- [99] K.M. Hasan, D.L. Parker, and A.L. Alexander. Magnetic resonance water self-diffusion tensor encoding optimization methods for full brain acquisition. *Image Analysis and Stereology*, 21(2):87–96, 2002.
- [100] U. Hasson, M. Harel, I. Levy, and R. Malach. Large-scale mirror-symmetry organization of human occipito-temporal object areas. *Neuron*, 37:1027–1041, 2003.
- [101] U. Hasson, I. Levy, M. Behrmann, T. Hendler, and R. Malach. Eccentricity bias as an organizing principle for human high-order object areas. *Neuron*, 34:479–490, 2002.

- [102] L. Hoffart, J. Conrath, N. Wotawa, E. Castet, F. Chavane, G. Masson, and B. Ridings. Etude en IRM fonctionnelle de l'organisation retinotopique du cortex visuel et de la representation corticale de scotomes d'origine retinienne. In *Congr Annuel de la SociFranise d'Ophthalmologie*, May 2005.
- [103] L. Hoffart, N. Wotawa, E. Castet, F. Chavane, J. Conrath, B. Ridings, and G. Masson. Effect of visual scotomas on the retinotopic organization of the human visual cortex: A quantitative fMRI study. In *ARVO conference (Association for Research in Vision and Ophthalmology)*, May 2005.
- [104] G. Holmes. Disturbances of vision by cerebral lesions. *Brit. Journal of Ophthalmology*, 2:353–384, 1918.
- [105] G. Holmes. The organization of the visual cortex in man. *Brit. Proc. Royal Society London Series B (Biol)*, 132:348–361, 1945.
- [106] J.C. Horton and W.F. Hoyt. Quadrantic visual field defects. A hallmark of lesions in extrastriate (V2/V3) cortex. *Brain*, 114:1703–1718, 1991.
- [107] J.C. Horton and W.F. Hoyt. The representation of the visual field in human striate cortex. *Archives of Ophthalmology*, 109:816–824, 1991.
- [108] J.C. Horton, K. Landau, P. Maeder, and W.F. Hoyt. Magnetic resonance imaging of the human lateral geniculate body. *Archives of Neurology*, 47(11):1201–1206, November 1990.
- [109] D.H. Hubel and T.N. Wiesel. Receptive fields, binocular interaction and functional architecture in the cat visual cortex. *J Physiol*, 160:106–154, 1962.
- [110] D.H. Hubel and T.N. Wiesel. Receptive fields and functional architecture in two nonstriate visual areas (18 and 19) of the cat. *Journal of Neurophysiology*, 28:229–289, 1965.
- [111] D.H. Hubel and T.N. Wiesel. Functional architecture of macaque monkey. *Proceedings of the Royal Society, London [B]*, pages 1–59, 1977.
- [112] A. Huk, R. Dougherty, and D. Heeger. Retinotopy and functional subdivision of human areas MT and MST. *The Journal of Neuroscience*, 22(16):7195–7205, August 2002.
- [113] A. Huk, D. Ress, and D. Heeger. Neuronal basis of the motion aftereffect reconsidered. *Neuron*, 32:161–172, October 2001.
- [114] A.C. Huk and D.J. Heeger. Pattern-motion responses in human visual cortex. *Nature neuroscience*, 5(1):72–75, January 2002.

- [115] M. Jackowski, C.Y. Kao, M. Qiu, R.T. Constable, and L.H. Staib. White matter tractography by anisotropic wavefront evolution and diffusion tensors imaging. *Medical Image Analysis*, 9:427–440, 2005.
- [116] S. Jbabdi, P. Bellec, G. Marrelec, and H. Benali. A level set method for building anatomical connectivity paths between brain areas using DTI. In *Proceedings of ISBI*, pages 1024–1027, Arlington, VA, April 2004. IEEE, NIH.
- [117] P. Jezzard and R. S. Balaban. Correction for geometric distortions in echoplanar images from b0 field variations. *Magnetic Resonance in Medicine*, 34:65–73, 1995.
- [118] T. Johnstone, K. Ores-Walsh, L. Greischar, A. Alexander, A. Fox, R. Davidson, and T. Oakes. Motion correction and the use of motion covariates in multiple-subject fMRI analysis. *Human Brain Mapping*, 2006. to appear.
- [119] E.R. Kandel, J.H. Schwartz, and T.M. Jessel. *Principles of Neural Science*. McGraw-Hill, 4th edition, 2000.
- [120] N. Kanwisher and G. Yovel. The Fusiform Face Area: A cortical region specialized for the perception of faces. *Philosophical Transactions of the Royal Society of London*, 2005. in press.
- [121] F. Kherif. *Applications de modèles statistiques multivariés a la résolution de problèmes posés par les données d'imagerie fonctionnelle cérébrale*. PhD thesis, Université Pierre et Marie Curie, Paris, France, January 2003.
- [122] A. Kline, D. Smith, and M. K. Hurdal. Comparison of human cortical surface reconstructions from Magnetic Resonance Imaging data. In *NeuroImage (HBM'05)*, Toronto, Canada, 2005.
- [123] J.J. Koenderink. The structure of images. *Biological Cybernetics*, 50:363–370, 1984.
- [124] A. Kohn and J. Movshon. Adaptation changes the direction tuning of macaque MT neurons. *Nature Neuroscience*, 7:764–772, 2004.
- [125] Z. Kourtzi and E. Huberle. Spatiotemporal characteristics of form analysis in the human visual cortex revealed by rapid event-related fMRI adaptation. *NeuroImage*, 28:440–452, 2005.
- [126] Z. Kourzi and N. Kanwisher. Cortical regions involved in perceiving object shape. *The Journal of Neuroscience*, 20(9):3310–3318, May 2000.
- [127] A. Kraft, M.M. Schira, H. Hagendorf, J. Brocke, and S.A. Brandt. fMRI localizer technique: efficient acquisition and functional properties of single

- retinotopic positions in the human visual cortex. *NeuroImage*, 28:453–463, 2005.
- [128] S. LaConte, J. Anderson, M. Suraj, J. Ashe, S. Frutiger, K. Rehm, L. K. Hansen, E. Yacoub, X. Hu, D. Rottenberg, and S. Strother. The evaluation of preprocessing choices in single-subject BOLD fMRI using NPAIRS performance metrics. *NeuroImage*, 18(1):10–27, 2003.
- [129] P.C. Lauterbur. Image formation by induced local interactions: examples employing nuclear magnetic resonance. *Nature*, 242:190–191, 1973.
- [130] M. Lazar, D.M. Weinstein, J.S. Tsuruda, K.M. Hasan, K. Arfanakis, M.E. Meyerand, B. Badie, H.A. Rowley, V. Haughton, A. Field, and A.L. Alexander. White matter tractography using diffusion tensor deflection. In *Human Brain Mapping*, volume 18, pages 306–321, 2003.
- [131] D. LeBihan, E. Breton, D. Lallemand, P. Grenier, E. Cabanis, and M. Laval-Jeantet. MR imaging of intravoxel incoherent motions: Application to diffusion and perfusion in neurologic disorders. *Radiology*, 161(2):401–407, 1986.
- [132] S. Lehericy, C. Lenglet, J. Doyon, H. Benali, P.F. Van de Moortele, G. Sapiro, O. Faugeras, R. Deriche, and K. Ugurbil. Activation shifts from the premotor to the sensorimotor territory of the striatum during the course of motor sequence learning. In *11th Annual Meeting of the Organization for Human Brain Mapping*, Toronto, June 2005.
- [133] C. Lenglet, R. Deriche, and O. Faugeras. Diffusion tensor magnetic resonance imaging: Brain connectivity mapping. Technical Report 4983, INRIA, November 2003.
- [134] C. Lenglet, R. Deriche, and O. Faugeras. Inferring white matter geometry from diffusion tensor MRI: Application to connectivity mapping. In T. Pajdla and J. Matas, editors, *Proceedings of the 8th European Conference on Computer Vision*, Prague, Czech Republic, May 2004. Springer-Verlag.
- [135] C. Lenglet, M. Rousson, R. Deriche, and O. Faugeras. Statistics on multivariate normal distributions: A geometric approach and its application to diffusion tensor MRI. Technical Report 5242, INRIA, June 2004.
- [136] T.T. Liu, L.R. Frank, E.C. Wong, and R.B. Buxton. Detection power, estimation efficiency and predictability in event-related fMRI. *NeuroImage*, 13:759–773, 2001.
- [137] N. K. Logothetis. The neural basis of the Blood-Oxygen-Level-Dependent functional Magnetic Resonance Imaging signal. *Philos. Trans. Royal Society London*, 357(1424):1003–1037, August 2002.

- [138] N.K. Logothetis, J. Pauls, M. Augath, T. Trinath, and A. Oeltermann. Neurophysiological investigation of the basis of the fMRI signal. *Nature*, 412(6843):150–157, 2001.
- [139] L. Lopez-Perez, R. Deriche, and N. Sochen. The beltrami flow over triangulated manifolds. In Milan Sonka, Ioannis A. Kakadiaris, and Jan Kybic, editors, *Computer Vision and Mathematical Methods in Medical and Biomedical Image Analysis: ECCV 2004 Workshops CVAMIA and MMBIA, Prague, Czech Republic, May 15, 2004, Revised Selected Papers*, volume 3117 of *Lecture Notes in Computer Science*, pages 135–144. Springer-Verlag Heidelberg, October 2004.
- [140] D.C. Lyon and J.H. Kaas. Evidence for a modified V3 with dorsal and ventral halves in macaque monkeys. *Neuron*, 33:453–461, January 2002.
- [141] D.C. Lyon and J.H. Kaas. Evidence from V1 connections for both dorsal and ventral subdivisions of V3 in three species of new world monkeys. *Journal of Comparative Neurology*, 449(3):281–297, 2002.
- [142] J-F. Mangin. Entropy minimization for automatic correction of intensity nonuniformity. In *IEEE MMBIA Workshop*, pages 162–169, Hilton Head Island, South Carolina, 2000. IEEE Press.
- [143] J-F. Mangin, O. Coulon, and V. Frouin. Robust brain segmentation using histogram scale-space analysis and mathematical morphology. In W. M. Wells, A. Colchester, and S. Delp, editors, *Proc. 1st MICCAI*, LNCS-1496, pages 1230–1241, MIT, Boston, October 1998. Springer Verlag.
- [144] J.-F. Mangin, V. Frouin, I. Bloch, J. Régis, and J. Lopez-Krahe. From 3D Magnetic Resonance Imaging to structural representations of the cortex topography using topology preserving deformations. *Journal of Mathematical Imaging and Vision*, 5:297–318, 1995.
- [145] J.-F. Mangin, C. Poupon, Y. Cointepas, D. Rivière, D. Papadopoulos-Orfanos, C. A. Clark, J. Régis, and D. Le Bihan. A framework based on spin glass models for the inference of anatomical connectivity from Diffusion-Weighted MR data. *NMR in Biomedicine*, 15:481–492, 2002.
- [146] G. Marrelec, H. Benali, P. Ciuciu, and J.-B. Poline. Bayesian estimation of the hemodynamic response function in functional MRI. In *MAXENT 2001 (21st Int. Work. on Bayesian Inference and Maximum Entropy Methods in Science and Engineering)*, 2001.

- [147] G. Marrelec, P. Ciuciu, M. Péligrini-Issac, and H. Benali. Estimation of the hemodynamic response function in event-related functional MRI: Bayesian networks as a framework for efficient bayesian modeling and inference. *IEEE Trans. Med. Imag.*, 23(8):959–967, August 2004.
- [148] D.J. McKeefry and S. Zeki. The position and topography of the human color centre as revealed by functional Magnetic Resonance Imaging. *Brain*, 120(12):2229–2242, 1997.
- [149] F. Méholi, G. Sapiro, and S. Osher. Solving variational problems and partial differential equations mapping into general target manifolds. *Journal of Computational Physics*, 195(1):263–292, 2004.
- [150] R.S. Menon, S. Ogawa, J.P. Strupp, and K. Ugurbil. Ocular dominance in human V1 demonstrated by functional Magnetic Resonance Imaging. *Journal of Neurophysiology*, 77(5):2780–2787, May 1997.
- [151] A. Mikami, W. Newsome, and R. Wurtz. Motion selectivity in macaque visual cortex. ii. spatiotemporal range of directional interactions in MT and V1. *Journal of Neurophysiology*, 55(6):1328–1339, 1986.
- [152] A.D. Milner and M.A. Goodale. *The visual brain in action*. Oxford University Press, 1995.
- [153] S. Mori, B.J. Crain, V.P. Chacko, and P.C.M. Van Zijl. Three-dimensional tracking of axonal projections in the brain by Magnetic Resonance Imaging. *Annals of Neurology*, 45(2):265–269, February 1999.
- [154] S.O. Murray and E. Wojciulik. Attention increases neural selectivity in the human lateral occipital complex. *Nature Neuroscience*, 7(1):70–74, January 2004.
- [155] L. Naccache and S. Dehaene. The priming method : imaging unconscious repetition priming reveals an abstract representation of number in the parietal lobes. *Cerebral Cortex*, 11:966–974, 2001.
- [156] T.R. Oakes, T. Johnstone, K. Ores Walsh, L. Greischar, A. Alexander, A. Fox, and R. Davidson. Comparison of fMRI motion correction software tool. *Neuroimage*, 2006. to appear.
- [157] L. O’Donnell, S. Haker, and C.F. Westin. New approaches to estimation of white matter connectivity in Diffusion Tensor MRI: Elliptic PDEs and geodesics in a tensor-warped space. In *MICCAI*, 2002. 459–466.

- [158] S. Ogawa, T.M. Lee, A.R. Kay, and D.W. Tank. Brain magnetic resonance imaging with contrast dependent on blood oxygenation. In *Proceedings of the National Academy of Sciences of the United States of America*, volume 87, pages 9868–9872, December 1990.
- [159] S. Ogawa, T.M. Lee, A.S. Nayak, and P. Glynn. Oxygenation-sensitive contrast in magnetic resonance image of rodent brain at high magnetic field. *Magnetic Resonance in Medicine*, 14(1):68–78, 1990.
- [160] C. Olman, I. Ronen, K. Ugurbil, and D.-S. Kim. Retinotopic mapping in cat visual cortex using high-field functional Magnetic Resonance Imaging. *Journal Neuroscience Methods*, 131:161–170, 2003.
- [161] G. Orban, D. Fize, et al. Similarities and differences in motion processing between the human and macaque brain: evidence from fMRI. *Neuropsychologia*, 41:1757–1768, 2003.
- [162] G.A. Orban, H. Kennedy, and J. Bullier. Velocity sensitivity and direction selectivity of neurons in areas V1 and V2 of the monkey: influence of eccentricity. *Journal of Neurophysiology*, 56(2):462–480, August 1986.
- [163] G.A. Orban, D. Van Essen, and W. Vanduffel. Comparative mapping of higher visual areas in monkeys and humans. *Trends Cognitive Sciences*, 8(7):315–324, 2004.
- [164] S. Osher. A level set formulation for the solution of the dirichlet problem for a hamilton-jacobi equations. *SIAM Journal on Mathematical Analysis*, 24(5):1145–1152, 1993.
- [165] E. Ozarslan, B. C. Vemuri, and T. Mareci. Fiber orientation mapping using generalized diffusion tensor imaging. In *ISBI*, pages 1036–1039, 2004.
- [166] S. Palmer. *Vision Science : Photons to Phenomenology*. MIT Press, 1999.
- [167] G.J.M. Parker. Tracing fibers tracts using Fast Marching. In *Proceedings of the International Society of Magnetic Resonance*, volume 85, 2000.
- [168] G.J.M. Parker, K.E. Stephan, G.J. Barker, J.B. Rowe, D.G. MacManus, C.A.M. Wheeler-Kingshott, O. Ciccarelli, R.E. Passingham, R.L. Spinks, R.N. Lemon, and R. Turner. Initial demonstration of in vivo tracing of axonal projections in the macaque brain and comparison with the human brain using Diffusion Tensor Imaging and Fast Marching Tractography. *NeuroImage*, 15(4):797–809, April 2002.

- [169] G.J.M. Parker, C.A.M. Wheeler-Kingshott, and G.J. Barker. Estimating distributed anatomical connectivity using Fast Marching Methods and Diffusion Tensor Imaging. *Trans. Med. Imaging*, 21(5):505–512, 2002.
- [170] L. Pauling and C.D. Coryell. The magnetic properties and structure of hemoglobin, oxyhemoglobin and carbonmonoxyhemoglobin. *Proceedings of the National Academy of Science*, 22:206–216, 1936.
- [171] V. Perlberg, P. Bellec, G. Marrelec, S. Jbabdi, and H. Benali. Selection of spatially independent components to explain functional connectivity in fMRI. In *Proceedings of ISBI*, Arlington, VA, April 2004. IEEE.
- [172] V. Perlberg, P. Bellec, G. Marrelec, S. Jbabdi, M. Prini-Issac, S. Lehic, J. Doyon, and H. Benali. Selection of spatially independent components to reduce physiological noise in fMRI data. In *NeuroImage (HBM'04)*, June 2004.
- [173] M. Piazza, V. Izard, P. Pinel, D. Le Bihan, and S. Dehaene. Tuning curves for approximate numerosity in the human intraparietal sulcus. *Neuron*, 44:547–555, October 2004.
- [174] C. Pierpaoli, P. Jezzard, P.J. Basser, A. Barnett, and G. Di Chiro. Diffusion Tensor MR imaging of human brain. *Radiology*, 201:637–648, 1996.
- [175] Jean-Philippe Pons. *Contributions méthodologiques et appliquées à la méthode des modèles déformables*. PhD thesis, Ecole Nationale des Ponts et Chaussées, 2005.
- [176] E. Prados, C. Lenglet, J.P. Pons, N. Wotawa, R. Deriche, O. Faugeras, and S. Soatto. Control theory and fast marching methods for brain connectivity mapping. In *Proc. IEEE Computer Society Conference on Computer Vision and Pattern Recognition*, New York, NY, June 2006.
- [177] W. Press, A. Brewer, R. Dougherty, A. Wade, and B. Wandell. Visual areas and spatial summation in human visual cortex. *Vision Research*, 41:1321–1332, 2001.
- [178] N. Priebe and S. Lisberger. Constraints on the source of short-term motion adaptation in macaque area MT. II. Tuning of neural circuit mechanisms. *Journal of Neurophysiology*, 88:370–382, 2002.
- [179] N. Priebe and S. Lisberger. Constraints on the source of short-term motion adaptation in macaque area MT.I. The role of input and intrinsic mechanisms. *Journal of Neurophysiology*, 88:354–369, 2002.

- [180] M.E. Raichle. Images of the mind: Studies with modern imaging techniques. *Annual Review of Psychology*, 45:333–356, 1994.
- [181] M.E. Raichle, W.R. Martin, P. Herscovitch, M.A. Mintun, and J. Markham. Brain blood flow measured with intravenous H<sub>2</sub>(<sup>15</sup>)O. II. implementation and validation. *Journal of Nuclear Medicine*, 9:790–798, 1983.
- [182] G. Rees, C.D. Frith, and N. Lavie. Modulating irrelevant motion perception by varying attentional load in an unrelated task. *Science*, 278:1616–1619, November 1997.
- [183] C.S. Roy and C.S. Sherrington. On the regulation of the blood supply of the brain. *Journal of Physiology (London)*, 11:85–108, 1890.
- [184] H. Sawamura, S. Georgieva, R. Vogels, W. Vanduffel, and G.A. Orban. Using functional Magnetic Resonance Imaging to assess adaptation and size invariance of shape processing by humans and monkeys. *Journal of Neuroscience*, 25(17):4294–4306, April 2005.
- [185] H. Sawamura, G.A. Orban, and R. Vogels. Selectivity of neuronal adaptation does not match response selectivity: a single-cell study of the fMRI adaptation paradigm. *Neuron*, 49:307–318, 2006.
- [186] P. Schiller, B. Finlay, and S. Volman. Quantitative studies of single-cell properties in monkey striate cortex. v. multivariate statistical analyses and models. *Journal of Neurophysiology*, 39(6):1362–1374, November 1976.
- [187] M.M. Schira, M. Fahle, T.H. Donner, A. Kraft, and S.A. Brandt. Differential contribution of early visual areas to the perceptual process of contour processing. *Journal of Neurophysiology*, 91(4):1716–1721, 2004.
- [188] K.A. Schneider and S. Kastner. Visual responses of the human superior colliculus: a high resolution functional magnetic resonance imaging study. *Journal of Neurophysiology*, 94:2491–2503, October 2005.
- [189] K.A. Schneider, M.C. Richter, and S. Kastner. Retinotopic organization and functional subdivisions of the human Lateral Geniculate Nucleus: A high-resolution functional Magnetic Resonance Imaging study. *Journal of Neuroscience*, 24(41):8975–8985, October 2004.
- [190] W. Schneider, D.C. Noll, and J.D. Cohen. Functional topographic mapping of the cortical ribbon in human vision with conventional MRI scanners. *Nature*, 365:150–153, 1993.

- [191] S. Schwartz, P. Vuilleumier, C. Hutton, A. Maravita, R. Dolan, and J. Driver. Attentional load and sensory competition in human vision: modulation of fMRI responses by load at fixation during task-irrelevant stimulation in the peripheral visual field. *Cerebral Cortex*, September 2004.
- [192] M.I. Sereno, A.M. Dale, J.B. Reppas, K.K. Kwong, J.W. Belliveau, T.J. Brady, B.R. Rosen, and R.B.H. Tootell. Borders of multiple visual areas in humans revealed by functional Magnetic Resonance Imaging. *Science*, pages 889–893, 1995.
- [193] M.I. Sereno, C.T. McDonald, and J.M. Allman. Analysis of retinotopic maps in extrastriate cortex. *Cerebral Cortex*, 4:601–620, 1994.
- [194] M.I. Sereno, S. Pitzalis, and A. Martinez. Mapping of contralateral space in retinotopic coordinates by a parietal cortical area in humans. *Science*, 294:1350–1354, November 2001.
- [195] M.I. Sereno and R.B.H. Tootell. From monkeys to humans: what do we now know about brain homologies? *Current Opinion in Neurobiology*, 15:135–144, 2005.
- [196] M.I. Sereno, H.H. Yu, and E.K. Vogel. Mapping retinotopy in higher level extrastriate visual areas in humans. In *Meeting of the Society for Neuroscience*, San Diego, 2001.
- [197] J.A. Sethian. *Level Set Methods*. Cambridge University Press, 1996.
- [198] D. Shafir, N. Sochen, and R. Deriche. Regularization of mappings between implicit manifolds of arbitrary dimension and codimension. In *Variational, Geometric, and Level Set Methods in Computer Vision: Third International Workshop, VLSP*, volume 3752 of *Lecture Notes in Computer Science*, page 344, Beijing, China, October 2005. Springer-Verlag GmbH.
- [199] A. Shmuel, M. Augath, A. Oeltermann, J. Pauls, and N.K. Logothetis. Decreases in neuronal activity and negative BOLD response in non-stimulated regions of monkey V1. In *Journal of Vision*, volume 4, 2004.
- [200] S. Slotnick and S. Yantis. Efficient acquisition of human retinotopic maps. *Human Brain Mapping*, 18:22–29, 2003.
- [201] S.M. Smirnakis, A.A. Brewer, M.C. Schmid, A.A. Tolias, A. Schz, M. Augath, W. Inhoffen, B.A. Wandell, and N.K. Logothetis. Lack of long-term cortical reorganization after macaque retinal lesions. *Nature*, 435:300–307, May 2005.

- [202] A. Smith, M. Greenlee, K. Singh, F. Kramer, and J. Hennig. The processing of first- and second-order motion in human visual cortex assessed by functional Magnetic Resonance Imaging (fMRI). *The Journal of Neuroscience*, 18(10):3816–3830, May 1998.
- [203] A.T. Smith, K.D. Singh, A.L. Williams, and M.W. Greenlee. Estimating receptive field size from fMRI data in human striate and extrastriate visual cortex. *Cerebral cortex*, 11:1182–1190, 2001.
- [204] A.T. Smith, A.L. Williams, and K.D. Singh. Negative BOLD in the visual cortex: evidence against blood stealing. *Human Brain Mapping*, 21:213–220, 2004.
- [205] N. Sochen, R. Deriche, and L. Lopez-Perez. Variational Beltrami flows over manifolds. In *International Conference on Image Processing*, volume 1, pages 861–864, 2003.
- [206] E.O. Stejskal and J.E. Tanner. Spin diffusion measurements: spin echoes in the presence of a time-dependent field gradient. *Journal of Chemical Physics*, 42:288–292, 1965.
- [207] J. Stern, K. Schaper, K. Rehm, M. Hurdal, D. Sumners, and D. Rottenberg. Automatic surface extraction by discrete, topologically-controlled, region growing. In *NeuroImage (HBM'01)*, London, UK, 2001.
- [208] S. Sunaert. *Functional magnetic resonance imaging studies of visual motion processing in the human brain*. PhD thesis, Leuven University, 2001.
- [209] S. Sunaert, P. Van Hecke, G. Marchal, and G.A. Orban. Motion-responsive regions of the human brain. *Experimental Brain Research*, 127(4):355–70, August 1999.
- [210] J.S. Sunness, T. Liu, and S. Yantis. Retinotopic mapping of the visual cortex using fMRI in a patient with central scotomas from atrophic macular degeneration. *Ophthalmology*, 111:1595–1598, 2004.
- [211] D. Tadin, J. Lappin, L. Gilroy, and R. Blake. Perceptual consequences of centre-surround antagonism in visual motion processing. *Nature*, 424:313–315, July 2003.
- [212] Bertrand Thirion. *Analyse de données d'IRM fonctionnelle: statistiques, information et dynamique*. PhD thesis, École Doctorale Télécom Paris, October 2003.

- [213] A. Tolias, G. Keliris, S. Smirnakis, and N. Logothetis. Neurons in macaque area V4 acquire directional tuning after adaptation to motion stimuli. *Nature Neuroscience*, 8(5):591–593, May 2005.
- [214] A.S. Tolias, S.M. Smirnakis, M.A. Augath, T. Trinath, and N.K. Logothetis. Motion processing in the macaque: revisited with functional Magnetic Resonance Imaging. *The Journal of Neuroscience*, 21(21):8594–8601, November 2001.
- [215] A. Toosy, O. Ciccarelli, et al. Characterising function-structure relationships in the human visual system with functional MRI and Diffusion Tensor Imaging. *NeuroImage*, 21:1452–1463, 2004.
- [216] R. Tootell, N. Hadjikhani, J. Mendola, S. Marrett, and A. Dale. From retinotopy to recognition: fMRI in human visual cortex. *Trends in Cognitive Sciences*, 2(5):174–183, May 1998.
- [217] R. Tootell, N. Hadjikhani, W. Vanduffel, A. Liu, J. Mendola, M. Sereno, and A. Dale. Functional analysis of primary visual cortex (v1) in humans. In *Proceedings of the National Academy of Sciences USA*, volume 95, pages 811–817, February 1998.
- [218] R. Tootell, J. Reppas, K. Kwong, et al. Functional analysis of human MT and related visual cortical areas using Magnetic Resonance Imaging. *The Journal of Neuroscience*, 15(4):3215–3230, April 1995.
- [219] R. Tootell, J. Reppas, K. Kwong, R. Malach, R. Born, T. Brady, B. Rosen, and J. Belliveau. Visual motion aftereffect in human cortical area MT revealed by functional Magnetic Resonance Imaging. *Nature*, 375:139–141, May 1995.
- [220] R. Tootell, E. Switkes, M. Silverman, and S. Hamilton. Functional anatomy of the macaque striate cortex. ii. retinotopic organization. *Journal of neuroscience*, 8(5):1531–1568, 1988.
- [221] R. Tootell, D. Tsao, and W. Vanduffel. Neuroimaging weights in: humans meet macaques in "primate" visual cortex. *The Journal of Neuroscience*, 23(10):3981–3989, May 2003.
- [222] R.B. Tootell and N. Hadjikhani. Where is 'Dorsal V4' in human visual cortex? retinotopic, topographic and functional evidence. *Cerebral Cortex*, 11:298–311, April 2001.
- [223] R.B. Tootell and J.B. Taylor. Anatomical evidence for MT and additional cortical visual areas in humans. *Cerebral Cortex*, 5:39–55, 1995.

- [224] R.B.H. Tootell, J.D. Mendola, N.K. Hadjikhani, P.J. Ledden, A.K. Liu, J.B. Reppas, M.I. Sereno, and A.M. Dale. Functional analysis of V3A and related areas in human visual cortex. *The journal of Neuroscience*, 17(18):7060–7078, September 1997.
- [225] D. Tschumperlé and R. Deriche. Variational frameworks for DT-MRI estimation, regularization and visualization. In *Proceedings of the 9th International Conference on Computer Vision*, pages 116–121, Nice, France, 2003. IEEE Computer Society, IEEE Computer Society Press.
- [226] D. Tuch. Q-ball imaging. *Magnetic Resonance in Medicine*, 52(6):1358–1372, 2004.
- [227] C.W. Tyler, L.T. Likova, C-C. Chen, L.L. Kontsevich, M.M. Schira, and A.R. Wade. Extended concepts of occipital retinotopy. *Current Medical Imaging Reviews*, 2005. in press.
- [228] L.G. Ungerleider and M. Mishkin. *Two cortical visual systems.*, pages 549–586. MIT Press, 1982.
- [229] L.M. Vaina, J. Solomon, S. Chowdhury, P. Sinha, and J.W. Belliveau. Functional neuroanatomy of biological motion perception in humans. *Proceedings of the National Academy of Science*, 98(20):11656–11661, 2001.
- [230] D. Van Essen and S. Zeki. The topographic organization of rhesus monkey prestriate cortex. *Journal of Neurophysiology*, 277:193–226, April 1978.
- [231] D.C. Van Essen. A tension-based theory of morphogenesis and compact wiring in the central nervous system. *Nature*, 385:313–318, January 1997.
- [232] D.C. Van Essen, J.H.R. Maunsell, and J.L. Bixby. The Middle Temporal visual area in the macaque: myeloarchitecture, connections, functional properties and topographic organization. *Journal of Comparative Neurology*, 199:293–326, 1981.
- [233] S. Van Oostende, S. Sunaert, P. Van Hecke, G. Marchal, and G. Orban. The Kinetic Occipital (KO) region in man: an fMRI study. *Cerebral Cortex*, 7:690–701, 1997.
- [234] W. Vanduffel, D. Fize, H. Peuskens, K. Denys, S. Sunaert, J.T. Todd, and G. A. Orban. Extracting 3d from Motion: Differences in Human and Monkey Intraparietal Cortex. *Science*, 298:413–415, 2002.
- [235] S. Vanni, L. Henriksson, and A.C. James. Multifocal fMRI mapping of visual cortical areas. *NeuroImage*, 27:95–105, 2005.

- [236] A. Vazquez and D. Noll. Nonlinear aspects of the BOLD response in functional MRI. *NeuroImage*, 7(2):108–118, 1998.
- [237] A. Wade, A. Brewer, J. Rieger, and B. Wandell. Functional measurements of human ventral occipital cortex : retinotopy and colour. *Phil. Trans. R. Soc. Lond.*, 357:963–973, 2002.
- [238] B.A. Wandell, A.A. Brewer, and R.F. Dougherty. Visual field map clusters in human cortex. *Phil. Trans. of the Royal Society London*, 360:693–707, 2005.
- [239] J. Warnking. *Délimitation des aires visuelles rétinotopiques chez l’homme par IRM fonctionnelle*. PhD thesis, Université Joseph Fourier-Grenoble I, July 2002.
- [240] J. Warnking, M. Dojat, A. Guerin-Dugue, C. Delon-Martin, S. Olympeff, N. Richard, A. Chehikian, and C. Segebarth. fMRI retinotopic mapping - step by step. *NeuroImage*, 17:1665–1683, 2002.
- [241] J. Watson, R. Myers, R. Frackowiak, J. Hajnal, R. Woods, J. Mazziotta, S. Shipp, and S. Zeki. Area V5 of the human brain: evidence from a combined study using Positron Emission Tomography and Magnetic Resonance Imaging. *Cerebral Cortex*, 3:79–94, 1993.
- [242] D.J. Werring, C.A. Clark, G.J.M. Parker, D.H. Miller, A.J. Thompson, and G.J. Barker. A direct demonstration of both structure and function in the visual system: combining Diffusion Tensor Imaging with functional Magnetic Resonance Imaging. *NeuroImage*, 9:352–361, 1999.
- [243] C.F Westin, S.E Maier, H. Mamata, A. Nabavi, F.A. Jolesz, and R. Kikinis. Processing and visualization of diffusion tensor MRI. In *In proceedings of Medical Image Analysis*, volume 6(2), pages 93–108, 2002.
- [244] A.P. Witkin. Scale-space filtering. In *International Joint Conference on Artificial Intelligence*, pages 1019–1021, 1983.
- [245] K.J. Worsley and K.J. Friston. Analysis of fMRI time-series revisited - again. *NeuroImage*, 2:173–181, 1995.
- [246] K.J. Worsley, C.H. Liao, J. Aston, V. Petre, G.H. Duncan, F. Morales, and Evans A.C. A general statistical analysis for fMRI data. *NeuroImage*, 15:1–15, 2002.
- [247] K.J. Worsley, S. Marett, P. Neelin, A.C. Vandal, K.J. Friston, and A.C. Evans. A unified statistical approach for determining significant signals in images of cerebral activation. In *Human Brain Mapping*, volume 4, pages 58–73, 1996.

- [248] K.J. Worsley, S. Marrett, P. Neelin, and A.C. Evans. A three-dimensional statistical analysis for CBF activation studies in human brain. *Journal of Cerebral Blood Flow and Metabolism*, 12:900–918, 1992.
- [249] K.J. Worsley, J-B. Poline, K.J. Friston, and Evans A.C. Characterizing the response of PET and fMRI data using multivariate linear models. *NeuroImage*, 6:305–319, 1997.
- [250] N. Wotawa, C. Lenglet, M. Roth, B. Nazarian, J.-L. Anton, R. Majhoub, R. Deriche, and O. Faugeras. Combined fMRI and DTI of the human low level visual cortex. In *NeuroImage (HBM'05)*, Toronto, Canada, 2005.
- [251] N. Wotawa, J.-P. Pons, L. Lopez, R. Deriche, and O. Faugeras. fMRI data smoothing constrained to the cortical surface: a comparison of the level-set and mesh-based approaches. In *NeuroImage (HBM'04)*, 2004.
- [252] N. Wotawa, B. Thirion, E. Castet, J-L. Anton, and O. Faugeras. Efficient human retinotopic mapping using fMRI. In Tomas Paus, Ed Bullmore, and Jonathan D. Cohen, editors, *NeuroImage (HBM'03)*, New York, USA, 2003. Academic Press.
- [253] S. Zeki. Representation of central visual fields in prestriate cortex of monkey. *Brain Research*, 14:271–291, 1969.
- [254] S. Zeki. Improbable areas in the visual brain. *Trends in Neurosciences*, 26(1):23–26, January 2003.
- [255] S. Zeki. Thirty years of a very special visual area, area V5. *The Journal of Physiology*, 557(1):1–2, May 2004.
- [256] S. Zeki. The Ferrier lecture 1995. behind the seen: the functional specialization of the brain in space and time. *Philosophical Transactions of the Royal Society*, 360:1145–1183, 2005.
- [257] S. Zeki, J. Watson, C. Lueck, K. Friston, C. Kennard, and R. Frackowiack. A direct demonstration of functional specialization in human visual cortex. *Journal of neuroscience*, 11(3):641–649, 1991.

